

# **Development of Plasma Polymer Thin Films for Control of Cell and Microbe Attachment**

Yali Li

BEng (Hons. I)

*A thesis for the degree of Doctor of Philosophy under a joint  
research program with Monash University and CSIRO*

*Oct 2014*

Department of Materials Engineering  
Monash University

## ERRATA

p 96, replace Table 4.1 with the following table,

Atomic %	C	O	Si
20 W on Si wafer	$70.93 \pm 0.36$	$28.97 \pm 0.17$	-
20 W - Topside ITO	$70.16 \pm 0.78$	$29.44 \pm 0.80$	-
20 W - Underside	$70.13 \pm 0.13$	$25.43 \pm 0.33$	$4.22 \pm 0.14$
50 W on Si wafer	$79.55 \pm 1.99$	$20.46 \pm 1.99$	-
50 W - Topside ITO	$81.22 \pm 2.83$	$18.68 \pm 2.84$	-
50 W - Underside	$72.23 \pm 1.78$	$27.19 \pm 0.87$	$0.55 \pm 0.1$

p 123, In figure 5.2, replace labels 'HM10B', 'HM20B', 'DG20B', 'DG40B', 'AA20B' and 'AA40B' with 'HM10', 'HM20', 'DG20', 'DG40', 'AA20' and 'AA40'. Apply same changes to figure 5.3.

## ADDENDUM

p 67, add after 3.2.2 plasma polymerisation the following figure

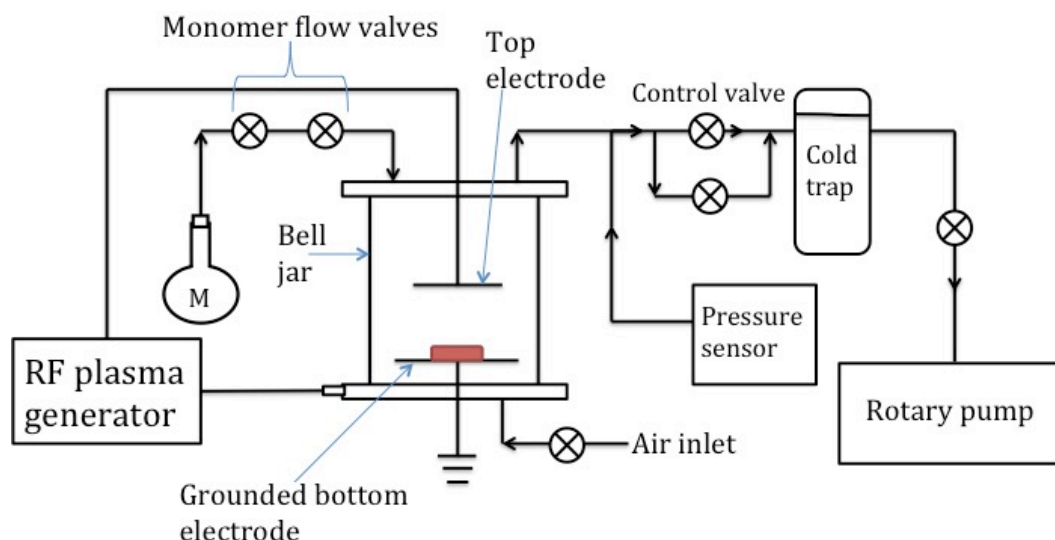


Figure 3.1 Schematic of the standard radio frequency plasma reactor vacuum system. The red item indicates the sample position, which is on the bottom electrode. The load power of the system is shown on the radio frequency generator. The base pressure of the reaction chamber is less than 0.1 Pa.

There are various reactor designs for plasma polymerisation processes, and no standard way was established for measuring film deposition rates. For capacitively coupled electrode design, deposition rates differ and depend on the monomer of choice, the reactor geometry and the processing parameters. Low deposition rates can be less than  $0.1 \text{ nm s}^{-1}$ , while high rates can reach  $2 \text{ nm s}^{-1}$ . [Ref. 4 & 14 of Chapter 3.]

p 68, add to last line, “some micropatterned films were analysed using Stylus Profilometry to determine the thickness. “

p 79, add after 2<sup>nd</sup> line of paragraph 2, “The film thickness was > 100 nm at the centre and reduced continuously to ~ 35 nm (dark brown region in between circles). This pattern repeated periodically when measured from one circular feature to another. The deposition rate directly under the holes of the upper electrode is 0.86 nm s<sup>-1</sup>, and gradually decreased to less than 0.3 nm s<sup>-1</sup> in between the holes.”

p 93, add to caption of Scheme 4.1, “ DGpp coated ITO glass were placed on a flat surface in the fume hood. A piece of CDST (7 mm long) was applied to cover one side of the sample using a smooth even motion. The CDST was pressed with the middle part of a sterile tweezers for a few seconds to make sure the tape fully adhered to the surface, without any bubbles. The surface of the sample was held flat with the tip of the tweezers and the CDST was peeled back at an angle of approximately 120 – 150 degrees.

p 164, add after paragraph 2, “the change in size and number of round clustered features may be a result of loosely bound plasma polymer fragments being removed by immersion in MilliQ water and the azide solution.”

Under the Copyright Act 1968, this thesis must be used only under the normal conditions of scholarly fair dealing. In particular no results or conclusions should be extracted from it, nor should it be copied or closely paraphrased in whole or in part without the written consent of the author. Proper written acknowledgement should be made for any assistance obtained from this thesis.

I certify that I have made all reasonable efforts to secure copyright permissions for third-party content included in this thesis and have no knowingly added copyright content to my work without the owner's permission.

Dedicated to my parents,  
Li Chen Liang and Duan Cui Rong

## Thesis abstract

Functional plasma polymer films have gained increasing attention in recent decades to selectively modify the surface of biomaterials. Although many applications have been identified for plasma polymerisation, the fundamental aspects of plasma polymer film growth are still poorly understood. In this thesis, both the film growth mechanism and applications of the coatings to control cell and microbe attachment *in vitro* were investigated.

The main part of the thesis focused on fabrication of diethylene glycol dimethyl ether (diglyme, DG) plasma polymer films via radio frequency glow discharge (RFGD) plasma polymerisation. By manipulation of process parameters, diglyme plasma polymer films (DGpp) could perform as low-fouling coatings that was similar to poly(ethylene glycol) (PEG) grafted layers. Systematic study on the effect of load powers to DGpp film chemistry was carried out. The surface chemistry of the synthesised films was studied by X-ray photoelectron spectroscopy (XPS) and near edge X-ray absorption fine structure (NEXAFS) spectroscopy. It was found that higher load power led to more fragmentation of the monomer, therefore less retention of ether functionality. The resultant films were used for protein adsorption, cell culture and microbe attachment studies *in vitro*. Films produced with high ether concentration generally were resistant to fouling, meanwhile, relatively low ether concentration allowed a higher quantity of protein adsorption, cell and microbe attachment. The DGpp films were very smooth in nature. They have been deposited onto amyloid fibril networks (AFNs) that have roughness greater than the film *per se*. The change in roughness resulted in differences in amount of cell attachment and spreading. The unique structure of the AFNs was still visible under atomic force microscopy (AFM) after DGpp deposition, thus a study to decipher the mechanism of film growth was conducted.

During the deposition of the films, various substrates, such as silicon wafers, glass and polymers, were used to test the adhesion strength of DGpp films. On silicon wafers, the films were stable in atmospheric conditions but became patchy after immersion in water or cell culture solutions for prolonged times. In addition, it was found DGpp films were most stable on polymeric substrates but were easily delaminated from indium tin oxide (ITO) coated glass. The low adhesion strength on ITO glass was exploited further in this thesis to expose the substrate-film interface by peeling off the film using double-sided tape. This simple method allowed investigation of the chemistry of the DGpp films growth at the initial stage. Adhesion of plasma polymer film to the substrate depends on the interaction of gas phase species in the plasmas with the top surface of the material. In order to gain a better understanding of the interface mixing between plasma polymer films and polymeric substrates, DGpp films were deposited (under the same conditions) onto six types of plasma polymer films. Non-invasive methods, neutron and X-ray reflectometry (NR, XRR) were employed to characterise these bilayer constructs and showed changes in interfacial width depending on the base plasma polymer layer.

Since the DGpp film was not very efficient in antimicrobial application for the long term, a new plasma polymer based route was selected to combat the infection problem of biomaterial surfaces. A brominated coating was produced using RFGD plasma polymerisation and modified with sodium azide to incorporate azide functionality onto the surface. The resultant coatings were tested *in vitro* against *Staphylococcus epidermidis*, *Pseudomonas aeruginosa* and *Candida albicans*. Excellent antimicrobial property was presented on azide immobilised surfaces. On the other hand, those coatings are compatible with HeLa cell culture and induced minimal lysis of human erythrocytes.

## Statement of originality

I, Yali Li hereby declare that, this thesis contains no materials previously published or written by another person, except where due reference is made in the text of this thesis. I also declare that this thesis has not been submitted, either in part or whole, for any degree at any university or other institute of tertiary education.

**Signed:** \_\_\_\_\_

**Date:** \_\_\_\_\_

## Acknowledgements

I would like to thank my supervisors, Associated Professor John Forsythe, Dr. Ben Muir and Dr. David Nisbet for their support, guidance and encouragement throughout my entire PhD journey. I am very grateful for their valuable, knowledgeable feedback and advice. I would also like to thank Monash University and Faculty of Engineering for scholarship fundings during three and a half year of my PhD.

I would like to acknowledge Dr. Christ Easton from CSIRO. I was very fortunate to have him as my personal trainer on several instruments, my advisor on project design, as well as my friend with shared interests in life. I appreciated the kindness and patience he has shown to me all the time.

I would also like to thank Nick Reynolds, Katie Styan, Yue Qu, Paul Pasic, Veronica Glattauer, Thomas Gengenbach for their help. The knowledge that they have instilled in me accelerated the completion of my PhD.

I would like to acknowledge the PhD students in Monash Biomaterials group, past and present. Andrew Rodda, Kun Zhou, Deniece Fon, Kelly Tsang, Ana Phan, Jerani Pettikiriarachchi, ThingYi Wang, Julian Ratcliffe, Yue Shi, Sepideh Motamed, Subhadeep Das, Richard Fernando, Jason Marroquin and Xiaolin Li. I will miss the meetings very much. Thanks to all of them who have listened to my presentations many times, and have given me great suggestions. Thanks to their hospitality and made me felt welcomed in this country.

I also appreciated the company and support of all my friends at CSIRO. Behnoosh Tajik, Jessica Qie, Sabu Lakhey and Katrin Kästle, thanks for the lunch time delight. Emmy Wijaya, friend and sister! I will always remember her warm heart.

Finally, I would like to thank my parents and WBT for their love and support.

---

## Publications obtained during PhD

Yali, Li; Benjamin, W. Muir; Christopher, D. Easton; Lars, Thomsen; David, R. Nisbet; John, S. Forsythe, A study of the initial film growth of PEG-like plasma polymer films via XPS and NEXAFS. *Applied Surface Science* 288 (2014), 288-294.

Yali, Li; Andrew, Nelson; Christopher, D. Easton; David, R. Nisbet; John, S. Forsythe; Benjamin, W. Muir, Probing the interfacial structure of bilayer plasma polymer films via neutron reflectometry. In preparation

Yali, Li; Nicholas, P. Reynolds; Katie, E. Styan; Benjamin, W. Muir; John, S. Forsythe; Christopher, D. Easton, Investigation of the growth mechanics of diglyme plasma polymer onto amyloid fibril networks. *Applied Surface Science*, In preparation

Yali, Li; Yue, Qu; Christopher, D. Easton; David, R. Nisbet; John, S. Forsythe; Trevor, Lithgow; Benjamin, W. Muir, Antimicrobial coatings created from brominated plasma polymer films, *Applied Materials & Interfaces*, submitted

Nicholas, P. Reynolds; Katie, E. Styan; Christopher, D. Easton; Yali, Li; Lynne, Waddington; Cecile, Lara; John, S. Forsythe; Raffaele Mezzenga; Patrick, G. Hartley; Benjamin W. Muir, Nanotopographic surfaces with defined surface chemistries from amyloid fibril networks can control cell attachment. *Biomacromolecules* 2013, 14 (7), 2305-2316.

Yue Qu; Yali Li; David, Cameron; Iain, Hay; Mario, Salwiczek; Benjamin, W. Muir; Helmut, Thissen; Keith, McLean; Jonathan, Wilksch; Richard, A. Strugnell; Tianyu, Zhang; Anton, Y. Peleg, John, S. Forsythe, Trevor, Lithgow. Biofilm formation of *Staphylococcus capitis* on biomedical polymers: critical roles for environmental influences and biomaterials surface chemistry. *PLOS one*, submitted

## **PART A: General Declaration**

### **Monash University**

Declaration for thesis based or partially based on conjointly published or unpublished work

### General Declaration

**In accordance with Monash University Doctorate Regulation 17.2 Doctor of Philosophy and Research Master's regulations the following declarations are made:**

**I hereby declare that this thesis contains no material which has been accepted for the award of any other degree or diploma at any university or equivalent institution and that, to the best of my knowledge and belief, this thesis contains no material previously published or written by another person, except where due reference is made in the text of the thesis.**

This thesis includes 2 original papers published in peer reviewed journals and 3 unpublished publications. The core theme of the thesis is the development of plasma polymer nanometer thin films for control of mammalian and microbial cell attachment. The ideas, development and writing up of all the papers in the thesis were the principal responsibility of myself, the candidate, working within the department of Materials Engineering under the supervision of Associate Professor John Forsythe, Dr. Benjamin W. Muir of CSIRO Manufacturing Flagship, and Dr. David Nisbet of ANU.

**[The inclusion of co-authors reflects the fact that the work came from active collaboration between researchers and acknowledges input into team-based research.]**

In the case of chapters 4, 5, 6, 7 and appendix 3, my contribution to the work involved the following:

Thesis chapter	Publication title	Publication status*	Nature and extent of candidate's contribution
4	A study of the initial film growth of PEG-like plasma polymer films via XPS and NEXAFS	Published	Experimental design, conduct, data processing and writing
5	Probing the interfacial structure of bilayer plasma polymer films via neutron reflectometry	In draft	Experimental design, conduct, data processing and writing
6	Investigation of the growth mechanics of diglyme plasma polymer onto amyloid fibril networks	In draft	Experimental design, conduct, data processing and writing
7	Antimicrobial coatings created from brominated plasma polymer films	Submitted	Experimental design, conduct, data processing and writing
Appendix 3	Nanotopographic Surfaces with Defined Surface Chemistries from Amyloid Fibril Networks Can Control Cell Attachment	Published	Experimental conduct and writing

I have / have not (circle that which applies) renumbered sections of submitted or published papers in order to generate a consistent presentation within the thesis.

Signed: .....

Date: .....

---

## List of Abbreviations

AA	Allylamine
AFM	Atomic force microscopy
AFN	Amyloid fibril network
BE	Binding energy
<i>C. albicans</i>	<i>Candida albicans</i>
CDST	Conductive double sided carbon adhesive tape
CFU	Colony forming unit
CLSM	Confocal laser scanning microscopy
CV	Crystal violet
DG	Diglyme / Diethylene glycol dimethyl ether
dDG	Deuterated diglyme
DMEM	Dulbeccos modified Eagle's media
DRIs	Device related infections
ECM	Extracellular matrix
eDNA	Extracellular DNA
EPS	Extracellular polymeric substance
FBS	Fetal bovine serum
FIB-SEM	Focused ion beam scanning electron microscopy
HEWL	Hen egg white lysozyme
HMDSO	Hexamethyldisiloxane
ITO	Indium tin oxide
mES	Mouse embryonic
NEXAFS	Near edge X-ray absorption fine structure spectroscopy
NR	Neutron reflectometry
<i>P. aeruginosa</i>	<i>Pseudomonas aeruginosa</i>
PBS	Phosphate-buffered saline
PEG	Poly(ethylene glycol)
pp	Plasma polymer
QACs	Quaternary ammonium compounds
QCM-D	Quartz crystal microbalance with dissipation
RFGD	Radio frequency glow discharge
SAM	Self-assembled monolayer
<i>S. epidermidis</i>	<i>Staphylococcus epidermidis</i>

SLD	Scattering length density
TCPS	Tissue culture polystyrene
TEY	Total electron yield
ToF-SIMS	Time of flight secondary ion mass spectroscopy
XPS	X-ray photoelectron microscopy
XRR	X-ray reflectometry

# Table of Contents

<b>Thesis abstract.....</b>	<b>iii</b>
<b>Statement of originality .....</b>	<b>v</b>
<b>Acknowledgements .....</b>	<b>vi</b>
<b>Publications obtained during PhD .....</b>	<b>vii</b>
<b>PART A: General Declaration .....</b>	<b>viii</b>
<b>List of Abbreviations.....</b>	<b>x</b>
<b>Chapter 1 Introduction .....</b>	<b>1</b>
<b>1.1 General background .....</b>	<b>2</b>
<b>1.2 Aims and scope of this PhD thesis.....</b>	<b>4</b>
<b>1.3 Reference.....</b>	<b>6</b>
<b>Chapter 2 Literature review.....</b>	<b>8</b>
<b>2.1 Overview.....</b>	<b>9</b>
<b>2.2 Surface modification: general introduction .....</b>	<b>9</b>
<b>2.3 Plasma-assisted modification of biomaterials .....</b>	<b>11</b>
2.3.1 What is plasma? .....	11
2.3.2 Plasma treatment in biomaterials engineering.....	14
<b>2.4 Plasma polymerisation.....</b>	<b>20</b>
<b>2.5 Plasma polymer films to direct cell fate .....</b>	<b>25</b>
2.5.1 Cell adhesive functional coatings .....	26
2.5.2 Antifouling coatings .....	28
2.5.3 Patterns and gradients.....	30
<b>2.6 Plasma polymer films for improved antimicrobial property.....</b>	<b>32</b>
2.6.1 Microbe attachment and biofilm formation .....	34
2.6.2 Approaches for antimicrobial surface modification .....	37
2.6.3 Anti-fouling plasma polymer coatings.....	42
2.6.4 Release of antimicrobial compounds .....	42

2.6.5 Surface-bound antimicrobial molecules .....	44
<b>2.7 Summary.....</b>	<b>47</b>
<b>2.8 Reference.....</b>	<b>48</b>
<b>Chapter 3 Diglyme Plasma polymer film characterisation.....</b>	<b>65</b>
<b>3.1 Introduction .....</b>	<b>66</b>
<b>3.2 Materials and methods .....</b>	<b>67</b>
3.2.1 Substrate materials .....	67
3.2.2 Plasma polymerisation .....	67
3.2.3 X-ray photoelectron spectroscopy.....	69
3.2.4 Near edge X-ray absorption fine structure spectroscopy.....	70
3.2.5 Protein adsorption.....	70
3.2.6 Quartz crystal microbalance with dissipation.....	71
3.2.7 Biofilm cultivation and quantitative determination .....	71
3.2.8 Confocal laser scanning microscopy.....	72
3.2.9 Protein adsorption and cell adhesion on micropatterned DGpp films .....	73
<b>3.3 Results and discussion.....</b>	<b>74</b>
3.3.1 Surface chemistry of uniform DGpp films .....	74
3.3.2 Protein resistance of uniform DGpp films .....	76
3.3.3 Micropattern produced by plasma polymerisation .....	79
3.3.4 Antimicrobial property of DGpp films .....	81
<b>3.4 Conclusions.....</b>	<b>84</b>
<b>3.5 Reference.....</b>	<b>85</b>
<b>Chapter 4 Diglyme film chemistry at substrate-film interface.....</b>	<b>88</b>
<b>Abstract.....</b>	<b>89</b>
<b>4.1 Introduction .....</b>	<b>90</b>
<b>4.2 Materials and methods .....</b>	<b>92</b>
4.2.1 Substrate preparation.....	92
4.2.2 Plasma polymerisation .....	92
4.2.3 Plasma polymer delamination procedure.....	93
4.2.4 X-ray photoelectron spectroscopy.....	94
4.2.5 Near edge X-ray absorption fine structure spectroscopy.....	94
4.2.6 Masking .....	94

4.2.7 Atomic force microscopy .....	95
4.2.8 Focused ion beam scanning electron microscopy .....	95
<b>4.3 Results and discussion .....</b>	<b>95</b>
4.3.1 Surface chemistry on different substrates .....	95
4.3.2 Analysis of top- and underside .....	103
<b>4.4 Conclusions .....</b>	<b>106</b>
<b>4.5 Reference .....</b>	<b>106</b>
<b>Chapter 5 Interfacial structure of bilayer plasma polymer films .....</b>	<b>110</b>
<b>Abstract .....</b>	<b>111</b>
<b>5.1 Introduction .....</b>	<b>112</b>
<b>5.2 Materials and methods .....</b>	<b>114</b>
5.2.1 Samples preparation .....	114
5.2.2 Plasma polymerisation .....	115
5.2.3 X-ray photoelectron spectroscopy .....	116
5.2.4 Neutron and X-ray reflectometry .....	116
<b>5.3. Results and discussion .....</b>	<b>117</b>
5.3.1 Surface chemistry .....	117
5.3.2 Characterisation of films by XRR and NR in air .....	122
5.3.2 Chemical bonds at the interface .....	128
<b>5.4. Conclusions .....</b>	<b>131</b>
<b>5.5 References .....</b>	<b>131</b>
<b>Chapter 6 Diglyme film growth on amyloid fibril network .....</b>	<b>135</b>
<b>Abstract .....</b>	<b>136</b>
<b>6.1 Introduction .....</b>	<b>137</b>
<b>6.2 Materials and methods .....</b>	<b>138</b>
6.2.1 Substrate preparation .....	138
6.2.2 Amyloid fibril network .....	139
6.2.3 Plasma polymerisation .....	139
6.2.4 Profilometry .....	139
6.2.5 Focused Ion Beam Scanning Electron Microscopy .....	140
6.2.6 Atomic force microscopy .....	140
6.2.7 X-ray photoelectron spectroscopy .....	141

<b>6.3 Results and discussion</b> .....	<b>141</b>
6.3.1 Thickness measurements of DGpp + AFN constructs.....	141
6.3.2 Retention of the AFN topography with increasing DGpp deposition times.....	143
6.3.3 Elemental distribution through DGpp + AFN constructs.....	145
<b>6.4 Conclusions</b> .....	<b>150</b>
<b>6.5 References</b> .....	<b>150</b>
<b>Chapter 7 Antimicrobial coatings</b> .....	<b>155</b>
<b>Abstract</b> .....	<b>156</b>
<b>7.1. Introduction</b> .....	<b>157</b>
<b>7.2. Materials and methods</b> .....	<b>159</b>
7.2.1 Substrate materials .....	159
7.2.2 Plasma polymerisation .....	159
7.2.3 Azide nucleophilic exchange .....	160
7.2.4 X-ray photoelectron spectroscopy.....	161
7.2.5 Atomic force microscopy .....	161
7.2.6 Biofilm cultivation and quantitative determination .....	161
7.2.7 Confocal laser scanning microscopy.....	162
7.2.8 Haemolysis assay .....	163
7.2.9 HeLa cell culture .....	163
<b>7.3. Results and discussion</b> .....	<b>164</b>
7.3.1 Surface topography .....	164
7.3.2 Surface chemistry.....	166
7.3.3 Anti-microbial performance.....	169
7.3.4 Initial studies on toxicity towards cells.....	172
<b>7.4. Conclusions</b> .....	<b>174</b>
<b>7.5 References</b> .....	<b>174</b>
<b>Chapter 8 Conclusions and outlook</b> .....	<b>178</b>
<b>8.1 Conclusions</b> .....	<b>179</b>
8.1.1 DGpp film chemistry and its applications.....	179
8.1.2 DGpp growth on different substrates.....	180
8.1.3 Antimicrobial coatings.....	182
<b>8.2 Future outlook</b> .....	<b>183</b>

<b>Appendix 1 .....</b>	<b>186</b>
<b>Supporting Information for Chapter 4 .....</b>	<b>186</b>
<b>Appendix 2 .....</b>	<b>187</b>
<b>Supporting Information for Chapter 5 .....</b>	<b>187</b>
<b>Appendix 3 .....</b>	<b>189</b>
<b>Supporting Information for Chapter 6 .....</b>	<b>189</b>

# Chapter 1 Introduction

*“To raise new questions, new possibilities, to regard old problems from a new angle,  
requires creative imagination and marks real advance in science.”*  
—Albert Einstein

## 1.1 General background

The biomaterials industry is now well established and the global market for biomaterials was estimated to reach \$88.4 billion by 2017.<sup>1</sup> Biomaterials can be made from synthetic materials such as metal, ceramic, polymer or naturally derived biological components. However, despite the variety of its constituents, all biomaterials must fulfill the basic requirement that when in contact with the living organism, it is biocompatible.<sup>2</sup>

A biocompatible material that is used for a specific biomedical application must perform its function without initiating adverse host response. Much effort has been made throughout the twentieth century to design and fabricate biomaterials with appropriate mechanical properties, durability and functionality, and at the same time be compatible with the living tissue. Indeed, those products have been used worldwide to improve the quality of life for millions of people. Nonetheless, a great proportion of the biomaterials and devices require frequent exchange or intervention in order to function properly in the long run. Those failures are commonly associated with a lack of biointegration, adverse inflammatory responses, tumor formation and infections. This renders the search for materials that can affect or manipulate the biological response to a desirable direction. To cite a few examples: a degradable porous scaffold which enables cardiac cell growth with potential to integrate into the host myocardium and carries directional cues to guide reconstruction of functional heart muscle;<sup>3</sup> a self-assembled hydrogel network supports neural cell growth and function for treatment of disease or injury in the central nervous system;<sup>4</sup> a central venous catheter coated with antimicrobial agents to reduce risk of infection hence appropriate for longer use in patients.<sup>5</sup>

The quest for biocompatible and bioactive materials has perpetuated the rapid growth of surface engineering research field as biological responses are largely governed by surface chemistry and structure. By changing the interfacial layer, the biomaterials or devices gain improved biocompatibility, increased functionality, optimized architecture and tribology. Also, selectively modifying the material surface by-passes the often expansive and time-consuming process of developing new biomaterials. Before long, surface modification utilising physical, chemical or biological methods has become

common practice. In fact, it is now widely accepted that not one particular factor but a combination of chemistry, topography, and the stiffness of the surfaces determines the host responses. Thus, the functionalisation is done through a process that encompasses a few techniques. For instance, electrospun nanofibres can be plasma activated first, followed with layer-by-layer assembly of polyelectrolyte multilayers, and then conjugated with growth factors or enzymes on the surface.<sup>6</sup>

Amongst the plethora of modification methods, plasma assisted techniques have gained more popularity over the last few decades, especially plasma polymerisation.<sup>7-10</sup> Plasma polymerisation is a convenient and versatile technique that produces pin-hole free and conformal coatings in a single step without the use of solvents. Furthermore, the deposition process is especially advantageous for biomaterials preparation as it provides a sterile environment within the reactor.

Plasma polymerisation is the process of forming polymeric materials under the influence of plasma. The precursor molecules are fragmented by processes such as electron impact and UV radiation with the formation of free radicals that recombine either in a gas phase or on substrate surfaces.<sup>11</sup> Depending on the process conditions, the surface of the generated films can possess high concentrations of specific functional groups. The functional films can be broadly separated into two categories: a) low fouling surfaces that prevent cell adhesion by polymerising ether containing monomers, for example, those of the glyme family;<sup>12-15</sup> b) bioactive surfaces which are intended to enable sophisticated biological interactions by the fabrication of groups such as amines,<sup>16, 17</sup> aldehydes<sup>18</sup> and carboxylic acids.<sup>19</sup>

However, plasma polymerisation does have associated drawbacks. Poor stability and fast aging of plasma polymer films in biological environments have always been a major concern. In addition, the emergence of characterisation methods that are capable of probing soft materials at the nanoscale have challenged the conventional assumptions, such that the process is substrate independent or plasma polymer films has uniform chemistry throughout the entirety of the coating. In fact, the formation of the plasma polymer film at the initial stage, both the growth rate and composition, is affected by the substrate underneath.<sup>20-22</sup> In order to precisely control the composition of the plasma

polymer, more research is needed to understand the phenomenon at the substrate-plasma polymer film interface.

## 1.2 Aims and scope of this PhD thesis

The overall aim of this project is to fabricate plasma polymer films that are capable of manipulating biological responses *in vitro*. In more specific terms, this project will investigate the formation mechanism of plasma polymer coatings under different process conditions and apply the obtained thin films to cell and microbial cultures. The following sections lead the way to the overall goal:

- i. Better understand the substrate-plasma polymer interactions and investigate the interfacial chemistry
- ii. Explore and explain the hybrid plasma polymer films and amyloid fibril networks, and decipher the film growth mechanism
- iii. Apply plasma polymer films as antimicrobial coatings, explore the effect and identify potential mechanisms of action

Following this introductory chapter, more details about the surface modification methods will be given in **Chapter 2**, where a thorough literature review on the achievements of surface engineering related to the topic of this thesis will be presented. The subsequent chapters (**Chapters 3 – 7**) show the results obtained in this PhD project. In **Chapter 3**, diethylene glycol dimethyl ether (Diglyme) plasma polymers were studied as a model to demonstrate the effect of plasma process parameters on the chemistry of the bulk of resultant coatings. This chapter also examines how power input, substrate, and storage conditions influence the stability of the coating. Next, diglyme plasma polymers were employed in cell and microbial culture to test their antifouling behaviours. The knowledge gained from this chapter was used further in the design of the other sections of the thesis and in an associated project (**Appendix 3**).

**Chapters 4 to 6** focus on the interfacial phenomena that occur in plasma polymer formation processes. **Chapter 4** investigates the substrate-film interfaces. This study

exploits the poor adhesion of diglyme plasma polymer films on indium tin oxide (ITO) coated glass to expose the substrate-plasma polymer interface thus allowing characterisation of the underside (as opposed to the air-plasma polymer interface, i.e. topside). It was found that a rapid increase in pressure at the start of the plasma polymerisation leads to a chemistry that is significantly different from the film composition of the topside. In addition, subtle variations in plasma polymer chemistry were observed between different substrates.

**Chapter 5** probes the film-film intermixing. Diglyme, allylamine and hexamethyldisiloxane (HMDSO) plasma polymer films were selected as the base materials, which consist of different functional groups and vary in mass density and cross-link density. It was hypothesised that the properties of these films have an effect on the growth of another layer on top. In this work, deuterated diglyme (dDG) plasma polymer films were deposited as the overlying layer. The inter-diffusion between two plasma polymer films can be characterised through modelling of data obtained from neutron reflectometry. Intuitively, one would assume that the base film formed from a monomer that is similar to the top layer may result in a broader interface region as compared to other types of plasma polymer films. Surprisingly, it is found that the interface region of HMDSO–dDG film pair is the widest.

**Chapter 6** examines the amyloid fibril network (AFN)–film interactions by collecting chemical information at designated intervals from the bulk of the film through to the amyloid fibril network. This quest originated from an observation in a collaborative project (**Appendix 3**) where it was discovered that the nanostructure of the AFN was retained after deposition of plasma polymer films (in excess of 100 nm) on top. This chapter answers how the film builds up on AFN so that the fibres still can be seen under the AFM and what is the limit in thickness that the fibre skeleton will be covered completely.

**Chapter 7** moves away from the fundamentals of plasma polymerisation and explores the application in antimicrobial coatings utilising a brominated plasma polymer (Brpp) coating. In this chapter, Brpp film was used to incorporate azide functional group that is capable of interfering with bacteria and fungi actions. A series of sodium azide solutions

were used to determine the optimum concentration for nucleophilic exchange. It was found that varying degree of azide immobilisation showed different percentage of antimicrobial activity *in vitro* against *Staphylococcus epidermidis*, *Pseudomonas aeruginosa* and *Candida albicans*. In addition, these coatings are compatible with HeLa cell culture and induced minimal lysis of human erythrocytes.

In addition to a conclusion in each chapter, a general conclusion of the thesis is given in **Chapter 8**. Also the contribution of this thesis to the concepts and theories in the field is outlined. Finally, a sketch on future prospects capturing a few essential points on how to move forward is discussed.

### 1.3 Reference

1. MarketsandMarkets, Biomaterials market and applications - Global forecasts to 2017, <http://www.marketsandmarkets.com/Market-Reports/biomaterials-393.html> (2013), accessed on 2014.
2. F. J. Schoen, in *Biomaterials Science (Third Edition)*, eds. B. D. Ratner, A. S. Hoffman, F. J. Schoen and J. E. Lemons, Academic Press, 2013, pp. 499-503.
3. L. R. Madden, D. J. Mortisen, E. M. Sussman, S. K. Dupras, J. A. Fugate, J. L. Cuy, K. D. Hauch, M. A. Laflamme, C. E. Murry and B. D. Ratner, *Proceedings of the National Academy of Sciences*, 2010, 107, 15211-15216.
4. M. J. Mahoney and K. S. Anseth, *Biomaterials*, 2006, 27, 2265-2274.
5. E. Perez, M. Williams, J. T. Jacob, M. D. Reyes, S. Chernetsky Tejedor, J. P. Steinberg, L. Rowe, S. R. Ganakammal, S. Changayil, M. R. Weil and R. M. Donlan, *Journal of Clinical Microbiology*, 2014, 52, (3), 823-831.
6. H. S. Yoo, T. G. Kim and T. G. Park, *Advanced Drug Delivery Reviews*, 2009, 61, 1033-1042.
7. M. T. v. Os, *Surface modification by plasma polymerization: film deposition, tailoring of surface properties and biocompatibility*, Enschede, 2000.
8. F. S. Denes and S. Manolache, *Progress in Polymer Science*, 2004, 29, 815-885.
9. S. Swaraj, U. Oran, A. Lippitz, R.-D. Schulze, J. F. Friedrich and W. E. S. Unger, *Plasma Processes and Polymers*, 2005, 2, 310-318.

10. T. Desmet, R. Morent, N. D. Geyter, C. Leys, E. Schacht and P. Dubruel, *Biomacromolecules*, 2009, 10, 2351-2378.
11. J. Friedrich, *Plasma Processes and Polymers*, 2011, 8, 783-802.
12. M. N. Mar, B. D. Ratner and S. S. Yee, *Sensors and Actuators B: Chemical*, 1999, 54, 125-131.
13. F. Brétagnol, O. Kylián, M. Hasiwa, L. Ceriotti, H. Rauscher, G. Ceccone, D. Gilliland, P. Colpo and F. Rossi, *Sensors and Actuators B: Chemical*, 2007, 123, 283-292.
14. M. Salim, G. Mishra, G. J. S. Fowler, B. O'Sullivan, P. C. Wright and S. L. McArthur, *Lab on a Chip*, 2007, 7, 523-525.
15. E. Sardella, L. Detomaso, R. Gristina, G. S. Senesi, H. Agheli, D. S. Sutherland, R. d'Agostino and P. Favia, *Plasma Processes and Polymers*, 2008, 5, 540-551.
16. A. M. Sandstrom, M. Jasieniak, H. J. Griesser, L. Grøndahl and J. J. Cooper-White, *Plasma Processes and Polymers*, 2013, 10 (1), 19-28.
17. E. R. David, E. S. Louise, A. S. David, D. S. Robert and D. W. Jason, *Biomaterials Science*, 2014, 2, (6), 875-882.
18. B. R. Coad, T. Scholz, K. Vasilev, J. D. Hayball, R. D. Short and H. J. Griesser, *ACS Applied Materials & Interfaces*, 2012, 4, 2455-2463.
19. N. Wells, M. A. Baxter, J. E. Turnbull, P. Murray, D. Edgar, K. L. Parry, D. A. Steele and R. D. Short, *Biomaterials*, 2009, 30, 1066-1070.
20. K. Vasilev, A. Michelmore, H. J. Griesser and R. D. Short, *Chemical Communications*, 2009, 3600-3602.
21. D. E. Robinson, D. J. Buttle, J. D. Whittle, K. L. Parry, R. D. Short and D. A. Steele, *Plasma Processes and Polymers*, 2010, 7, 102-106.
22. C.-H. Lo, K.-S. Liao, M. De Guzman, V. Rouessac, T.-C. Wei, K.-R. Lee and J.-Y. Lai, *Langmuir*, 2010, 26, 17470-17476.

## Chapter 2 Literature review

*“Creativity, as has been said, consists largely of rearranging what we know in order to find out what we do not know. Hence, to think creatively, we must be able to look afresh at what we normally take for granted.”*

— George Kneller

## 2.1 Overview

This chapter reviews the literature to address the need for surface modification of biomaterials and details the development of plasma-assisted treatment methods – with an emphasis on plasma polymerisation and its applications. Firstly, it presents a review of the use of nonthermal plasma for selective surface modification. Next, it examines the extent research on plasma polymerisation mechanisms, interaction of processing parameters, and the usage of plasma polymer films in biomedical engineering. Then, it focuses on the formation of antimicrobial surfaces by plasma polymerisation, which includes elaboration on microorganism attachment and biofilm formation. Finally, it summarises the research conducted in this field and briefly states the design for studies in this thesis.

## 2.2 Surface modification: general introduction

In the field of biomaterials, tissue engineering and regenerative medicine, requirements for applied materials are high due to the complexity of biological environments. For instance, a cranial implant needs to be strong yet lightweight, allow unique shaping for individual cosmetic appearance, whilst also being cheap to manufacture; a kidney dialysis membrane must facilitate the diffusion of uremic toxins and excess water while also blocking blood cells; a total joint replacement should bear the load associated with walking, running or twisting for 10-15 years without revision surgery. The mechanical properties, durability and functionality are governed by the shape, size, bulk compositions and organisation of the materials. Not surprisingly, various materials including polymers, metals, ceramics and their composites are tested for the design and fabrication of biomaterials and biomedical devices.

However, the host responses to biomaterials are largely affected by their surface chemistry and microstructure. Once the biomaterial is brought into contact with physiological fluids or implanted in the body, water molecules and proteins will adsorb onto the surface within seconds. The structure and function of the adsorbed molecular entities influence the cell responses in a direct and dramatic way.<sup>1</sup> Modification of the

outmost surface of the material is commonly used to maintain device function and to promote the desired biological response. As such, the material gains improved biocompatibility or specific factors that can affect the cell-material interactions.<sup>2,3</sup> For example, subtle variations of surface morphology can lead to changes in cell attachment and proliferation, and in the case of stem cells, differentiation.<sup>4-8</sup> Blasting<sup>9</sup> and spraying<sup>10</sup> of particles are quick and inexpensive ways to generate random nano- to microscale features on a substrate surface. Generally speaking a roughened surface will show higher cell proliferation than the untreated smooth substrates.<sup>11</sup> To obtain reproducible and well-organised structures, laser ablation<sup>12</sup>, lithography<sup>7</sup>, and ion implantation<sup>13</sup> can be employed but have the disadvantage of high costs due to complex laboratory facilities and high energy radiation. A simpler and cheaper process is “soft lithography” which can fabricate high quality patterns with good fidelity.<sup>14, 15</sup> A drawback of these techniques is that the generated surface structures do not mimic the typical morphology of the extracellular matrix (ECM) where cells normally reside. Therefore, exploration of biomimetic surface architecture has attracted considerable attention. A promising approach to obtain a nanostructured network structure relies on self-assembly of molecules, such as peptides or proteins, into fibrils, which then can be deposited onto a surface as an amyloid fibril network (AFN).<sup>16-18</sup>

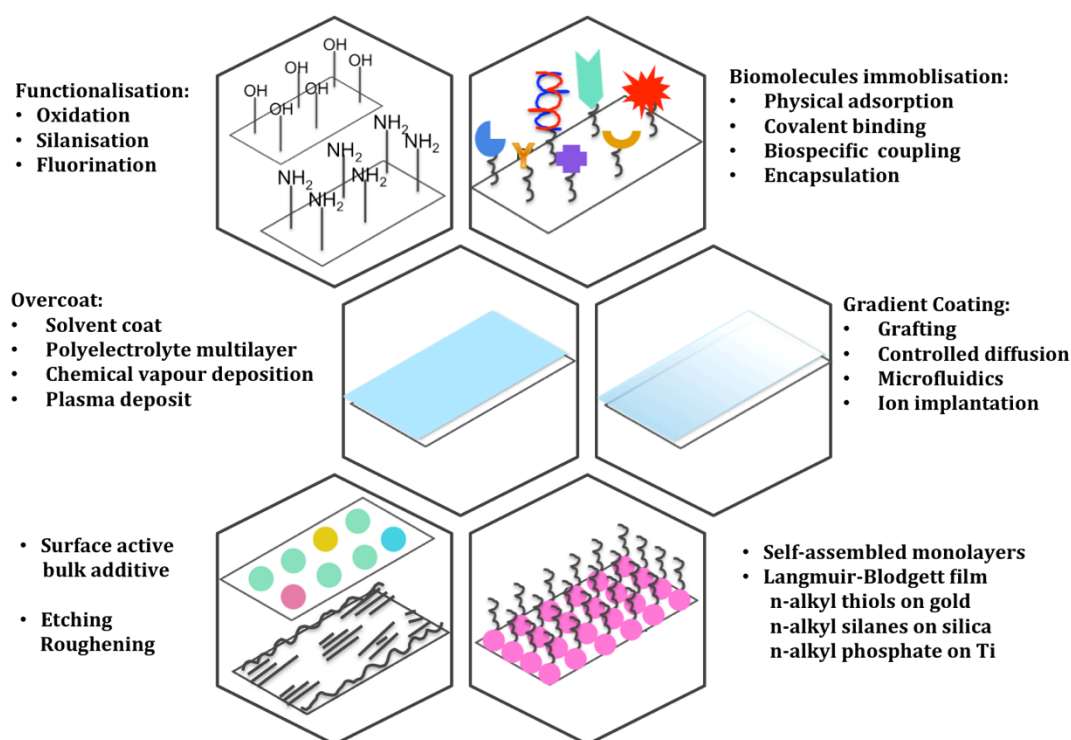


Figure 2.1, Schematic representations of methods for surface modification of materials.

On the whole, the surface of materials can be engineered to suit its application using mechanical, physicochemical and biological methods. Synthetic surfaces have progressed over the past decades from well-defined simple chemical functionality presentation to more complex, patterned or gradient surfaces. Figure 2.1 illustrates these strategies schematically with generalised examples. The categories may sometimes be ambiguous because many methods can introduce not only new functional groups but also change the surface texture or morphology, and vice versa. For example, if plasma etching is used for removal of surface layers, whether it is O<sub>2</sub> or H<sub>2</sub>O plasma treatment, there will be high quantity of -C-O- groups, such as hydroxyl and peroxy groups, incorporated onto the surface.<sup>19, 20</sup> This also indicates that a modified surface requires a combination of characterisation techniques to fully capture the changes.<sup>21</sup> Generally, modified surface layers should be the minimum thickness needed for uniformity, durability and functionality, as well as biocompatibility.<sup>22</sup>

It is beyond the scope of this literature review to introduce in detail all the surface modification and characterisation techniques due to the enormous amount of research activities in this field. The main focus of this review is plasma-based strategies for surface modification.

## **2.3 Plasma-assisted modification of biomaterials**

### **2.3.1 What is plasma?**

During the late 1920's, Irving Langmuir introduced the term "plasma" to describe a partially ionised gas.<sup>23</sup> It is in the form of a gaseous mixture that contains free electrons, ions, radicals, and neutral particles (atoms, molecules), with an overall neutral charge. Plasma is often referred to as the fourth state of matter as it is significantly different from non-ionised gases. Plasmas are ubiquitous in the cosmos, forming 99 % of the visible universe. Plasmas can be subdivided into thermal (equilibrium/high-temperature/hot) and non-thermal (nonequilibrium/low-temperature/cold) plasmas. Thermal plasma implies that the temperature of all species is the same, which is often

true for stars and fusion plasmas. The temperatures required to form equilibrium plasmas range from roughly 4000 K (for easy to ionise elements, such as cesium) to 20,000 K (for hard to ionise elements, such as helium).<sup>24, 25</sup> On the other hand, nonthermal plasmas refer to nonequilibrium plasmas where the electron temperature is much higher than that of heavy particles (close to ambient temperature). Thus, nonthermal plasmas are more widespread in surface modification applications of biomaterials as the substrate can withstand the conditions of cold plasma treatment.

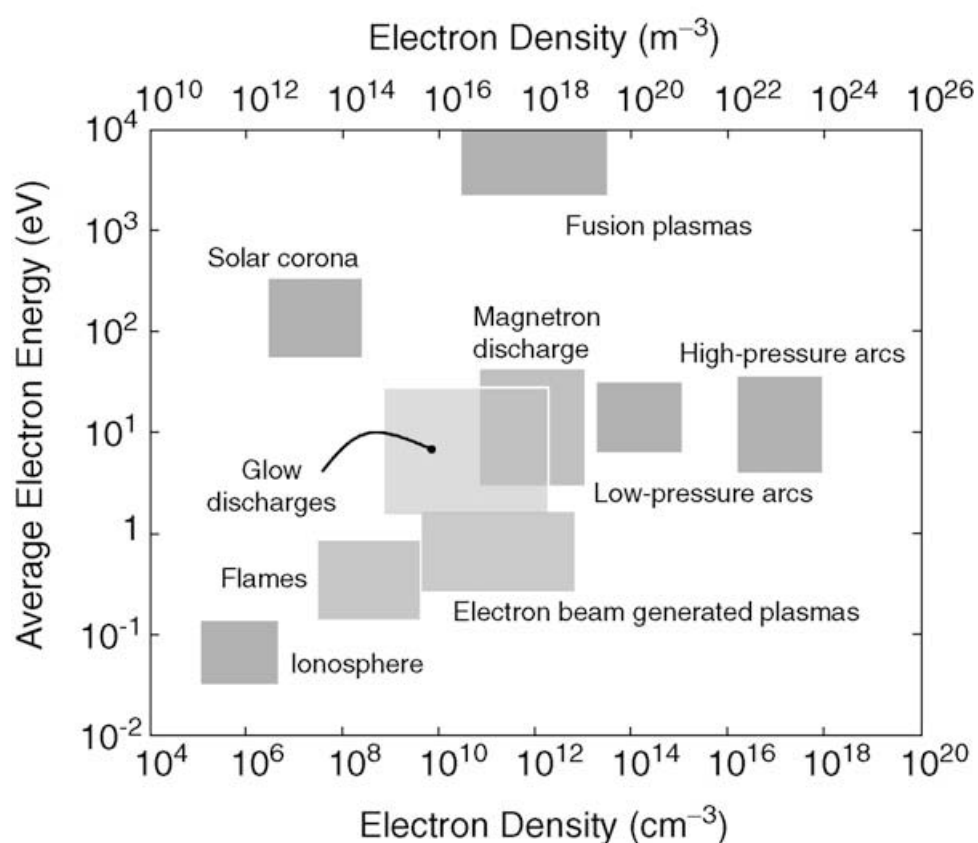


Figure 2.2, The range of average electron density and energy typical of various naturally occurring and human-made plasmas. Reprinted with permission from Elsevier.<sup>26</sup> Copyright © 2010 Peter M. Martin. Published by Elsevier Ltd.

There are various types of plasmas that differ in density of free electrons and ions. Figure 2.2 shows some commonly observed naturally occurring and human-made plasmas, separated by their electron densities and energies.<sup>26</sup> Within these categories, the most common types of plasmas used in biomaterials processing are discharge plasmas, while arcs,<sup>27</sup> flames,<sup>28, 29</sup> and electron beam generated<sup>30</sup> plasmas have also found their niches for the surface modification of materials. Glow discharge plasmas can

be obtained by applying an electrical field to excite a volume of gas. Typical sources are radio frequency (RF), microwave, or electrons from a hot filament discharge.

Radio frequency glow discharge (RFGD) is one of the most widely used sources in plasma surface modification because it can generate a large area of uniform and stable plasma. Urano et al. has demonstrated this feature to an extreme by producing 1 m diameter argon plasma with uniformity of several percent in front of a substrate at low-pressure regime ( $<1$  Pa).<sup>31</sup> Most often 13.56 MHz is used in RFGD, but 27.2 MHz can also be used.<sup>32</sup> The power source can be continuous wave or pulsed. The RF power can be supplied capacitively (between the plates of a capacitor) or inductively (within a coil). In both modes of operation, internal or external electrodes can be used. Electrode-less deposition is especially useful when aggressive chemical vapours are used to generate plasmas, as the sputtering or etching events of the metal electrode and subsequent surface contamination is obviated. Figure 2.3 depicts the general reactor designs for RF driven plasmas.<sup>33</sup> Simple planar diodes shown in figure 2.3 (a) is the type used in this thesis for plasma polymerisation experiments. A detailed review of the various types of reactor embodiments for laboratory use can be found elsewhere.<sup>34</sup>

RFGD can be ignited at vacuum conditions with pressures ranging from a few Pa to atmospheric pressure.<sup>35</sup> Typically the resultant electron density varies from  $10^9$  to  $10^{11}$   $\text{cm}^{-3}$ , but can reach as high as  $10^{12}$   $\text{cm}^{-3}$ .<sup>36</sup> For gases that can polymerise into thin films, the plasma density is in the range of  $10^{13}$  –  $10^{16}$  ions  $\text{m}^{-3}$ .<sup>37</sup> In contrast, the neutral density of the plasma phases is usually  $10^4$  –  $10^5$  times higher. Due to the large number of neutral species that exist in plasma, it was generally believed that they are the main component that forms plasma polymer films. Until recently, however, the contribution of ions species to the formation of plasma polymer has been reorganised.<sup>34, 38</sup>

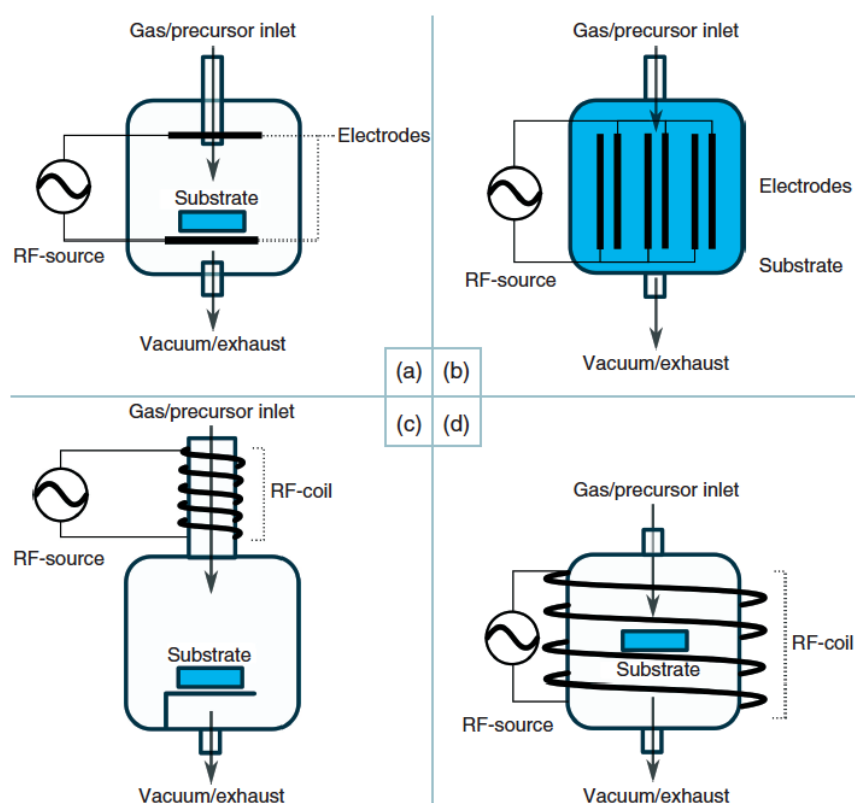


Figure 2.3, Schematic representation of the generic reactor designs for RFGD plasmas: (a) parallel plate, capacitively coupled, surface load; (b) capacitively coupled, volume load; (c) barrel reactor, inductively coupled, substrate outside the glow region; and (d) flat coil reactor, inductively coupled, substrates within the glow. Reprinted with permission from John Wiley and Sons.<sup>33</sup> Copyright © 2013 Wiley-VCH Verlag GmbH & Co KGaA, Weinheim.

### 2.3.2 Plasma treatment in biomaterials engineering

Plasma is a highly reactive environment due to the high-energy electrons that can travel freely in the system. The electrons accumulate kinetic energy that is transferred to heavy particles via inelastic collisions, resulting in excitation, dissociation, or ionisation of the heavier gas molecules and atoms. Table 2.1 summarises the inelastic collision processes in low-pressure plasmas.<sup>39</sup> The production of energetic species and their interactions with surfaces is non-trivial. The plasmas bombard the surfaces in contact by those excited and ionised species, including ions, electrons, radicals, metastables, and photons in the short-wave ultraviolet (UV) range, resulting in a variety of chemical and physical changes.

Table 2.1, Inelastic collision processes in the plasma. Reprinted with permission from John Wiley and Sons.<sup>39</sup> Copyright © 2012 Wiley-VCH Verlag GmbH & Co KGaA, Weinheim.

	<i>Elementary process</i>	<i>Names given to the process</i>
1	$e^- + A \Rightarrow A^+ + e^-_1 + e^-_2$	Ionisation
2	$e^- + A \Rightarrow A^* + e^-_1$	Excitation
3	$A^* + B \Rightarrow A + B^+ + e^-_1$	Penning ionisation
4	$A^* \Rightarrow A + h\nu$	Radiative deactivation
5	$A^+ + B \Rightarrow A + B^+$	Recharging
6	$A^+ + e^- + M \Rightarrow A + M^*$	Recombination by three-body collision
7	$A^+ + e^- \Rightarrow A + h\nu$	Radiative recombination
8	$A^+ + B \Rightarrow AB^+$	Ion-molecule reaction
9	$A^* + B \Rightarrow AB^+ + e^-$	Hornbeck-Molnar process
10	$ABCD^+ + e^- \Rightarrow ABCD^*$	Recombination with internal excitation of vibrations
11	$AB^+ + e^- \Rightarrow A^* + B$	Dissociative recombination
12	$A^+ + B^- + M \Rightarrow AB + M^*$ Or $\Rightarrow A + B + M^*$	Recombination of ions
13	$A + e^- (+M) \Rightarrow A^- (+h\nu, M^*)$	Formation of negative ions
14	$AB + e^- \Rightarrow A^+ + B^- + e^-_1$	Ion-pair formation (at high kinetic energies)

In practice, plasma processing is used in the biomedical field to change the chemical composition and properties such as wettability, adhesion strength, dyeability, refractive index, hardness, chemical reactivity, lubricity, and biocompatibility. The applications of plasma-based techniques is diverse, such as sterilisation or sanitisation of medical devices,<sup>40</sup> functionalisation of implant surfaces,<sup>41, 42</sup> and coating or depositing films for specific bioactivity.<sup>43, 44</sup> Table 2.2 gives examples of applications of plasma treatment in biomaterials surface modification. The outcomes of plasma surface modification and deposition generally fall into three main categories: i) etching (surface roughness control); ii) introduction of functional groups; iii) thin film coatings.

Table 2.2 Examples of biomaterials applications utilising plasma surface treatment.

<b>Applications</b>	<b>Devices</b>	<b>Materials</b>	<b>Ion Source</b>	<b>Purpose</b>
Biosensor	Diagnostic sensor	SWCNT	O <sub>2</sub>	Immobilisation of biomolecules (DNA <sup>45</sup> , PNA <sup>46</sup> )
	membranes	ta-C	H <sub>2</sub>	
			ePTFE-g-PEGMA	Ar
Bioseparation	Separation	PP	AA/H <sub>2</sub> O	Enhanced wettability <sup>48</sup>
		PES	Ar-O <sub>2</sub>	Anti-fouling surfaces <sup>49</sup>
	Hemodialysis	PVDF	Ar	Improved biocompatibility <sup>50</sup>
Cardiovascular	Vascular grafts	PTFE	Ar/H <sub>2</sub>	Improved SMCs attachment <sup>51</sup>
	Catheters	PU	O <sub>2</sub> /NH <sub>3</sub>	Improved biocompatibility <sup>52</sup>
		PE/PP	Ar	Lubricious coatings <sup>53</sup>
		PS	N <sub>2</sub> /H <sub>2</sub>	Antimicrobial coatings <sup>54</sup>
Orthodontic	Dental implant	Titanium	Ar-O <sub>2</sub>	Enhanced wettability and osteoblastic cell spreading <sup>55</sup>
Orthopedic	Metal implants	Titanium	CO <sub>2</sub>	Improved attachment of MC3T3-E1 cells <sup>56</sup>
	Joints	UHMWPE	He/O <sub>2</sub>	Improved adhesion <sup>57</sup>
			Ar	Wear resistance <sup>58</sup>
Ophthalmic	Contact lenses	FSA	Ar	Improved hydrophilicity <sup>59</sup>
			HA	Antimicrobial coatings <sup>60-62</sup>
	Artificial cornea	Collagen	Ar	Enhanced cell growth <sup>63</sup>
Barrier coatings	Release of drug	Quartz	HA	Controlled release rate <sup>64</sup>
Cell culture	Tissue culture	PS	Ar	Enhanced cell adhesion <sup>65</sup>
	vessels	PTFE	NH <sub>3</sub>	Enhanced wettability <sup>66</sup>
Others	General	Glass/ Metal	O <sub>2</sub> / H <sub>2</sub>	Sterilisation/surface cleaning <sup>67, 68</sup>

\*Abbreviations: SWCNT: single-walled carbon nanotube; ta-C: tetrahedral amorphous carbon; DNA: deoxyribonucleic acid; PNA: peptide nucleic acid; ePTFE-g-PEGMA: poly(ethylene glycol) methyl ether methacrylate (PEGMA) monomer coated expanded poly(tetrafluoroethylene) (ePTFE); PP: polypropylene; AA: acrylic acid; PES: polyethersulfone; PVDF: poly(vinylidene fluoride); PTFE: poly-tetra-fluoro-ethylene; SMCs: smooth muscle cells; PE: polyethylene; UHMWPE: ultra-high molecular weight polyethylene; FSA: fluorosilicone acrylate; HA: n-heptylamine.

If simple monoatomic or diatomic gases such as Ar, O<sub>2</sub>, N<sub>2</sub> (cases in table 2.2) are used in plasma treatment, there are no reactive fragments that can polymerise from the molecules. These plasmas do not produce coatings but will create or substitute functional groups on the surface, and possibly create radicals for postirradiation grafting. Most of the time, plasma treatment from Ar, O<sub>2</sub>, N<sub>2</sub>, NH<sub>3</sub> and so forth, are used to render a more hydrophilic surface.<sup>48, 55, 59, 66</sup> In addition, the functional groups are suitable for covalent binding of biomolecules to obtain desired bioactivity.<sup>45, 46</sup>

If, however, an organic monomer (often a volatile liquid) is used for the generation of the plasma, reactive intermediates will form and polymerise at the substrate surface (sometimes in the plasma bulk as well<sup>69</sup>), thus a film will be deposited on the surface. During deposition, the coating and the substrate will both be impinged by ions from the plasma, which leads to etching.<sup>70</sup> It is a competitive process where only the right combination of parameters gives a rapid growth of the coating. As seen in table 2.2, n-heptylamine treatments are in the form of plasma polymer films. Al-Bataineh and co-workers used n-heptylamine to obtain an amine rich layer in order to covalently link furanones onto the surface for antibacterial purposes.<sup>60</sup> On the other hand, Vasilev et al. employed two thin n-heptylamine plasma polymer layers for controlled release of levofloxacin. The first layer was coated to the biomaterial surface, which served to promote spreading of the drug, before an additional plasma polymer coating was deposited on top of levofloxacin to adjust the rate of drug diffusion into the surrounding via changes in overlayer thickness.<sup>64</sup> This mode of tunable levofloxacin release inhibited Methicillin-resistant *Staphylococcus aureus* (MRSA) biofilm development on or near the vicinity of the coated biomaterial.

Beside direct plasma polymer film formation, there are two approaches commonly used to induce polymerisation via plasma treatment. One method is to create radicals on the surface of a material first and utilise these active sites to graft the polymer. For instance, in order to prepare biomaterials with lubricious surface, poly(N,N-dimethylacrylamide) (PDMAA) vapour was allowed to react with Ar plasma treated polymer substrates. With 15 s of Ar plasma treatment to activate the substrate, PDMAA was successfully bound to the sample surfaces. The effectiveness of this technique can be further improved by treating the polymer substrates with benzoyl peroxide (BPO)

solution prior to plasma irradiation. BPO activates the surface resulting in a higher percentage of PDMAA binding.<sup>53</sup> Note that the grafted polymer is not subjected to plasma in this method. Hence the composition of the coating should be the same as attained from conventional polymerisation. In contrast to the post plasma grafting approach, a coating can be grafted to a surface through induced crosslinking. Initially a layer of monomer is adsorbed onto the material surface and then plasma treated. The direct energy transfer from energetic particles and radiation to the monomer layer and substrate surface will produce radicals which lead to the formation of a crosslinked polymer top layer.<sup>47</sup> The figure below summarises the four different plasma surface modification techniques.

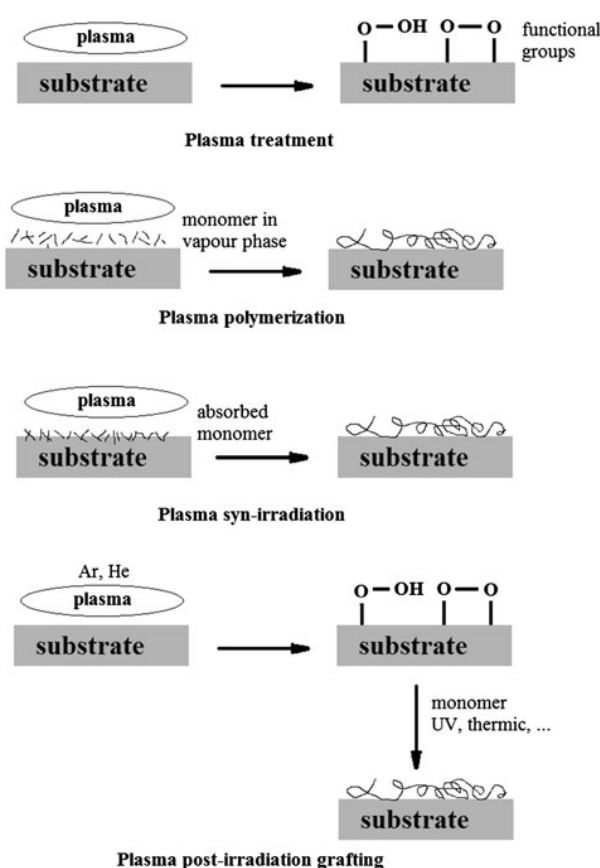


Figure 2.4, Schematic representation of different surface modification outcomes by plasma treatments. Reprinted with permission from Springer.<sup>71</sup> Copyright © 2012, Springer Science + Business Media, LLC.

In addition to modification in the surface chemistry, exposing a material to a plasma will also etch the surface due to high-energy particle bombardment. A study by Bae et al. illustrates the diverse morphology changes plasma treatment can induce to

microporous polypropylene (PP) membranes.<sup>48</sup> A few reagents were used to generate plasmas, including acrylic acid, allylamine, water and Freon-116 (hexafluoroethane) gas. The surface topography of PP membranes modified with these plasmas is shown in figure 2.5, where the original structure of the microporous membrane is included.

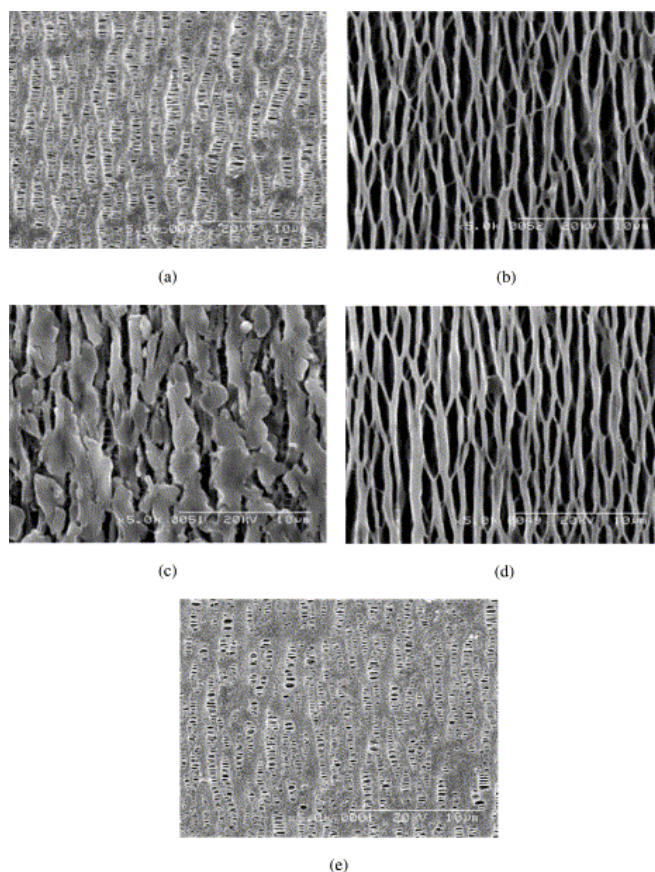


Figure 2.5, SEM images of the surface of PP membrane and those treated with plasma for 40 mins: (a) no gas; (b) acrylic acid; (c) allylamine; (d) water; (e) Freon-116, respectively. Reprinted with permission from Elsevier.<sup>48</sup> Copyright © 2001 Published by Elsevier Ltd.

From the SEM images, it is clear that acrylic acid (Fig. 2.5 b) and water (Fig. 2.5 d) plasma changed the morphology of the membrane significantly through deterioration of the membrane pores. On the other hand, an allylamine plasma (Fig. 2.5 c) produced thin films that covered the surface. However, Freon-116 treated (Fig. 2.5 e) membrane was similar to the original topography. Although it is arguable that changes might be visible if the Freon-116 plasma treated surface was examined at the nanoscale as well. Atomic force microscopy (AFM) reveals more details of the minor changes, as it is capable of imaging surface features down to less than 1 nanometer.<sup>72</sup> For instance, Mirmohammadi and co-workers<sup>73</sup> investigated the effects of O<sub>2</sub> and CO<sub>2</sub> plasma

treatment on poly(3-hydroxybutyrate) (PHB) films with both SEM and AFM. The results indicated that the irregular and coralloid surface of PHB films changed to a regular surface morphology with nanoindentation and nanoprotrusion as a consequence of O<sub>2</sub> plasma treatment.

So far, we have discussed the general strategies of plasma treatment on biomaterials and medical devices. The following section will focus on plasma polymerisation methodology and some important factors that affect the film properties in relation to biomaterials applications. In section 2.6 this will be focused further to the formation of plasma polymer films that aim to prevent biofilm formation on materials surfaces, reviewing both anti-fouling and bactericidal approaches.

## 2.4 Plasma polymerisation

Plasma polymerisation, which is frequently denoted as plasma-enhanced chemical vapour deposition (PECVD) in the literature, is a solvent-less process that produces uniform, pin-hole free coatings in one-step. This convenient and versatile technology permits the use of an exceptionally wide range of monomers (gases, most volatile compounds and solids which can release vapour upon sublimation). Unlike other polymerisation methods, monomers that contain only saturated bonds can also form polymer films under the influence of plasma.<sup>74, 75</sup> Additionally, plasma polymer films contain unique structures distinctively different from conventional polymers due to fragmentation, ionisation and recombination processes that exist in the plasma phase. The starting monomer composition and structure generally do not predict all the structural components and chemistry of the resulting plasma polymer. Fluoropolymers, as an example, in most plasma polymerisation conditions, forms -CF<sub>3</sub>, -CF<sub>2</sub>-, >CF-, and >C< moieties interconnected in a random fashion rather than in ordered -(CF<sub>2</sub>-CF<sub>2</sub>)<sub>n</sub> polytetrafluoroethylene (PTFE) chains.<sup>76, 77</sup>

The phenomenon of polymer formation in plasma glow was systematically and extensively studied from the 1960s.<sup>78, 79</sup> Depending on the choice of precursor molecules, films with special physicochemical properties can be produced rapidly.

Properties such as strong adherence, or lubricious, tunable permeability, optical clearance, scratch- and abrasion resistance, flame-retardant, corrosion inhibition, anti-fogging, etc. are favored for their commercial values.<sup>80-88</sup> In the past several decades, plasma polymer films have been utilised in biomedical engineering to interact with cells and tissues to gain control over biological responses both *in vitro* and *in vivo*.<sup>89-91</sup>

Plasma polymerisation is commonly used to produce functional coatings for direct biological interactions or to facilitate the binding of biomolecules that can control cell attachment and proliferation.<sup>92, 93</sup> The retention of functional groups in the monomer largely depends on the process conditions, therefore one type of starting material can generate a variety of deposits rather than only yield a well-discernible polymer, as shown in Figure 2.6. PEG-like plasma polymers (high in ether content) were generated using a different combination of gas precursors and processing conditions. Following deconvolution of the XPS C 1s spectra, new functional groups (different binding environment of C) arise after plasma treatment such as hydrocarbon, ethers, carbonyls and acids or esters.

From figure 2.6, there are two further important points for discussion: 1) plasma polymerisation is highly system dependent, meaning the reactor and operation conditions, especially load powers can not be compared in isolation; 2) If all other deposition parameters are fixed, i.e., monomer of choice, flow rate, reactor geometry and so on, then with the increases in electrical power, there is an increasing amount of fragmentation and recombination, which results in a film chemistry far deviated from the monomer composition. In the case for PEG-like films, high power processing creates films with higher concentration of hydrocarbon, and as a consequence, less ether (linked to low-fouling property of PEG). Cultured fibroblast L929 cells show good adhesion and growth on high power deposited coatings but are unable to attach on the lower 1 W plasma power generated film.<sup>94</sup>

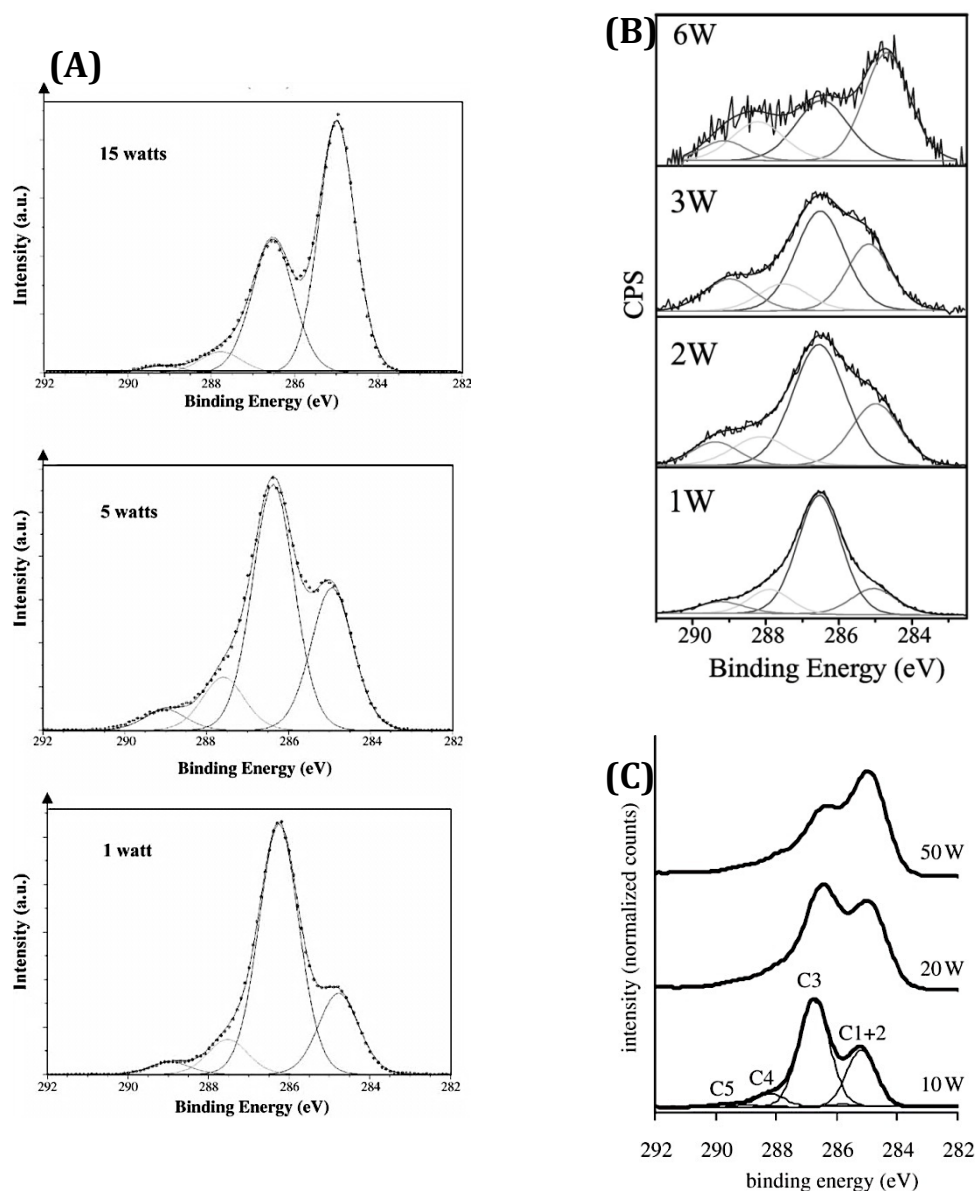


Figure 2.6, XPS high resolution C 1s spectra for several PEG-like coatings deposited using plasma: (a) 15 % diethylene glycol dimethyl ether vapour in Ar as starting monomer, RFGD, deposited on silicon wafers as a function of power (20 mTorr, deposition time = 30 min). Reprinted with permission from Elsevier.<sup>94</sup> Copyright © 2005 Acta Materialia Inc. Published by Elsevier Ltd.; (b) di(ethylene glycol) vinyl ether in Ar as starting monomer, plasma polymerised by atmospheric pressure surface dielectric barrier discharge (SDBS) at different average powers. Reprinted with permission from John Wiley and Sons.<sup>95</sup> Copyright © 2012 Wiley-VCH Verlag GmbH & Co KGaA, Weinheim.; (c) diethylene glycol dimethyl ether (99 % purity), RFGD, thin films deposited under load powers of 10, 20, and 50 W for a treatment time of 35, 20 and 10 s, respectively. Reprinted with permission from The Royal Society.<sup>96</sup> Copyright © 2012 The Royal Society.

The majority of the published literature in this field focuses on the influence of power (W), flow rate, and pressure to the deposition rate and final composition of the film, but

does not provide insight into the growth of the film at the molecular level. This is partly due to the fact that functional coatings can generally be obtained through trial and error, and partly the result of a lack of appropriate tools to measure the internal parameters of the plasmas. Nevertheless, the external parameters optimised for one reactor maybe useless for reactors with different geometries. Presently, a growing number of studies have turned their attention to the relationship between film properties and the various species generated in the plasmas, such as ions, radicals and neutrals.<sup>97-99</sup> A good example that shows the role of ion flux in predicating the deposition rate of plasma polymer films is the work by Michelmore and co-wokers.<sup>100</sup> Four precursors were fed into a parallel-plate electrode reactor with adjustable height, and the film growth rates were recorded under constant RF power or constant ion flux. The result showed that ion flux is a better indicator for the deposition of the plasma polymer films than RF power input (figure 2.7).

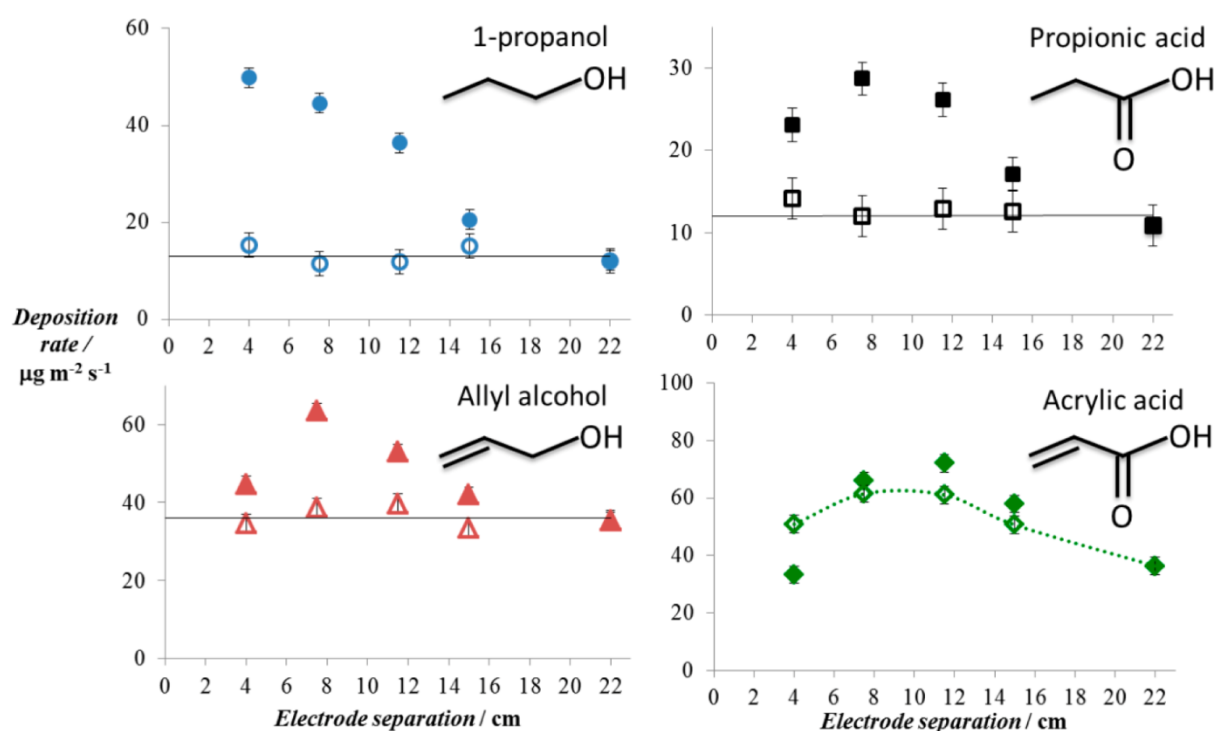


Figure 2.7, Deposition rates of four different starting monomers with changes in electrode separation at 1 Pa at constant RF power (5 W, closed symbols) and constant ion flux ( $7.5 \times 10^{17} \text{ m}^{-2} \text{ s}^{-1}$ , open symbols). Reprinted with permission from American Chemical Society.<sup>100</sup> Copyright © 2013 American Chemical Society.

As mentioned in section 2.3.1, although ions are relatively rare compared to neutrals and radicals in the plasmas, ions contribute to the mass of plasma polymer films.<sup>38,99,101</sup>

It is not only the concentration of the species but also their sticking probabilities that determine contributions to the deposition process. For instance, in fluorocarbon plasmas, the sticking probability of neutrals and radicals is normally less than 1 %, in contrast to  $\sim 16$  % sticking coefficient for  $C_2F_4^+$  ions.<sup>98</sup> More research focused on collecting data on the different components (electrons, ions, neutrals, radicals) is warranted in order to understand the molecular build up of plasma polymer films.

Beside the gas chemistry and plasma physics, the substrate surface chemistry is also an important factor affecting the growth of plasma deposits, which is in contrast to a commonly held belief that plasma polymerisation is a substrate independent technique. This is challenged by studies that showed significant variations in film growth rate, structure, chemistry and stability, depending on what substrates have been used.<sup>102-104</sup> Vasilev et al. investigated the growth of ultrathin amine containing plasma polymers (< 15 nm) onto gold and thiol-SAM-modified gold substrates. The deposited films were always thicker on thiol substrates than those deposited on the gold alone. Secondly, films deposited on these substrates (a few nanometer from the substrate surface) possessed significant differences in the nitrogen chemistries.<sup>102</sup> Another example that illustrated the influence of substrates on surface structure and chemistry was achieved by depositing perfluorocarbon plasma polymer films onto Si wafer, Ag and Al coated glass. AFM images revealed perceptible differences in film morphology and XPS data indicated distinct chemical bond formation of the coatings deposited on these three types of substrates.<sup>103</sup> The adhesion of a plasma polymer film to substrates correlates to the bond type and bond strength between the film and the substrate, and also the chemistry within the bulk of the film.<sup>104</sup> Therefore, the choice of substrate is not a trivial issue when the intended application requires deposition of nanometer thick plasma polymer films.

So far, the situation where plasma is uniformly grown on the surface has been considered, yet under certain plasma conditions, the polymerisation process can happen in the gas phase. Macromolecules may condense to particles, grow and deposit as a flaked plasma polymer layer that are highly crosslinked. Kobayashi et al. first reported on the formation of micron and sub-micron size particles of plasma polymers in the 1970s.<sup>105, 106</sup> Figure 2.8 is a phase diagram created by Kobayashi to illustrate the

dependence of ethylene film and power formation on monomer pressure and flow rate. High pressure ( $\sim 100$  Pa) and low monomer flow rate assist particle formation in the plasma. Such powder deposition was considered an unwanted effect back then, because the plasma deposits are not suitable for microelectronics applications. Later, powder or dust particle production was used as a probe for fundamental studies of plasma behaviour.<sup>107-109</sup> Apart from particle deposition, low pressure plasma polymerisation can generate other types of nanostructured films, a review on this topic is available.<sup>110</sup>

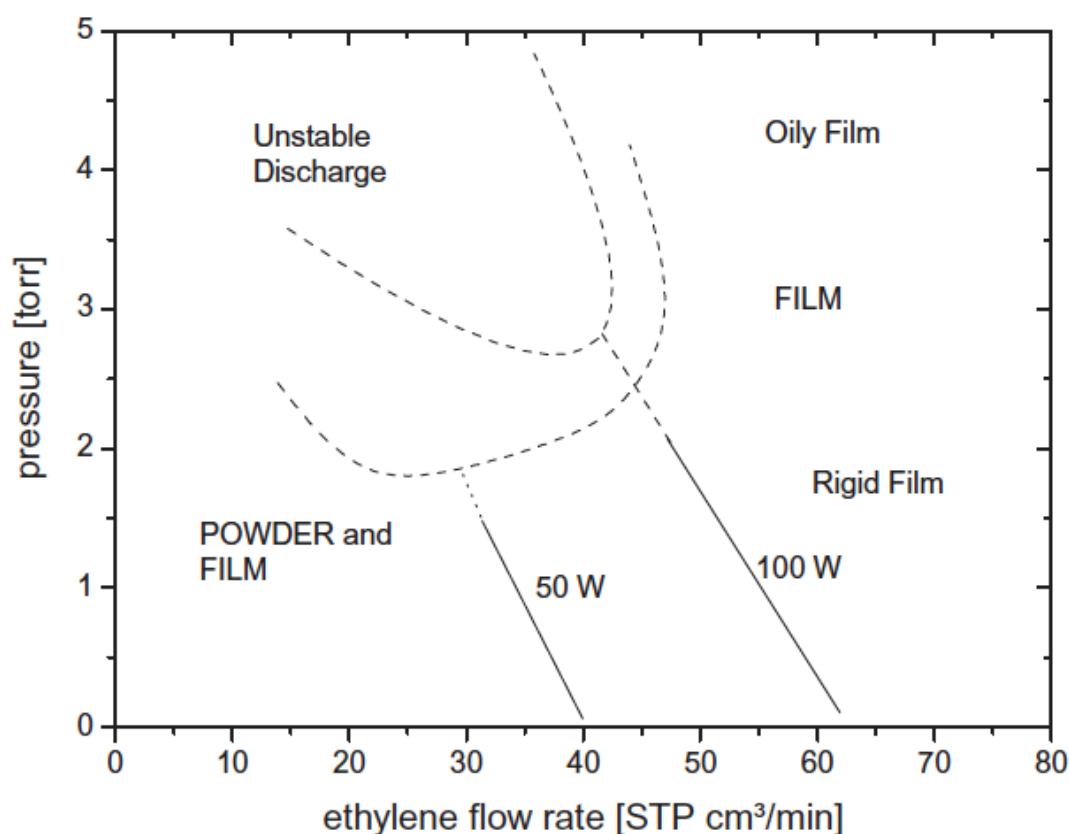


Figure 2.8, Influence of monomer pressure and flow rate on film and powder formation, in the plasma polymerisation of ethylene ( $C_2H_4$ ). Reprinted with permission from Taylor & Francis.<sup>106</sup> Copyright © 1974, Taylor & Francis.

## 2.5 Plasma polymer films to direct cell fate

The cell-material interaction is a complex matter and the requirements can be quite different depending on the applications of the biomaterials. In some cases, cell attachment, proliferation or differentiation is desired. In other situations, such as

catheters and stents, prevention of protein adsorption and cell adhesion is a priority. To suit these various purposes, plasma polymer films are prepared to exhibit specific functional groups. Cell adhesive coatings can be made from chemical compounds (such as amine or carbonyl containing monomers), with or without subsequent immobilisation of biomolecules (proteins, peptides, DNAs). Antifouling coatings are frequently produced from ether containing monomers to mimic conventional poly(ethylene glycol) (PEG) polymer layers. Noticeably, there is an emerging trend of direct plasma polymerisation of biological molecules to eliminate the need for complex wet-chemical binding reactions. Amino acids can be used on their own or copolymerised with different synthetic materials of mixed compositions.<sup>111-113</sup> However, the use of plasma polymerised amino acids and peptides for cell culture and biomedical applications are yet to be evaluated. This review will focus on functional thin films prepared for cell-materials interactions including i) cell-adhesive layers, ii) antifouling plasma polymers, and iii) pattern or gradient coatings for spatial control of cell attachment.

### **2.5.1 Cell adhesive functional coatings**

The most abundant reactive surfaces produced via plasma polymerisation are amine (-NH<sub>2</sub>) and carboxyl (-COOH) films, due to their good stability in aqueous environments and compatibility with widely used chemical reactions (carbodiimide chemistry is one common approach) for immobilisation of bioactive moieties such as proteins, enzymes, antibodies and glycosaminoglycans. Other chemical groups including hydroxyl (-OH), aldehyde (-C=O), epoxy, and esters have also been exploited as alternative templates for biomolecules covalent attachment.<sup>114</sup> Table 2.3 gives some examples on the direct use of these functional coatings for control of cell attachments; together with several studies that demonstrate their important roles in the grating of bioactive molecules. It is possible to mix two precursors so that the plasma polymer film contains a combination of functional groups. Sardella et al. copolymerised acrylic acid and allylamine at various compositions in a plasma deposition process and the films show tuneable acid-base properties.<sup>115</sup>

Table 2.3, Selected examples of plasma polymer films with bioactive groups and their influence on cell behaviours.

<b>Substrate</b>	<b>Monomer</b>	<b>Cell type</b>	<b>Responses</b>
Polysiloxane	Allylamine	Spinal cord neurons	Improved cell attachment and proliferation <sup>118</sup>
PDMS	Allylamine - bind EGF	Corneal epithelial cells	Promoting cell adhesion and proliferation <sup>119</sup>
Titanium	Heptylamine	L929 mouse fibroblast SaOs-2 osteoblast cell	Enhanced osteoblast growth and actin cytoskeleton development, with reduced fibroblast cell growth <sup>120</sup>
PET fibres	N-heptylamine - CMD/peptides	HUVECs	Improved cell adhesion, growth and spreading <sup>121</sup>
Si, glass, PS, PET	Acrylic Acid	hTERT-BJ1 fibroblast	Enhanced cell adhesion <sup>122</sup>
PET	Acrylic Acid - bind RGD	3T3 fibroblast cell	Improved cell adhesion <sup>123</sup>
PS	Isopropyl alcohol	Fibroblast cells	Increased attachment and proliferation of cells <sup>124</sup>
PTFE	Methanol and H <sub>2</sub> - collagen	Porcine aortic endothelial cells	Cells behaved in a manner similar to that of PAEC in natural conditions <sup>125</sup>
PS, Si	Propionaldehyde - Streptavidin - Enzymes, antibodies	Antigen-specific T cell	Selective attraction and binding of specific cell subpopulations onto solid surfaces <sup>126</sup>
316L SS	HMDSO/O <sub>2</sub>	Smooth muscle cells	Improved cell growth compared with uncoated substrate <sup>117</sup>

\* Abbreviations: PDMS: polydimethylsiloxane; EGF: epidermal growth factor; PET: polyethylenterephthalate; RGD: arginine-glycine-aspartic acid; HUVECs: human umbilical vein endothelial cells; PTFE: polytetrafluoroethylene; SS: stainless steel; HMDSO: hexamethyldisiloxane.

The last case study in table 2.3 represents a class of organosilicone plasma polymer film that exhibits superior chemical inertness, excellent corrosion and wear resistance, as well as biocompatibility.<sup>116, 117</sup> Plasma polymerised organosilicone coatings from a mixture of HMDSO/O<sub>2</sub> can be tuned to be polymer-like or silica-like through changes in the oxygen content. Gandhiraman et al. have fabricated two different types of thin films from pure HMDSO (polymer-like) and HMDSO/O<sub>2</sub> (silica-like). They have found differences in wettability and surface roughness, as well as adhesion strength to the substrate between these two films. The polymer-like film showed higher adsorption of fibrinogen and smooth muscle cell proliferation.<sup>116</sup>

What has not been shown in the above table are films made from inorganic monomers, such as diamondlike carbon (DLC),<sup>127, 128</sup> carbon nitride,<sup>129</sup> and silicon carbide<sup>130</sup> plasma polymer films, which have all demonstrated to be compatible surfaces for biomedical applications.

### 2.5.2 Antifouling coatings

Biofouling occurs when proteins, cells or pathogens grow on abiotic surfaces and affect the functioning of the material in a biological environment. In the context of medical devices and biomaterials, uncontrolled and irreversible protein attachment is the first step of the host defense system. It generally ends with fibrosis or fibrous encapsulation of the material. The biomaterial will ultimately fail to communicate effectively with the cells and surrounding tissue.<sup>22</sup> To resist nonspecific adsorption of proteins, and hence reduce the 'foreign body response' *in vitro* and *in vivo*, antifouling coatings are being exploited.

Studies have shown that very hydrophilic and uncharged surfaces are more likely to be protein repellent. Various molecules and macromolecules have been investigated for surface passivation. For example, poly (ethylene glycol) (PEG),<sup>131, 132</sup> poly(vinyl alcohol) (PVA),<sup>133, 134</sup> polyacrylamide,<sup>135</sup> and poly(hydroxyethyl methacrylate)<sup>136</sup> are all used for the creation of hydrogels that intrinsically inhibit protein adsorption. Among the low-fouling polymers that have been used, PEG has received the majority of attention. The

fact that the FDA has approved PEG for use in the body has made it an ideal material for biomedical applications. Surface PEGylation methods generally fall into two categories: covalent attachment and adsorption, with the latter comprising chemisorptive and physisorptive phenomena.<sup>137</sup>

In the literature, studies have been conducted to investigate the mechanisms of protein resistance of PEG polymers, however it remains to be fully elucidated.<sup>138-142</sup> Some of the theories include electrostatic double layer forces, adsorption of nanobubbles and hydroxide ion formation.<sup>143-145</sup> However, 'steric repulsion' theory and the effect of the 'water barrier' are two of the most widely cited in the literature. Steric repulsion suggests that an approaching protein causes compression of the PEG chains, resulting in conformational entropy loss which makes protein adsorption onto a PEG surface thermodynamically unfavourable.<sup>146</sup> This theory has been used to explain the inertness of long chain ( $n \geq 6$ ) PEG-based films, but does not explain at the molecular level for their antifouling property.

The water barrier theory proposes that the tight, between the water molecules and the PEG chains there is directional hydrogen bonding that forms a physical barrier against protein adsorption at the PEG-water interface.<sup>144, 147</sup> The theoretical thermodynamic modeling work by Latour<sup>148</sup> suggests that, both entropic and enthalpic effects should be considered. The entropic penalties arise from the bond formation between a surface tethered chain and a protein because this reduces the chains configurational space and freedom of gyration. In contrast, water is a small and mobile molecule that can readily move along with the tethered chain and exchange with other water molecules. Therefore bonding of water molecules minimally inhibits the configurational space of the PEG chains. On the other hand, the system enthalpy increases when protein adsorption occurs because of an increase in molecular strain energy of the chains, which results from the alignment of the hydrogen bondable functional groups of the protein and PEG chains.

Plasma polymerisation has been used to produce PEG-like polymer coatings, which covalently bond to a substrate. The ether groups in the PEG-like plasma polymer films give rise to the protein repellent properties. Monomers including diglyme,<sup>94, 96, 149-152</sup>

triglyme,<sup>153</sup> tetraglyme,<sup>154-156</sup> oligoglymes and crown ethers,<sup>142</sup> as well as diethylene glycol monovinyl ether,<sup>95, 157</sup> triethylene glycol monallyl ether<sup>140</sup> and allyl glycidal ether<sup>158</sup> have been used to generate PEG-like thin films. Choukourov et al. used poly(ethylene oxide) (PEO) macromolecules (M = 2500) as a source for generation of PEG-like films.<sup>159</sup> The presence of plasma during vacuum evaporation led to enhanced crosslinking compared to the original PEO, but at the expense of reduced retention of the ether groups. The protein resistant nature of these films in aqueous environment has been examined against proteins, such as fibrinogen, laminin, bovine serum album, and immunoglobulin.<sup>96, 159</sup> It was found that low load power deposits behave like PEG films that is protein resistant.

### 2.5.3 Patterns and gradients

Besides the formation of uniform coatings, plasma polymerisation has extended its use to generate gradient and patterned surfaces.<sup>160-163</sup> Chemical gradient stimuli are relevant to a number of physiological and biological processes, such as the maintenance of homeostatic equilibrium and chemotaxis.<sup>164</sup> The generation of surface chemistry gradients allows high throughput screening of factors that influence the interactions of biomolecules and cells with material surfaces. Plasma polymer gradients can be formed by a few strategies: i) use an aperture or shutter so that small areas of the sample were sequentially exposed to the plasma of changing composition;<sup>165</sup> ii) move the substrate at a controlled speed to meet plasmas with various molecular fragments;<sup>166</sup> iii) use a mask on top of the substrate to control the diffusion of the plasma species;<sup>163</sup> iv) use knife edge electrodes to produce non-uniform plasma generating a symmetrical chemical gradient on substrates placed directly underneath the plasma glow.<sup>150</sup> Readers interested in other methods of gradient fabrication, such as grafting, adsorption, diffusion, printing and so forth, will find information in the review by Genzer.<sup>167, 168</sup>

Plasma polymer films presented with chemical gradients have been used to assess the responses of various types of cells. Zelzer et al. created surfaces with varying hydrophobic and hydrophilic groups by depositing hexane plasma polymer film first, and then used a mask to control the growth of allylamine plasma coatings. 3T3

fibroblast cells showed high density attachment to the allylamine end of the gradient, while very few or no cell attachment to the hexane plasma polymer film coated part.<sup>163</sup> Another study used the opposite of this design, where a cell adhesive substrate (glass coverslips treated with oxygen plasma) was coated with a hexane plasma polymer film with a gradually decreasing thickness or coverage controlled by a mask.<sup>169</sup> Hippocampal cells grown on those surfaces displayed increased cell density, number of processes and average process length with increasing hydrophilicity, as shown in figure 2.9. This trend of change from repellent to adhesive depends on the wettability changes of the surface and holds true for other types of cells, such as L929 fibroblast,<sup>170</sup> endothelial,<sup>171</sup> and embryonic stem cells.<sup>172, 173</sup> Except from simple designs that incorporate only chemical gradients, researchers have tried to combine topography cues for assessing cell behavior. In a study by Michelmore and co-workers, conformal gradient films with concentration of carboxylic acid groups varying between 0.7 to 3 % from one end to another were deposited onto silicon surfaces with nanopores or were flat. It was found that at same density of adhesion, cells showed a greater degree of spreading on surfaces with nanoscale pores.<sup>174</sup> More regular topography, e.g. grooves, has also been tested concurrently with plasma polymerised chemical gradients.<sup>175</sup>

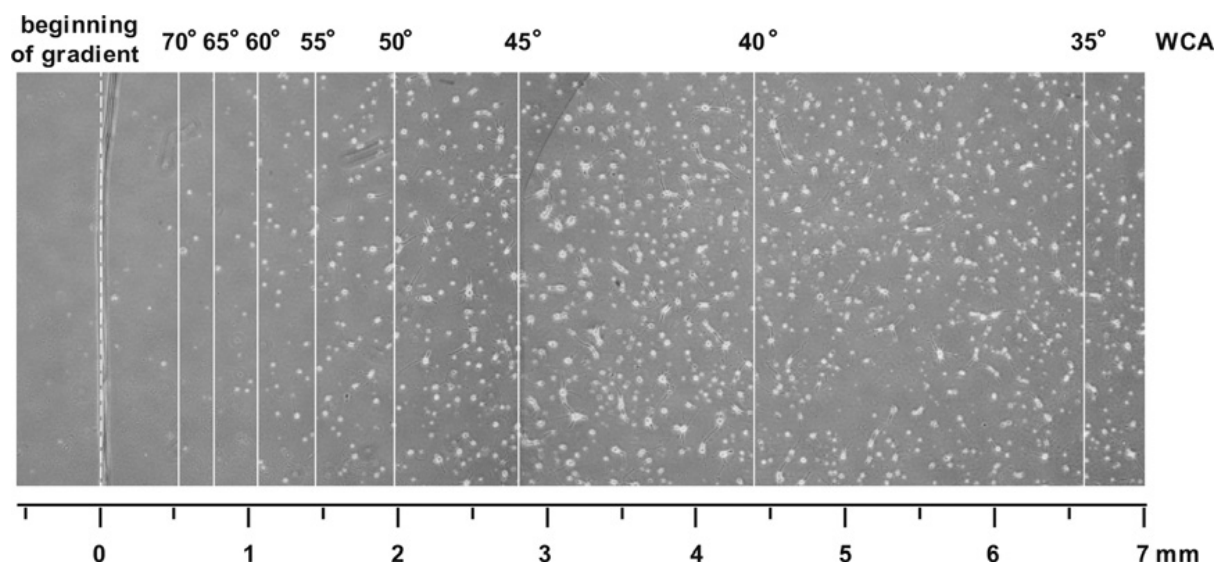


Figure 2.9, Representative images of hippocampal cells after 2 days of culture on the linear gradient produced from plasma polymerisation of hexane using a mask. White lines separate the areas used to measure the cell density within specific water contact angle regions on the surface. White dashed line marks the beginning of the gradient. Reprinted with permission from Elsevier.<sup>169</sup> Copyright © 2011 Published by Elsevier Ltd.

With advances in nanotechnology, artificial materials with chemical and physical patterns that mimic cellular and extracellular organisations have been fabricated to gain insights into cell-substrate and cell-cell interactions.<sup>176, 177</sup> Much of the work reported on the patterned plasma polymer films relies on the deposition of a low fouling coating, followed by photolithographic methods to spatially remove regions of the top-layer thereby exposing the underlying reactive sites.<sup>162</sup> This multiple step approach generally provides good patterns but is laborious and time consuming. On the other hand, a physical mask can be placed over the substrate during deposition to create chemical patterns in a single step.<sup>161</sup> Using engineered surfaces to spatially control and drive the interfaces of proteins and cells provides useful information to help gain insights into basic cellular functions, which in turn helps to create better biomaterials, sensors and medical devices.<sup>178-180</sup>

## **2.6 Plasma polymer films for improved antimicrobial property**

The colonisation of biomaterial surfaces by pathogenic bacterial and fungal species is known to adversely affect the function of such devices.<sup>181-183</sup> These so-called device related infections (DRIs) are problematic because they pose great risk to the patient and increases costs associated with the health care system. For devices such as contact lenses and catheters, signs of infection are detected soon enough, which will result in the frequent replacement of the device. For indwelling implants, such as orthopedic joint replacements, diagnosed rates for DRIs are relatively low (around 1 – 2 % at most centres).<sup>184</sup> However, the consequence for the patient can be devastating because by the time the DRIs are detected, there might have been severe damage to the adjacent tissues. If systematic antibiotic therapy fails to resolve the DRI, partial or total removal of the implant is often required, which in some cases have led to death of the weakened patient.<sup>185</sup>

Infections are most likely acquired in nosocomial environment where the protective skin barrier is breached due to surgical intervention. Microorganisms are introduced to normally sterile sites of the body. Previously regarded innocuous species in immunocompetent host, such as *Staphylococcus epidermidis*, *Pseudomonas aeruginosa*

or other non-fermenter, mycobacteria and yeasts, are the leading cause of DRIs.<sup>186-188</sup> This is due to their capability to establish structured biofilms that are difficult to eradicate. Examples of biofilms formed on different surfaces are given in figure 2.10.

To some extent, the improvement in operation room (OR) facilities, including laminar flow air handling, and introduction of rigorous practices for surgeons and nurses can effectively reduce the risk of nosocomial infections. Considering this example, in a Canberra hospital, after a hospital-wide surveillance and intervention program was implemented, the number of blood stream infections per year fell from 110 in 1998 to 48 in 2005 (a greater than 50 % reduction) and the rate per 1000 patient-days fell from 0.6 to 0.3.<sup>189</sup> Unfortunately, for developing countries where shortage in facilities and skills are prevalent, a far greater threat to patient exists. In Shanghai, China, from 2004 to 2009, the overall rate is 5.3 % for DRIs and 6.4 DRIs per 1000 ICU-days (intensive care unit).<sup>190</sup>

The demand for synthetic devices will grow even further as the life spans in modern societies are increasing. Therefore, the overall rate of infections will rise. To combat this problem, antimicrobial surfaces have been exploited for the past decades to render a device with long-term resistance to infections. Antimicrobial surface modification can be physical (topography) or chemical (functionalisation or coatings) or a combination of both. The rationales behind those approaches generally fall into two categories: i) antifouling surfaces to prevent or reduce bacteria attachment and ii) biocidal surfaces to kill microbes on contact. This review will focus on surface modification based on or in part including plasma polymer films for antimicrobial purposes. However, before that, a description of the biofilm formation process will be given.

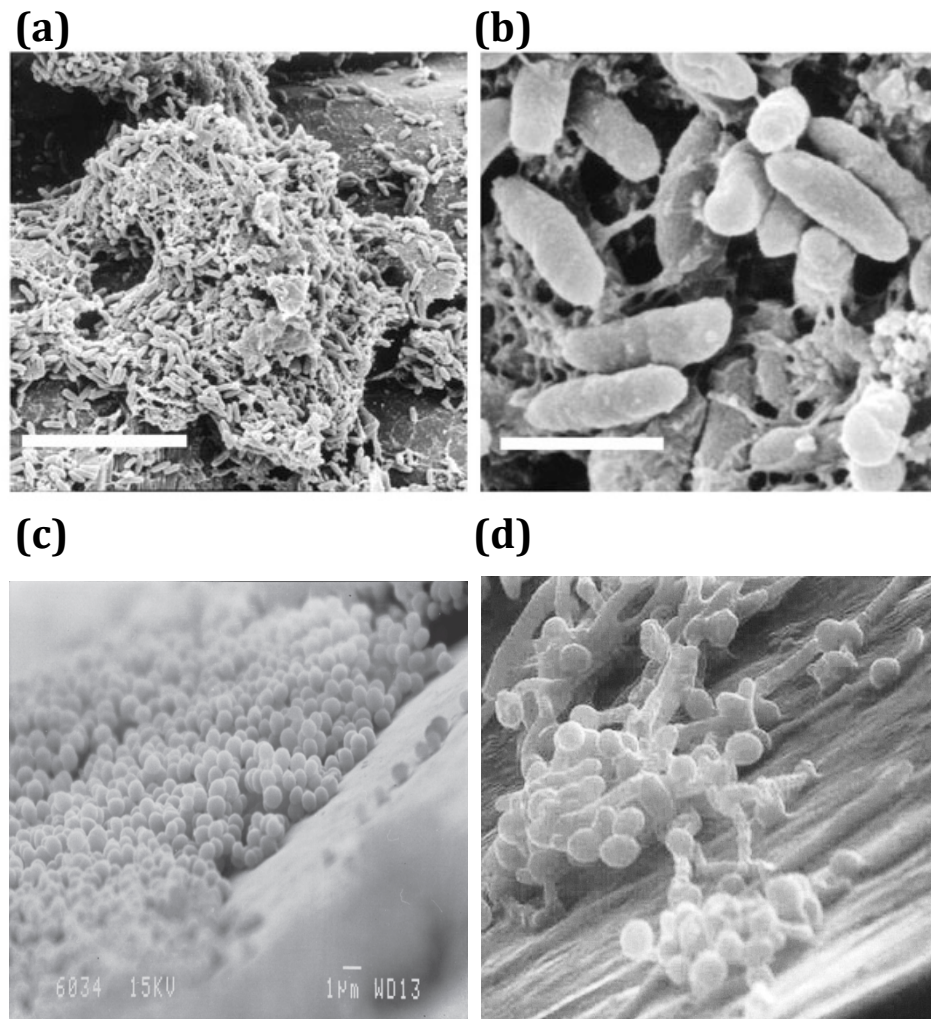


Figure 2.10, Scanning electron micrographs of biofilms formed on various surfaces. (a) SEM image of a *P. aeruginosa* biofilm on the surface of a granite pebble. Scale bar, 10  $\mu\text{m}$ ; (b) High magnification of a biofilm featuring rod-shaped *P. aeruginosa* and stings of dehydrated EPS connecting bacterial cells. Scale bar, 1  $\mu\text{m}$ ; Reprinted with permission from Nature Publishing Group.<sup>191</sup> (c) SEM image of grape like *S. epidermidis* biofilm grown onto the surface of polystyrene pegs. Reprinted with permission from John Wiley and Sons.<sup>192</sup> Copyright © 2008 Royal Pharmaceutical Society of Great Britain (d) SEM image of a *Candida albicans* biofilm that has formed *in vitro* on the surface of a vascular catheter. Reprinted with permission from American Society for Microbiology.<sup>193</sup> Copyright © 2002 American Society for Microbiology.

### 2.6.1 Microbe attachment and biofilm formation

Microorganisms are the oldest forms of life on earth and have developed versatile adaptive strategies for the colonisation of surfaces over the timeline of evolution.<sup>194-196</sup> The mature communities of microbes are termed biofilms, which are more resistant to environmental stresses, such as dehydration, toxicity, antibiotics, and UV light exposure

than their planktonic counterparts due to the extracellular polymeric substance (EPS) secreted by the cells.<sup>193</sup> Figure 2.11 shows the key processes in biofilm development of mixed bacteria population (i.e. motile and nonmotile) in five phases: attachment, production of EPS, expansion, maturation, and detachment.

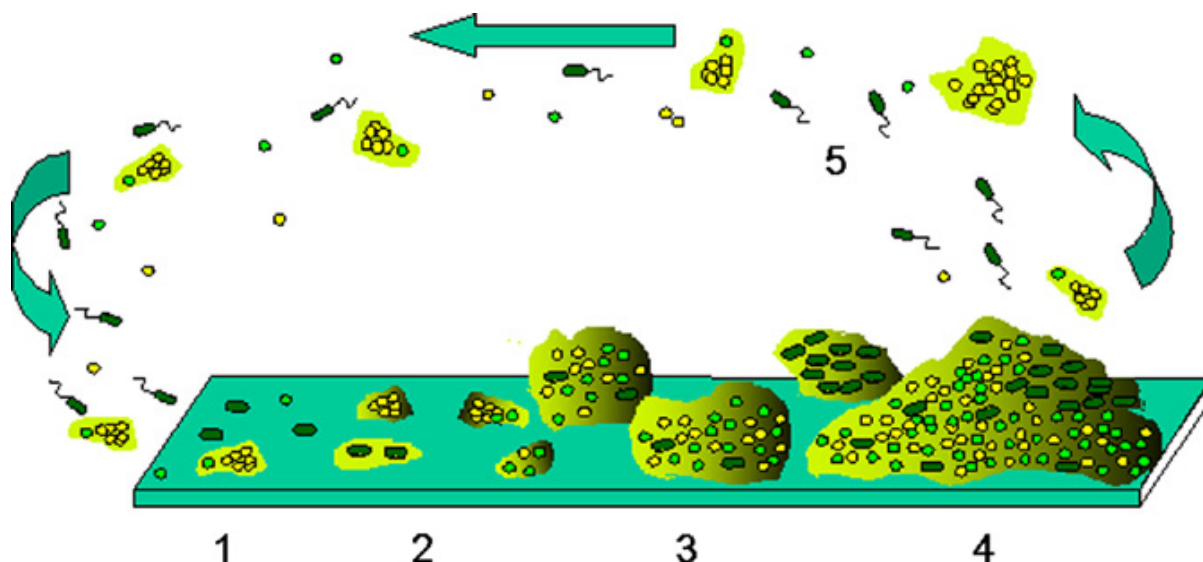


Figure 2.11, Schematic of key steps in biofilm formation process. This illustration shows a mixed biofilm consisting of *P. aeruginosa* shown in dark green (rods have swimming motility) and *S. aureus* and *S. epidermidis* shown in light green and yellow (two non-motile cocci). The extracellular polymeric substance (EPS) (or slimes) surrounding the cell is shown in green. (1) At the initial stage, single cells or clumps of detached biofilm bacteria from the surrounding environment attached to a surface. (2) Production of the EPS to make the cells adhere to the surface more firmly. (3) Clonal expansion. (4) A pseudo steady state where the biofilm matures. (5) The continues grow of biofilm is balanced by dispersion of single cells by motility-driven swarming dispersion (*P. aeruginosa*) together with the detachment of biofilms clusters containing EPS and cells. Reprinted with permission from Elsevier.<sup>197</sup> Copyright © 2013 Elsevier Inc.

The formation of biofilms always begins with the adhesion of a small number of bacterial or fungal cells to a surface. The interplay between the species of bacteria, the substrate and the fluidic environment dictates the initial attachment of bacteria and their growth into a mature biofilm.<sup>198</sup> A model illustrating this interaction is shown in figure 2.12. Once in contact with the surface, microorganisms can grow in different patterns.<sup>199</sup> For a motile organism, such as *Pseudomonas aeruginosa*, they actuate flagella to begin the attachment, then use type IV pili for twitching motility, mediated by extracellular DNA (eDNA) to plough on the surface and form elaborate structures.<sup>200, 201</sup>

For nonmotile bacteria, e.g. *Staphylococcus epidermidis*, it is assumed that the biofilm architecture is developed through clonal expansion.

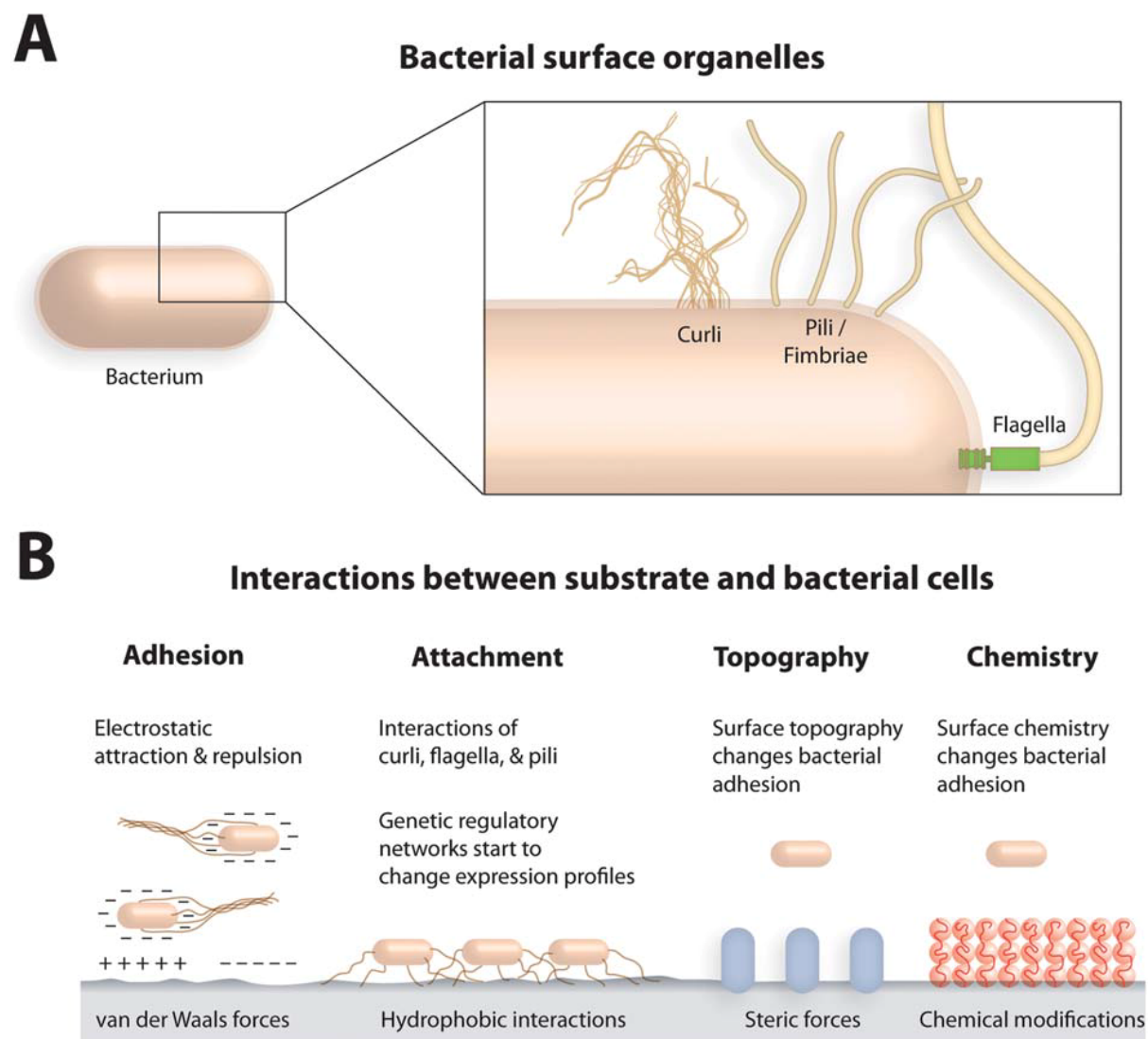


Figure 2.12, Several parameters that influence the interactions between bacteria and materials surfaces. (A) The bacterial cell wall has a range of organelles that govern the interactions with substrates, such as curli, pili or fimbriae, and flagella. (B) Physicochemical properties of the surface including charge, hydrophobicity, topography, and chemical functionality interacts with the bacterial cells and direct attachment process. Reprinted with permission from Royal Society of Chemistry.<sup>202</sup> Copyright © 2013, Royal Society of Chemistry.

Bacteria use a variety of extracellular organelles and proteins, including flagella, pili (also called fimbriae) and curli fibers (figure 2.12), to facilitate the adhesion to surfaces. The first step of adherence is reversible, in which the primary forces are hydrodynamic and electrostatic interactions. At appropriate conditions, twitching of the pili or the

rotation of the flagella can lead the cells to detach from the surfaces.<sup>203</sup> Once adherent cells start to change their gene expression and secrete EPS, the attachment process becomes irreversible. EPS consists of polysaccharides, proteins, lipids, metabolites and eDNA, which contains specific adhesins that anchors the cells toward the surfaces. For example, the protein SadB of *P. aeruginosa* has been shown to be important for the regulation of the irreversible attachment process.<sup>204</sup> As the cells proliferate and grow into microcolonies, greater amounts of EPS are produced to form a physical barrier between the cell community and the physiological environment. The cells will continuously draw nutrients from the surrounding area and replicate, thus the community grows and matures into a biofilm. The process of growth is balanced by the detachment of cells into the fluid. In the case of virulence pathogens, spreading and propagation of the microbes leads to more damage to the human body. Since the mature biofilm has increased resistance to antibiotic treatments and other remedy actions, the most promising way is to intervene at the initial attachment phase by presenting a surface with physicochemical properties unfavorable to the attachment of microorganisms. In the next section, different surface modification strategies for resisting microbial attachment will be reviewed in detail.

### **2.6.2 Approaches for antimicrobial surface modification**

Physical strategies for preventing attachment are often inspired by natural materials such as cicada wings,<sup>205, 206</sup> shark skin, and lotus leaves.<sup>207</sup> For instance, the surface of cicada wings contains nanopillars that can penetrate the bacteria cells (*Pseudomonas aeruginosa*) thus killing bacteria on contact. Mimicking the structure and distribution of the nanopillars can be useful in the production of antimicrobial surface coatings. In depth reviews on topographical changes for reducing attachment of microorganisms are available.<sup>208, 209</sup>

Chemical modifications are concerned with functionalisation, derivatisation, or polymerisation approaches to treat surfaces. It generally starts with a polymeric coating with functional groups, which have the ability to prevent biofouling or can be used to bind antifouling or biocidal elements. Polymeric coatings can be incorporated onto a material surface via different methods. Dip coating, spin coating, grafting, layer by layer

(LBL), self-assembled monolayers (SAMs), plasma polymerisation, to name a few. Based on the action of these coatings towards microorganisms, they can be divided in four major categories, as shown in figure 2.13: i) antifouling films that prevent microbe attachment; ii) coatings that kill microbes on contact; iii) antimicrobial agents release from a surface reservoir; iv) smart coatings that only release biocidal agents upon contact with the pathogen.

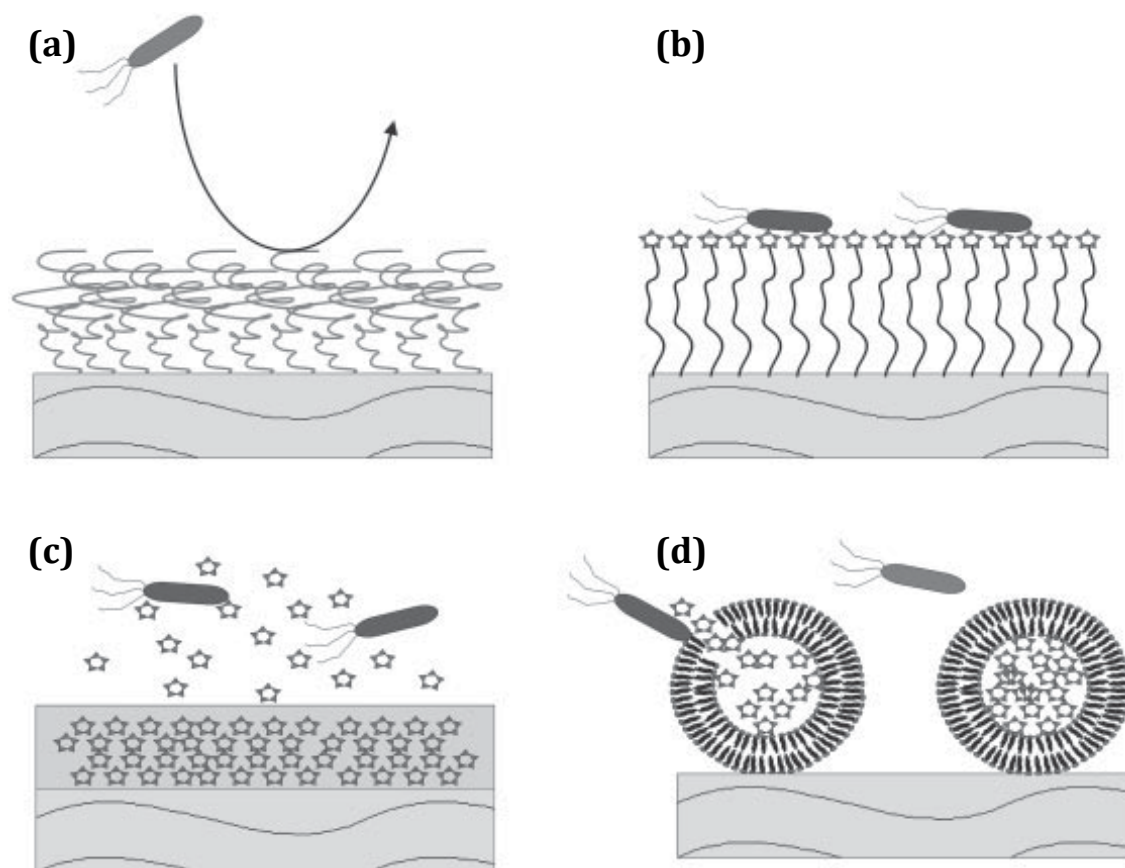


Figure 2.13, Schematic representation of the four major strategies used to create antimicrobial coatings: (a) antifouling surfaces that prevent microorganism adhesion; (b) surfaces that kill microbe on contact; (c) coatings that loaded with antimicrobial agents and release at controlled rate; (d) smart coatings that release biocidal agents upon the presence of pathogenic microorganisms. Reprinted with permission from John Wiley and Sons.<sup>210</sup> Copyright © 2012 John Wiley & Sons, Inc.

Microbe adhesion to a substrate sometimes occur through a layer of adsorbed proteins, including those contained in the surrounding environment and proteins secreted by the microorganisms.<sup>202</sup> It was suggested that surface coatings that resist protein adsorption should also be efficient in combating causative microbes. To investigate the direct correlation between amount of protein reduction and the ability to resist microbe

attachment, Ostuni et al. designed SAMs presenting oligo(ethylene glycol) groups, along with SAMs of alkanethiolates ending with different functional groups. These SAMs were investigated for protein adsorption against fibrinogen and lysozyme, bacterial adhesion against *S. aureus* and *S. epidermidis*. In this study, no correlation was found between surfaces that resist protein adsorption and their capability in combat bacterial adhesion. The authors argue that the mechanisms of protein, microbe, and mammalian cells adsorption/adhesion are different therefore the criteria used to design surfaces resisting protein adsorption are not sufficient to render a surface preventing bacteria colonisation.<sup>211</sup> Nevertheless, PEG was well known in reducing protein adhesion to a substrate, and many studies have used PEG or PEG-like coatings to resist biofilm formation.<sup>50, 211-216</sup> Saldarriaga Fernández et al. tested the antimicrobial behaviour of a cross-linked PEG-based polymer coating (OptiChem®). They have concluded that the PEG-based coating significantly slows down *Staphylococcal* biofilm formation both *in vitro* and *in vivo*.<sup>212</sup>

Roosjen and colleagues studied the influence of PEG chain length in microbial adhesion.<sup>213</sup> PEG chains having molecular weights of 526, 2000, or 9800 Da, with estimated lengths in water of 2.8-, 7.5-, and 23.7-nm respectively, were grafted onto glass substrates. The adhesion of two bacterial (*Staphylococcus epidermidis* and *Pseudomonas aeruginosa*) and two yeast (*Candida albicans* and *Candida tropicalis*) strains to these PEG coated layers were studied. It was found that higher molecular weight PEG resisted the microbial adhesion more strongly, as shown in figure 2.14. Another interesting observation is that relatively hydrophobic microbes (*P. aeruginosa* and *C. tropicalis*) adhered in larger numbers to the PEG coated surfaces than the hydrophilic ones (*S. epidermidis* and *C. albicans*), which suggests that hydrophobic interactions favor the attachment of microorganisms to the PEG surfaces. The microbes that attached to the PEG brushes can be more easily removed compared with that adhered to the bare glass by a passing air bubble, indicating the interaction force is weaker on the PEG brush coated surfaces.

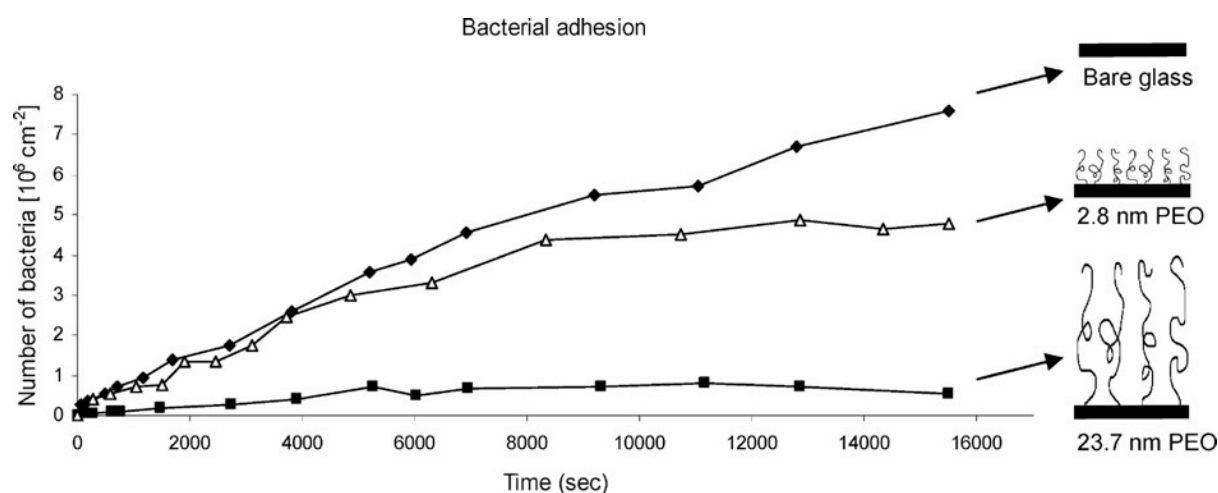


Figure 2.14, Number of bacterial adhesion after 4 hr on glass slide and glass coated with PEG brushes made from MW 526 and 9800. Reprinted with permission from American Chemical Society.<sup>213</sup> Copyright © 2004 American Chemical Society.

Other strategies involve the killing of pathogenic microbes to reduce microbe attachment hence eliminating biofilm formation. Synthetic bactericidal polymers,<sup>217-220</sup> antimicrobial peptides (AMPs),<sup>158, 221</sup> quaternary amine compounds,<sup>222-224</sup> biocidal agents<sup>225-227</sup> and naturally derived compounds<sup>228-230</sup> have all been used for antimicrobial purposes. Some of these materials, such as bactericidal polymers, can be directly applied to a surface as a coating, whereas other low molecular weight molecules and ions need to be tethered to the surface or encapsulated in a reservoir. Thus, three approaches, as depicted in figure 2.13 (b) – (d), were developed to accommodate the various biocides used. The main issue with this type of approach is that they tend to cause adverse effects to mammalian cells. Therefore, careful examination of the optimal amount of material for both antimicrobial activity and biocompatibility is important. For instance, antimicrobial composite coatings made from zinc oxide nanoparticles dispersed in poly(N-isopropylacrylamide) (PNIPAAm) hydrogel is prepared by mixing the polymer and nanoparticles, followed by spin coating and photocrosslinking.<sup>231</sup> The released ZnO kills *E. coli*, but is compatible with 3T3 fibroblast cells at low levels.

For DRIs, short-term release of antimicrobial substances is not a complete solution when the implant is likely to accompany the patient for many years. A stable microbial resistant surface would be ideal in this scenario. Several studies have been reported to combine those approaches. For example, Li and colleagues constructed thin film coatings with both release killing and contact killing capabilities.<sup>232</sup> The substrate was

first coated with poly(allylamine hydrochloride) (PAH) and poly(acrylic acid) (PAA) bilayers through LBL assembly, which serves as a reservoir for loading of Ag nanoparticles. SiO<sub>2</sub> nanoparticles were then modified with a quaternary ammonium silane (OQAS) and attached to the top of the LBL assembly. The coating process is illustrated in figure 2.15. The resultant coatings showed very high percentage of bacterial killing towards *E. coli* and *S. epidermidis*, initially due to the release of Ag ions, and sustained efficiency because of the immobilised OQAS layer.

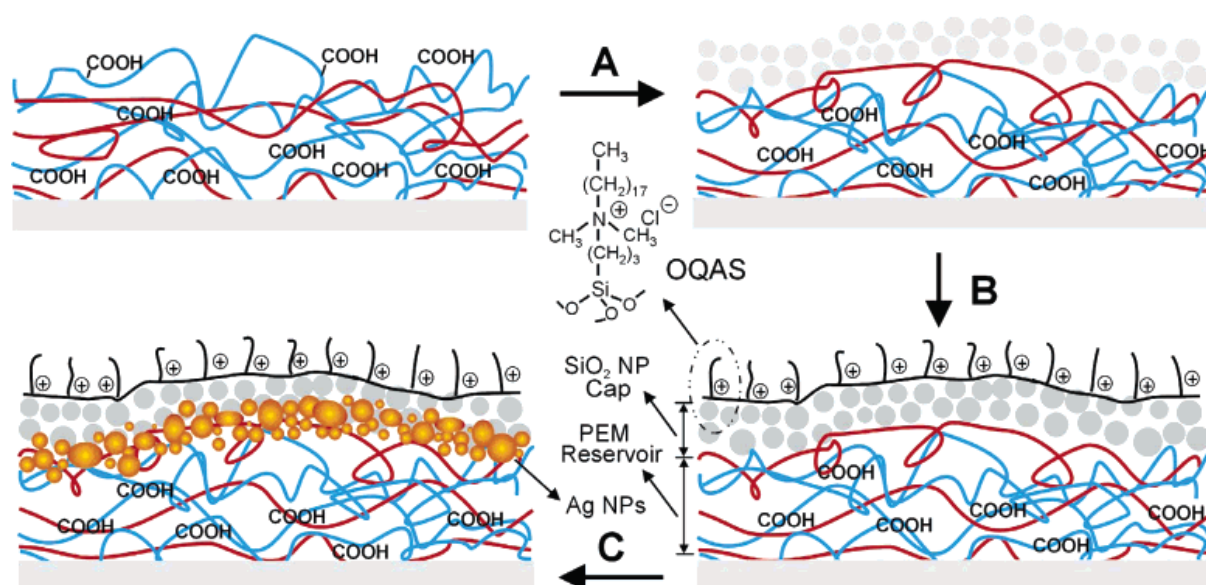


Figure 2.15, A schematic diagram showing the process to form an antibacterial coating with both quaternary ammonium salts and silver that are capable of release and contact killing. A substrate is coated with PAH and PAA multilayers through LBL assembly. (A) A cap region consists of PAH and SiO<sub>2</sub> nanoparticles is added to the top of the LBL structure; (B) The cap is modified to immobilise a quaternary ammonium silane, OQAS; (C) silver ions are loaded inside the PAH and PAA reservoir utilising the unreacted carboxylic acid groups, then reduced to Ag nanoparticles. Reprinted with permission from American Chemical Society.<sup>232</sup> Copyright © 2006 American Chemical Society.

A recent study by Cheng et al. combines the low-fouling strategy with antimicrobial agent release.<sup>233</sup> Salicylate was incorporated into a hydrogel to kill planktonic bacteria near the surface. Meanwhile, the surface of the hydrogel exhibits low fouling properties upon the hydrolysis of carboxybetaine esters into zwitterionic groups, prevent bacterial accumulation. This hydrogel shows excellent efficiency in resisting *E. coli* and *S. epidermidis* biofilms formation. The combinatorial antifouling and antimicrobial design has analogs in plasma polymer film based approach.<sup>234</sup> So far, a general review of the

different strategies is given; the next section will focus on plasma polymer thin film production of antimicrobial surfaces.

### 2.6.3 Anti-fouling plasma polymer coatings

As discussed in section 2.5.2, various monomers can be used in plasma polymerisation to obtain PEG-like thin films that display anti-fouling properties towards proteins and cells. Those PEG-like films have also been tested against bacteria attachment. Johnston and co-workers<sup>235</sup> fabricated PEG-like surfaces from glymes, dioxane, and crown-ethers. They have observed that the attachment of *P. aeruginosa* was reduced most dramatically on tetraglyme coated surfaces compared to a glass control. Triglyme plasma polymer films have been shown to reduce bacterial attachment and biofilm formation.<sup>236</sup> Balazs et al. employed diglyme as a precursor to render the surface PEG-like, and adhesion of *P. aeruginosa* to the surfaces was evaluated.<sup>234</sup> They claim that the number of adherent bacteria is nearly the same on medical-grade poly(vinyl chloride) (PVC) substrate and diglyme plasma polymer film coated surfaces. It was argued that the ether concentration, obtained in this study, might be too low to show sufficient reduction in bacterial attachment. However, one surface coated with PEG-like film and silver nanoparticles prevented the adhesion of the four *P. aeruginosa* strains completely. The question remaining for this type of coating is their longer-term stability and performance in a biological environment.

### 2.6.4 Release of antimicrobial compounds

The local release of antimicrobial compounds, such as metallic ions, antibiotics, or germicides, offers a critical advantage over systemic drug delivery such that high-doses can be administered without exceeding systemic toxicity levels of the drug. The important concern is the release kinetics of the compounds. Fast release provides one-off action, while slow-release may not reach the required therapeutic level. To control the diffusion rate of the antimicrobial compounds, a polymer coating can be used. In the case of plasma polymer films, varying their crosslink density or thickness can achieve different release rates.

The use of metallic silver, silver nanoparticles and ions has been a constant theme in antimicrobial surface engineering due to their activity against a broad spectrum of pathogenic microbes.<sup>237-239</sup> One way to incorporate silver nanoparticles into a plasma polymer matrix is by sputtering silver concurrently with plasma deposition. This has been done with PEG-like films,<sup>234</sup> organosilicon plasma polymer films<sup>240, 241</sup> and coatings deposited from a reactive gas/monomer mixture of CO<sub>2</sub>/C<sub>2</sub>H<sub>2</sub> yielding a hydrocarbon matrix.<sup>242</sup> Alternatively, silver ions can be loaded into the plasma polymer film via in-diffusion then reduced into silver using a reducing agent, which aggregate into nanoparticles.<sup>243</sup> This construct showed complete inhibition of *S. epidermidis* adhesion.

One step generation of silver containing coatings have also been practiced, where a silver-organo compound was synthesised and plasma deposited on several substrates.<sup>244</sup> It was found that such a coating prevented the attachment and growth of *P. aeruginosa* on both polystyrene petri dish and polypropylene non-woven fabrics. Other plasma related technologies for fabrication of silver containing polymer coatings have also been studied.<sup>245-247</sup> However, there is still some contradiction in the literature with regard to the potential toxicity of silver containing surfaces to human cells and tissues.<sup>227, 248, 249</sup> Options such as short-term contact wound dressings or urinary catheters where silver is unlikely to build up due to fast removal are often exploited.<sup>226</sup>

A number of other transition metal ions, e.g. Cu,<sup>250</sup> Zn,<sup>231, 251</sup> and Co,<sup>252</sup> have also been incorporated into plasma polymer film matrix for resisting microbe attachment to materials surface. Similar to Ag ions, the systemic toxicity of these metallic ions need to be considered when tuning dosage and choosing applications.<sup>253</sup>

Plasma polymer films can also be used to control the release of antibiotics. The use of organic molecules as a precursor is rare but doable. Braceras et al. produced a plasma polymer film from silylated ciprofloxacin that can release the antibiotic by a hydrolysis reaction at the outer layers.<sup>254</sup> The released ciprofloxacin from plasma polymer film demonstrated comparable antimicrobial activity against *E. coli*, *P. aeruginosa*, and *S. aureus*, to that of silylciprofloxacin without plasma treatment. Alternatively, antibiotics

can be added into the plasma polymer film after deposition, by immersion of the coated substrate in a solution of organic molecules. For instance, Garcia-Fernandez and co-workers deposited ethylene plasma polymer films rich in bonded oxygen groups onto PET films using  $C_2H_4/Ar/O_2$  gas mixture. The resultant thin film impeded vancomycin penetration due to steric hindrance but allowed ciprofloxacin diffusion in and out. The ciprofloxacin loaded coatings inhibit the growth of *S. aureus* biofilms.<sup>255</sup> In addition, plasma polymer films can be used as a diffusion barrier where antibiotics were spread onto a surface,<sup>64, 256</sup> or loaded in reservoir.<sup>257, 258</sup> The figure below shows the design of a nanoporous alumina template for antibiotic loading, and controlled release through a plasma polymer coating.<sup>257</sup>

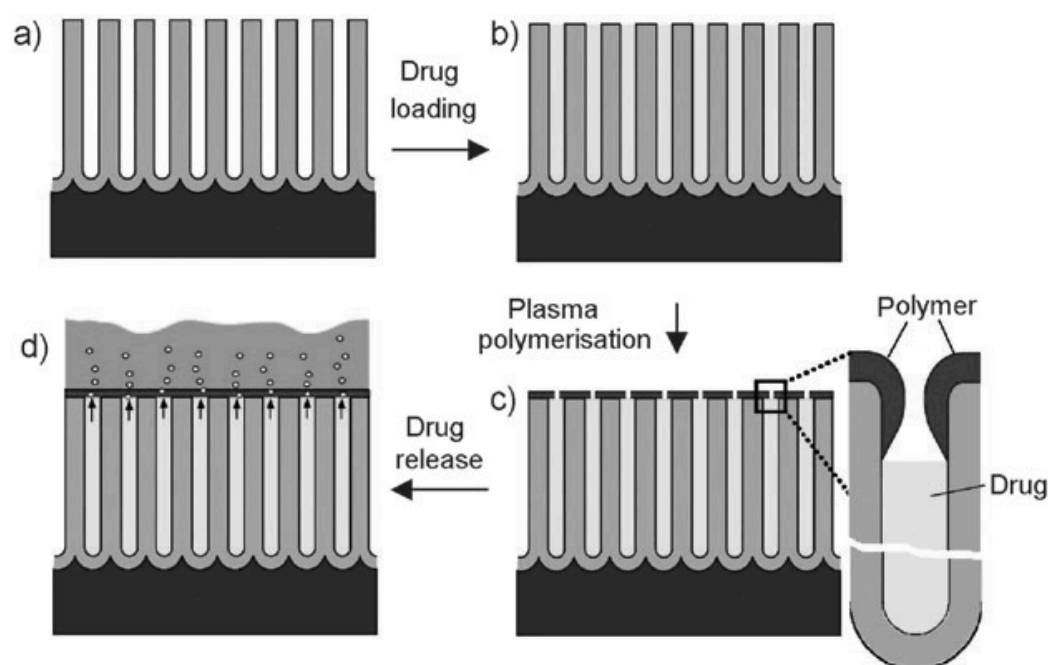


Figure 2.16, Schematic representation of plasma modification of a porous platform for controlled drug release. (a) anodic alumina oxide (AAO) porous layer produced by electrochemical anodisation; (b) vancomycin loading inside the pores; (c) deposition of an allylamine layer on top of the pores; (d) the release of the drug from the pores into the solution. Reprinted with permission from Royal Society of Chemistry.<sup>257</sup> Copyright © 2010, Royal Society of Chemistry.

### 2.6.5 Surface-bound antimicrobial molecules

A release approach is appropriate for short-term protection but is unlikely to be efficient over months or years. Especially for plasma polymer thin films, there is only

limited space for loading of the drug compared with bulk polymer or solvent-coated thick layers. For long-term effective antimicrobial action, a permanent surface chemical functional coating is desired. One approach to fabricate surfaces for prolonged microbial resistivity is via covalent grafting of antibacterial compounds onto biomaterial surfaces. Surface tethering of quaternary ammonium compounds (QACs)<sup>223,224, 232</sup>, other cationic compounds<sup>259, 260</sup>, and antibiotics<sup>261, 262</sup> is a subject of intensive research and fast development. Plasma polymer films have often been used as adhesive interlayers for the covalent immobilisation of organic molecules due to their ease of manufacture and diverse functionality achievable.

QACs have been used widely as potent biocides for both gram-positive and gram-negative bacteria. The commonly cited mechanism is that QACs disrupt the cytoplasmic membrane, resulting in necrosis.<sup>222</sup> Direct plasma deposition of QACs has been investigated in atmospheric plasma polymerisation systems. Donegan et al. used dimethyloctadecyl-[3-(trimethoxysilyl)-propyl] ammoniumchloride (ODAMO) mixed with helium to produce nanometer thick QAC coatings.<sup>263</sup> The coating was found to solubilise slowly in PBS buffer under flow conditions. In another study, Sarghini and co-workers used ODAMO and butylamine as precursors mixed with nitrogen or air for plasma deposition of antibacterial coatings.<sup>264</sup> The retention of ammonium groups in ODAMO based films was dependent on load power. In addition, ODAMO based layers proved to be effective in reducing *E. coli* attachment and growth in 24 hr incubation period.

Another route for QACs immobilisation is done in two-step process, where an amine plasma polymer is deposited on a substrate, followed by quaternisation with hexyl bromide.<sup>265</sup> Similarly, a poly(4-vinyl pyridine) plasma polymer film can be made and subsequently quaternised with bromobutane to yield antibacterial activity.<sup>266</sup> Unfortunately, it is possible that QACs can induce membrane disruption and lysis to human cells through the same mechanisms as to bacteria cells. Additionally, evidence suggests that certain bacteria are able to develop resistance towards the QACs modified surfaces.<sup>267, 268</sup> Therefore, the long-term use of QACs in medical devices may be unsuitable.

Other cationic compounds, e.g. peptides, and natural macromolecules<sup>269</sup> have also been reported to be antimicrobial after being immobilised onto biomaterial surfaces. For example, nisin peptides have been anchored onto an amino containing plasma polymer film via carbodiimide reactions, and the resultant coating showed excellent resistance to gram-positive bacteria attachment.<sup>259</sup> In another study, nisin peptides together with other two antibacterial peptides were tethered to an allyl glycidyl ether plasma polymer through reaction with the epoxy groups in the coating. The peptide-grafted surfaces prevented biofilm formation.<sup>260</sup>

Established antibiotics, such as commercially available penicillin, vancomycin and novobiocin, represent another route for medical devices surface modification to resolve the problem of DRIs. Covalent grafting of organic molecules offer better retention of functionality and stronger attachment strength compared with physically adsorbed molecular layers.<sup>270</sup> Aumsuwan et al. used microwave maleic anhydride plasma to form carboxylic acid groups on the substrate surface, onto which ampicillin,<sup>271</sup> penicillin and gentamicin<sup>261</sup> were grafted via a PEG spacer. A further example is the study by Braceras et al. where vancomycin was chemically modified and conjugated onto a surface by a “click” reaction.<sup>262</sup> The method began with the deposition of acrylic acid plasma polymer films, resulting in carboxylic groups that then reacted with propargylamine to render an alkyne-terminated surface. Finally, modified azido-vancomycin molecules were incorporated via Cu(I)-catalyzed alkyne-azide click reaction. Figure 2.17 shows molecular structure and immobilisation sequence for the click reaction approach. Resultant coatings proved lasting antibacterial activity against *S. epidermidis*. By using the plasma polymer film, the functional groups used for binding of antibiotics can be tuned by changing process parameters hence different amounts of organic molecules could be immobilised. The potential downsides for cationic compounds and antibiotics are adverse effects to the surrounding biological environment, or restricted effectiveness to a specific genus of microorganism.<sup>183</sup> In order to find optimal surfaces that show both antimicrobial effects and low side effects to human host, natural derived agents are being tested as well, such as furanones,<sup>272</sup> serrulatane.<sup>273</sup>

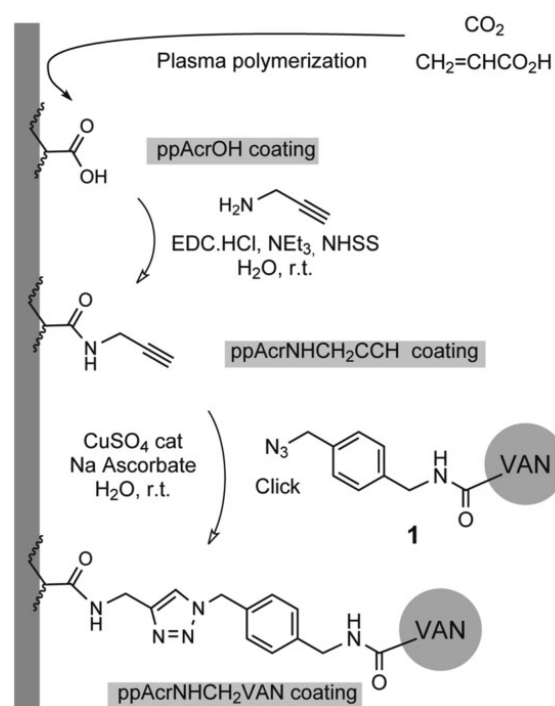


Figure 2.17, Molecular structure and immobilisation steps for a combined plasma polymer deposition/click reaction method to vancomycin antibacterial surfaces. Reprinted with permission from John Wiley and Sons.<sup>262</sup> Copyright © 2013 Wiley-VCH Verlag GmbH & Co KGaA, Weinheim.

## 2.7 Summary

Non-thermal plasma-assisted modification techniques have provided versatile platforms for control of cell and microbe attachment. In particular, plasma polymer thin films offer a diverse range of functional groups with capability to influence biological responses. In this thesis, several functional plasma polymer films will be made to investigate their interactions with mammalian cells and pathogenic microorganisms in order to obtain new knowledge on surface parameters that affect cell and microbe adhesion. Beside the biological responses, the chemical and structure stability of the resultant plasma polymer films in environments similar to physiological conditions need to be addressed as well. In this work, plasma polymer films will be deposited onto several substrates, including silicon wafer, glass, polymers, protein self-assembled networks, etc. to gather information about the differences in deposition rates, film chemistry and film stability.

## 2.8 Reference

1. K. S. Masters and K. S. Anseth, in *Advances in Chemical Engineering*, eds. A. Peppas and M. V. Sefton, Academic Press, 2004, vol. 29, pp. 7-46.
2. C. Werner, in *Polymer Surfaces and Interfaces*, ed. M. Stamm, Springer Berlin Heidelberg, 2008, DOI: 10.1007/978-3-540-73865-7\_15, pp. 299-318.
3. K. Kolind, K. W. Leong, F. Besenbacher and M. Foss, *Biomaterials*, 2012, 33, 6626-6633.
4. A. S. G. Curtis and C. D. W. Wilkinson, *Journal of Biomaterials Science, Polymer Edition*, 1998, 9, 1313-1329.
5. D. D. Deligianni, N. Katsala, S. Ladas, D. Sotiropoulou, J. Amedee and Y. F. Missirlis, *Biomaterials*, 2001, 22, 1241-1251.
6. K. Anselme and M. Bigerelle, *Acta Biomaterialia*, 2005, 1, 211-222.
7. M. J. Dalby, N. Gadegaard, R. Tare, A. Andar, M. O. Riehle, P. Herzyk, C. D. W. Wilkinson and R. O. C. Oreffo, *Nat Mater*, 2007, 6, 997-1003.
8. L. E. McNamara, R. Burchmore, M. O. Riehle, P. Herzyk, M. J. P. Biggs, C. D. W. Wilkinson, A. S. G. Curtis and M. J. Dalby, *Biomaterials*, 2012, 33, 2835-2847.
9. A. Citeau, J. Guicheux, C. Vinatier, P. Layrolle, T. P. Nguyen, P. Pilet and G. Daculsi, *Biomaterials*, 2005, 26, 157-165.
10. J. Huang, S. N. Jayasinghe, S. M. Best, M. J. Edirisinghe, R. A. Brooks and W. Bonfield, *Journal of Materials Science*, 2004, 39, 1029-1032.
11. J. N. Barry, B. Twomey, A. Cowley, L. O'Neill, P. J. McNally and D. P. Dowling, *Surface and Coatings Technology*, 2013, 226, 82-91.
12. A. Kurella and N. B. Dahotre, *Journal of Biomaterials Applications*, 2005, 20, 5-50.
13. J. Jagielski, A. Piatkowska, P. Aubert, L. Thomé, A. Turos and A. Abdul Kader, *Surface and Coatings Technology*, 2006, 200, 6355-6361.
14. Y. Xia and G. M. Whitesides, *Angewandte Chemie - International Edition*, 1998, 37, 550-575.
15. A. Perl, D. N. Reinhoudt and J. Huskens, *Advanced Materials*, 2009, 21, 2257-2268.
16. N. P. Reynolds, M. Charnley, R. Mezzenga and P. G. Hartley, *Biomacromolecules*, 2014, 15, 599-608.
17. C. c. Lara, J. Adamcik, S. Jordens and R. Mezzenga, *Biomacromolecules*, 2011, 12, 1868-1875.

18. A. Shekaran and A. J. Garcia, *Biochimica et Biophysica Acta (BBA) - General Subjects*, 2011, 1810, 350-360.
19. L. Dai, H. J. Griesser and A. W. H. Mau, *The Journal of Physical Chemistry B*, 1997, 101, 9548-9554.
20. Y. Wan, X. Qu, J. Lu, C. Zhu, L. Wan, J. Yang, J. Bei and S. Wang, *Biomaterials*, 2004, 25, 4777-4783.
21. D. R. Baer and S. Thevuthasan, in *Handbook of Deposition Technologies for Films and Coatings (Third Edition)*, ed. P. M. Martin, William Andrew Publishing, Boston, 2010, pp. 749-864.
22. B. D. Ratner, A. S. Hoffman, F. J. Schoen and J. E. Lemons, Elsevier, 2<sup>nd</sup> edition, 2004.
23. H. M. Mott-Smith, *Nature*, 1971, 233, 219-219.
24. A. Bogaerts, E. Neyts, R. Gijbels and J. van der Mullen, *Spectrochimica Acta Part B: Atomic Spectroscopy*, 2002, 57, 609-658.
25. M. A. Lieberman and A. J. Lichtenberg, in *Principles of Plasma Discharges and Materials Processing*, John Wiley & Sons, Inc., 2005, pp 1-22.
26. S. G. Walton and J. E. Greene, in *Handbook of Deposition Technologies for Films and Coatings (Third Edition)*, ed. P. M. Martin, William Andrew Publishing, Boston, 2010, pp. 32-92.
27. M. M. M. Bilek, D. R. McKenzie, R. N. Tarrant, S. H. M. Lim and D. G. McCulloch, *Surface and Coatings Technology*, 2002, 156, 136-142.
28. P. Cheang and K. A. Khor, *Biomaterials*, 1996, 17, 537-544.
29. S. W. K. Kweh, K. A. Khor and P. Cheang, *Biomaterials*, 2000, 21, 1223-1234.
30. E. H. Lock, D. Y. Petrovykh, P. Mack, T. Carney, R. G. White, S. G. Walton and R. F. Fernsler, *Langmuir*, 2010, 26, 8857-8868.
31. Y. Urano, Y. Li, K. Kanno, S. Iizuka and N. Sato, *Thin Solid Films*, 1998, 316, 60-64.
32. J. Schäfer, R. Foest, A. Ohl and K. D. Weltmann, *Plasma Physics and Controlled Fusion*, 2009, 51, 124045.
33. S. Mathur, T. Singh, M. Maleki and T. Fischer, in *Biomaterials Surface Science*, Wiley-VCH Verlag GmbH & Co. KGaA, 2013, pp. 375-408.
34. A. Michelmore, D. A. Steele, J. D. Whittle, J. W. Bradley and R. D. Short, *RSC Advances*, 2013, 3, 13540-13557.

35. J. Park, I. Henins, H. W. Herrmann, G. S. Selwyn and R. F. Hicks, *Journal of Applied Physics*, 2001, 89, 20-28.
36. S. Miyake, Y. Setsuhara, Y. Sakawa and T. Shoji, *Surface and Coatings Technology*, 2000, 131, 171-176.
37. D. Barton, J. W. Bradley, D. A. Steele and R. D. Short, *The Journal of Physical Chemistry B*, 1999, 103, 4423-4430.
38. A. Michelmore, P. M. Bryant, D. A. Steele, K. Vasilev, J. W. Bradley and R. D. Short, *Langmuir*, 2011, 27, 11943-11950.
39. J. Friedrich, in *The Plasma Chemistry of Polymer Surfaces*, Wiley-VCH Verlag GmbH & Co. KGaA, 2012, DOI: 10.1002/9783527648009.ch3, pp. 35-54.
40. P. T. Jacobs and S. M. Lin, Google Patents, 1988.
41. D. D. Lee, A. Nagras, P. Chakravarthy and A. M. Majahad, Google Patents, 2000.
42. S. Mändl, R. Sader, G. Thorwarth, D. Krause, H. F. Zeilhofer, H. H. Horch and B. Rauschenbach, *Biomolecular Engineering*, 2002, 19, 129-132.
43. T. Nakatani, K. Okamoto, Y. Nitta, A. Mochizuki, H. Hoshi and A. Homma, *Journal of Photopolymer Science and Technology*, 2008, 21, 225-230.
44. F. Brétaganol, A. Valsesia, G. Ceccone, P. Colpo, D. Gilliland, L. Ceriotti, M. Hasiwa and F. Rossi, *Plasma Processes and Polymers*, 2006, 3, 443-455.
45. K. Joon Hyub, L. Jun-Yong, J. Joon-Hyung, P. Eun Jin and M. Nam Ki, *Japanese Journal of Applied Physics*, 2013, 52, 01AE02.
46. H. Yu, P. Li and J. Robertson, *Diamond and Related Materials*, 2011, 20, 1020-1025.
47. A. Venault, Y. Chang, H.-H. Hsu, J.-F. Jhong, H.-S. Yang, T.-C. Wei, K.-L. Tung, A. Higuchi and J. Huang, *Journal of Membrane Science*, 2013, 439, 48-57.
48. B. Bae, B. H. Chun and D. Kim, *Polymer*, 2001, 42, 7879-7885.
49. N. Saxena, C. Prabhavathy, S. De and S. DasGupta, *Separation and Purification Technology*, 2009, 70, 160-165.
50. Y. Chang, Y.-J. Shih, C.-Y. Ko, J.-F. Jhong, Y.-L. Liu and T.-C. Wei, *Langmuir*, 2011, 27, 5445-5455.
51. Y. K. Cho, D. Park, H. Kim, H. Lee, H. Park, H. J. Kim and D. Jung, *Applied Surface Science*, 2014, 296, 79-85.
52. D. J. Wilson, N. P. Rhodes and R. L. Williams, *Biomaterials*, 2003, 24, 5069-5081.

53. M. Onishi and K. Shimura, *Journal of Photopolymer Science and Technology*, 1993, 6, 331-336.
54. D. S. Trentin, F. Bonatto, K. R. Zimmer, V. B. Ribeiro, A. L. S. Antunes, A. L. Barth, G. V. Soares, C. Krug, I. J. R. Baumvol and A. J. Macedo, *Surface and Coatings Technology*, 2014, 245, 84-91.
55. K. Duske, I. Koban, E. Kindel, K. Schröder, B. Nebe, B. Holtfreter, L. Jablonowski, K. D. Weltmann and T. Kocher, *Journal of Clinical Periodontology*, 2012, 39, 400-407.
56. X. Hu, H. Shen, K. Shuai, E. Zhang, Y. Bai, Y. Cheng, X. Xiong, S. Wang, J. Fang and S. Wei, *Applied Surface Science*, 2011, 257, 1813-1823.
57. E. C. Preedy, E. Brousseau, S. L. Evans, S. Perni and P. Prokopovich, *Colloids and Surfaces A: Physicochemical and Engineering Aspects*, 460 (2014), 83-89
58. H. Liu, Y. Pei, D. Xie, X. Deng, Y. X. Leng, Y. Jin and N. Huang, *Applied Surface Science*, 2010, 256, 3941-3945.
59. S. Yin, Y. Wang, L. Ren, L. Zhao, T. Kuang, H. Chen and J. Qu, *Applied Surface Science*, 2008, 255, 483-485.
60. S. A. Al-Bataineh, M. Jasieniak, L. G. Britcher and H. J. Griesser, *Analytical Chemistry*, 2007, 80, 430-436.
61. H. Zhu, A. Kumar, J. Ozkan, R. Bandara, A. Ding, I. Perera, P. Steinberg, N. Kumar, W. Lao, S. S. Griesser, L. Britcher, H. J. Griesser and M. D. P. Willcox, *Optometry & Vision Science*, 2008, 85 (5), 292-300
62. K. Vasilev, J. Cook and H. J. Griesser, *Expert Review of Medical Devices*, 2009, 6, 553-567.
63. M. Rafat, M. Griffith, M. Hakim, L. Muzakare, F. Li, K. C. Khulbe and T. Matsuura, *Journal of Applied Polymer Science*, 2007, 106, 2056-2064.
64. K. Vasilev, N. Poulter, P. Martinek and H. J. Griesser, *ACS Applied Materials & Interfaces*, 2011, 3, 4831-4836.
65. T. G. van Kooten, H. T. Spijker and H. J. Busscher, *Biomaterials*, 2004, 25, 1735-1747.
66. F. R. Pu, R. L. Williams, T. K. Markkula and J. A. Hunt, *Biomaterials*, 2002, 23, 2411-2428.
67. P. Krüger, R. Knes and J. Friedrich, *Surface and Coatings Technology*, 1999, 112, 240-244.

68. S. Lerouge, M. R. Wertheimer and L. H. Yahia, *Plasmas and Polymers*, 2001, 6, 175-188.
69. A. Michelmore, P. Martinek, V. Sah, R. D. Short and K. Vasilev, *Plasma Processes and Polymers*, 2011, 8, 367-372.
70. K. Yasuda H, in *Plasma Polymerization*, American Chemical Society, 1979, vol. 108, ch. 2, pp. 37-52.
71. T. Jacobs, R. Morent, N. De Geyter, P. Dubruel and C. Leys, *Plasma Chem Plasma Process*, 2012, 32, 1039-1073.
72. G. Binnig, C. F. Quate and C. Gerber, *Physical Review Letters*, 1986, 56, 930-933.
73. S. A. Mirmohammadi, M. T. Khorasani, H. Mirzadeh and S. Irani, *Polymer-Plastics Technology and Engineering*, 2012, 51, 1319-1326.
74. H. Hiratsuka, G. Akovali, M. Shen and A. T. Bell, *Journal of Applied Polymer Science*, 1978, 22, 917-925.
75. C. De Vos, N. Vandencastelee, A. Kakaroglou, B. Nisol, I. de Graeve, G. Van Assche, B. Van Mele, H. Terryen and F. Reniers, *Plasma Processes and Polymers*, 2013, 10, 51-59.
76. F. Pietro, in *Plasma Polymer Films*, Published by Imperial College Press and distributed by World Scientific Publishing CO., 2004, pp. 25-55.
77. C. B. Labelle, R. Opila and A. Kornblit, *Journal of Vacuum Science & Technology A*, 2005, 23, 190-196.
78. J. Friedrich, *Plasma Processes and Polymers*, 2011, 8, 783-802.
79. J. Goodman, *Journal of Polymer Science*, 1960, 44, 551-552.
80. E. M. Liston, L. Martinu and M. R. Wertheimer, *Journal of Adhesion Science and Technology*, 1993, 7, 1091-1127.
81. J. L. Shohet, *Plasma Science, IEEE Transactions on*, 1991, 19, 725-733.
82. D. Çökeliler, *Applied Surface Science*, 2013, 268, 28-36.
83. O. Polonskyi, O. Kylián, M. Petr, A. Choukourov, J. Hanuš and H. Biederman, *Thin Solid Films*, 2013, 540, 65-68.
84. H. P. Schreiber, M. R. Wertheimer and A. M. Wrobel, *Thin Solid Films*, 1980, 72, 487-494.
85. T. Wydeven, *Appl. Opt.*, 1977, 16, 717-721.
86. P. K. Tien, G. Smolinsky and R. J. Martin, *Appl. Opt.*, 1972, 11, 637-642.
87. L. Shi, in *Journal of Polymer Engineering*, 2000, vol. 20, p. 313.

88. D. Y. Huang and C. T. Wei, Google Patents, 1999.
89. R. Förch, Z. Zhang and W. Knoll, *Plasma Processes and Polymers*, 2005, 2, 351-372.
90. L. Cao, M. Chang, C.-Y. Lee, D. G. Castner, S. Sukavaneshvar, B. D. Ratner and T. A. Horbett, *Journal of Biomedical Materials Research Part A*, 2007, 81A, 827-837.
91. H. Biederman and D. Slavínská, *Surface and Coatings Technology*, 2000, 125, 371-376.
92. T. Desmet, R. Morent, N. D. Geyter, C. Leys, E. Schacht and P. Dubruel, *Biomacromolecules*, 2009, 10, 2351-2378.
93. M. C. Vasudev, K. D. Anderson, T. J. Bunning, V. V. Tsukruk and R. R. Naik, *ACS Applied Materials & Interfaces*, 2013, 5, 3983-3994.
94. F. Brétaganol, M. Lejeune, A. Papadopoulou-Bouraoui, M. Hasiwa, H. Rauscher, G. Ceccone, P. Colpo and F. Rossi, *Acta Biomaterialia*, 2006, 2, 165-172.
95. I. Gordeev, A. Choukourov, M. Šimek, V. Prukner and H. Biederman, *Plasma Processes and Polymers*, 2012, 9, 782-791.
96. D. J. Menzies, A. Nelson, H.-H. Shen, K. M. McLean, J. S. Forsythe, T. Gengenbach, C. Fong and B. W. Muir, *Journal of The Royal Society Interface*, 2012, 9, 1008-1019.
97. J. B. Alison, C. Sennur, D. S. Robert, G. Alec and J. B. Nick St, *The Journal of Physical Chemistry B*, 2001, 105.
98. C. Nelson, S. Sant, L. Overzet and M. Goeckner, *Plasma Sources Science and Technology*, 2007, 16, 813.
99. A. Michelmore, P. Gross-Kosche, S. A. Al-Bataineh, J. D. Whittle and R. D. Short, *Langmuir*, 2013, 29, 2595-2601.
100. A. Michelmore, C. Charles, R. W. Boswell, R. D. Short and J. D. Whittle, *ACS Applied Materials & Interfaces*, 2013, 5, 5387-5391.
101. A. Michelmore, D. A. Steele, D. E. Robinson, J. D. Whittle and R. D. Short, *Soft Matter*, 2013, 9, 6167-6175.
102. K. Vasilev, A. Michelmore, H. J. Griesser and R. D. Short, *Chemical Communications*, 2009, 3600-3602.
103. K. Furuya, R. Nakanishi, H. Okumura, M. Makita and A. Harata, *Thin Solid Films*, 2008, 516, 6028-6032.
104. D. E. Robinson, D. J. Buttle, J. D. Whittle, K. L. Parry, R. D. Short and D. A. Steele, *Plasma Processes and Polymers*, 2010, 7, 102-106.

105. H. Kobayashi, A. T. Bell and M. Shen, *Journal of Applied Polymer Science*, 1973, 17, 885-892.
106. H. Kobayashi, M. Shen and A. T. Bell, *Journal of Macromolecular Science: Part A - Chemistry*, 1974, 8, 373-391.
107. J. Pelletier, *Plasma Physics and Controlled Fusion*, 2000, 42, 227.
108. J. Berndt, E. Kovačević, I. Stefanović, O. Stepanović, S. H. Hong, L. Boufendi and J. Winter, *Contributions to Plasma Physics*, 2009, 49, 107-133.
109. M. Bonitz, C. Henning and D. Block, *Reports on Progress in Physics*, 2010, 73, 066501.
110. O. Kylián, A. Choukourov and H. Biederman, *Thin Solid Films*, 2013, 548, 1-17.
111. P. Heyse, A. Van Hoeck, M. B. J. Roeffaers, J.-P. Raffin, A. Steinbüchel, T. Stöveken, J. Lammertyn, P. Verboven, P. A. Jacobs, J. Hofkens, S. Paulussen and B. F. Sels, *Plasma Processes and Polymers*, 2011, 8, 965-974.
112. K. D. Anderson, J. M. Slocik, M. E. McConney, J. O. Enlow, R. Jakubiak, T. J. Bunning, R. R. Naik and V. V. Tsukruk, *Small*, 2009, 5, 741-749.
113. K. D. Anderson, S. L. Young, H. Jiang, R. Jakubiak, T. J. Bunning, R. R. Naik and V. V. Tsukruk, *Langmuir*, 2011, 28, 1833-1845.
114. B. R. Coad, M. Jasieniak, S. S. Griesser and H. J. Griesser, *Surface and Coatings Technology*, 2013, 233, 169-177.
115. E. Sardella, P. Favia, E. Dilonardo, L. Petrone and R. d'Agostino, *Plasma Processes and Polymers*, 2007, 4, S781-S783.
116. R. P. Gandhiraman, M. K. Muniyappa, M. Dudek, C. Coyle, C. Volcke, A. J. Killard, P. Burham, S. Daniels, N. Barron, M. Clynes and D. C. Cameron, *Plasma Processes and Polymers*, 2010, 7, 411-421.
117. G. R. Prasad, S. Daniels, D. C. Cameron, B. P. McNamara, E. Tully and R. O'Kennedy, *Surface and Coatings Technology*, 2005, 200, 1031-1035.
118. A. Harsch, J. Calderon, R. B. Timmons and G. W. Gross, *Journal of Neuroscience Methods*, 2000, 98, 135-144.
119. B. J. Klenkler, M. Griffith, C. Becerril, J. A. West-Mays and H. Sheardown, *Biomaterials*, 2005, 26, 7286-7296.
120. J. H. Zhao, W. P. Michalski, C. Williams, L. Li, H.-S. Xu, P. R. Lamb, S. Jones, Y. M. Zhou and X. J. Dai, *Journal of Biomedical Materials Research Part A*, 2011, 97A, 127-134.

121. A. Hadjizadeh, C. J. Doillon and P. Vermette, *Biomacromolecules*, 2007, 8, 864-873.
122. L. Detomaso, R. Gristina, G. S. Senesi, R. d'Agostino and P. Favia, *Biomaterials*, 2005, 26, 3831-3841.
123. L. C. Lopez, R. Gristina, G. Ceccone, F. Rossi, P. Favia and R. d'Agostino, *Surface and Coatings Technology*, 2005, 200, 1000-1004.
124. S. A. Mitchell, M. R. Davidson, N. Emmison and R. H. Bradley, *Surface Science*, 2004, 561, 110-120.
125. N. S. Ludwig, C. Yoder, M. McConney, T. G. Vargo and K. N. Kader, *Journal of Biomedical Materials Research Part A*, 2006, 78A, 615-619.
126. K. R. Diener, S. N. Christo, S. S. Griesser, G. T. Sarvestani, K. Vasilev, H. J. Griesser and J. D. Hayball, *Acta Biomaterialia*, 2012, 8, 99-107.
127. M. Allen, B. Myer and N. Rushton, *Journal of Biomedical Materials Research*, 2001, 58, 319-328.
128. S. Linder, W. Pinkowski and M. Aepfelbacher, *Biomaterials*, 2002, 23, 767-773.
129. Y. Ohgoe, T. Wada, Y. Shiraishi, H. Miura, K. K. Hirakuri, A. Funakubo, T. Yambe and Y. Fukui, *MRS Online Proceedings Library*, 2013, 1498, 103-108.
130. C. Iliescu, B. Chen, D. P. Poenar and Y. Y. Lee, *Sensors and Actuators B: Chemical*, 2008, 129, 404-411.
131. G. Whitesides, *Applied Biochemistry and Biotechnology*, 1993, 41, 233-234.
132. T. G. Vladkova, *International Journal of Polymer Science*, 2010, 2010.
133. I. Strzinar and M. V. Sefton, *Journal of biomedical materials research*, 1992, 26, 577-592.
134. B. Baroli, *Journal of Pharmaceutical Sciences*, 2007, 96, 2197-2223.
135. S. Varvarenko, A. Voronov, V. Samaryk, I. Tarnavchyk, N. Nosova, A. Kohut and S. Voronov, *Reactive and Functional Polymers*, 2010, 70, 647-655.
136. H. Jacobs, D. Grainger, T. Okano and S. W. Kim, *Artificial Organs*, 1988, 12, 506-507.
137. S. R. Meyers and M. W. Grinstaff, *Chemical Reviews*, 2012, 112 (3), pp 1615-1632.
138. S. Igal, *Current Opinion in Solid State and Materials Science*, 1997, 2, 337-344.
139. J. Israelachvili, *Proceedings of the National Academy of Sciences*, 1997, 94, 8378-8379.
140. D. Beyer, W. Knoll, H. Ringsdorf, J.-H. Wang, R. B. Timmons and P. Sluka, *Journal of biomedical materials research*, 1997, 36, 181-189.

141. E. Ostuni, R. G. Chapman, R. E. Holmlin, S. Takayama and G. M. Whitesides, *Langmuir*, 2001, 17, 5605-5620.
142. E. E. Johnston, J. D. Bryers and B. D. Ratner, *Langmuir*, 2004, 21, 870-881.
143. I. Szleifer, D. Kramer, A. Ben-Shaul, W. M. Gelbart and S. A. Safran, *The Journal of Chemical Physics*, 1990, 92, 6800-6817.
144. A. J. Pertsin and M. Grunze, *Langmuir*, 2000, 16, 8829-8841.
145. H. I. Kim, J. G. Kushmerick, J. E. Houston and B. C. Bunker, *Langmuir*, 2003, 19, 9271-9275.
146. S. I. Jeon, J. H. Lee, J. D. Andrade and P. G. De Gennes, *Journal of Colloid and Interface Science*, 1991, 142, 149-158.
147. L. Li, S. Chen, J. Zheng, B. D. Ratner and S. Jiang, *The Journal of Physical Chemistry B*, 2005, 109, 2934-2941.
148. R. A. Latour, *Journal of Biomedical Materials Research Part A*, 2006, 78A, 843-854.
149. B. W. Muir, A. Tarasova, T. R. Gengenbach, D. J. Menzies, L. Meagher, F. Rovere, A. Fairbrother, K. M. McLean and P. G. Hartley, *Langmuir*, 2008, 24, 3828-3835.
150. D. J. Menzies, B. Cowie, C. Fong, J. S. Forsythe, T. R. Gengenbach, K. M. McLean, L. Puskar, M. Textor, L. Thomsen, M. Tobin and B. W. Muir, *Langmuir*, 2010, 26, 13987-13994.
151. F. Brétagnol, O. Kylián, M. Hasiwa, L. Ceriotti, H. Rauscher, G. Ceccone, D. Gilliland, P. Colpo and F. Rossi, *Sensors and Actuators B: Chemical*, 2007, 123, 283-292.
152. E. Sardella, L. Detomaso, R. Gristina, G. S. Senesi, H. Agheli, D. S. Sutherland, R. d'Agostino and P. Favia, *Plasma Processes and Polymers*, 2008, 5, 540-551.
153. M. N. Mar, B. D. Ratner and S. S. Yee, *Sensors and Actuators B: Chemical*, 1999, 54, 125-131.
154. C. R. Hurley, R. E. Ducker, G. J. Leggett and B. D. Ratner, *Langmuir*, 2010, 26, 10203-10209.
155. M. Salim, G. Mishra, G. J. S. Fowler, B. O'Sullivan, P. C. Wright and S. L. McArthur, *Lab on a Chip*, 2007, 7, 523-525.
156. L. Cao, S. Sukavaneshvar, B. D. Ratner and T. A. Horbett, *Journal of Biomedical Materials Research Part A*, 2006, 79A, 788-803.
157. L.-Q. Chu, W. Knoll and R. Förch, *Biosensors and Bioelectronics*, 2009, 25, 519-522.

158. C. Vreuls, G. Zocchi, B. Thierry, G. Garitte, S. S. Griesser, C. Archambeau, C. Van de Weerd, J. Martial and H. Griesser, *Journal of Materials Chemistry*, 2010, 20, (37), 8092-8098.
159. A. Choukourov, I. Gordeev, O. Polonskyi, A. Artemenko, L. Hanyková, I. Krakovský, O. Kylián, D. Slavínská and H. Biederman, *Plasma Processes and Polymers*, 2010, 7, 445-458.
160. M. Singh, C. Berkland and M. S. Detamore, *Tissue engineering. Part B, Reviews*, 2008, 14, 341-366.
161. Q. Cheng, S. Li and K. Komvopoulos, *Biomaterials*, 2009, 30, 4203-4210.
162. E. Sardella, P. Favia, R. Gristina, M. Nardulli and R. d'Agostino, *Plasma Processes and Polymers*, 2006, 3, 456-469.
163. M. Zelzer, R. Majani, J. W. Bradley, F. R. A. J. Rose, M. C. Davies and M. R. Alexander, *Biomaterials*, 2008, 29, 172-184.
164. J. T. Smith, J. K. Tomfohr, M. C. Wells, T. P. Beebe, T. B. Kepler and W. M. Reichert, *Langmuir*, 2004, 20, 8279-8286.
165. W. G. Pitt, *Journal of Colloid and Interface Science*, 1989, 133, 223-227.
166. J. H. Lee, H. G. Kim, G. S. Khang, H. B. Lee and M. S. Jhon, *Journal of Colloid and Interface Science*, 1992, 151, 563-570.
167. J. Genzer and R. R. Bhat, *Langmuir*, 2008, 24, 2294-2317.
168. J. Genzer, *Annual Review of Materials Research*, 2012, 42, 435-468.
169. M. Zelzer, M. R. Alexander and N. A. Russell, *Acta biomaterialia*, 2011, 7, 4120-4130.
170. D. Mangindaan, W.-H. Kuo and M.-J. Wang, *Biochemical Engineering Journal*, 2013, 78, 198-204.
171. D. Bhattacharyya, H. Xu, R. R. Deshmukh, R. B. Timmons and K. T. Nguyen, *Journal of Biomedical Materials Research Part A*, 2010, 94A, 640-648.
172. N. Wells, M. A. Baxter, J. E. Turnbull, P. Murray, D. Edgar, K. L. Parry, D. A. Steele and R. D. Short, *Biomaterials*, 2009, 30, 1066-1070.
173. F. J. Harding, L. R. Clements, R. D. Short, H. Thissen and N. H. Voelcker, *Acta Biomaterialia*, 2012, 8, 1739-1748.
174. Andrew Micheltore, Lauren Clements, David A. Steele, Nicolas H. Voelcker and E. J. Szili, *Journal of Nanomaterials*, 2012, 2012, 7.

175. J. Yang, F. R. A. J. Rose, N. Gadegaard and M. R. Alexander, *Advanced Materials*, 2009, 21, 300-304.
176. A. Curtis and C. Wilkinson, *Biomaterials*, 1997, 18, 1573-1583.
177. L. E. McNamara, R. J. McMurray, M. J. Dalby and P. M. Tsimbouri, in *Comprehensive Biomaterials*, ed. D. Editor-in-Chief: Paul, Elsevier, Oxford, 2011, pp. 115-126.
178. C. S. Chen, M. Mrksich, S. Huang, G. M. Whitesides and D. E. Ingber, *Science*, 1997, 276, 1425-1428.
179. H. G. Craighead, C. D. James and A. M. P. Turner, *Current Opinion in Solid State and Materials Science*, 2001, 5, 177-184.
180. E. K. F. Yim and K. W. Leong, *Nanomedicine: Nanotechnology, Biology and Medicine*, 2005, 1, 10-21.
181. J. W. Costerton, P. S. Stewart and E. P. Greenberg, *Science*, 1999, 284, 1318-1322.
182. R. O. Darouiche, *New England Journal of Medicine*, 2004, 350, 1422-1429.
183. B. R. Coad, S. E. Kidd, D. H. Ellis and H. J. Griesser, *Biotechnology Advances*, 2014, 32, 296-307.
184. P.-H. Hsieh, M. S. Lee, K.-Y. Hsu, Y.-H. Chang, H.-N. Shih and S. W. Ueng, *Clinical Infectious Diseases*, 2009, 49, 1036-1043.
185. J. D. Bryers, *Biotechnology and Bioengineering*, 2008, 100, 1-18.
186. G. Pierce, *J IND MICROBIOL BIOTECHNOL*, 2005, 32, 309-318.
187. M. E. Rupp and G. L. Archer, *Clinical Infectious Diseases*, 1994, 19, 231-245.
188. R. M. Donlan, *Emerging infectious diseases*, 2001, 7, 277.
189. P. J. Collignon, D. E. Dreimanis, W. D. Beckingham, J. L. Roberts and A. Gardner, *Medical Journal of Australia*, 2007, 187, 551-555.
190. L. Tao, B. Hu, V. D. Rosenthal, X. Gao and L. He, *International Journal of Infectious Diseases*, 2011, 15, e774-e780.
191. M. Whiteley, M. G. Banger, R. E. Bumgarner, M. R. Parsek, G. M. Teitzel, S. Lory and E. P. Greenberg, *Nature*, 2001, 413, 860-864.
192. M. T. McCann, B. F. Gilmore and S. P. Gorman, *The Journal of pharmacy and pharmacology*, 2008, 60, 1551-1571.
193. R. E. Lewis, D. P. Kontoyiannis, R. O. Darouiche, I. I. Raad and R. A. Prince, *Antimicrobial Agents and Chemotherapy*, 2002, 46, 3499-3505.
194. A. M. Kraigsley and S. E. Finkel, *FEMS Microbiology Letters*, 2009, 293, 135-140.

195. T. Das and M. Manefield, *PLoS ONE*, 2012, 7, e46718.
196. L. Hall-Stoodley and P. Stoodley, *Trends in Microbiology*, 2005, 13, 7-10.
197. P. Stoodley, L. Hall-Stoodley, B. Costerton, P. DeMeo, M. Shirtliff, E. Gawalt and S. Kathju, in *Biomaterials Science (Third Edition)*, eds. B. D. Ratner, A. S. Hoffman, F. J. Schoen and J. E. Lemons, Academic Press, 2013, pp. 565-583.
198. L. D. Renner and D. B. Weibel, *MRS bulletin / Materials Research Society*, 2011, 36, 347-355.
199. K. C. Marshall, R. Stout and R. Mitchell, *Canadian Journal of Microbiology*, 1971, 17, 1413-1416.
200. K. B. Barken, S. J. Pamp, L. Yang, M. Gjermansen, J. J. Bertrand, M. Klausen, M. Givskov, C. B. Whitchurch, J. N. Engel and T. Tolker-Nielsen, *Environmental Microbiology*, 2008, 10, 2331-2343.
201. T. Das, S. K. Kutty, N. Kumar and M. Manefield, *PLoS ONE*, 2013, 8, e58299.
202. H. H. Tuson and D. B. Weibel, *Soft Matter*, 2013, 9, 4368-4380.
203. J. W. McClaine and R. M. Ford, *Applied and Environmental Microbiology*, 2002, 68, 1280-1289.
204. N. C. Caiazza and G. A. O'Toole, *Journal of bacteriology*, 2004, 186, 4476-4485.
205. E. P. Ivanova, J. Hasan, H. K. Webb, V. K. Truong, G. S. Watson, J. A. Watson, V. A. Baulin, S. Pogodin, J. Y. Wang, M. J. Tobin, C. Löbbe and R. J. Crawford, *Small*, 2012, 8, 2489-2494.
206. S. Pogodin, J. Hasan, Vladimir A. Baulin, Hayden K. Webb, Vi K. Truong, The H. Phong Nguyen, V. Boshkovikj, Christopher J. Fluke, Gregory S. Watson, Jolanta A. Watson, Russell J. Crawford and Elena P. Ivanova, *Biophysical Journal*, 104, 835-840.
207. K. Bazaka, R. J. Crawford and E. P. Ivanova, *Biotechnology Journal*, 2011, 6, 1103-1114.
208. K. Bazaka, M. Jacob, R. Crawford and E. Ivanova, *Appl Microbiol Biotechnol*, 2012, 95, 299-311.
209. J. Hasan, R. J. Crawford and E. P. Ivanova, *Trends in Biotechnology*, 2013, 31, 295-304.
210. H. J. Griesser, H. Hall, T. A. Jenkins, S. S. Griesser and K. Vasilev, in *Intelligent Surfaces in Biotechnology*, John Wiley & Sons, Inc., 2012, pp. 183-241.

211. E. Ostuni, R. G. Chapman, M. N. Liang, G. Meluleni, G. Pier, D. E. Ingber and G. M. Whitesides, *Langmuir*, 2001, 17, 6336-6343.
212. I. C. Saldarriaga Fernández, H. C. v. d. Mei, S. Metzger, D. W. Grainger, A. F. Engelsman, M. R. Nejadnik and H. J. Busscher, *Acta Biomaterialia*, 2010, 6, 1119-1124.
213. A. Roosjen, H. C. van der Mei, H. J. Busscher and W. Norde, *Langmuir*, 2004, 20, 10949-10955.
214. M. R. Nejadnik, H. C. van der Mei, W. Norde and H. J. Busscher, *Biomaterials*, 2008, 29, 4117-4121.
215. Y.-C. Chiag, Y. Chang, W.-Y. Chen and R.-c. Ruaan, *Langmuir*, 2011, 28, 1399-1407.
216. N.-J. Lin, H.-S. Yang, Y. Chang, K.-L. Tung, W.-H. Chen, H.-W. Cheng, S.-W. Hsiao, P. Aimar, K. Yamamoto and J.-Y. Lai, *Langmuir*, 2013, 29, 10183-10193.
217. J. C. Tiller, C.-J. Liao, K. Lewis and A. M. Klibanov, *Proceedings of the National Academy of Sciences*, 2001, 98, 5981-5985.
218. B. Gottenbos, H. C. Van Der Mei, H. J. Busscher, D. W. Grijpma and J. Feijen, *Journal of materials science. Materials in medicine*, 1999, 10, 853-855.
219. T. P. Martin, S. E. Kooi, S. H. Chang, K. L. Sedransk and K. K. Gleason, *Biomaterials*, 2007, 28, 909-915.
220. E.-R. Kenawy, A. E.-R. R. El-Shanshoury, N. Omar Shaker, B. M. El-Sadek, A. H. B. Khattab and B. Ismail Badr, *Journal of Applied Polymer Science*, 2011, 120, 2734-2742.
221. F. Costa, I. F. Carvalho, R. C. Montelaro, P. Gomes and M. C. L. Martins, *Acta Biomaterialia*, 2011, 7, 1431-1440.
222. J. A. Loontjens, in *Biomaterials Associated Infection*, eds. T. F. Moriarty, S. A. J. Zaat and H. J. Busscher, Springer New York, 2013, ch. 15, pp. 379-404.
223. B. Gottenbos, H. C. van der Mei, F. Klatter, P. Nieuwenhuis and H. J. Busscher, *Biomaterials*, 2002, 23, 1417-1423.
224. A. Siddiqui and A. K. Schultz, Google Patents, 2001.
225. S. Lischer, E. Körner, D. J. Balazs, D. Shen, P. Wick, K. Grieder, D. Haas, M. Heuberger and D. Hegemann, *Journal of The Royal Society Interface*, 2011, 8, 1019-1030.

- 
226. J. J. Castellano, S. M. Shafii, F. Ko, G. Donate, T. E. Wright, R. J. Mannari, W. G. Payne, D. J. Smith and M. C. Robson, *International Wound Journal*, 2007, 4, 114-122.
227. D. W. Brett, *Ostomy/wound management*, 2006, 52, 34-41.
228. D. Raafat and H.-G. Sahl, *Microbial Biotechnology*, 2009, 2, 186-201.
229. J. Wang, Y. P. Chen, K. Yao, P. A. Wilbon, W. Zhang, L. Ren, J. Zhou, M. Nagarkatti, C. Wang, F. Chu, X. He, A. W. Decho and C. Tang, *Chemical Communications*, 2012, 48, 916-918.
230. M. B. Dickerson, A. A. Sierra, N. M. Bedford, W. J. Lyon, W. E. Gruner, P. A. Mirau and R. R. Naik, *Journal of Materials Chemistry B*, 2013, 1, 5505-5514.
231. V. B. Schwartz, F. Thétiot, S. Ritz, S. Pütz, L. Choritz, A. Lappas, R. Förch, K. Landfester and U. Jonas, *Advanced Functional Materials*, 2012, 22, 2376-2386.
232. Z. Li, D. Lee, X. Sheng, R. E. Cohen and M. F. Rubner, *Langmuir*, 2006, 22, 9820-9823.
233. G. Cheng, H. Xue, G. Li and S. Jiang, *Langmuir*, 2010, 26, 10425-10428.
234. D. J. Balazs, K. Triandafillu, E. Sardella, G. Iacoviello, P. Favia, R. d'Agostino, H. Harms and H. J. Mathieu, in *Plasma Processes and Polymers*, Wiley-VCH Verlag GmbH & Co. KGaA, 2005, ch26, pp. 351-372.
235. E. Johnston, B. Ratner and J. Bryers, *NATO ASI Series E Applied Sciences-Advanced Study Institute*, 1997, 346, 465-476.
236. A. R. Denes, E. B. Somers, A. C. L. Wong and F. Denes, *Journal of Applied Polymer Science*, 2001, 81, 3425-3438.
237. R. Kumar and H. Münstedt, *Biomaterials*, 2005, 26, 2081-2088.
238. M. Ip, S. L. Lui, V. K. M. Poon, I. Lung and A. Burd, *Journal of Medical Microbiology*, 2006, 55, 59-63.
239. J. S. Kim, E. Kuk, K. N. Yu, J.-H. Kim, S. J. Park, H. J. Lee, S. H. Kim, Y. K. Park, Y. H. Park, C.-Y. Hwang, Y.-K. Kim, Y.-S. Lee, D. H. Jeong and M.-H. Cho, *Nanomedicine: Nanotechnology, Biology and Medicine*, 2007, 3, 95-101.
240. B. Despax and P. Raynaud, *Plasma Processes and Polymers*, 2007, 4, 127-134.
241. C. Saulou, B. Despax, P. Raynaud, S. Zanna, P. Marcus and M. Mercier-Bonin, *Applied Surface Science*, 2009, 256, S35-S39.
242. E. Körner, M. H. Aguirre, G. Fortunato, A. Ritter, J. Rühle and D. Hegemann, *Plasma Processes and Polymers*, 2010, 7, 619-625.

243. K. Vasilev, V. Sah, K. Anselme, C. Ndi, M. Mateescu, B. r. Dollmann, P. Martinek, H. Ys, L. Ploux and H. J. Griesser, *Nano Letters*, 2009, 10, 202-207.
244. N. Poulter, X. Munoz-Berbel, A. L. Johnson, A. J. Dowling, N. Waterfield and A. T. A. Jenkins, *Chemical Communications*, 2009, 7312-7314.
245. H. Jiang, S. Manolache, A. C. L. Wong and F. S. Denes, *Journal of Applied Polymer Science*, 2004, 93, 1411-1422.
246. N. Alissawi, V. Zaporajtchenko, T. Strunskus, T. Hrkac, I. Kocabas, B. Erkartal, V. S. K. Chakravadhanula, L. Kienle, G. Grundmeier, D. Garbe-Schönberg and F. Faupel, *J Nanopart Res*, 2012, 14, 1-12.
247. S. Taheri, A. Cavallaro, S. N. Christo, L. E. Smith, P. Majewski, M. Barton, J. D. Hayball and K. Vasilev, *Biomaterials*, 2014, 35, 4601-4609.
248. M. D. Arjun Srinivasan, M. M. Tobi Karchmer, B. S. Ann Richards, M. D. Xiaoyan Song and M. D. M. Trish M. Perl, *Infection Control and Hospital Epidemiology*, 2006, 27, 38-43.
249. C. Greulich, D. Braun, A. Peetsch, J. Diendorf, B. Siebers, M. Epple and M. Koller, *RSC Advances*, 2012, 2, 6981-6987.
250. A. Daniel, C. Le Pen, C. Archambeau and F. Reniers, *Applied Surface Science*, 2009, 256, S82-S85.
251. N. Poulter, M. Donaldson, G. Mulley, L. Duque, N. Waterfield, A. G. Shard, S. Spencer, A. T. A. Jenkins and A. L. Johnson, *New Journal of Chemistry*, 2011, 35, 1477-1484.
252. Y.-M. Jeong, J.-K. Lee, S.-C. Ha and S. H. Kim, *Thin Solid Films*, 2009, 517, 2855-2858.
253. J. A. Lemire, J. J. Harrison and R. J. Turner, *Nat Rev Micro*, 2013, 11, 371-384.
254. I. Braceras, P. Azpiroz, N. Briz, R. M. Fratila, J. Oyarbide, E. Ipiñazar, N. Álvarez, G. Atorrasagasti and J. M. Aizpurua, *Plasma Processes and Polymers*, 2011, 8, 599-606.
255. M. J. Garcia-Fernandez, L. Martinez-Calvo, J.-C. Ruiz, M. R. Wertheimer, A. Concheiro and C. Alvarez-Lorenzo, *Plasma Processes and Polymers*, 2012, 9, 540-549.
256. C. Susut and R. B. Timmons, *International Journal of Pharmaceutics*, 2005, 288, 253-261.

257. S. Simovic, D. Losic and K. Vasilev, *Chemical Communications*, 2010, 46, 1317-1319.
258. S. K. Hendricks, C. Kwok, M. Shen, T. A. Horbett, B. D. Ratner and J. D. Bryers, *J Biomed Mater Res*, 2000, 50, 160-170.
259. D. Duday, C. Vreuls, M. Moreno, G. Frache, N. D. Boscher, G. Zocchi, C. Archambeau, C. Van De Weerd, J. Martial and P. Choquet, *Surface and Coatings Technology*, 2013, 218, 152-161.
260. C. Vreuls, G. Zocchi, B. Thierry, G. Garitte, S. S. Griesser, C. Archambeau, C. Van de Weerd, J. Martial and H. Griesser, *Journal of Materials Chemistry*, 2010, 20, 8092-8098.
261. N. Aumsuwan, M. S. McConnell and M. W. Urban, *Biomacromolecules*, 2009, 10, 623-629.
262. I. Braceras, J. Oyarbide, P. Azpiroz, N. Briz, E. Ipiñazar, N. Álvarez, G. Atorrasagasti, R. M. Fratila and J. M. Aizpurua, *Plasma Processes and Polymers*, 2013, 10 (4), 328-335.
263. M. Donegan and D. P. Dowling, *Plasma Processes and Polymers*, 2013, 10, 526-534.
264. S. Sarghini, S. Paulussen and H. Terry, *Plasma Processes and Polymers*, 2011, 8, 59-69.
265. S. N. Jampala, M. Sarmadi, E. B. Somers, A. C. L. Wong and F. S. Denes, *Langmuir*, 2008, 24, 8583-8591.
266. W. C. E. Schofield and J. P. S. Badyal, *ACS Applied Materials & Interfaces*, 2009, 1, 2763-2767.
267. S. Takenaka, T. Tonoki, K. Taira, S. Murakami and K. Aoki, *Applied and Environmental Microbiology*, 2007, 73, 1797-1802.
268. M. Tandukar, S. Oh, U. Tezel, K. T. Konstantinidis and S. G. Pavlostathis, *Environmental Science & Technology*, 2013, 47, 9730-9738.
269. A. Conte, G. G. Buonocore, M. Sinigaglia, L. C. Lopez, P. Favia, R. d'Agostino and M. A. Del Nobile, *Journal of Food Protection*, 2008, 71, 119-125.
270. B. R. Coad, T. Scholz, K. Vasilev, J. D. Hayball, R. D. Short and H. J. Griesser, *ACS Applied Materials & Interfaces*, 2012, 4, 2455-2463.
271. N. Aumsuwan, R. C. Danyus, S. Heinhorst and M. W. Urban, *Biomacromolecules*, 2008, 9, 1712-1718.

- 
272. S. A. Al-Bataineh and U. o. S. A. I. W. R. Institute, *Spectroscopic Characterisation of Surface-immobilised Antibacterial Furanone Coatings*, University of South Australia, 2006.
273. H. Ys and I. W. R. Institute, *Antibacterial Coatings for Biomedical Devices by Covalent Grafting of Serrulatane Diterpenes*, University of South Australia, 2011.

## Chapter 3 Diglyme Plasma polymer film characterisation



*"I have to spend countless hours, above and beyond the basic time,  
to try and perfect the fundamentals."  
- Julius Erving*

### 3.1 Introduction

Plasma polymerisation has been utilised to generate PEG-like surfaces since the early 1990s.<sup>1</sup> Precursor molecules containing ether functional groups are fragmented in the plasma environment, then recombined due to collision and condensation, forming a highly crosslinked polymer film. The extent of retention of ethers in the plasma polymerised films affects the degree of protein repellency and cell adhesion.<sup>2-6</sup> In this chapter, diethylene glycol dimethyl ether (diglyme) was used as a precursor to prepare plasma polymer (pp) thin films with varying degrees of ether groups. Chemical characterisation of the films was performed using X-ray photoelectron spectroscopy (XPS) and near edge X-ray absorption fine structure (NEXAFS) spectroscopy. The ability of the surfaces to resist protein adsorption was examined using a quartz crystal microbalance with dissipation (QCM-D). The resultant films were used further for fibroblast cell adhesion and pathogenic microbial attachment studies.

In continuous wave RFGD plasma polymerisation processes, the degree of functional group retention is related to the amount of fragmentation of the monomers. In a given reactor, with fixed reactor geometry and flow rate of monomer, increasing load power leads to more bond dissociation events. In this chapter, uniform diglyme plasma polymer (DGpp) films were produced at several load powers, including 10, 20, 30, 40 and 50 W. Surface chemistry characterisation indicated that DGpp films deposited at lower load powers are more effective in retaining the ether functionality from the starting monomer. With higher ether content, i.e. more PEG-like, DGpp films were resistant to protein, cell and microbial fouling. However, this is not to say that low load powers can only make films with PEG-like chemistry. In this chapter, micropatterned films containing cell adhesive and repellent regions were prepared via plasma polymerisation at 5 W load power in a single step. The reactor was the same, but with a different upper electrode. The specially designed electrode contains arrays of open holes that can induce variation in monomer fragmentation underneath the electrode, resulting in a film with defined areas of low-fouling chemistry.

For biological tests, the stability of the coating in biological fluids is of primary concern. To examine the stability of the films obtained in this chapter, they were incubated in phosphate-buffered saline (PBS) and cell culture media at 37 °C for designated time intervals. The DGpp films delaminated from the Si wafer or glass substrate more easily after a prolonged incubation period compared with films on polymer substrates. Overall, the observations from this chapter guided the experimental design for the rest of the thesis.

## **3.2 Materials and methods**

### **3.2.1 Substrate materials**

Ultra-flat single crystal silicon wafers (<100>, 1 cm<sup>2</sup> x 0.5 mm thick, M.M.R.C P/L), and thin copper shim (100 μm) were used as substrates for the deposition of diethylene glycol dimethyl ether (BDH, 99 % purity) plasma polymer films. Prior to plasma polymerisation all substrates were cleaned by ultrasonication in a surfactant solution of 2 % ethanol with 2 % RBS-35 (Pierce, U.S.A.) for 30 min, followed by multiple rinsing with Milli-Q water. The substrates were dried in a high-pressure stream of high purity nitrogen (BOC Gas, Australia). Tissue culture polystyrene (TCPS) 96-well flat-bottom microplates (FALCON®) and Thermanox™ coverslips (∅ = 25 mm, NUNC™, Denmark) were used directly from sterile packages.

### **3.2.2 Plasma polymerisation**

Deposition of DGpp film was carried out in a custom-built plasma reactor. The reactor is composed of a cylindrical glass chamber (height of 35 cm and diameter of 17 cm) and is fitted with two capacitively coupled copper electrodes. The top electrode (d=9.5 cm) was connected to a RF power supply (200 kHz), while the bottom electrode (d=14 cm) was grounded. The monomer DG which was contained in a round-bottom flask was connected to the reactor chamber via a stainless steel line and was degassed three times before film deposition. A manual valve was used to adjust the flow of DG vapours.

Substrates were placed on the lower electrode for plasma polymer coating. The reaction chamber was evacuated to base pressure prior to deposition.

#### *Uniform DGpp films for surface chemistry analysis*

The parameters chosen for RFGD deposition of DGpp films on copper were: frequency of 200 kHz, load powers of 10, 20, 30, 40 and 50 W and an initial monomer pressure of 20 Pa for a treatment time of 35, 25, 20, 15 and 10 seconds respectively. The plasma depositions of DGpp films on Si wafer were performed using the same frequency and initial monomer pressure for 180 seconds at load powers of 20 and 50 W. Once the deposition was finished, the reactor was evacuated to base pressure and the samples were taken out from the chamber after venting. All copper samples were stored in clean tissue culture grade petri dishes under ambient conditions until further analysis.

#### *Uniform DGpp films for antimicrobial application*

The reactor geometry is the same as described above, however, the bottom electrode changed to a rectangular copper electrode (length = 12 cm, width = 8 cm). TCPS 96-well microplates were placed on the bottom electrode. The parameters chosen for DGpp film deposition were load powers of 5, 10, 20 and 50 W, at an initial monomer pressure of 20 Pa and frequency of 125 kHz, for a treatment of 360, 360, 240, and 120 seconds, respectively. The samples were wrapped around with parafilm and stored under ambient conditions.

#### *Micropatterned DGpp films*

Thermanox™ coverslips were used as the substrate for direct deposition of DGpp patterns. The plasma polymerisation was performed in the same reactor but the upper electrode was changed to a patterned electrode with regular arrays of 2 mm holes. The electrode was lowered to sit approximately 1 mm above the substrate. The process parameters chosen for RFGD deposition of pattern DGpp were a load power of 5W, a frequency of 125 kHz, a treatment time of 120 seconds, and an initial monomer pressure of 20 Pa.

### 3.2.3 X-ray photoelectron spectroscopy

For surface chemical analysis of the DGpp films, X-ray photoelectron spectroscopy (XPS) characterisation was performed using an AXIS HSi spectrometer (Kratos Analytical Ltd, U.K.) equipped with a monochromated Al-K $\alpha$  X-ray source at a power of 144 W (12 mA, 12 kV). An internal flood gun was employed to compensate the charging of the samples due to irradiation. The survey spectra (acquired at a pass energy of 160 eV) were recorded to identify all the elements contained in the surface. The atomic concentrations of the elements were calculated in Casa XPS using integral peak intensities and the sensitivity factors that were provided by the manufacturer. High resolution C 1s spectra were obtained at a pass energy of 40 eV and quantified using a minimisation algorithm. Five peak components were used for curve fitting of C 1s spectra to represent specific functional groups. At the lowest binding energy (BE), that is 285 eV, component C1 was assigned to aliphatic hydrocarbons (neutral carbon). A second component, C2 used to account for all C 1s photoelectrons that underwent a secondary BE shift was placed at a slight higher BE compared with C1. The 3<sup>rd</sup> component, C3 (C1 + 1.5 eV) represents C-O based groups (e.g., C-O-C, C-OH). C4 (C1 + 3 eV) refers to C=O based groups (e.g., O-C-O) and C5 (C1 + 4 - 4.5 eV) accounts for O-C=O containing groups (e.g., acids and esters).

For patterned films, the samples were analysed using AXIS Ultra DLD spectrometer (Kratos Analytical Inc., Manchester, U.K.) with a monochromated Al K $\alpha$  source at a power of 150 W, a hemispherical analyser operating in the fixed analyser transmission mode and the standard aperture. During sample analysis, the pressure of the main vacuum chamber was typically pumped to 10<sup>-8</sup> mbar. Survey spectra were acquired at a pass energy of 160 eV to gather information on all elements presented. For information on chemical structure, oxidation states etc., high resolution spectra were recorded for individual peaks (i.e. C, N separately) at 40 eV pass energy (for polymers the resulting peak width is 1.0 eV).

### 3.2.4 Near edge X-ray absorption fine structure spectroscopy

NEXAFS characterization was carried out on the soft X-ray beamline (SXR, 14-ID) at the Australian Synchrotron.<sup>7</sup> The beamline is equipped with an Apple II undulator, which generates horizontally polarised soft X-rays that are subsequently passed through a monochromator (Peterson plane grating, 1200 lines mm<sup>-1</sup>). The photon flux on the beamline varied from 1 – 3 x 10<sup>11</sup> photons/s/200mA at an energy of 600 eV. The photon spot size on the sample was approximately 1 mm x 0.4 mm. Samples were transferred into a UHV chamber with a base pressure of 2 x 10<sup>-10</sup> mbar. Both the C (275 – 320 eV) and O (520 – 560 eV) K-edge NESAFS spectra were acquired in total electron yield (TEY) mode with the beam at 90° with respect to the sample surface. Multiple spectra were recorded at one spot to eliminate the possibility of radiation damage to the films. Same spectral features were obtained during this test; therefore the soft X-ray do not change the surface chemistry. Each NEXAFS spectrum was normalised to the incident photon flux by referencing to the drain current from a fine Au mesh placed in front of the sample. At the same time, a clean sputtered Au foil was measured for comparison to account for possible carbon and oxygen contamination. Spectra were then normalised with the method described by Watts et al.<sup>8</sup>

### 3.2.5 Protein adsorption

To access the relative adsorption of various proteins on DGpp films, samples were incubated in mouse embryonic stem (mES) cell culture medium which was composed of Dulbeccos modified Eagle's media (DMEM) supplemented with 15 % (v/v) fetal bovine serum, glutaMAX-1, nonessential amino acids (NEAA), sodium pyruvate (100X), penicillin/streptomycin solution, and 2-mercaptoethanol. DGpp uniform coatings were placed in mES medium for both 2 and 24 h incubation times at 37 °C in a laboratory water bath (Thermoline L+M, Australia). Duplicates were treated as the same except at room temperature. All samples were rinsed with large amount of MilliQ water to remove loosely bound proteins before being blown dry with a high pressure stream of nitrogen. Samples were then analysed using XPS to detect the presence of elemental N on the DGpp films which confirms the adsorption of protein on the surfaces.

### 3.2.6 Quartz crystal microbalance with dissipation

Protein adsorption on DGpp films was monitored in real time using a quartz crystal microbalance with dissipation (QCM-D, Q-sense, Gothenburg, Sweden) at 37 °C. DGpp films were deposited on gold 5 MHz quartz crystal chips that were cleaned by UV/Ozone (BioForce, U.S.A.) radiation for 30 min. The DGpp films coated crystal chips were hydrated overnight with PBS flowing over the QCM-D chamber at 30  $\mu$ l/min. A stable baseline was reached prior to mES medium introduction. mES medium flowed through the chambers for 2 h. Then the chips were washed with PBS to remove loosely adsorbed proteins. Shifts of the oscillating frequency (Df) were detected at the third, fifth, and seventh harmonic and plotted against time.

### 3.2.7 Biofilm cultivation and quantitative determination

Three biofilm-forming reference strains: *Staphylococcus epidermidis* RP62a (ATCC35984), *Pseudomonas aeruginosa* ATCC 27853 and *Candida albicans* DAY185 were used in this study. Bacterial stocks (stored at -80 °C in nutrient broth with 15 % glycerol) were streaked onto nutrient agar (NA, Oxoid) plates for use as the working stock. *C. albicans* (stored at -80 °C in 15 % glycerol) was streaked onto YPD (2 % glucose, 2 % peptone, 1 % yeast extract, 2 % agar) plates for use as the working stock. These working stocks were stored at 4 °C (*S. epidermidis* and *P. aeruginosa*) or room temperature (*C. albicans*) and replaced every two weeks.

Bacterial biofilm culture was set up using a modification of an established method.<sup>9</sup> Briefly, an overnight bacterial culture grown in nutrient broth (NB) was diluted 1:100 into biofilm-specific growth media, including tryptic soya broth for *S. epidermidis* (TSB, Oxoid), or Luria-Bertani (LB) broth for *P. aeruginosa*. 100  $\mu$ l of the diluted bacterial suspensions were pipetted into a well in a 96-well flat-bottom polystyrene microplates which had received different DGpp coating treatments and were incubated for 20 h at 37 °C with gentle agitation (75 rpm). To grow fungal biofilms, 100  $\mu$ l of cultures of *C. albicans* ( $10^7$  CFU/ml in Spider medium, 1 % nutrient broth, 1 % D-mannitol, 2 g  $K_2HPO_4$ ) were added to wells and incubated at 37 °C with gentle shaking (75 rpm) for

90 min (adhesion phase).<sup>10</sup> Non-adherent cells were discarded and the microplates were washed once with sterile PBS before 100  $\mu$ l of fresh Spider medium was added into the microwells. Biofilms were allowed to further develop for 48 h. The medium was replenished after 24 h by aspiration and addition of fresh Spider medium. After overnight or 48 h incubation, the cell suspensions were aspirated and the microwells were rinsed twice with 110  $\mu$ L of PBS per well to remove non-adherent cells. To quantify biofilms formed on surfaces of different treatments, the microplate containing biofilms was heat-fixed in a 60 °C oven for 1 h and then stained with 110  $\mu$ l of 1 % (W/V) crystal violet (CV) for 10 min. The CV solution in the wells was then discarded and the microplates were washed four times to remove excess stain by submerging them in tubs of clean water. The microplates were gently tapped on paper towels to remove excess water in the microwells. 200  $\mu$ l of 95 % ethanol and 5 % acetic acid were added into each well and incubated at room temperature for 15 min. 100  $\mu$ l of solution from each well was transferred to a new microplate. The amount of biofilm formed in the microwell was determined by reading its optical density with a Tecan Infinite M200 Plate Reader at 595 nm.

### 3.2.8 Confocal laser scanning microscopy

Polystyrene pieces were cut from the bottom of a 96-well microplate, with extreme caution to avoid any scratch to the treated or control surfaces. The polystyrene pieces were then transferred to a well in a 24 well microplate containing 1 ml of a bacterial suspension ( $\sim 10^7$  CFU/mL) or fungal suspensions ( $\sim 10^7$  CFU/mL), followed by 24 h incubation for bacteria or 90 min adherence and 48 h incubation for *C. albicans* at 37 °C, as described above. The polystyrene pieces were then rinsed three times with 0.9 % saline to remove planktonic bacteria or fungal cells. The bacterial biofilms were then stained with a LIVE/DEAD BacLight viability kit, containing 3.35  $\mu$ M SYTO-9 and 20  $\mu$ M propidium iodide (PI), at 22 °C for 15 min in the dark.<sup>11</sup> The *C. albicans* biofilm was stained with calcofluoro white (1 mg/ml) for 15 min.<sup>12</sup> The polystyrene pieces were washed twice with 0.9 % saline after staining. The structure of the biofilm was immediately examined with an inverted confocal laser scanning microscope (CLSM, Leica SP5) after washing twice with 0.9 % saline. All samples were sequentially

scanned, frame-by-frame, first at 488 nm and then at 561 nm to minimise artefacts associated with simultaneous dual wavelength excitation. A 63 × oil objective was used in all imaging experiments. Three-dimensional structure of bacterial biofilms was built-up with the software Amira 5.4.1.

### **3.2.9 Protein adsorption and cell adhesion on micropatterned DGpp films**

#### *Protein adsorption*

Patterned films were incubated in mES medium for 1 day and 7 days at 37 °C for protein adsorption. All samples were rinsed with large amount MilliQ water and dried under a stream of nitrogen.

#### *SNL cell adhesion and growth*

The micropatterned coverslips were transferred to separate wells of a 6-well culture plate and sterilised overnight in 5 ml of 1 × PBS containing 200 units/ml penicillin and 200 µg/ml streptomycin (Invitrogen). SNL cells were seeded onto the coverslips at a density of 20,000 cells/well in 3 ml of fresh mES medium. Cells were incubated for 48 h at 37 °C in humidified air containing 5 % CO<sub>2</sub>. Cell morphology and attachment on the micropatterned coverslips were examined using an inverted microscope. Phase contrast images were obtained using 4 X and 10 X objectives. After 2 days in culture, the medium was removed and each coverslip rinsed with sterile 1 × PBS (pH = 7.4). Cells were stained for 20 min with hematoxylin (Gill No. 3, Sigma Aldrich) at room temperature, and then washed with PBS. Cell colonies turned blue and an image of a micropatterned coverslip was taken with a digital camera.

### 3.3 Results and discussion

#### 3.3.1 Surface chemistry of uniform DGpp films

The elemental composition of the as deposited DGpp films at load powers of 10, 20, 30, 40 and 50 W are summarised in Table 3.1. The atomic ratio of varies functional groups relative to total carbon are also presented in Table 3.1. All plasma polymer films have thickness greater than 10 nm, which is the XPS analysis depth, as indicated by the absence of silicon in the obtained survey spectra. The XPS survey reveals DGpp coatings comprising only carbon and oxygen with atomic concentrations varying from 70 – 76 % and 30 – 24 % respectively for the load powers used herein. This is consistent with previous reports of these type of DGpp coatings.<sup>3, 13</sup> The chemical composition of the higher power films differs substantially from the monomer, for which the oxygen content is higher (33 % O, 67 % C). As can be seen, higher power glow discharges produced DGpp films have reduced oxygen related groups and increased amount of hydrocarbon containing species.

Table 3.1. Elemental composition (atomic %) of DGpp films deposited on copper. Values were derived from XPS survey spectra. Presented in mean  $\pm$  standard deviation. The theoretical diglyme monomer composition is shown . The concentration of different functional groups derived from high resolution C 1s spectra (atomic ratios relative to total carbon, X/C) of the DGpp films are presented as well. C1 denotes hydrocarbons; C2 is the secondary shift; C3 refers to C-O based groups (ethers and alcohols); C4 represents C=O and O-C-O based groups (e.g. aldehyde, ketone); C5 is for O-C=O based groups (e.g. acid, ester).

	<i>Atomic %</i>		<i>Atomic ratio relative to total carbon, X/C</i>			
	<i>C 1s</i>	<i>O 1s</i>	<i>C1 + C2</i>	<i>C3</i>	<i>C4</i>	<i>C5</i>
Diglyme monomer	66.6	33.3	-	-	-	-
10 W	70.1 $\pm$ 0.2	29.8 $\pm$ 0.2	25.7 $\pm$ 0.4	61.9 $\pm$ 0.4	10.8 $\pm$ 0.8	1.7 $\pm$ 0.0
20 W	71.6 $\pm$ 0.3	28.2 $\pm$ 0.3	31.6 $\pm$ 0.3	55.6 $\pm$ 0.7	10.5 $\pm$ 0.0	2.3 $\pm$ 0.4
30 W	73.4 $\pm$ 0.2	26.3 $\pm$ 0.3	43.3 $\pm$ 1.1	45.1 $\pm$ 1.1	9.4 $\pm$ 0.1	2.2 $\pm$ 0.1
40 W	75.2 $\pm$ 0.0	24.6 $\pm$ 0.0	49.4 $\pm$ 0.7	40.5 $\pm$ 0.3	6.3 $\pm$ 0.9	3.9 $\pm$ 0.5
50 W	76.4 $\pm$ 0.4	23.3 $\pm$ 0.4	54.1 $\pm$ 0.5	35.6 $\pm$ 0.3	7.0 $\pm$ 1.8	3.3 $\pm$ 1.0

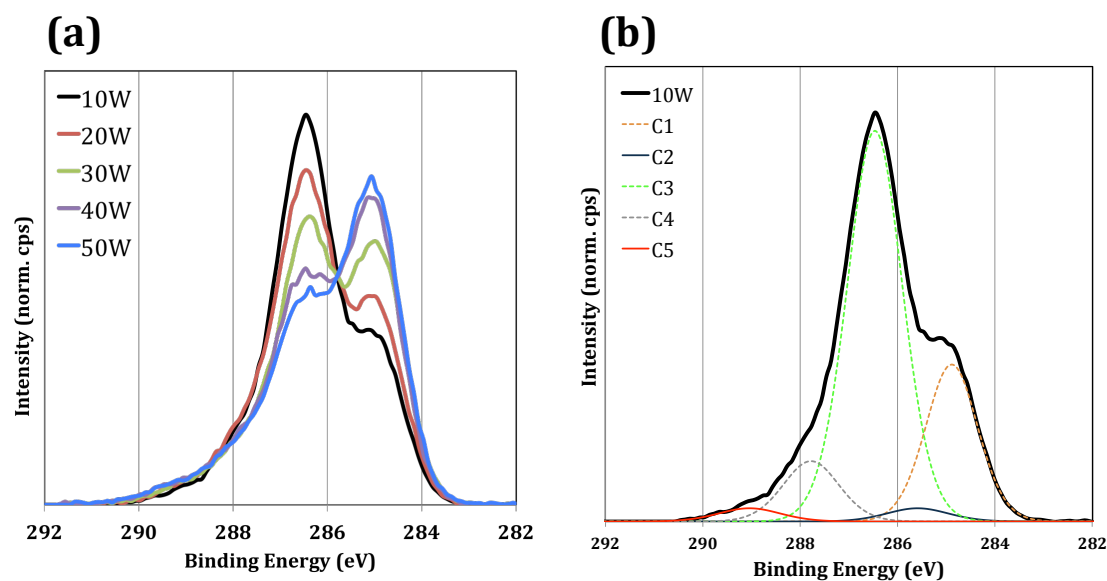


Figure 3.1, XPS C 1s high resolution spectra of the DGpp films produced at 10, 20, 30, 40 and 50 W load powers. (a) Overlay of the C 1s spectra of five DGpp films deposited on copper; (b) Fitting for the 10 W DGpp film based on five composition model, where C1 denotes hydrocarbons; C2 is the secondary shift; C3 refers to C-O based groups (ethers and alcohols); C4 represents C=O and O-C-O based groups (e.g. aldehyde, ketone); C5 is for O-C=O based groups (e.g. acid, ester).

From the above figure, it is obvious that DGpp films are rich in C-O moieties such as ether. It has been well documented that a lower power discharge leads to less intensive fragmentation of precursor molecules, hence produces thin films retain higher concentration of ether functionality.<sup>3, 13, 14</sup> DGpp films deposited in this work also have the trend that increasing load power leads to a higher introduction of neutral hydrocarbon species (C-C/C-H) and a decreased retention of C-O ether and alcohol functional groups (Figure 3.1, a). To further analyse the chemistry of the DGpp films, determining whether the terminal chains are orientated at molecular level and distinguishing the various resonances arising from the unsaturated species, NEXAFS spectroscopy was utilised to collect carbon and oxygen K-edge spectra.

The four main resonance features of the C 1s spectra, including C 1s  $\rightarrow$   $\pi^*$  (C=C) excitation at 285.2 eV, C 1s  $\rightarrow$   $\sigma^*$  (C-H) at 286.8 eV, C 1s  $\rightarrow$   $\sigma^*$  (C=O) at 289.3 eV and finally a broader C 1s  $\rightarrow$   $\sigma^*$  (C-C, C-O) feature above 293.1 eV are shown in figure 3.2. A comparison of the five NEXAFS C 1s spectra indicated, in accordance with XPS data, that films deposited at higher load power have a higher amount of hydrocarbon (C-H) and unsaturated (C=C) species. To test for possible orientation of polymer chains at the surface of the DGpp films, 50 W deposited thin films were analysed additionally at 45 °

with respect to the sample surface. Same spectra features were seen compared with spectra obtained at 90 °, indicating an amorphous and crosslinked nature of the plasma polymer films.

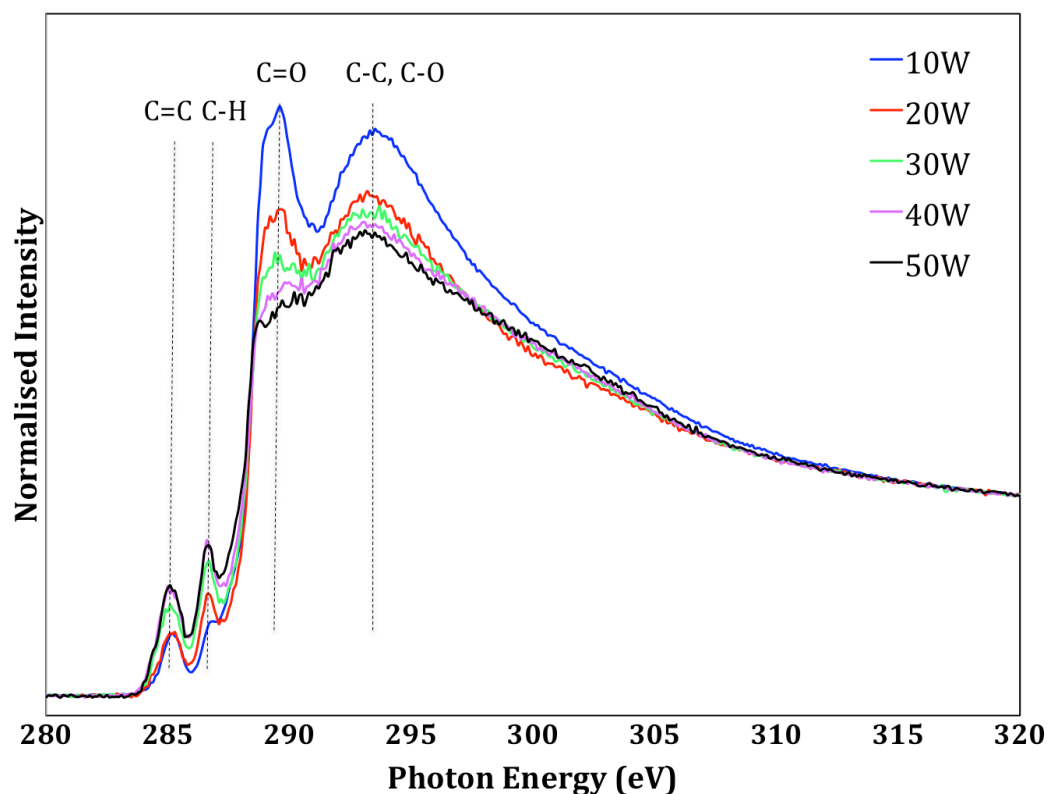


Figure 3.2, Carbon 1s K-edge TEY NEXAFS spectra of DGpp films deposited at 10, 20, 30, 40 and 50 W load powers on copper. The peaks for C 1s spectra are: C=C  $\pi^*$ , C-H  $\sigma^*$ , C=O  $\sigma^*$ , and C-C, C-O  $\sigma^*$ .

### 3.3.2 Protein resistance of uniform DGpp films

To demonstrate the ability of the uniform DGpp films to resist non-specific protein adsorption, 20 and 50 W load powers produced thin films were selected for analysis. The films were deposited onto Si wafer, then incubated in solutions of mES cell culture medium, which contains 15 % fetal bovine serum (FBS). The absence of elemental nitrogen in the DGpp films (confirmed by use of a control), allows the use of XPS elemental survey analysis to examine protein adsorption on these films. Results presented in Table 3.2 shows that DGpp films deposited under 20 W load power adsorbed less protein (on average 3 % less) than those deposited under 50 W load powers. The results correlate with film chemistry, the retention of higher residual ether content in 20 W films compared with that of 50 W coatings leads to low-fouling.

Samples placed in 37 °C water bath adsorbed 2 % more protein as compared to those incubated at room temperature. Longer incubation times results in a higher concentration of protein adsorbed on all the films. However, 24 h incubation in mES cell culture media also led to the delamination of 20 W load power deposited films (presents of Si signal in XPS survey). Especially, increasing the incubation temperature dramatically decreased the film adhesion strength on the Si wafer substrate.

Table 3.2, Elemental composition (atomic %) of 20 and 50 W DGpp films deposited on Si wafers after protein adsorption derived from XPS survey spectra.

<b>Room temperature</b>				
Atomic %	<b>20 W 2 h</b>	<b>20 W 24 h</b>	<b>50 W 2 h</b>	<b>50 W 24 h</b>
O 1s	26.9 ± 0.1	25.1 ± 0.3	21.0 ± 0.1	20.9 ± 0.0
N 1s	2.5 ± 0.1	3.8 ± 0.3	5.6 ± 0.5	7.5 ± 0.1
C 1s	70.7 ± 0.0	70.8 ± 0.5	73.5 ± 0.6	71.6 ± 0.1
Si 2p	-	0.3 ± 0.1	-	-
<b>37 °C incubation</b>				
	<b>20 W 2 h</b>	<b>20 W 24 h</b>	<b>50 W 2 h</b>	<b>50 W 24 h</b>
O 1s	25.6 ± 0.3	23.2 ± 2.4	21.0 ± 0.2	20.7 ± 0.2
N 1s	4.4 ± 0.3	2.3 ± 0.9	7.4 ± 0.0	8.5 ± 0.0
C 1s	70.0 ± 0.5	22.7 ± 3.6	71.6 ± 0.2	70.8 ± 0.2
Si 2p	-	51.8 ± 5.1	-	-

Real time protein adsorption was monitored using QCM-D, where mES cell culture medium (same batch as in above static adsorption) was flowed through chambers containing gold crystals coated with DGpp films. The frequency response is correlated to mass change on top of the 20 and 50 W plasma polymer films. Again, the level of protein adsorption increased with rising plasma deposition power, as seen in figure 3.3. Furthermore, the fluctuation of frequency during media incubation is a strong indication that the films were not stable when submerged in those solutions at physiological temperature.

It was clear at this point that DGpp film had poor adhesion on the Si wafer and gold quartz crystal after it was incubated in PBS for a prolonged time at 37 °C. One solution is to deposit multilayer plasma polymers to increase the stability of DGpp. For example, allalyimine (AA) has been used as a pre-coating; and the system showed no sign of film delamination (data not shown). Alternatively, the DGpp films can be deposited onto polymeric substrates, which also gives rise to strong adhesion and retention of the films after incubation in cell culture media. In the following chapters, polymeric substrates were used most frequently for *in vitro* biological tests.

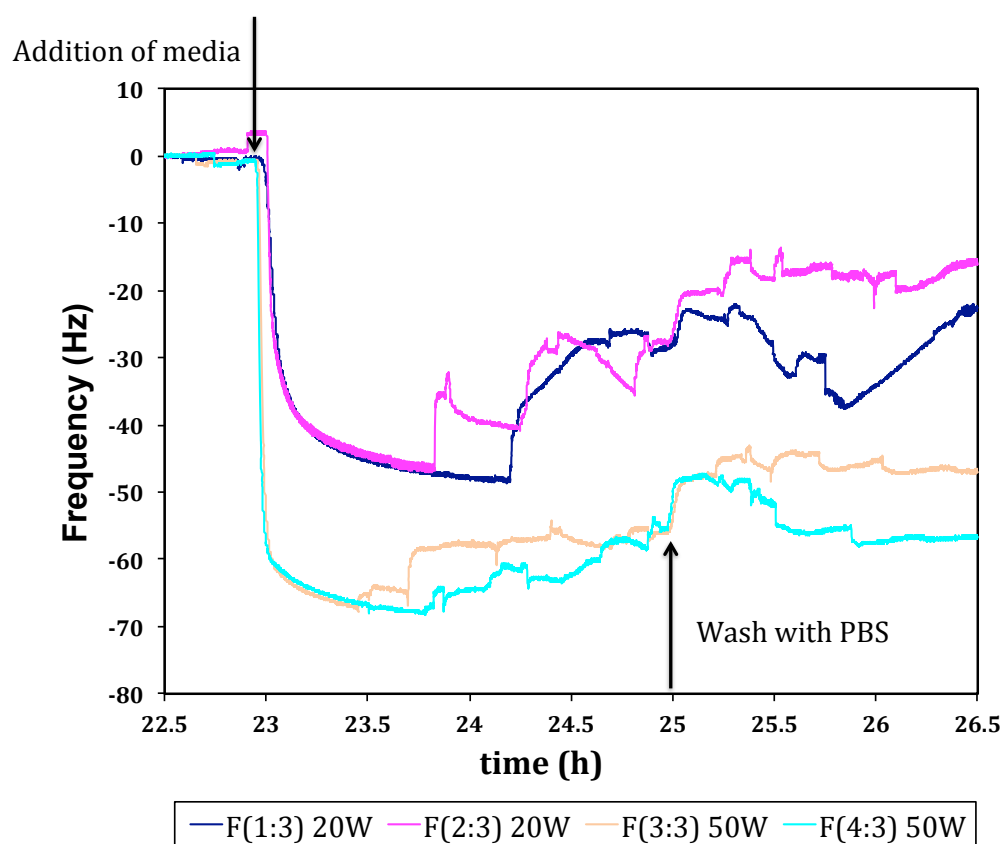


Figure 3.3, QCM-D frequency response of the third overtone on the 20 and 50 W plasma polymer films after incubation with mES media for 2 h (all sensors were hydrated in PBS overnight). F(1:3) denotes the 3 harmonic frequency response from crystal located in chamber 1, F (2:3) from chamber 2, and so forth. The arrows indicate when the mES media and PBS solution were flowed over the coated crystal.

From these investigations, it is clear that differences in ether content induced various amounts of protein adsorption. The next step was to examine the ability of these DGpp films to control cell and microorganisms adhesion. For cell attachment studies, both uniform and micropatterned DGpp films were used. For uniform DGpp coatings, the

results are discussed in **Appendix 3**. In this chapter, the spatial control of cell attachment by chemically patterned DGpp films is presented (section 3.3.3). For microbe attachment studies, DGpp films deposited from 5, 10, 20 and 50 W were evaluated (section 3.3.4).

### 3.3.3 Micropattern produced by plasma polymerisation

A DGpp thin film that had spatial variation in ether content was produced in one step by employing a patterned electrode, as shown in figure 3.4. The features produced are the same size as the open holes in the upper electrode with good fidelity. The 'PEG-like' character of the surface increased radically from the centre of the patterned spots. That is to say the centre contains less ether and it was found that protein adsorption was highest within the centre of the circles. Also after 7 days incubation in culture medium only the central area of the circles contain proteins.

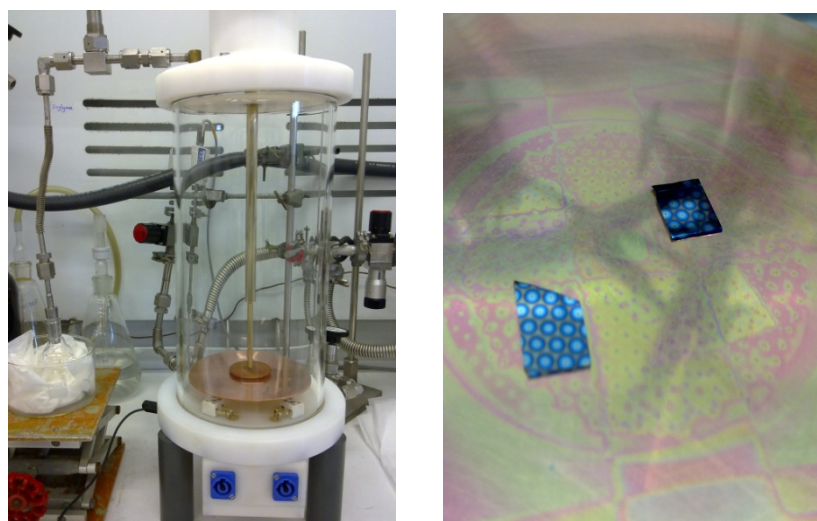


Figure 3.4, On the left, reactor configuration for the deposition of micropatterned DGpp surfaces. The patterned upper electrode is brought to 1 mm above the substrate upon which the patterns are to be deposited. The patterned holes allow a variation in density of the plasma sheath and result in chemically patterned surfaces in one step. On the right, the resultant pattern on two pieces of Si wafer substrates.

XPS confirmed the spatial variation of the surface chemistry, specifically the C-C and C-O-R bonds fluctuated across the pattern area. The percentage of the different chemical bonds were obtained through fitting of high resolution C 1s spectra, the same as

described in section 3.3.1. Figure 3.5 illustrates the chemical pattern produced by an electrode with arrays of 2 mm open holes. Underneath the centre of the holes, lower percentage of C-O-R is retained, while hydrocarbon content increased. For regions in between the open holes, the chemistry has the opposite trend. Notably, the highest ether concentration is below 50 % of the total C species, which is not typical for that of uniform 5 W deposited DGpp films (> 70 %). This could be due to the distance between the electrodes was too small in this pattern production ( $D = 1$  mm), therefore, the generated plasma had higher density compared with uniform DGpp film deposition (where  $D = 10$  cm) that results in more fragmentation. By changing the size of the holes, smaller patterns can also be made. Figure 3.6 presents the cell colonies formed on a 1 mm patterned DGpp film by an adherent mouse fibroblast cell line after 48 h incubation.

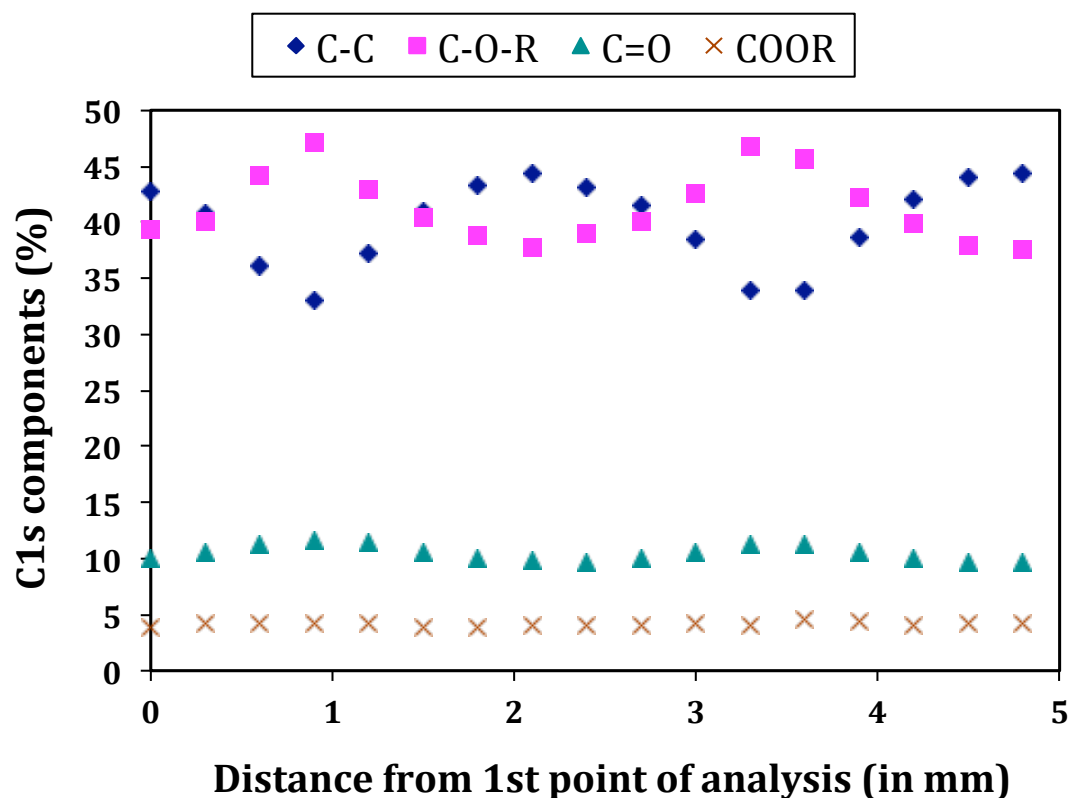


Figure 3.5, Relative percentage of C 1s components of DGpp film produced from patterned electrode (with 2 mm open holes). The starting point is randomly selected from the surface, and then 0.3 mm step interval was used to measure the next point straight down from the 1<sup>st</sup> spot, and so forth. Some points go through the middle of the patterned features.

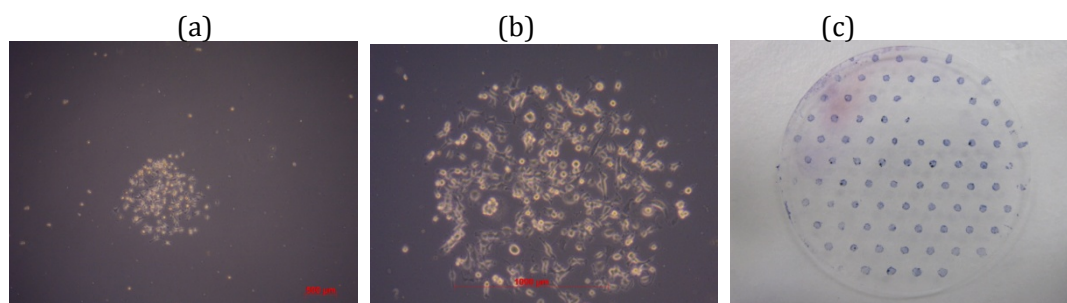


Figure 3.6, Phase contrast images of spatially confined SNL cells after 48 h incubation, using (a) 4 X and (b) 10 X objectives; (c) Image of the Thermanox™ coverslip (25 mm in diameter) with patterned SNL cell colonies. The cell nuclei were stained blue with hematoxylin.

In contrast to protein absorption, the patterned films showed that a relatively small change in ether content can make a big difference in cell adhesion. Although, a more comprehensive characterisation of the patterned films, e.g. thickness variation, modulus change, crosslinking, etc., may or may not reinforce this observation. Later on in this thesis, patterned films were not pursued further. Only because the pattern *per se* will greatly increase the analytical difficulty if using the methods proposed in the following chapters, hence, uniform DGpp films and other types of pp films were used.

### 3.3.4 Antimicrobial property of DGpp films

As overviewed in chapter 2, biomaterials and biomedical devices are potent targets for pathogenic microorganisms. In ‘the race to the surface’, mammalian cells and microbes compete with each other to colonise a material surface.<sup>15</sup> Once bacteria or fungi species become established before host cells, and form a biofilm, the consequence can be risky. Therefore, a constant research endeavour is to study surfaces that resist microbe attachment, thus preventing biofilm formation. PEG and PEG-like films have been tested frequently for antimicrobial applications. In this thesis, DGpp films were examined against clinically relevant bacterial pathogens, *Staphylococcus epidermidis* and *Pseudomonas aeruginosa*, and a fungal pathogen *Candida albicans*.

DGpp films were deposited onto TCPS 96-well microplates directly. The bottom of the well was cut-out using a drill after film deposition and analysed by XPS to confirm the chemistry change. Due to the large size of the microplates, and the insulation effect of

polymer, film growth is much slower compared with the deposition speed on the Si wafer. Therefore, to completely cover up the chemical signals from TCPS, longer deposition times were chosen during DGpp coating procedures. A range of DGpp films were prepared at four load powers to generate different ether concentration at the surface.

Figure 3.7 is the quantitative results showing the biofilm formation of DGpp treated surfaces relative to TCPS control. Amongst the three microorganisms tested in this study, *P. aeruginosa* displayed excellent growth not only on TCPS control but also all of the DGpp treated surfaces. In contrast, a significant reduction was found with 5 W DGpp coated plate, where *S. epidermidis* and *C. albicans* fail to form a biofilm (maximum 2 days cell culture experiments).

DGpp deposited at 50 W which contained low C-O groups, showed no difference in number of microorganisms attachment to the surface compared with the TCPS control. Interestingly, DGpp coatings obtained at 20 W load power, where C-O content is at least 50 % higher than that of 50 W DGpp films, the same amount of bacteria and fungi growth were found. This indicates that the mechanism of microorganism attachment is different from that of protein adsorption. When load power was reduced further to 10 W, the DGpp films produced gained the ability to prevent *S. epidermidis* biofilm formation. However, 10 W DGpp films did not resist *P. aeruginosa* and *C. albicans* attachment and growth.

For the 5 W DGpp film treated surfaces, cell viability was assessed by staining with reagents and imaged with confocal laser scanning microscopy (CLSM). Figure 3.8 shows the CLSM images for all three microbial species attached on TCPS and 5 W DGpp coated samples.

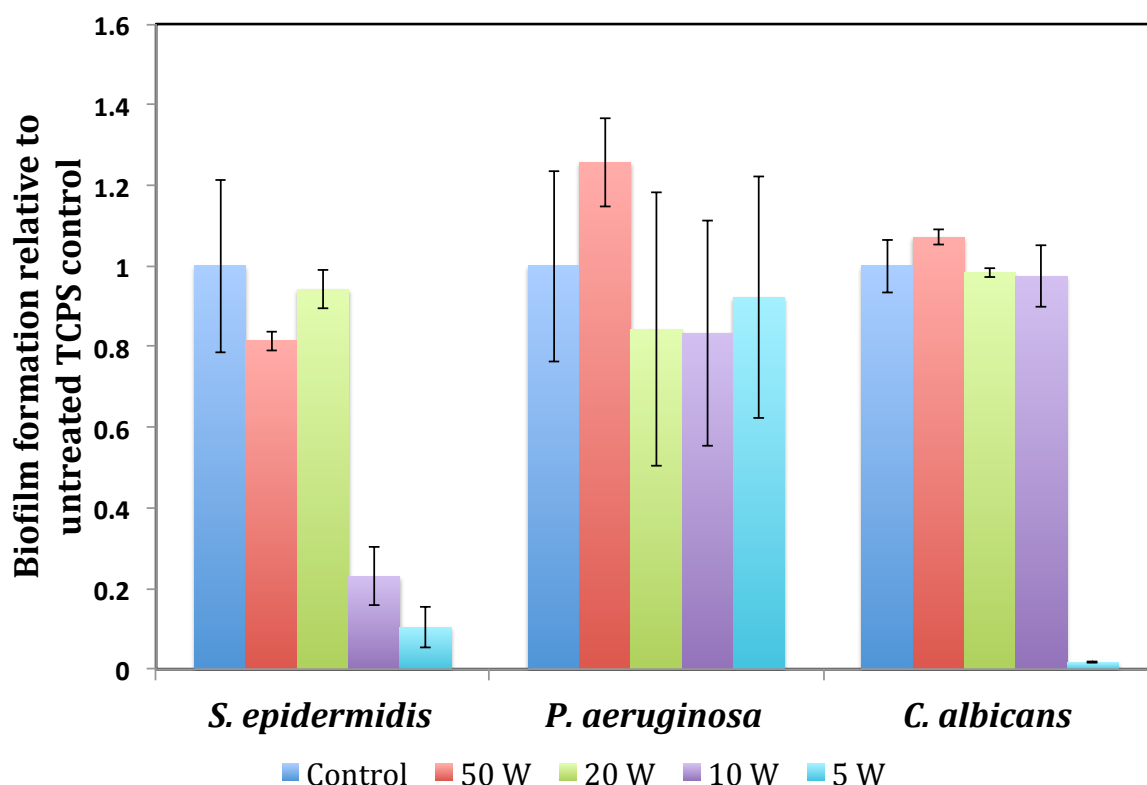


Figure 3.7, Biofilm formation of three representative microorganisms on surfaces receiving different treatments relative to the TCPS control. Biofilms of *S. epidermidis* were grown in TSB medium at 37 °C for 18 h with agitation (75 rpm). Biofilms of *P. aeruginosa* were grown in LB medium 37 °C for 18 h with agitation (75 rpm) and *C. albicans* biofilms were grown in Spider medium 37 °C for 48 h with agitation (75 rpm). Biofilm production on different surfaces was assessed by a crystal violet staining assay and represented as percentage relative to that grown on the TCPS control. There are considerable differences in the amount of *C. albicans* and *S. epidermidis* attached to the 5 W DGpp treated surfaces from the TCPS control.

In the case of *S. epidermidis*, there was a large amount of dead cells on 5 W DGpp coated substrates. For *P. aeruginosa*, large numbers of dead bacteria were found on the TCPS substrate but were not present on the 5 W DGpp surface, although the average number of live cells was the same. For *C. albicans* strain studied, relatively few viable cells were attached to the surface to form colonies compared with the TCPS control. Unfortunately, if the DGpp coated micrplates were stored for one-week in cell culture media prior to bacterial or fungal seeding, the ability to resist biofilm formation would be lost. This suggests that low-fouling DGpp coatings resists initial bacterial and fungal attachment, and possibly delay biofilm formation but not efficient in the long term. Other studies employing DGpp coatings for antibacterial purpose has tested *P. aeruginosa* only, and the results are the same as reported here.<sup>16, 17</sup> There is no significant difference in

bacterial number between control samples and DGpp coated ones. In order to find a surface chemistry that resists a broad spectrum of clinically relevant bacterial and fungal pathogens, another plasma polymer film was used and the results are reported later in the thesis (**Chapter 7**).

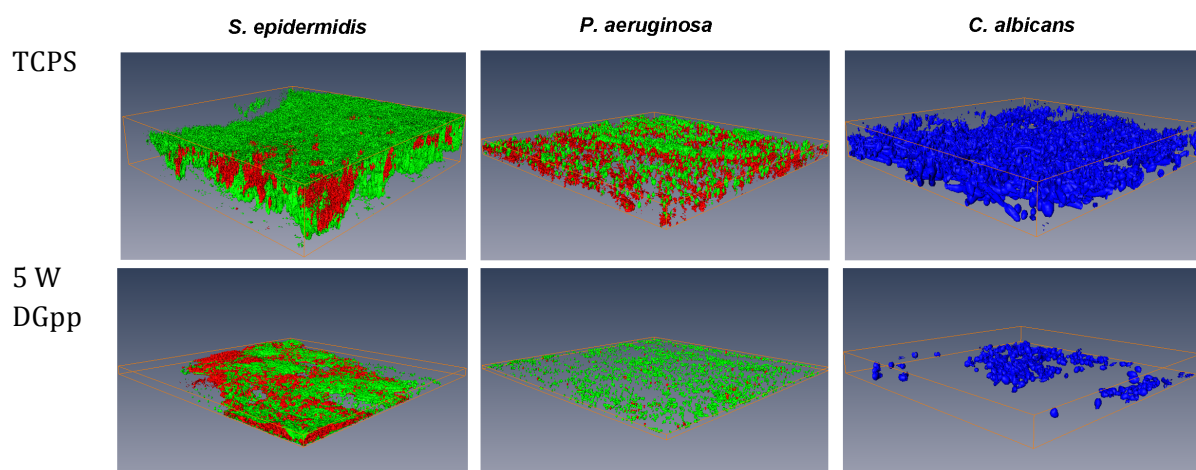


Figure 3.8, Confocal laser scanning microscopy (CLSM) of biofilms produced by *S. epidermidis*, *P. aeruginosa* and *C. albicans* on surfaces of TCPS and 5 W DGpp coated TCPS. Biofilms of *S. epidermidis* and *P. aequinosa* were grown for 18 h in TSB and LB respectively, and then stained with SYTO-9 (bright green for live cells) and PI (red or orange, or loss of bright green for dead cells). Biofilms of *C. albicans* were grown for 48 h in Spider medium, and then stained with calcofluor white (1 mg/ml for 1 minute). 3D structure of biofilms was reconstructed with software Amira 5.4. 1.

### 3.4 Conclusions

The functional group retention in a plasma polymer film is dependent on the process parameters. Provided that all other factors are fixed, increasing the load power leads to more forceful fragmentation of the precursor molecules, thus greater loss of the original functional groups. Herein, DGpp films were used to demonstrate this effect, where the concentration of ether and hydrocarbon groups can be manipulated easily. The resultant DGpp coatings showed differences in their capability to resist protein adsorption, cell adhesion and microbe attachment. However, there was no universal DGpp surface chemistry that prevented the fouling of all microbial species tested. Therefore, other antimicrobial plasma polymer films were exploited in this thesis. On the other hand, DGpp films deposited on several substrates, such as Si wafer, copper,

gold crystal and TCPS, displayed considerable differences in film growth speed and stability in cell culture conditions. This means that the plasma polymerisation process is substrate dependent and the physicochemical properties of the resultant films are different. A closer look at the substrate-film interactions is necessary to decipher the mechanisms of film growth and guide future designs of process parameters. In the following chapters, the interactions of DGpp films with glass, plasma polymer films and amyloid fibril network coated substrates are reported

### 3.5 Reference

1. G. P. López, B. D. Ratner, C. D. Tidwell, C. L. Haycox, R. J. Rapoza and T. A. Horbett, *Journal of Biomedical Materials Research*, 1992, 26, 415-439.
2. F. Brétaganol, M. Lejeune, A. Papadopoulou-Bouraoui, M. Hasiwa, H. Rauscher, G. Ceccone, P. Colpo and F. Rossi, *Acta Biomaterialia*, 2006, 2, 165-172.
3. B. W. Muir, A. Tarasova, T. R. Gengenbach, D. J. Menzies, L. Meagher, F. Rovere, A. Fairbrother, K. M. McLean and P. G. Hartley, *Langmuir*, 2008, 24, 3828-3835.
4. D. J. Menzies, A. Nelson, H.-H. Shen, K. M. McLean, J. S. Forsythe, T. Gengenbach, C. Fong and B. W. Muir, *Journal of The Royal Society Interface*, 2012, 9, 1008-1019.
5. A. Choukourov, I. Gordeev, D. Arzhakov, A. Artemenko, J. Kousal, O. Kylián, D. Slavínská and H. Biederman, *Plasma Processes and Polymers*, 2012, 9, 48-58.
6. D. J. Menzies, M. Jasieniak, H. J. Griesser, J. S. Forsythe, G. Johnson, G. A. McFarland and B. W. Muir, *Surface Science*, 2012, 606, 1798-1807.
7. B. C. C. Cowie, A. Tadich and L. Thomsen, *AIP Conference Proceedings*, 2010, 1234, 307-310.
8. B. Watts, L. Thomsen and P. C. Dastoor, *Journal of Electron Spectroscopy and Related Phenomena*, 2006, 151, 105-120.
9. M. A. Deighton, J. Capstick, E. Domalewski and T. van Nguyen, *Methods in enzymology*, 2001, 336, 177-195.
10. Y. Jin, H. K. Yip, Y. H. Samaranyake, J. Y. Yau and L. P. Samaranyake, *Journal of clinical microbiology*, 2003, 41, 2961-2967.
11. Y. Qu, T. S. Istivan, A. J. Daley, D. A. Rouch and M. A. Deighton, *Journal of Medical Microbiology*, 2009, 58, 442-450.

12. J. Chandra, P. K. Mukherjee and M. A. Ghannoum, *Nat. Protocols*, 2008, 3, 1909-1924.
13. D. J. Menzies, A. Nelson, H.-H. Shen, K. M. McLean, J. S. Forsythe, T. Gengenbach, C. Fong and B. W. Muir, *Journal of The Royal Society Interface*, 2012, 9, (70), 1008-1019.
14. A. Choukourov, I. Gordeev, O. Polonskyi, A. Artemenko, L. Hanyková, I. Krakovský, O. Kylián, D. Slavínská and H. Biederman, *Plasma Processes and Polymers*, 2010, 7, 445-458.
15. A. G. Gristina, P. Naylor and Q. Myrvik, *Medical progress through technology*, 1988, 14, 205-224.
16. E. Johnston, B. Ratner and J. Bryers, *NATO ASI Series E Applied Sciences-Advanced Study Institute*, 1997, 346, 465-476.
17. D. J. Balazs, K. Triandafillu, E. Sardella, G. Iacoviello, P. Favia, R. d'Agostino, H. Harms and H. J. Mathieu, in *Plasma Processes and Polymers*, Wiley-VCH Verlag GmbH & Co. KGaA, 2005, DOI: 10.1002/3527605584.ch26, pp. 351-372.

## PART B: Suggested Declaration for Thesis Chapter

[This declaration to be completed for each conjointly authored publication and to be placed at the start of the thesis chapter in which the publication appears.]

### Monash University

#### Declaration for Thesis Chapter 4

##### Declaration by candidate

In the case of Chapter 4, the nature and extent of my contribution to the work was the following:

Nature of contribution	Extent of contribution (%)
Experimental design, conduct, data processing and writing	

The following co-authors contributed to the work. If co-authors are students at Monash University, the extent of their contribution in percentage terms must be stated:

Name	Nature of contribution	Extent of contribution (%) for student co-authors only
<b>Benjamin W. Muir</b>	Assisted in planning, experimental design and manuscript correction	N/A
<b>Christopher D. Easton</b>	Assisted in experiment	N/A
<b>Lars Thomsen</b>	Assisted in experiment	N/A
<b>David R. Nisbet</b>	Manuscript correction	N/A
<b>John S. Forsythe*</b>	Assisted in planning, experimental design and manuscript correction	N/A

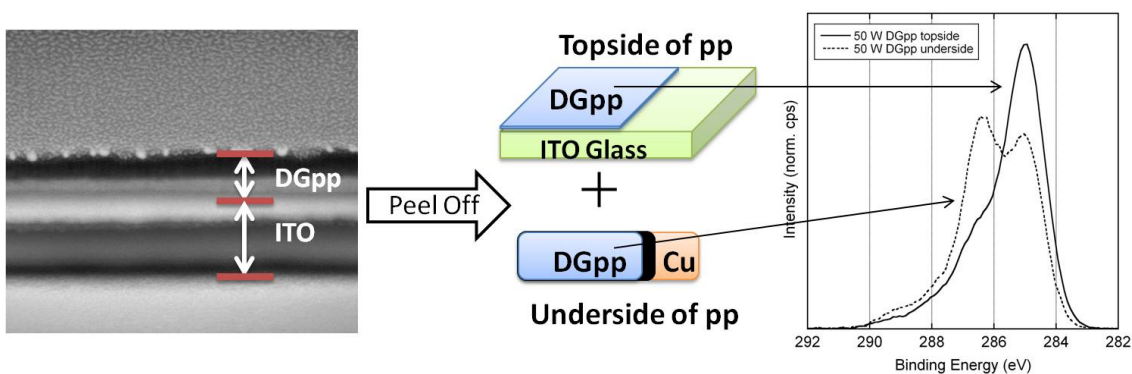
The undersigned hereby certify that the above declaration correctly reflects the nature and extent of the candidate's and co-authors' contributions to this work\*.

<b>Candidate's Signature</b>		<b>Date</b>
------------------------------	--	-------------

<b>Main Supervisor's Signature</b>		<b>Date</b>
------------------------------------	--	-------------

\*Note: Where the responsible author is not the candidate's main supervisor, the main supervisor should consult with the responsible author to agree on the respective contributions of the authors.

## Chapter 4 Diglyme film chemistry at substrate-film interface



*"Leave no stone unturned"*  
- English Proverb

**Abstract\***

The chemistry of substrate-film interface (underside) of di(ethylene glycol) dimethyl ether plasma polymer (DGpp) films has been studied directly and compared to the top layer of the film (topside). By depositing the plasma polymer films onto indium tin oxide (ITO) glass, the films were easily delaminated from the substrate. The top- and underside of the films were examined by X-ray photoelectron spectroscopy (XPS) and near edge X-ray absorption fine structure (NEXAFS) spectroscopy. It was found that a rapid increase in pressure during plasma polymerisation resulted in steep chemical gradients in the films, while small pressure changes did not lead to chemical gradient formation. These observations validated the findings of previous neutron reflectometry modeling studies of this class of plasma polymer thin film. In addition, subtle variations in plasma polymer film chemistry were observed between different substrates they were deposited onto. This approach will allow additional studies on the mechanisms of early plasma polymer thin film formation with various monomers.

\*Reproduced with permission from Elsevier. Yali, Li; Benjamin, W. Muir; Christopher, D. Easton; Lars, Thomsen; David, R. Nisbet; John, S. Forsythe, A study of the initial film growth of PEG-like plasma polymer films via XPS and NEXAFS. *Applied Surface Science* 288 (2014), 288-294. Copyright © 2013 Elsevier Inc

<http://dx.doi.org/10.1016/j.apsusc.2013.10.022>

## 4.1 Introduction

In the past two decades, there has been an increasing interest in the use of plasma polymer (pp) thin films for selective surface modification.<sup>1-3</sup> The plasma polymerisation process is a versatile technique to deposit thin coatings with various properties and chemical functionalities, such as amines,<sup>4, 5</sup> aldehydes<sup>6</sup> and carboxylic acids.<sup>7</sup> Low fouling surfaces can also be created by polymerising ether containing monomers such as those of the glyme family.<sup>8-11</sup> During the plasma thin film deposition process, complex chemical reactions occur under the influence of the monomer, the substrate and the process conditions.<sup>8, 12-14</sup> Ongoing research is being conducted to gather further knowledge about the plasma glow discharge reaction mechanisms that take place during the initial stages of thin film growth. Different spectroscopic<sup>15-20</sup> and diagnostic tools<sup>21-26</sup> (e.g., Langmuir probes, mass and optical spectrometry, laser-induced fluorescence, X-ray photoelectron spectroscopy (XPS), near-edge X-ray absorption fine structure spectroscopy (NEXAFS) and neutron reflectometry) have been employed to shed light on the bulk glow discharge processes and plasma-substrate interactions.

Most attention has been given to the investigation of applied plasma parameters and gases on film structure, chemistry and composition. However, significant information can also be obtained by investigating the influence of the substrate, which has not been reported widely in the field. A study by Lo et al. investigated plasma polymerised SiOCH films formed on different substrates and showed hemispherical macrostructures. The pp thin film deposition rate was dependent on the porosity-related properties of the underlying substrate material.<sup>27</sup> Other groups have investigated the effect of cross-link density,<sup>28</sup> optical properties<sup>29</sup> and specific functionalities of the pp films produced and the affect of the substrate interface in the initial growth stages of pp thin films.<sup>30-32</sup> It has proven difficult to directly characterise the chemistry of the substrate-plasma polymer interface without ambiguity in results or artifacts from the various characterisation techniques employed. One approach is to deposit ultrathin pp films (<10 nm) and examine their chemistry and morphology at the substrate interface via XPS and infrared spectroscopy (IR).<sup>4, 33-36</sup> However, there are associated limitations with this method as

the chemical information of the top- and underside of the films are collected together indiscriminately due to analytical depth of XPS and IR spectroscopy. As such, another commonly used approach is to perform thin film depth profile measurements, which effectively bombards the surface and etch away the film.<sup>37-39</sup> It is not surprising that this method induces artifacts in surface chemistry.<sup>40</sup> Previously, we have deposited plasma polymers on salt crystals and shown they can be delaminated in order to analyse the underside of brominated and aminated pp thin films.<sup>41</sup> Here, we have developed a delamination procedure that can lift the film away from an underlying indium tin oxide (ITO) coated surface thus allowing us to directly analyse the underside of pp thin films deposited from di(ethylene glycol) dimethyl ether (DG). Although the factors that alter the adhesion strength of pp films on different substrates are not well understood,<sup>42</sup> this simple delamination process that has been developed by our group allows the underside of the films to be analysed.

This work reports on the characterisation of the top- and underside of di(ethylene glycol) dimethyl ether plasma polymer films (DGpp), via delamination from an ITO glass substrate. The use of diglyme to generate low-fouling (PEG-like) films via plasma polymerisation has been widely studied for biomedical applications.<sup>43-45</sup> Our group has reported on one-step generation of DGpp films that can produce chemical gradients and micropatterns with good fidelity for cell culture studies.<sup>46, 47</sup> Moreover, a mass density model of the DGpp films produced under several load powers has been proposed using neutron reflectometry data indicating a dependence of chemistry and cross-linking on the plasma power during radio frequency glow discharge (RFGD) plasma polymerisation.<sup>48</sup> Herein, chemical and structural analysis of the top- and underside of the DGpp films were carried out using XPS and NEXAFS. NEXAFS spectroscopy has become a routine method for organic thin film analyses due to its sensitivity in distinguishing different types of unsaturated bonds. The results obtained from XPS and NEXAFS provide a chemical confirmation to the density model of DGpp films previously reported by our group and demonstrate the wider applicability of this simple delamination technique in probing the substrate-plasma polymer interface.

## 4.2 Materials and methods

### 4.2.1 Substrate preparation

Ultra-flat single crystal silicon wafers (<100>, 1 cm<sup>2</sup> x 0.5 mm thick, M.M.R.C P/L) and indium tin oxide (ITO) coated (single sided) aluminosilicate glass, (1.1 mm thick, Delta Technologies, Corning 1737, CB-50IN) were used as substrates for the deposition of di(ethylene glycol) dimethyl ether (BDH, 99 % purity) plasma polymer films. All substrates were cleaned immediately prior to plasma polymer deposition by ultrasonication in a surfactant solution of 2 % ethanol with 2 % RBS-35 (Pierce, U.S.A.) for 30 min, followed by multiple rinsing with Milli-Q water and finally dried in a high-pressure stream of high purity nitrogen (BOC Gas, Australia).

### 4.2.2 Plasma polymerisation

Deposition of DGpp thin films was carried out in the custom-built plasma reactor as described in **chapter 3**. The parameters chosen for the RFGD (200 KHz) deposition of DGpp films were load powers of 20 and 50 W with an initial monomer pressure of 20 Pa for a treatment time of 180 seconds, with final pressures of 41 and 65 Pa, respectively. The monomer flow rate calculated by application of equation 1 was estimated to be around 10 standard cm<sup>3</sup> per min for the diglyme used in all plasma depositions.

$$F = ( dp / dt ) \times 16172 V / T \quad [1]$$

where F = flow rate (cm<sup>3</sup> / min)

p = pressure (mbar)

t = time (s)

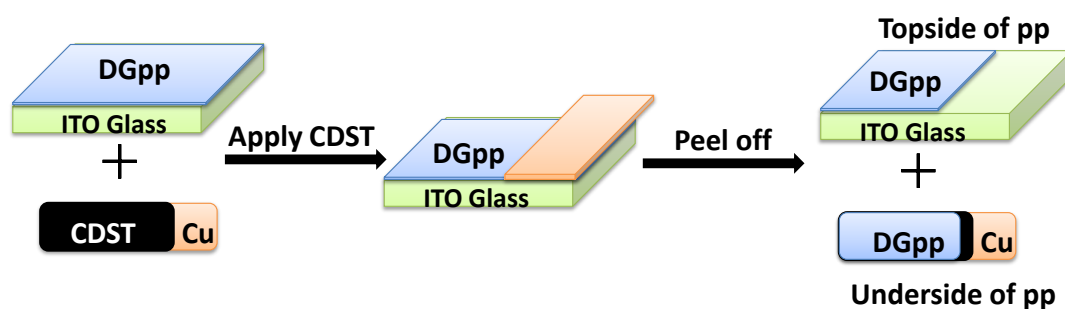
V = volume of the plasma reactor

T = temperature (room temperature = 293 K)

After deposition, the reactor was immediately pumped down to base pressure before venting. The samples were stored in clean tissue culture grade petri dishes under ambient conditions until further analysis. To account for batch to batch variations, the experiments were repeated 3 times on different days.

#### 4.2.3 Plasma polymer delamination procedure

Conductive double sided carbon adhesive tape (CDST) (SPI supplies) was stuck onto small thin sheets of copper (0.5 x 1 mm). This allowed the tape to be easily handled and analysed under XPS and NEXAFS spectroscopy. The tape was lightly and briefly applied onto a section of freshly deposited DGpp films on the ITO glass substrate. The tape was then removed, inverting and exposing the underside of the DGpp section (Scheme 4.1). This delamination process is a mechanical method to remove the DGpp from the ITO glass. No chemical reactions occur in the process hence there is no possibility of changes in film composition. The result of delamination was confirmed with XPS analysis of the delaminated area in comparison to the bare ITO substrate (see **Appendix 1**).



Scheme 4.1, Schematic illustration of the procedure used to expose the underside of the plasma polymer film by delamination from ITO glass using conductive double sided tape (CDST). CDST was applied onto a thin sheet of copper for easy handling and to prevent charging during spectroscopic analysis.

#### 4.2.4 X-ray photoelectron spectroscopy

XPS analysis was performed using an AXIS HSi spectrometer (Kratos Analytical Ltd, U.K.) as described in **chapter 3**. All elements presented were identified from survey spectra (acquired at a pass energy of 160 eV). In addition, high resolution C 1s spectra were obtained at a pass energy of 40 eV yielding a typical peak width (full width at half maximum) of 1.0 - 1.1 eV for polymers. For DGpp, the FWHM used for the C 1s components is typically larger than that of conventional polymers due to a greater number of chemical environments present in these films, herein, a FWHM of 1.1 – 1.5 eV was used.

#### 4.2.5 Near edge X-ray absorption fine structure spectroscopy

NEXAFS measurements were performed on the soft X-ray beamline (SXR, 14-ID) at the Australian Synchrotron.<sup>49</sup> The experimental conditions are the same as the NESAFS study in **chapter 3**. Spectra were then normalised following the method outlined by Watts et al.<sup>50</sup>

#### 4.2.6 Masking

Masked areas were prepared using a method described previously, which employed a 10 % (w/v) solution of poly(D,L-lactide) (Boehringer Ingelheim) in acetone.<sup>51</sup> One drop of the solvent was placed on top of the substrate prior to pp deposition and dried in air. Following pp, the mask was readily lifted off the substrate using tweezers without damaging the surrounding film producing well defined step heights for film thickness analysis.

### 4.2.7 Atomic force microscopy

An Asylum Research MFP-3D atomic force microscope (Santa Barbara, CA, USA) was utilized to measure film thickness, via step height analysis from tapping mode images collected with ultrasharp silicon nitride tips (NSC15 noncontact silicon cantilevers, MikroMasch, Spain). The tips used in this study had a typical force constant of 40 N/m and a resonant frequency of 320 kHz. Typical scan settings involved the use of an applied piezo deflection voltage of 0.75 V at a scan rate of 0.8 Hz.

### 4.2.8 Focused ion beam scanning electron microscopy

The thickness of DGpp films deposited on Si wafer at 50 W and on ITO glass at 50 W and 20 W was determined using a focused ion beam scanning electron microscope (FIB-SEM) (FEI Helios NanoLab 600 DualBeam FIB-SEM, Eindhoven, Netherlands). Cross-sections were milled using a focused ion beam (FIB) of Ga<sup>+</sup> ions emitted with an accelerating voltage of 30 kV at normal incidence to the sample surface. Each sample was first coated with a 0.5 μm layer of platinum deposited by the FIB at 93 pA. All cross-sections were then milled at an ion beam current of 93 pA, followed by a cleaning step at 28 pA to minimise FIB-induced artifacts in the cross-sectional images. The milled cross-sections were then imaged in situ using the SEM capability of the FIB-SEM.

## 4.3 Results and discussion

### 4.3.1 Surface chemistry on different substrates

The elemental compositions, as determined from analysis of the XPS survey spectra of DGpp films deposited at load powers 20 and 50 W, are summarised in table 4.1. The corresponding atomic ratio and quantitative results of five components fitting for high resolution carbon (C 1s) spectra are compiled in table 4.2.

Table 4.1, Elemental compositions (atomic %) DGpp films on Si wafer, the topside on ITO and underside on tape derived from high resolution XPS survey spectra.

Atomic %	C	O	Si
20 W on Si wafer	70.93 ± 0.36	28.97 ± 0.17	-
20 W – Topside ITO	70.16 ± 0.78	27.77 ± 0.80	-
20 W – Underside	70.13 ± 0.13	25.43 ± 0.33	4.22 ± 0.14
50 W on Si wafer	79.24 ± 1.99	20.77 ± 1.99	-
50 W – Topside ITO	78.66 ± 2.83	21.24 ± 2.84	-
50 W – Underside	71.36 ± 1.78	27.55 ± 0.87	1.08 ± 1.02

The atomic concentrations of carbon in the films varied from 70.1 % to 81.2 % and oxygen from 18.7 % to 29.4 %. This is consistent with previous studies on DGpp thin films.<sup>43, 48</sup> As expected, the oxygen content in the DGpp films is lower than that of the monomer. It is known that higher power glow discharges lead to greater fragmentation of gaseous precursor molecules, which leads to a lower amount of residual ether groups and conversely a greater degree of hydrocarbon species in resultant pp thin films. From this data we may conclude that the disparity in carbon and oxygen content for the 20 W films deposited on Si wafer and ITO glass is negligible, but for the 50 W films the difference is significant. However, if we study the batch to batch variations, it is more plausible that the carbon and oxygen content on the two substrates is similar. A slight difference was observed from samples made on different days (Figure 4.1).

Table 4.2, Elemental composition (atomic%) of di(ethylene glycol) dimethyl ether plasma polymer (DGpp) films derived from XPS survey spectra deposited onto Si wafers, ITO glass (Topside) and delaminated region on the tape (Underside). The theoretical monomer composition is shown for comparison. Also presented are results from quantification of the high resolution XPS C 1s spectra (atomic concentration relative to total carbon, X/C) of 20 and 50 W films, with C1 being hydrocarbons; C2 secondary shift; C3, C-O based groups (ethers and alcohols); C4, C=O and O-C-O based groups (e.g. aldehyde, ketone); C5, O-C=O based groups (e.g. acid, ester). Thickness of the films obtained using AFM and FIB-SEM techniques.

	<i>Atomic ratio (X/C)</i>					<i>Thickness</i>
	O 1s	C1+C2	C 3	C 4	C 5	nm
<b>DG monomer</b>	0.5	0.25	0.75	0.0	0.0	-
<b>20 W on Si wafer</b>	0.411 ± 0.001	0.319 ± 0.003	0.562 ± 0.010	0.100 ± 0.007	0.019 ± 0.000	150 ± 10
<b>20 W – Topside ITO</b>	0.420 ± 0.009	0.284 ± 0.016	0.602 ± 0.020	0.094 ± 0.002	0.021 ± 0.003	60 ± 10
<b>20 W – Underside</b>	0.363 ± 0.005	0.442 ± 0.007	0.478 ± 0.001	0.049 ± 0.004	0.031 ± 0.001	-
<b>50 W on Si wafer</b>	0.257 ± 0.001	0.632 ± 0.004	0.287 ± 0.003	0.050 ± 0.000	0.032 ± 0.001	180 ± 20
<b>50 W – Topside ITO</b>	0.230 ± 0.002	0.684 ± 0.002	0.244 ± 0.011	0.044 ± 0.007	0.027 ± 0.001	160 ± 20
<b>50 W – Underside</b>	0.376 ± 0.000	0.432 ± 0.002	0.460 ± 0.003	0.068 ± 0.001	0.041 ± 0.001	-

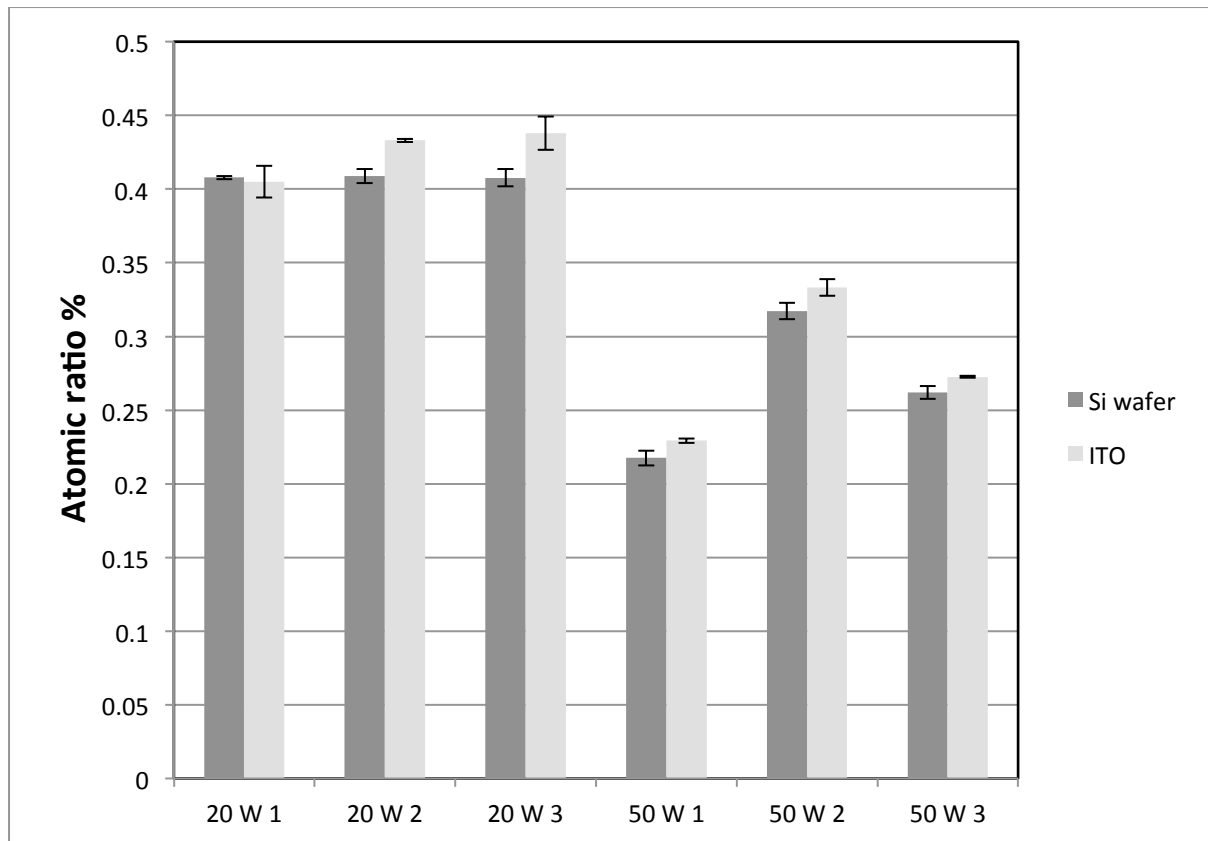


Figure 4.1, O/C ratio from DGpp films deposited onto Si wafer and ITO under 20 and 50 W conditions as stated in the paper. 1, 2, 3 denotes 3 separate experimental repeats on different days and all error bars show the standard deviation based on two analysis points.

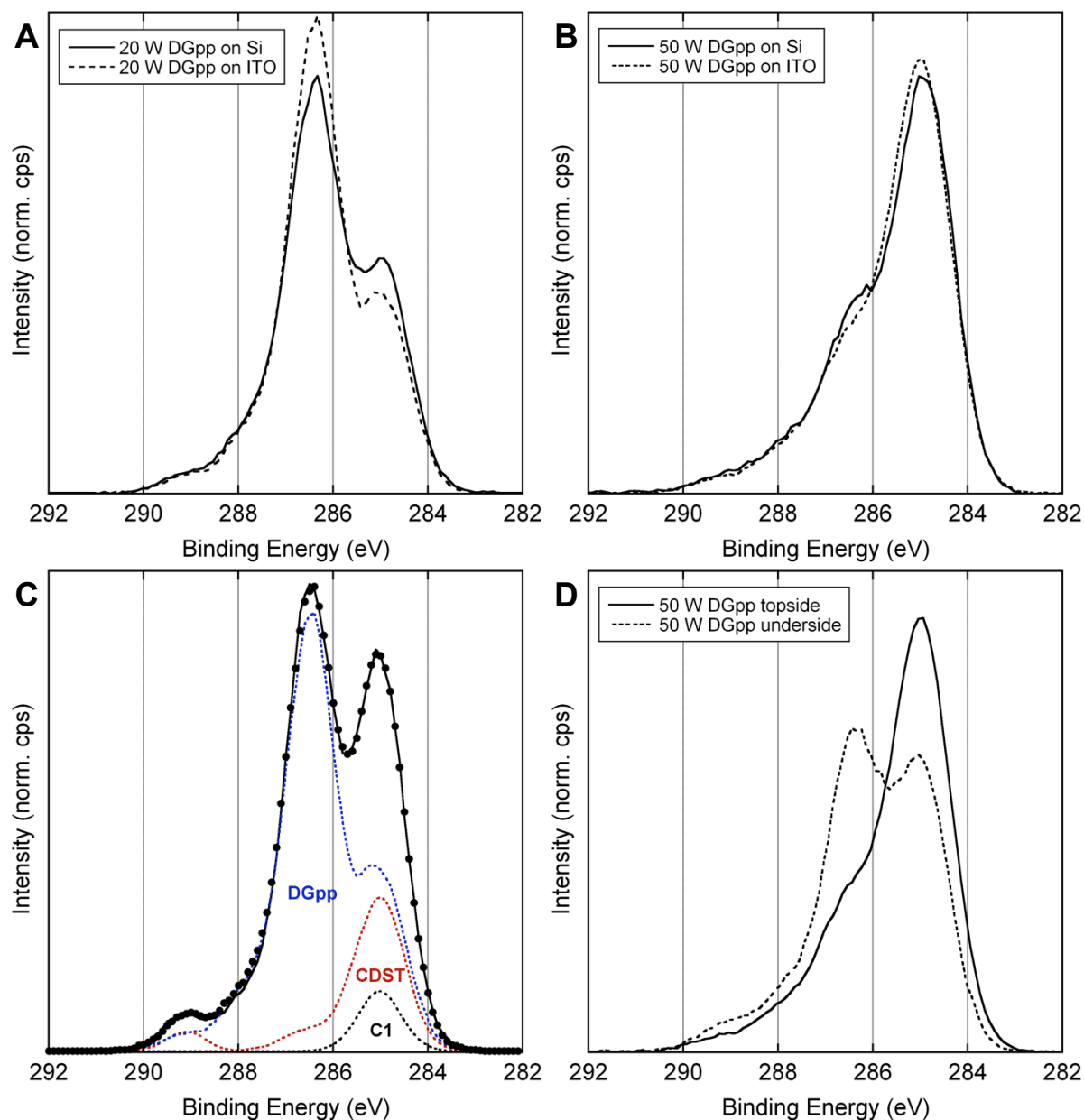


Figure 4.2, Selective, representative high resolution C 1s spectra of A) 20 W and B) 50 W DGpp film deposited on Si and ITO, respectively; C) 20 W DGpp underside spectrum fitted using a combination of model components based on experimental data (DGpp – 20 W DGpp topside, blue dotted line; and CDST, red dotted line) and standard components (C 1 – hydrocarbons, black dotted line), the black full line is the normalised data and the black dots represent the sum of the model components; D) 50 W DGpp topside and underside spectra.

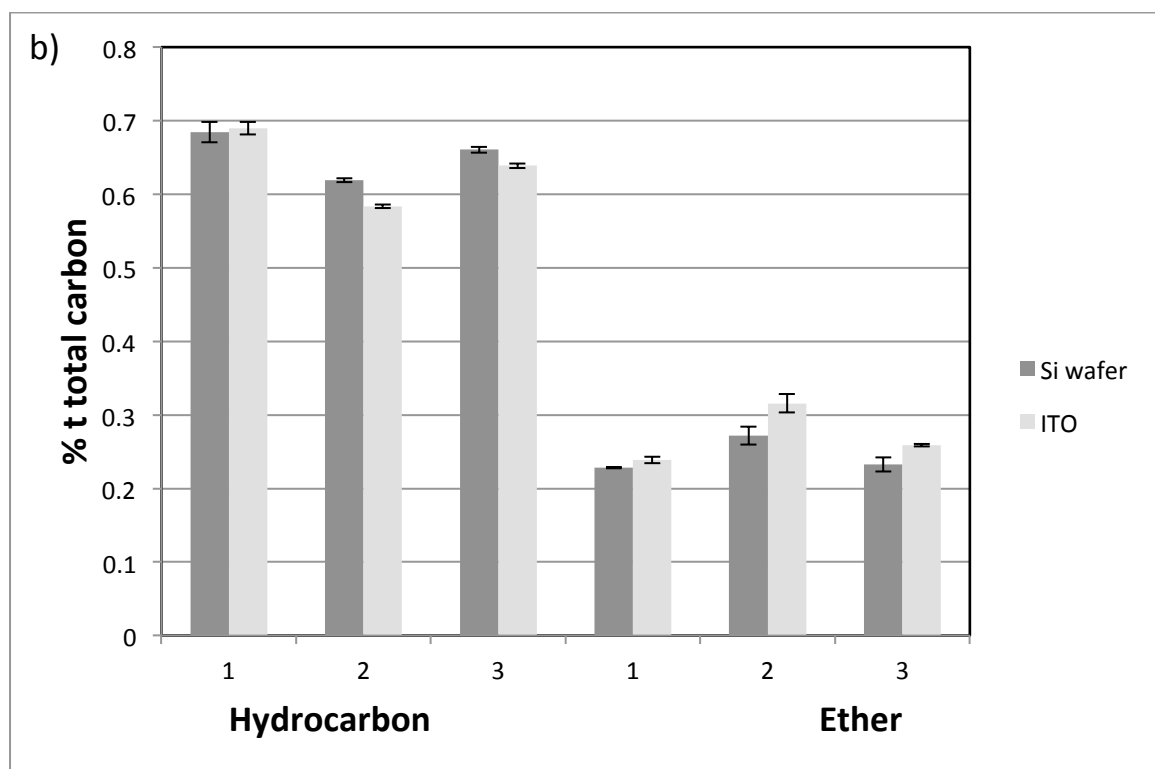
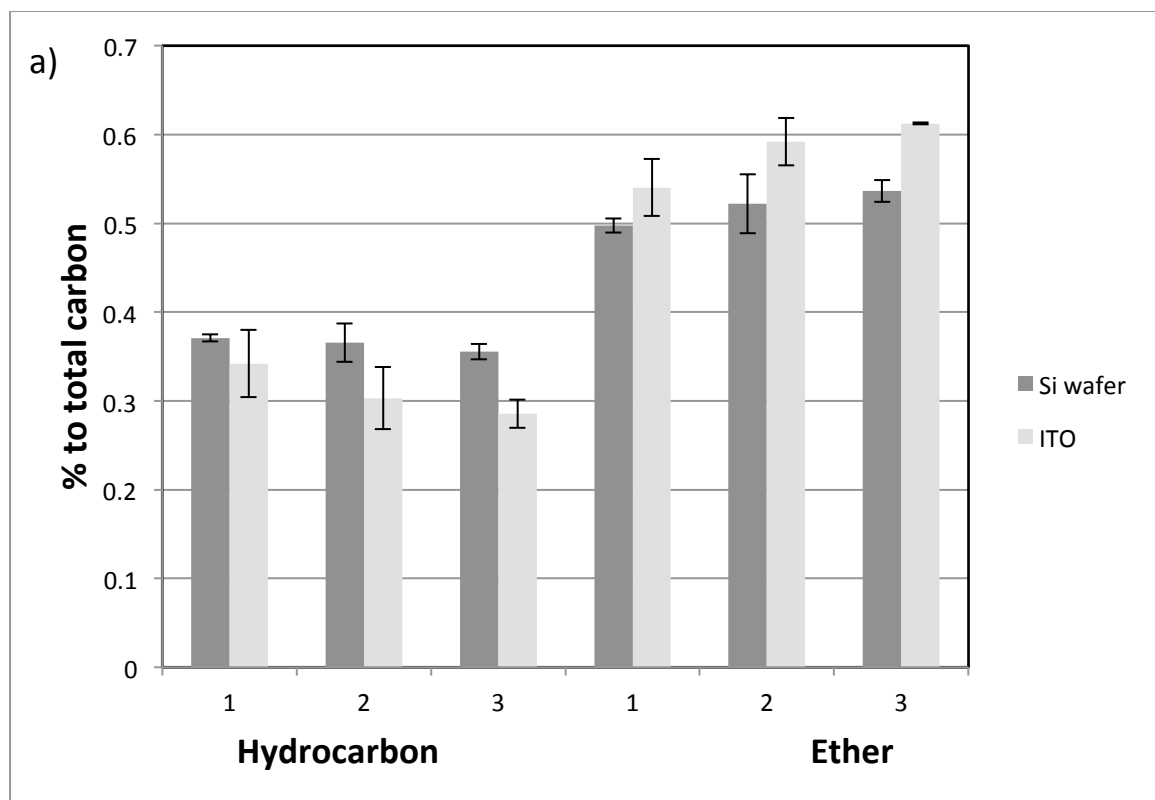


Figure 4.3, Hydrocarbon (C1+C2) and ether/hydroxyl (C3) components in a) 20 W deposited DGpp films; b) 50 W deposited DGpp films. 1, 2, 3 denotes 3 separate experimental repeats on different days and all error bars show the standard deviation based on two analysis points.

In Figure 4.2, the C1s spectra indicate subtle differences in surface functionality of the DGpp films depending on the substrate material used to deposit the thin film. The topside of the DGpp films deposited at 20 W (Figure 4.2A), showed more C-O (C3) and less hydrocarbon (C1 + C2) based functional groups for films on ITO glass compared to the Si wafer. Interestingly, the effect is reversed for the 50 W load power thin films (Figure 4.2B). The topside of the 50W DGpp film on ITO glass contains 8.2 % more hydrocarbon and 15.0 % less ether/hydroxyl species when compared to the film deposited on a Si wafer. Interestingly, repeated experiments showed that the trend stays for 20 W deposition conditions, but for 50 W, the disparity between those two components is negligible (Figure 4.3).

The effect of power input on film thickness is more pronounced. For the films deposited on Si wafers, thickness measurements were obtained via AFM. However, due to the roughness of the ITO glass, AFM step height measurements were not possible; samples were therefore examined with FIB-SEM (Figure 4.4). To assess the thin film thickness measurements using these two techniques, one Si wafer sample was tested via AFM and FIB-SEM and the difference in the thickness obtained was within 10 nm. It was found that for films deposited under a 20 W load power, the thickness of the coating on ITO glass ( $60 \pm 10$  nm) is only half of that on the Si wafer substrate ( $150 \pm 10$  nm). For the 50 W films, the measured thicknesses are closer with the film deposited on the Si wafer ( $180 \pm 20$  nm) was 20 nm thicker than that on ITO glass ( $160 \pm 20$  nm). It is known but rarely reported that film growth is affected by the physico-chemical properties of the substrate surface. Recent works suggest that plasma polymer film formation at the substrate interface is not only dependant on radical/neutral reactions but also ion reactions.<sup>52, 53</sup> It is evident that not only their concentration but also their relative arrival rates, sticking probabilities, and reaction rates at the surface will affect plasma polymer film growth.<sup>54</sup>

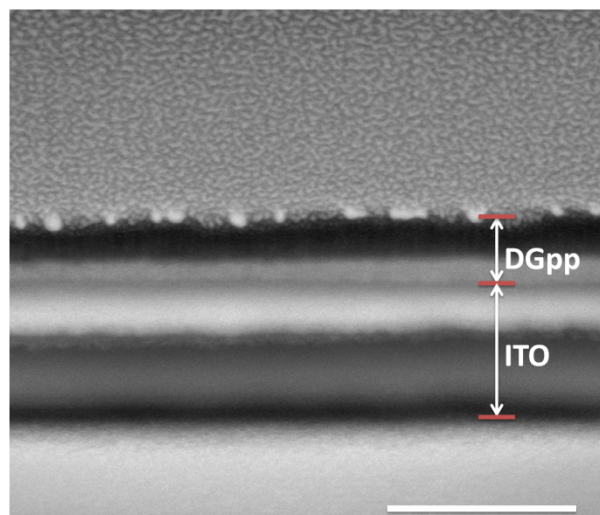


Figure 4.4, SEM image of the FIB-milled cross-section of 50 W DGpp film deposited on ITO glass. Scale bar is 400 nm.

In this study, the higher conductive ITO surface (5 – 15 Ohms) compared to the Si wafer (96 – 286 Ohms) would result in a surface potential and bias and possibly a plasma sheath that is different from one another due to the difference in the surface chemistry and conductivity of the two different substrates'. This bias may induce a difference in the amount of ions interacting and depositing on the surface to produce the pp thin film. Michelmore et al. have shown from ToF-SIMS analysis that during low power and pressure plasmas of DG, the  $C_3H_7O^+$  ( $m/z$  59.050 amu) fragment associated with methyl-terminated chain ends contribute significantly in DGpp films.<sup>55</sup> In our work, we hypothesise that the thinner DGpp films on ITO glass may result from fewer ions interacting with the surface when compared to the plasma deposition on Si wafers. At a 20 W load power, ion-substrate interactions appear to dominate initial film growth rather than radical or neutral species. As the applied power increases to 50 W, the DG monomer undergoes a higher degree of fragmentation, leading to a reduction in the concentration of methyl-terminated chains and increase in hydrocarbon species, thus the deposited mass from ion contributions decreases.<sup>56-58</sup> At higher powers radical-substrate interactions increase and contribute significantly to the deposition of the DGpp films. As radical sticking rates at the substrate interface are not strongly dependent on the substrate materials conductivity, the film thickness on ITO glass and Si wafer at 50 W are similar and do not differ when compared to the 20 W DGpp films (Table 4.2).

### 4.3.2 Analysis of top- and underside

XPS analysis indicates that there were marked differences in the elemental composition between the top- and underside of the high power DGpp film. There were considerably more hydrocarbon species in the initial stage of film deposition as compared to the later stage on the top of the film. For the lower power film however, a substantial amount of silicon was detected on the underside ( $\sim 4.2\%$ ). In addition, a significant contribution at a high binding energy was observed in the high resolution C 1s spectra (Figure 4.2C). These observations suggest that part of the measured signal intensity was associated with CDST. To better present the contributions from the underside of the 20 W DGpp film and deconvolute the contribution of the CDST, the high resolution C 1s spectrum for 20 W film underside was fitted via a combination of a standard Gaussian–Lorentzian function (C1 - hydrocarbon) and model C 1s spectra components based on experimental data (20 W DGpp topside and CDST) (Figure 4.2C). It was confirmed by NEXAFS analysis that the underside of the 20 W film contains resonance features which correspond to the peak found in the spectra of the CDST (data not shown). This confirms that the 20 W delaminated films were patchy and the bare tape also contributed to the film chemistry observed. By fitting the high resolution C 1s with a combination of components, we were able to confirm that there was negligible difference between the top- and underside of the 20 W DGpp films indicating a film that is more homogeneous in chemistry when compared to the 50 W DGpp film. The reason for this poor delamination of the 20W film is likely due to the presence of low molecular weight material (LMWM) which we have previously observed in films of this type.<sup>48</sup> This lightly crosslinked material will preferentially delaminate upon peeling off the CDST leaving bound pp material behind.

For the 50 W DGpp film, the underside contains a considerably greater concentration of oxygen ( $O/C = 0.376$ ) when compared to the topside ( $O/C = 0.230$ ). A small amount of Si ( $\sim 0.55$  atomic %) was detected on the underside of the coating, suggesting that part of the signal intensity was also due to CDST. Unlike the underside of the 20 W DGpp high resolution C 1s spectrum, it was not possible to fit the underside 50 W DGpp spectrum

with a model component based on CDST as there was no unique spectral intensity to define the contribution (i.e. no excess intensity at high BE). This is likely due to the amount of tape representing only a very small part of the overall signal. It is clear however from the overlay of the topside and underside data (Figure 4.2D) that more ether groups were present on the underside with the increase of intensity at  $\sim 286.5$  eV (i.e. C3) as confirmed in Table 4.2 (O/C: 0.244 for topside vs. 0.460 for underside), indicating a gradient through the film. This result is to be expected as the pressure increased by 40 Pa during plasma polymerisation at a load power of 50 W over approximately 10 s. As the pressure increases rapidly, more ionisation and fragmentation will take place in the glow discharge. This will result in greater dissociation of the monomer and ether units resulting in the generation of a higher concentration of unsaturated species in the outer layer of the plasma polymer film, which we have observed previously.<sup>48</sup> To characterise the various resonances arising from unsaturated species, C and O K-edge TEY NEXAFS spectroscopy was performed. Figure 4.5 shows the TEY C K-edge NEXAFS spectra from the top- and underside of the DGpp films with assignments of 4 main resonance peaks. Spectra were collected at different angles between the incoming beam and the surface film and no evidence of chain orientation observed. In Figure 4.5, the C 1s K-edge spectra clearly confirms the presence of unsaturated carbon species arising from an intense energy peak at 285.2 eV, which is typical of  $C\ 1s \rightarrow \pi^*$  (C=C) transition. The other resonances includes  $C\ 1s \rightarrow \sigma^*$  (C-H) at 286.5 eV,  $C\ 1s \rightarrow \pi^*$  (C=O) at 288.7 eV and finally a broader  $C\ 1s \rightarrow \sigma^*$  (C-C, C-O) feature above 293.4 eV.<sup>41, 59-61</sup> Due to the multiphoton resonance absorptions and the broader nature of the higher energy  $\pi^*$  (C=O) and  $\sigma^*$  (C-C, C-O) species, only the two lower energy features (A and B) will be compared herein. The ratio of the features (A and B) from  $C\ 1s \rightarrow \pi^*$  (C=C) unsaturated species and  $C\ 1s \rightarrow \sigma^*$  (C-H) species respectively is similar in the topside of the film while the contribution of  $C\ 1s \rightarrow \pi^*$  (C=C) species is less in the underside. In accordance with XPS analysis, it is clear that the topside is considerably more unsaturated than the underside due to the greater contribution of the C=C resonances at 285.2 eV.

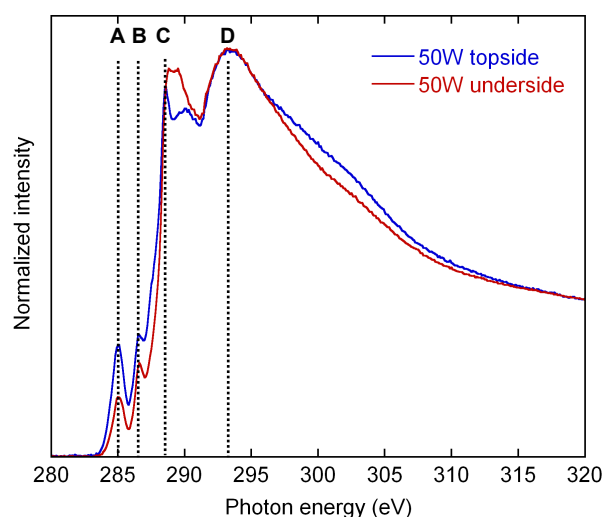


Figure 4.5, C 1s K-edge AEY NEXAFS spectra of top- and underside of a 50 W load power DGpp film. Spectra are normalised in height between the pre- and post-edge. (A, C 1s  $\rightarrow$   $\pi^*$ (C=C); B, C 1s  $\rightarrow$   $\sigma^*$ (C-H); C, C 1s  $\rightarrow$   $\pi^*$ (C=O); D, C 1s  $\rightarrow$   $\sigma^*$ (C-C, C-O).)

The difference in film composition of the 50 W DGpp top- and underside implies that the fragmentation of the DG monomer and deposition rate of the film is not constant during the course of plasma polymerisation. Over the first 10 seconds of deposition, as the load power delivery increased and stabilised, the pressure increased by approximately 40 Pa. This rapid pressure change was largely due to fragmentation of gaseous diglyme monomer species. We observed a significant increase in the oxygen content on the underside of the DGpp film which may be due in part to the reaction of trapped radicals with oxygen after delamination and less fragmentation of DG monomer species in the early stages of plasma polymer film deposition. We have observed a similar effect in plasma polymer films deposited on salt crystals.<sup>41</sup> The plasma deposition reactor pressure reached a maximum after 30 seconds and remained constant during plasma polymerisation. Our work suggests that there is a steep change in plasma polymer film chemistry several nanometers into the substrate-film interface. In comparison, during deposition of the 20 W DGpp, the rate of pressure change is lower (approximately 20 Pa over 40 seconds). There is no clear evidence of a chemical gradient in the film between the top- and underside and none was detected in previous neutron reflectivity studies by us of similar DGpp films. This empirical, quantitative technique has allowed us to validate the finding of a previous study on DGpp films by us where the observation of a strong chemical and mass density gradient was observed via modeling of neutron

reflectivity data of a 50 W DGpp thin film deposited on silicon and none in films produced at load powers of 20 W.<sup>48</sup> The method we introduced in this work to analyse the chemistry of the early stages of pp film formation will allow researchers in the field to further investigate the fundamental aspects of early plasma polymer film formation.

#### 4.4 Conclusions

Thin films of di(ethylene glycol) dimethyl ether have been generated by plasma polymerisation and studied using a number of surface analysis techniques. We showed that the chemistry of the substrate affects the initial stages of DGpp film formation, and DGpp films deposited at a greater rate on Si wafers when compared to ITO glass. We have used a simple method to analyse the underside of plasma polymer thin films via delamination from an oxide surface. By exploiting the poor adhesion of these films on ITO glass the chemical composition of the early plasma polymer film produced at a higher load power was able to be investigated and this results validated previous reports on the chemical gradient in these films observed from neutron reflectometry analysis. This simple delamination technique will allow researchers to probe the chemistry of plasma polymer films during early film formation. This will enable further insights into the mechanisms and important parameters to consider when depositing plasma polymer thin films onto various substrates.

#### 4.5 Reference

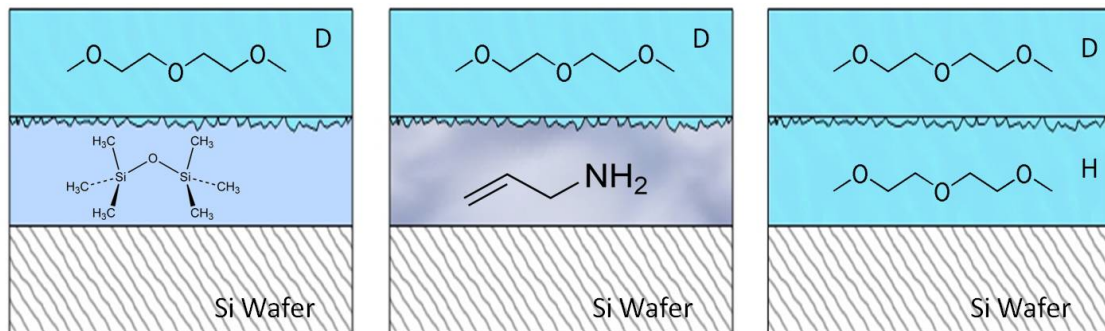
1. T. Desmet, R. Morent, N. D. Geyter, C. Leys, E. Schacht and P. Dubruel, *Biomacromolecules*, 2009, 10, 2351-2378.
2. H. Biederman and D. Slavínská, *Surface and Coatings Technology*, 2000, 125, 371-376.
3. F. Rossi and P. Colpo, *Journal of Physics D: Applied Physics*, 2011, 44, 174017.
4. A. Michelmore, P. Martinek, V. Sah, R. D. Short and K. Vasilev, *Plasma Processes and Polymers*, 2011, 8, 367-372.
5. D. Mangindaan, W.-H. Kuo, C.-C. Chang, S.-L. Wang, H.-C. Liu and M.-J. Wang, *Surface and Coatings Technology*, 2011, 206, 1299-1306.

6. A. M. Sandstrom, M. Jasieniak, H. J. Griesser, L. Grøndahl and J. J. Cooper-White, *Plasma Processes and Polymers*, 2013, 10 (1), 19-28.
7. N. Wells, M. A. Baxter, J. E. Turnbull, P. Murray, D. Edgar, K. L. Parry, D. A. Steele and R. D. Short, *Biomaterials*, 2009, 30, 1066-1070.
8. K. S. Siow, L. Britcher, S. Kumar and H. J. Griesser, *Plasma Processes and Polymers*, 2006, 3, 392-418.
9. L. M. Szott, M. J. Stein, B. D. Ratner and T. A. Horbett, *Journal of Biomedical Materials Research Part A*, 2011, 96A, 150-161.
10. M. Zhang and T. A. Horbett, *Journal of Biomedical Materials Research Part A*, 2009, 89A, 791-803.
11. M. N. Mar, B. D. Ratner and S. S. Yee, *Sensors and Actuators B: Chemical*, 1999, 54, 125-131.
12. H. Yasuda and T. Hsu, *Journal of Polymer Science: Polymer Chemistry Edition*, 1977, 15, 81-97.
13. J. Friedrich, *Plasma Processes and Polymers*, 2011, 8, 783-802.
14. J. D. Whittle, D. A. Steele and R. D. Short, *Plasma Processes and Polymers*, 2012, 9, 840-843.
15. W. E. S. Unger, S. Swaraj, U. Oran and A. Lippitz, *Surface and Interface Analysis*, 2006, 38, 522-525.
16. U. Oran, S. Swaraj, A. Lippitz and W. E. S. Unger, *Plasma Processes and Polymers*, 2006, 3, 288-298.
17. I. Retzko, J. F. Friedrich, A. Lippitz and W. E. S. Unger, *Journal of Electron Spectroscopy and Related Phenomena*, 2001, 121, 111-129.
18. Y. Kim, K.-J. Kim and Y. Lee, *Surface and Coatings Technology*, 2009, 203, 3129-3135.
19. B. W. Muir, A. Nelson, A. Fairbrother, C. Fong, P. G. Hartley, M. James and K. M. McLean, *Plasma Processes and Polymers*, 2007, 4, 433-444.
20. M. James, *Australian Journal of Chemistry*, 2001, 54, 487-491.
21. C. Amorosi, T. Fouquet, V. Toniazzo, D. Ruch, L. Averous, V. Ball and M. Michel, *Reactive and Functional Polymers*, 2012, 72, 341-348.
22. L. Peng and G. R. Kinsel, *Langmuir*, 2010, 26, 17477-17481.
23. J. A. Stillahn, K. J. Trevino and E. R. Fisher, in *Annual Review of Analytical Chemistry*, Annual Reviews, Palo Alto, 2008, vol. 1, pp. 261-291.
24. M. L. Steen, C. I. Butoi and E. R. Fisher, *Langmuir*, 2001, 17, 8156-8166.
25. E. R. Fisher, *Plasma Processes and Polymers*, 2004, 1, 13-27.
26. D. Barton, J. W. Bradley, D. A. Steele and R. D. Short, *The Journal of Physical Chemistry B*, 1999, 103, 4423-4430.

27. C.-H. Lo, K.-S. Liao, M. De Guzman, V. Rouessac, T.-C. Wei, K.-R. Lee and J.-Y. Lai, *Langmuir*, 2010, 26, 17470-17476.
28. A. M. Wróbel and G. Czeremuszkina, *Thin Solid Films*, 1992, 216, 203-210.
29. Y. Hatanaka, M. Ohkuwa and T. Yamaguchi, *Applied Surface Science*, 1993, 65-66, 507-510.
30. K. Furuya, R. Nakanishi, H. Okumura, M. Makita and A. Harata, *Thin Solid Films*, 2008, 516, 6028-6032.
31. K. Vasilev, A. Michelmore, H. J. Griesser and R. D. Short, *Chemical Communications*, 2009, 3600-3602.
32. K. Vasilev, A. Michelmore, P. Martinek, J. Chan, V. Sah, H. J. Griesser and R. D. Short, *Plasma Processes and Polymers*, 2010, 7, 824-835.
33. K. Wapner and G. Grundmeier, *Surface and Coatings Technology*, 2005, 200, 100-103.
34. G. Grundmeier and M. Stratmann, *Thin Solid Films*, 1999, 352, 119-127.
35. R. H. Turner and F. J. Boerio, *The Journal of Adhesion*, 2002, 78, 447-464.
36. P. I. Rosales and F. J. Boerio, *The Journal of Adhesion*, 2007, 83, 267-287.
37. P. Scott, D. Wieliczka and M. Kruger, *Plasma Chem Plasma Process*, 2009, 29, 559-566.
38. A. Holländer, S. Kröpke and F. Pippig, *Surface and Interface Analysis*, 2008, 40, 379-385.
39. H. Kim, M. D. Foster, H. Jiang, S. Tullis, T. J. Bunning and C. F. Majkrzak, *Polymer*, 2004, 45, 3175-3184.
40. J. Brison, S. Muramoto and D. G. Castner, *The Journal of Physical Chemistry C*, 2010, 114, 5565-5573.
41. R. T. Chen, B. W. Muir, L. Thomsen, A. Tadich, B. C. C. Cowie, G. K. Such, A. Postma, K. M. McLean and F. Caruso, *The Journal of Physical Chemistry B*, 2011, 115, 6495-6502.
42. F. Awaja, M. Gilbert, G. Kelly, B. Fox and P. J. Pigram, *Progress in Polymer Science*, 2009, 34, 948-968.
43. A. Choukourov, I. Gordeev, O. Polonskyi, A. Artemenko, L. Hanyková, I. Krakovský, O. Kylián, D. Slavínská and H. Biederman, *Plasma Processes and Polymers*, 2010, 7, 445-458.
44. V. Kumar, J. Pulpytel, G. Giudetti, H. Rauscher, F. Rossi and F. Arefi-Khonsari, *Plasma Processes and Polymers*, 2011, 8, 373-385.
45. Q. Cheng, S. Li and K. Komvopoulos, *Biomaterials*, 2009, 30, 4203-4210.
46. D. J. Menzies, T. Gengenbach, J. S. Forsythe, N. Birbilis, G. Johnson, C. Charles, G. McFarland, R. J. Williams, C. Fong, P. Leech, K. McLean and B. W. Muir, *Chemical Communications*, 2012, 48.
47. D. J. Menzies, B. Cowie, C. Fong, J. S. Forsythe, T. R. Gengenbach, K. M. McLean, L. Puskar, M. Textor, L. Thomsen, M. Tobin and B. W. Muir, *Langmuir*, 2010, 26, 13987-13994.

48. D. J. Menzies, A. Nelson, H.-H. Shen, K. M. McLean, J. S. Forsythe, T. Gengenbach, C. Fong and B. W. Muir, *Journal of The Royal Society Interface*, 2012, 9, (70), 1008-1019.
49. B. C. C. Cowie, A. Tadich and L. Thomsen, *AIP Conference Proceedings*, 2010, 1234, 307-310.
50. B. Watts, L. Thomsen and P. C. Dastoor, *Journal of Electron Spectroscopy and Related Phenomena*, 2006, 151, 105-120.
51. B. W. Muir, A. Fairbrother, T. R. Gengenbach, F. Rovere, M. A. Abdo, K. M. McLean and P. G. Hartley, *Advanced Materials*, 2006, 18, 3079-3082.
52. G. P. Wells, I. C. Estrada-Raygoza, P. L. S. Thamban, C. T. Nelson, C. W. Chung, L. J. Overzet and M. J. Goeckner, *Plasma Processes and Polymers*, 2013, 10, 119-135.
53. A. Michelmore, P. M. Bryant, D. A. Steele, K. Vasilev, J. W. Bradley and R. D. Short, *Langmuir*, 2011, 27, 11943-11950.
54. J. P. Chang and J. W. Coburn, *Journal of Vacuum Science & Technology A: Vacuum, Surfaces, and Films*, 2003, 21, S145-S151.
55. A. Michelmore, P. Gross-Kosche, S. A. Al-Bataineh, J. D. Whittle and R. D. Short, *Langmuir*, 2013, 29, 2595-2601.
56. D. B. Haddow, R. M. France, R. D. Short, J. W. Bradley and D. Barton, *Langmuir*, 2000, 16, 5654-5660.
57. C. Nelson, S. Sant, L. Overzet and M. Goeckner, *Plasma Sources Science and Technology*, 2007, 16, 813.
58. A. Michelmore, D. A. Steele, J. D. Whittle, J. W. Bradley and R. D. Short, *RSC Advances*, 2013, 3, 13540-13557.
59. S. G. Urquhart and H. Ade, *The Journal of Physical Chemistry B*, 2002, 106, 8531-8538.
60. V. Lee, L. Whittaker, C. Jaye, K. M. Baroudi, D. A. Fischer and S. Banerjee, *Chemistry of Materials*, 2009, 21, 3905-3916.
61. T. Okajima, K. Hara, M. Yamamoto and K. Seki, *Polymer*, 2012, 53, 2956-2963.

## Chapter 5 Interfacial structure of bilayer plasma polymer films



*"The strong were always eating the weak."  
- James Rollins, Deep Fathom*

## Abstract

Understanding and gaining insight into the mechanisms and chemistry behind the early stages of plasma polymer (pp) film deposition and the interface that forms between a plasma polymer and the substrate it is deposited onto is difficult. In this work we have used X-ray and neutron reflectometry in conjunction with X-ray photoelectron spectroscopy to analyse bilayer pp films. The plasma polymer bilayer film chemistry, thickness, mass density and structure of the layer-layer, and layer-air interfaces were examined, in order to gain a comprehensive understanding of the interface that forms between two chemically distinct pp films. Three different pp nanometer thick films were created from utilising three starting monomers: hexamethyldisiloxane (HMDSO), di(ethylene glycol) dimethyl ether (DG) and allylamine (AA). These films were used as a 'substrate' for the subsequent deposition of a deuterated di(ethylene glycol) dimethyl ether (dDG) film. We found that at low load powers, single layer HMDSO, DG and AA films showed the trend of AA > DG > HMDSO in roughness at pp/air interface. In addition, single layer films made at higher deposition powers have rougher surfaces than those deposited at lower powers. When a dDG layer is deposited on top of the initial film, the dDG/pp interfaces were rougher than single layer pp/air interface. It was also found that the extent of interface roughening is strongly dependent on the underlying pp film. When the starting monomer is the same, the dDG/pp film interfaces were typically broader if the underlying pp film was deposited at low power than at 40 W load power. Amongst the three starting monomers, the trend in interface roughening was that HMDSO > DG > AA. This discrepancy in intermixing among those pp films was attributed to their difference in surface chemistry and individual bond dissociation energy.

## 5.1 Introduction

Selective surface modification has a wide range of applications, includes but not limited to optical components, electronics, renewable energy systems (solar cell, fuel cells), and medical implants.<sup>1,2</sup> Surface engineered products offer improved performance, distinct functionality, and conservation in scarce raw materials over manufacturing of bulk materials. The use of plasma to assist surface manipulation has advanced rapidly over the last few decades and continues to grow.<sup>3-5</sup> Herein, we focus on the practice of plasma polymerisation, the process of which a monomer vapour is dissociated in a plasma environment and forms deposits of organic and inorganic polymer films in one-step, without any solvent, onto various substrates. It has the potential to create new products with mixed chemistry, structure and reactivity.

Plasma polymerised hexamethyldisiloxane (HMDSO), di(ethylene glycol) dimethyl ether (DG) and allylamine (AA) films are well known.<sup>6-10</sup> HMDSO plasma polymer film, is rich in Si content (organosilicone film), provides good optical and mechanical properties that has been used extensively in microelectronics and other applications.<sup>11</sup> DG monomer contains -C-O-C- functional groups which is a contributing factor of low-fouling nature of this class of plasma polymer films. Also the concentration of ether units is influenced by deposition conditions and as a result, the anti-adhesive property can be tuned in demand.<sup>12,13</sup> Plasma polymer films generated from AA retains reactive amines, imine and nitrile functionalities which are useful as supports for further grafting reactions, in particular in the biomedical science arena.<sup>14-16</sup>

Although single layer plasma polymer films hold enormous promise, a new trend that exploits laminated films has come into focus with the aim of combining the advantages of its components.<sup>17-19</sup> In practice, the key for advancement lies in better understanding of film's physical-chemical properties. Various analytical methods have been employed to fully elucidate the chemical composition of plasma polymer films, such as FTIR, XPS, NEXAFS and TOF-SIMS.<sup>20-23</sup> In terms of physical properties, generally, to investigate the thickness and topography/roughness at the surface, most accessible techniques are ellipsometry and AFM.<sup>8, 24</sup> The interactions of plasma polymer films with solution environments are commonly assessed by SPR and QCM. In addition, it is also desirable

to probe the internal structure of bulk film and interface mixing of multilayered plasma polymer coatings.

One way to visualise the interface is to scratch or section the multilayer samples and characterise using Scanning Force Microscopy (SFM). Zhang et al. examined HMDSO films deposited under alternating plasma conditions. The difference in mechanical contrast within each layer provides means for clear presentation of the interface and estimation in roughness.<sup>25</sup> Cech and co-workers used a similar set up to investigate hydrogenated amorphous carbon-silicon (a-SiC:H) multilayer films.<sup>26</sup> With this technique, one concern is that the sectioned surface may contain artifacts due to grinding. The other important design prospect is that the individual layers should be relatively thick in order to avoid interference from surrounding layers.

A non-destructive, complementary method for thin film analysis is the combination of neutron and X-ray reflectometry (NR, XRR). NR and XRR are exquisitely sensitive to sub-surface structures to the nanoscale and allow the determination of the full chemical composition of plasma deposited films (in concert with information obtained with XPS).<sup>27</sup> As a result of the dramatically different scattering lengths of hydrogen ( $-0.374 \times 10^{-12}$  cm) and deuterium ( $0.667 \times 10^{-12}$  cm), neutron reflection method is especially advantageous for multilayered films where deuterated materials are used.<sup>28</sup> Our group has reported on NR study of HMDSO (10 W),<sup>29</sup> AA (20 W),<sup>27</sup> DG (10, 20 and 50 W)<sup>30</sup> homopolymer films. Previous NR studies by other groups have focused on density profile and swollen behavior of plasma polymerised methylmethacrylate,<sup>31</sup> octafluorocyclobutane (OFCB)<sup>32</sup> and benzene.<sup>33</sup> Only the work by Kim et al. used NR and XRR to explore both single and multilayered plasma polymer films.<sup>34</sup> OFCB and deuterated benzene (dB) were used as starting monomers to produce both single layer and bilayer plasma polymer films. They found that the interface of the bilayer is significantly rougher compare to film-air interface and they argue that it is a result of chemistry occurring locally at the interface.

In this work, it is hypothesised that studying bilayer plasma polymer films would provide an excellent model system to investigate the interfacial properties of the films. This is due to the ability of producing atomically flat plasma polymer films of controlled

thickness, which makes them perfect for studying with NR and XRR.<sup>27, 29, 30</sup> By using a deuterated plasma polymer as the top film, and using a plasma polymer film that has been shown to not age, this approach should prove invaluable in investigating the interface of such a system which may provide an insight into the early stages of plasma polymer film formation.

In this study, we examined the properties of plasma polymerised HMDSO (10 and 20 W), DG (20 and 40 W) and AA (20 and 40 W) using NR and XRR in air. Additionally, the difference in their response to a second layer film deposition - in terms of density profile change and interface structure. To control film thickness, AFM measurements at step-edge (same masking method as described in **chapter 4**) on the films were taken at various time points and optimised conditions were used. Surface chemistry of the plasma polymer coatings was characterised using XPS. Stoichiometric composition and mass densities are estimated through combining XPS, XRR and NR data.

## 5.2 Materials and methods

### 5.2.1 Samples preparation

Ultra-flat single crystal, Si wafers (<111>, 10 cm diameter, 1 cm thick, *Silrec Corporaton*, San Jose and <100>, 1 cm<sup>2</sup> x 0.5 mm thick, from *M.M.R.C Pty Ltd*, Melbourne Australia) were used as substrates for the plasma polymerisation. Prior to plasma polymer deposition, all wafers were cleaned immediately by ultrasonication in a surfactant solution of 2 % ethanol with 2 % RBS-35 (*Pierce*, U.S.A) for 1 h, followed by rinsing with copious amount of MilliQ water and finally dried in a high-pressure stream of nitrogen. Large wafers (10 cm diameter x 1 cm thick) were used for neutron and X-ray reflectometry analysis and smaller wafers (1 cm<sup>2</sup> x 0.5 mm thick) were prepared for XPS characterisation. Plasma deposition was carried out simultaneously on both large and small wafers (where small wafers were placed around the edge of the large wafer).

The monomers hexamethyldisiloxane (HMDSO, Sigma-Aldrich, NMR grade, 99.5 %), diethylene glycol dimethyl ether (DG, BDH, 99 %), allylamine (AA, Sigma-Aldrich, 98 %)

and deuterated diethylene glycol dimethyl ether (dDG, Cambridge Isotope Laboratories, Inc. U.S.A. 98 %) were all used without further purification.

### 5.2.2 Plasma polymerisation

Deposition of HMDSO, DG and dDG plasma polymer films were carried out in the same reactor described in **chapter 3**. Similar to that design, the AA plasma polymerisation reactor consists of a chamber of the same size and fitted with two circular electrodes of 10.3 cm in diameter (distance = 15 cm). All cleaned wafers were placed on the lower electrode. HMDSO, DG and dDG monomer flasks were kept in ambient air, while highly volatile AA monomer flask was cooled in iced water, during experiments. All monomer liquid was degassed before plasma deposition.

The plasma polymerisation parameters of the four monomers were selected such that films of appropriate thicknesses for reflectivity measurements were produced. DGpp films were deposited at a frequency of 125 kHz, load powers of 20 and 40 W with initial monomer pressure of 20 Pa for a treatment time of 14 (final pressure 41 Pa) and 8 (final pressure 52 Pa) seconds respectively. The plasma deposition of HMDSO films was performed using a frequency of 200 kHz, load powers of 10 and 20 W and initial monomer pressure of 10 Pa for a treatment time of 8 (final pressure 13 Pa) and 5 (final pressure 15 Pa) seconds respectively. The AA films were also deposited at frequency of 200 kHz, load powers of 20 and 40 W with initial monomer pressure of 20 Pa for a treatment time of 17 (final pressure 37 Pa) and 10 (final pressure 42 Pa) seconds respectively. Six single layer plasma polymer films were produced using the above conditions; another six samples were made exactly the same then subjected to an additional dDG plasma polymerisation process. The dDG layer was formed under a frequency of 125 kHz and a load power of 20 W with initial monomer pressure of 20 Pa for a treatment time of 16 seconds, and the final pressure is 40 Pa. Prior to deposition, the reactor was evacuated to a base pressure of 0.1 Pa. After each deposition, the reactor was pumped down to base pressure and then vented to allow collecting of samples. All samples were placed in clean petri dishes under ambient conditions before chemical analysis. For simplicity, a sample name of "HM10" indicates that the film was

deposited using HMDSO monomer vapor and 10 W load power (applies to both single HMDSO layer and the 1<sup>st</sup> layer in the bilayer construct). In addition, “HM10D” imply that HM10 was further treated with dDG 20 W plasma polymerisation.

### 5.2.3 X-ray photoelectron spectroscopy

XPS analysis was performed using an AXIS HSi spectrometer (Kratos Analytical Ltd, U.K.) equipped with a monochromated Al-K $\alpha$  X-ray source at a power of 144 W (12 mA, 12 kV). The analyses details are the same as described in previous chapters. Samples were measured first in the as-deposited state and then at the time of reflectometry measurements to account for changes in chemistry of the plasma polymer film.

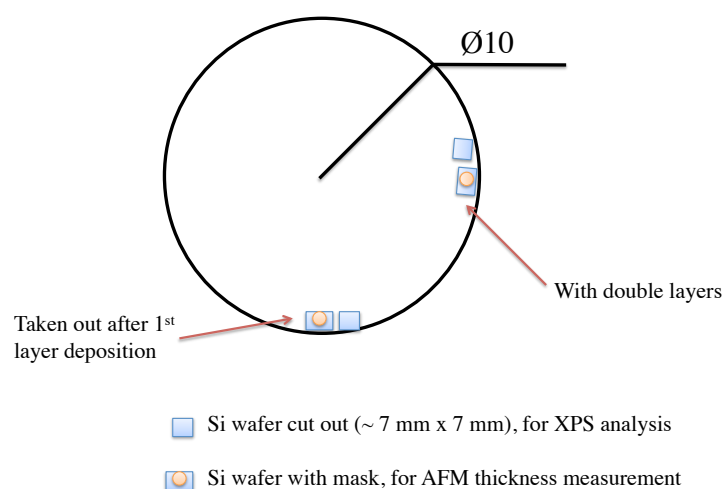
### 5.2.4 Neutron and X-ray reflectometry

Neutron and X-ray reflectometry (NR, XRR) data were collected at the NIST Center for Neutron Research. XRR data were collected using a Bruker diffractometer ( $\lambda = 1.5406$  Å). NR data were collected on the *Magik* horizontal scattering plane reflectometer.<sup>28</sup> In both cases the reflectivity, i.e. the ratio of specularly reflected intensity to incident beam intensity, was measured as a function of momentum transfer,  $Q$ . Momentum transfer is given by the relation  $Q = 4\pi/\lambda \sin\Omega$ , where  $\lambda$  is the wavelength of incident radiation and  $\Omega$  is the angle of incidence of the incoming beam. Some NR measurements were also performed on the Platypus reflectometer at the Australian Nuclear Science and Technology Organisation (ANSTO).<sup>35</sup> The reflectometry data were analysed using a standard least squares method in the *Motofit* program,<sup>36</sup> weighting data on a logarithmic scale and using the instrumental resolution functions.

## 5.3. Results and discussion

### 5.3.1 Surface chemistry

One of the challenges when working with plasma polymer films is their tendency to gradually age over time upon exposure to the atmosphere. This is generally due to post oxidation reactions within the films from residual radicals. Therefore, during this work, to allow for the possible change in surface chemistry of the film over time, samples were analysed via XPS immediately after deposition and then immediately before NR and XRR measurements. The surface chemistry of the single layer plasma polymer films, at the time of NR and XRR measurements, is shown in Figure 5.1, as derived from XPS elemental analysis. Compared to the freshly deposited (Table 5.1, a) state, the HMDSO and AA films showed signs of oxygen incorporation with approximately 1 at. % increase while the DG films do not appear to incorporate a significant amount of oxygen from the atmosphere. The increase observed in the HMDSO and AA films is likely due to post-plasma oxidation reactions upon exposure of the film to ambient atmosphere (approximately one week). For the DG and AA films, low levels of silicon (from the substrate) are also detected. It is likely due to the fact that the plasma glow only covers 8 – 9 cm diameter area uniformly, then fluctuates, but the XPS samples were placed at the outer most region of the 10 cm diameter Si block on the edges of the lower electrode (to avoid disruption of the centre of the film used for NR measurements) (Schematic 5.1). We have noted that the films deposited on the large Si block are slightly thicker than films deposited onto 0.7 cm<sup>2</sup> Si wafers under the same plasma deposition conditions. The smaller thickness plasma polymer films are close to the detection limit of XPS (10 nm), hence a small contribution from the background signal appears in the spectra.



Schematic 5.1. Illustration of the samples placement during plasma polymerisation. A 10 cm diameter Si wafer block was placed at the center of bottom electrode. Four small Si wafer cut out was placed at the edge of the big wafer and two of those samples was masked prior to deposition for subsequent thickness measurements.

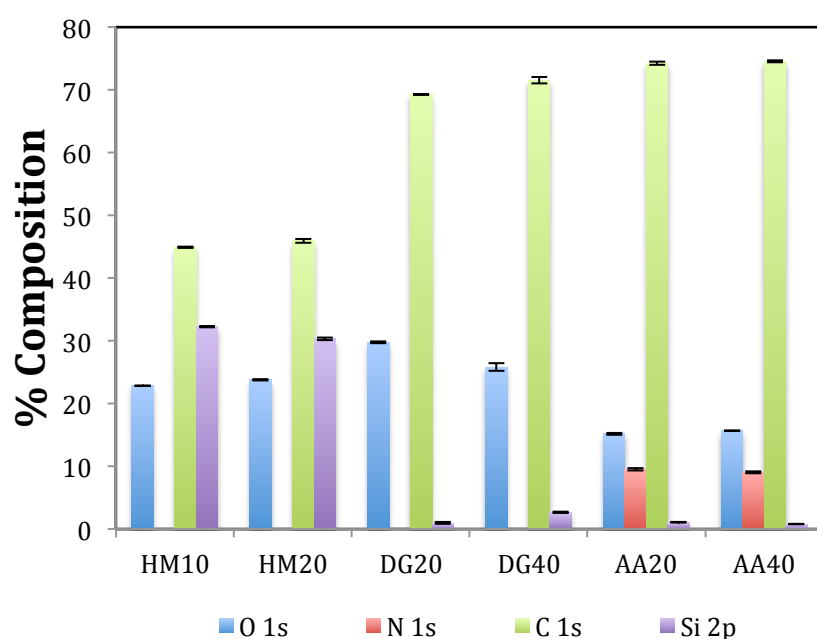


Figure 5.1. Elemental composition (atomic %) of the single layer plasma polymer films made from HMDSO, AA and DG derived from XPS survey spectra. Error bar is standard deviation. The difference between HMDSO films made under the load power of 10 and 20 W is minimal, with a slight increase in C content and decrease in Si concentration. For AA films, there is no significant different in film chemistry in term of elemental composition as determined here using XPS. However, for DG films, the oxygen content in 40 W deposited film is 4 atomic % lower than that of 20 W deposited film, coupled with a rise in carbon.

Table 5.1. Elemental composition (atomic %) derived from XPS survey spectra. XPS data collected immediately after deposition. Presented are the mean values with the standard deviation. (For single layer pp, a sample name of “HM10” indicates that the film was deposited using HMDSO monomer vapor and 10 W load power. For bilayer system, “HM10” refers to the 1<sup>st</sup> layer of HMDSO film, while “HM10D” imply that HM10 was further treated with dDG 20 W plasma polymerisation).

<b>a) Single layer</b>	<i>O 1s</i>	<i>N 1s</i>	<i>C 1s</i>	<i>Si 2p</i>
HM10	21.84 ± 0.13	-	45.67 ± 0.35	32.49 ± 0.48
HM20	21.97 ± 0.02	-	46.40 ± 0.38	31.63 ± 0.35
DG20	29.30 ± 0.62	-	70.07 ± 0.59	0.63 ± 0.03
DG40	26.72 ± 0.21	-	71.12 ± 0.33	2.17 ± 0.13
AA20	13.50 ± 0.35	10.16 ± 0.27	75.33 ± 0.13	1.02 ± 0.06
AA40	14.20 ± 0.18	9.71 ± 0.22	75.46 ± 0.37	0.64 ± 0.04
<b>b) Bilayer</b>	<i>O 1s</i>	<i>N 1s</i>	<i>C 1s</i>	<i>Si 2p</i>
HM10	21.78 ± 0.30	-	44.84 ± 0.13	33.38 ± 0.44
HM10D	28.23 ± 0.07	-	71.08 ± 0.17	0.70 ± 0.09
HM20	21.82 ± 0.23	-	46.85 ± 0.04	31.34 ± 0.20
HM20D	28.39 ± 0.15	-	70.94 ± 0.33	0.67 ± 0.18
DG20	30.08 ± 0.36	-	69.45 ± 0.37	0.48 ± 0.01
DG20D	28.09 ± 0.08	-	71.91 ± 0.08	-
DG40	25.20 ± 0.74	-	72.88 ± 0.61	1.93 ± 0.13
DG40D	28.10 ± 0.14	-	71.90 ± 0.14	-
AA20	13.81 ± 0.25	9.85 ± 0.22	75.65 ± 0.63	0.70 ± 0.16
AA20D	28.13 ± 0.01	-	71.87 ± 0.01	-
AA40	13.87 ± 0.31	9.82 ± 0.13	75.73 ± 0.34	0.59 ± 0.10
AA40D	28.44 ± 0.03	-	71.56 ± 0.03	-

However, for the HMDSO films, the high concentration of silicon (greater than 30%) is likely to be from the pp films, since the elemental composition of HMDSO films obtained

from this study was similar to that reported in the literature, where Si is one of the main components in HMDSO films.<sup>6, 29</sup> Both the 10 W and 20 W deposited HMDSO plasma polymer films contain greater amount of oxygen and silicon compared to the HMDSO monomer. Meanwhile, the carbon content (c.a. 46%) reduced dramatically in contrast to the starting monomer (66.7%). The well-established theory for this phenomenon is that during the plasma polymerisation of HMDSO, methyl abstraction is the major fragmentation and activation pathway in the radio frequency glow discharge (RFGD) whilst scission of Si-O bonds occurs to a much lesser extent.<sup>29, 37, 38</sup>

For the AA plasma polymer films, the main elemental components of the films were carbon, nitrogen and oxygen. Note XPS cannot measure the hydrogen content of the films. The carbon content differed slightly from the monomer, but the nitrogen content was less than half (75% C, 25% N). The oxygen incorporation originated from the air/water residues in the reactor chamber that were activated during plasma polymerisation and post plasma deposition oxidation reactions upon exposure to the atmosphere. We noted that the oxygen contents in these films are slightly higher compared to such films previously reported in the literature.<sup>15, 27, 39</sup>

For the DG plasma polymer films, the elemental analysis from XPS revealed films that consist of predominantly carbon and oxygen. The carbon (29%) and oxygen (70%) concentrations in the 20 W deposited DG films were consistent with previous studies of these films (also consistent with the results reported in **chapter 3 and 4**).<sup>7, 30, 40</sup> The chemical composition of the 40 W deposited film contains less carbon and more oxygen than 40 W films previously reported. We believe this is due to the fact that the film was made in 10 seconds rather than the longer deposition times usually used in our lab to make these films. The initial stage of plasma deposition is less energetic as evidenced by a weaker glow. Therefore in the initial stage of film deposition there are fewer dissociation/scission events of the gaseous monomers. As the deposition time increases, the plasma reaches equilibrium and film builds up and then the chemistry do not appear to change significantly. Hence there was a discrepancy in the film chemistry reported herein from what one may have expected for DG plasma polymer coatings deposited over longer plasma polymerisation time. **Chapter 4** has described this chemistry variation of DG plasma polymer films generated at 50 W load powers.

Table 5.2. Elemental composition (atomic %) derived from XPS survey spectra. Presented are the mean values with the standard deviation. (A sample name of “HM10” indicates the 1<sup>st</sup> layer, which the film was deposited using HMDSO monomer vapor and 10 W load power. In addition, “HM10D” represents the 2<sup>nd</sup> layer film whereby HM10 was further treated with a dDG 20 W plasma polymerisation). The same nomenclature applies to the rest of the films listed in this table.

<b><i>Bilayer</i></b>	<i>O 1s</i>	<i>N 1s</i>	<i>C 1s</i>	<i>Si 2p</i>
HM10	23.17 ± 0.16	-	44.72 ± 0.08	32.11 ± 0.24
HM10D	28.66 ± 0.16	-	70.52 ± 0.05	0.83 ± 0.11
HM20	23.25 ± 0.13	-	46.02 ± 0.16	30.73 ± 0.01
HM20D	29.23 ± 0.28	-	69.86 ± 0.40	0.93 ± 0.13
DG20	30.04 ± 0.66	-	69.37 ± 0.55	0.60 ± 0.11
DG20D	28.61 ± 0.04	-	71.39 ± 0.04	-
DG40	26.35 ± 0.29	-	71.79 ± 0.23	1.86 ± 0.06
DG40D	28.77 ± 0.27	-	71.21 ± 0.27	0.02 ± 0.01
AA20	15.21 ± 0.13	9.48 ± 0.13	74.43 ± 0.03	0.89 ± 0.02
AA20D	28.95 ± 0.11	-	70.96 ± 0.04	0.10 ± 0.13
AA40	15.60 ± 0.16	9.14 ± 0.11	74.53 ± 0.04	0.74 ± 0.10
AA40D	28.34 ± 0.28	-	71.57 ± 0.28	0.10 ± 0.00

The surface chemistry of the bilayer plasma polymer coatings produced in this work was assessed in two steps. After the first layer was deposited, which would become the substrate for the second plasma polymer film, a sample was removed from the plasma reactor for XPS analysis. Another identical sample was then further coated with a dDG plasma polymer. The use of dDG allows for a significant contrast enhancement due to the improvement in neutron scattering length density of deuterium over hydrogen. The results of XPS analysis of these systems are summarised in Table 5.2. A sample name of “HM10” indicates that the 1<sup>st</sup> layer film deposited using HMDSO monomer vapor and 10 W load power. Moreover, “HM10D” refers to the 2<sup>nd</sup> layer film whereby HM10 was

further treated with a dDG 20 W plasma polymerisation. The same nomenclature applies for all of the films listed in the table.

It is not surprising that the elemental composition of the layers close to the Si wafer substrate were the same as their respective single layer deposits. The dDG layers deposited on top of single layer pp were formed under fixed process parameters and displayed minimal variation in the carbon and oxygen concentrations across the six samples. Considering the carbon and oxygen atomic compositions only (as XPS cannot detect hydrogen or deuterium), the dDG films and DG 20 W film were alike in their surface chemistry. Furthermore, the dDG films were stable after 1 week of storage (Table 5.1, b). Later in this discussion, the XPS results will be used in conjunction with air-solid NR and XRR measurements to get an estimation of the full stoichiometric composition and mass density of the films.

### 5.3.2 Characterisation of films by XRR and NR in air

The air-solid NR measurements from both single layer plasma polymer films and bilayer films are shown in figure 5.2 along with the best model fit, while the structural parameters (*Motofit* model) of each film are summarised in table 5.3. The corresponding XRR measurements and model parameters are given in **appendix 2** (Figure S5.1 and Table S5.1). For each experimental data set, a model of the film structure was constructed in the form of one dimensional profile of scattering length density (SLD) with depth. The SLD profiles corresponding to each fit are shown in the inset of figure 5.2. SLDs obtained in this study are similar to that has been reported in the literature.<sup>27, 30</sup> The SLD at the dDG/pp interface was normalised and compared with the corresponding SLD of the single layer at pp/air interface, which are presented in figure 5.3. Based on the SLD profiles, it is clear that deposition of the overlying dDG film roughened the film underneath. The increase in roughness at the interface, however, is however not the same. To understand the cause of this discrepancy, it is necessary to examine both single layer pp films and bilayer film constructs in turn.

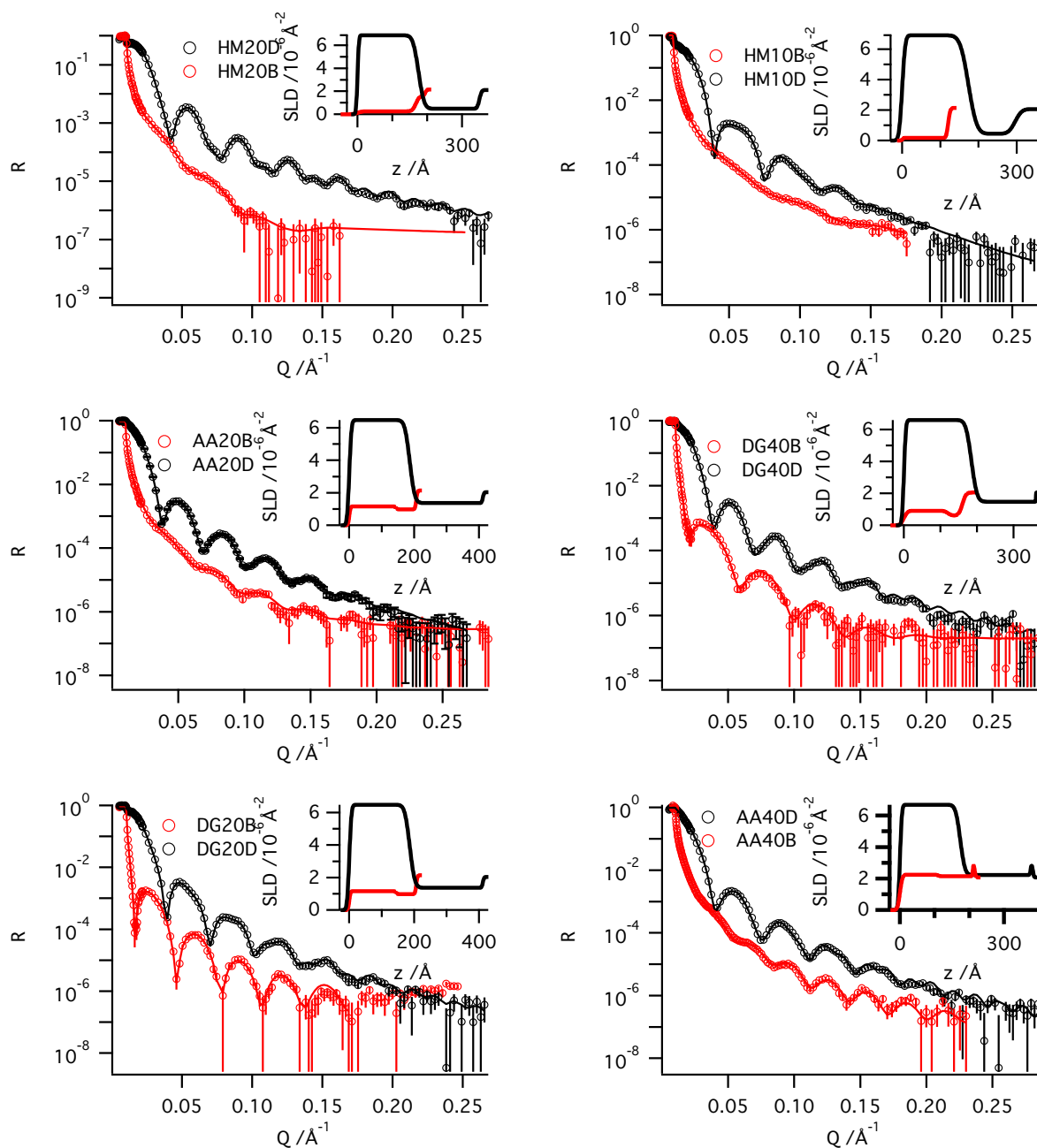


Figure 5.2. NR spectra from the air-plasma polymer film-Si system. Each figure contains the single and double layer spectra for a given base polymer layer, e.g. HM10 and HM10D. The symbols represent the observed reflectivity data while the solid lines are fits to the data determined from the structural models using *Motofit* software. The inset is the scattering length density profiles of the films.

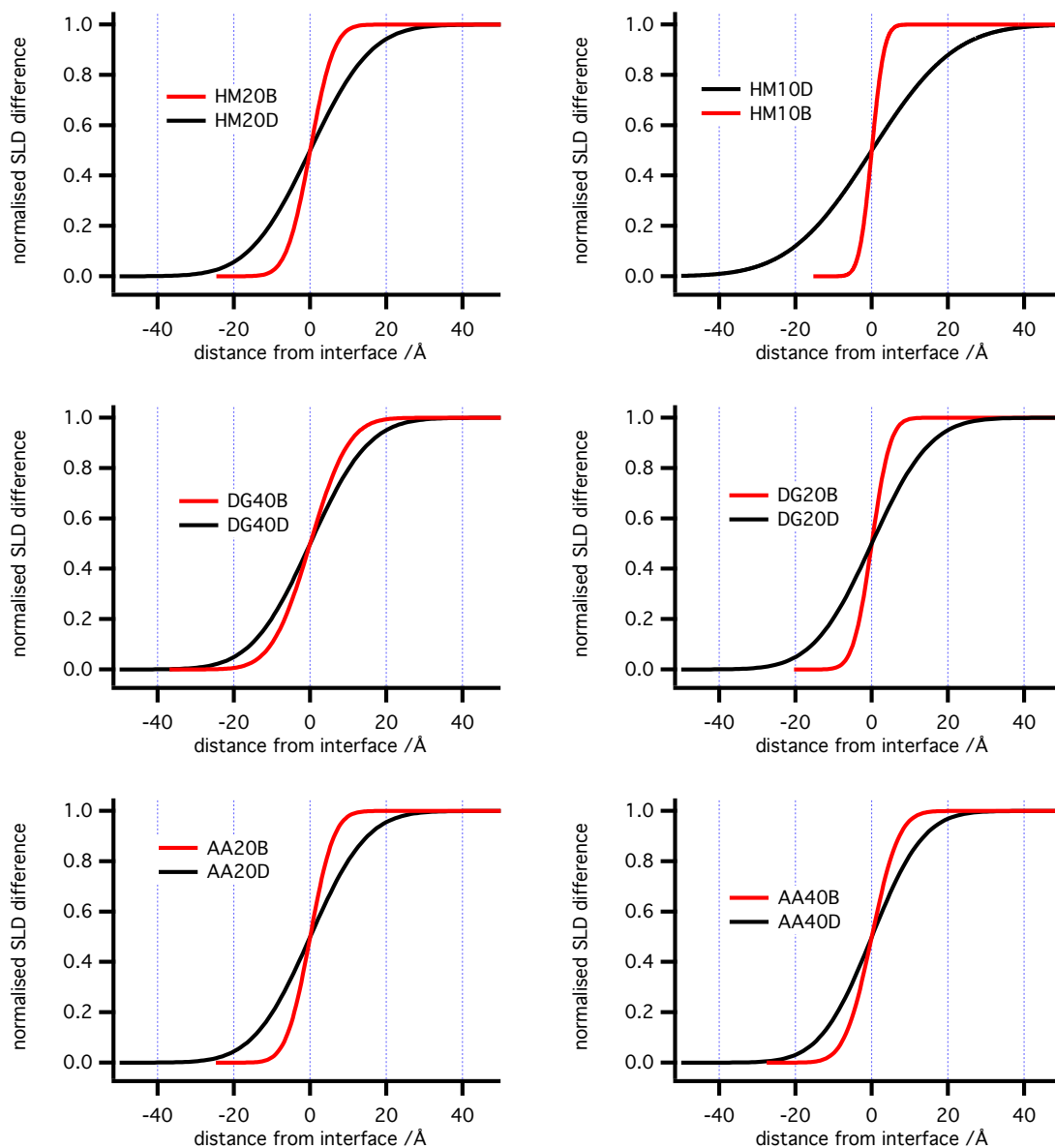


Figure 5.3. Normalised interfacial scattering length density profiles for the dDG/pp interface (e.g. HM10D) compared to that of the pp/air interface (e.g. HM10). Deposition of the overlying dDG film roughens the interface it is deposited on, which is magnified if the substrate plasma polymer is deposited at lower power.

Table 5.3. Film thickness, scattering length density and roughness of single and bilayer plasma polymer films as used for NR model fitting. For single layer film, layer 1 refers to the bulk of the pp, and layer 2 is the transition region between pp and Si wafer. For the bilayer system layer 1 means the deuterated DG layer on the top, while layer 2 refers to the underlying plasma polymer film that is close to the Si wafer substrate. For the single layer system it was possible to distinguish two regions of slightly different SLD, with a thin layer of different SLD adjacent to the Si wafer.

NR	Thickness (Å)		SLD ( $\times 10^6 \text{ \AA}^{-2}$ )		Roughness (Å)	
	1	2	1	2	Air/1	1/2
<b>Single</b>						
<b>HM10</b>	120.5±1.0		0.17±0.01		2.1±1.3	
<b>HM20</b>	167.6±2.6	26.6±2.5	0.27±0.01	1.61±0.18	10.9±2	8.2±3.8
<b>DG20</b>	144.0±1.6	62.3±1.6	1.17±0.01	0.99±0.01	3.2±1.0	2
<b>DG40</b>	106.7±13.6	57.8±1.2	0.94±0.02	0.78±0.32	11.1±1.0	15.8±5.0
<b>AA20</b>	163.9±3.4	29.9±6.0	1.95±0.01	2.16±0.03	4.9±0.4	7.5±2.1
<b>AA40</b>	110.4±0.7	99.8±2	2.25±0.01	2.15±0.01	5.6±0.2	5.0±1.2
<b>Bilayer</b>						
<b>HM10D</b>	173.4±0.2	122.4±0.5	6.92±0.04	0.45±0.04	6.4±0.1	17.1±0.2
<b>HM20D</b>	174.9±0.1	178.5±1.3	6.77±0.04	0.48±0.03	3.2±0.1	12.7±0.1
<b>DG20D</b>	186.2±0.1	225.3±0.5	6.47±0.02	1.33±0.02	5.5±0.09	12.3±0.1
<b>DG40D</b>	184.5±0.1	176.0±0.4	6.58±0.02	1.53±0.02	4.1±0.1	11.9±0.1
<b>AA20D</b>	189.5±0.2	171.2±4.6	6.59±0.03	1.98±0.05	4.9±0.1	11.8±0.2
<b>AA40D</b>	173.6±0.2	216.5±4.8	6.67±0.05	2.24±0.07	4.4±0.1	10.7±0.2

For single layer HMDSO, AA and DG films, the best structural model consists of a thin transition layer between the Si substrate and the layer describing the majority of the

plasma polymer film, except for HM10 (one layer) as shown in table 5.3. The depth of this transition layer varied depending on the starting monomers and deposition conditions used.

Considering films deposited from the same monomer, the data suggests that higher load powers resulted in rougher films (two fold increase in roughness). This can be expected because during plasma polymerisation, higher load powers will result in a greater degree of monomer fragmentation and faster recombination. The films with high deposition rates, which grow in thickness the fastest, may have larger clusters of molecules recombining in the plasma glow discharge that will result in rougher surfaces and interfaces.

A comparison of lower power deposited single layer plasma polymer films in terms of the calculated NR roughness displayed the general trend of AA > DG > HMDSO. HMDSO films resulted in the smoothest films and AA films were the roughest which could be attributed to many factors. For example, a number of complex processes occurring during plasma polymerisation and slight changes in the deposition parameters such as load power, monomer pressure, flow rate or electrode geometries may lead to a different finding.

For the double layer plasma polymer films, the model is simple, which includes the dDG film (layer 1) and underlying pp film deposited on the Si wafer (layer 2). In this model, the roughness of layer 2 manifests the interfacial length of the two plasma polymer films. It is evident that all films comprise an intermixing region, which is greater than 1 nm. The films produced at higher load powers (with same monomer) seem to withstand the modification better because they always show less of an increase in roughness. Amongst the pp films that used as layer 2, the interfacial region of HM10D (17.1 Å) demonstrated the most dramatic increase in roughness compared with HM10 single layer (2.1 Å). Although the DG20D has shown nearly 4 fold increase in roughening, it is only half of that of the HM10D film. For AA20D films, the interface mixing is much smaller compared with HM10D and DG20D. However, those lower load powers deposited films all have bigger changes in interface roughness in comparison with the 40 W generated films of the same starting monomer. For both HMDSO and DG films

deposited at 40 W, the dDG/pp interface roughness and single layer pp/air roughness were similar. The possible reasons for these changes will be discussed later.

Yet, looking closely at the model parameters again, it is easy to notice that the SLDs of HMDSO and DG layers in the bilayer system increased by an amount that is more than the measured experimental variation, and the SLDs for AA films stayed the same. One may suspect that the films chemistry and properties are somewhat different from the single layer HMDSO and DG films. A likely reason for this finding is that the interface region is composed of materials from both the base layer and the dDG layer, and the distinct scattering profile of the dDG20 is contributing to the final SLD of the base layer.

The structures of all six dDG20 films were alike although they are prepared from six individual reactions. In fact, this showed the reproducibility of plasma polymer films deposited under the same parameters. The data also showed that NR measurements are reliable for distinguishing small deviations in the multi layer plasma polymer films' properties. The large SLD of dDG20 (average  $6.67 \times 10^6 \text{ \AA}^{-2}$ ) compared with SLD of DG20 ( $1.17 \times 10^6 \text{ \AA}^{-2}$ ) was due to the increased deuterium scattering as all other elements in the film were the same (carbon and oxygen). One parameter that did change among the dDG20 films was the roughness values. All six dDG20 films displayed a rougher pp/air interface in contrast with the single layer DG20 film (3.2  $\text{\AA}$ ). It is hypothesised that the decrease in smoothness of the dDG layer (compared with DG20 film) is because the plasma polymer replicated the surface morphology of the substrate, in this case the underlying pp films. The base pp films had contour of their own, and were further modified during the second plasma polymerisation process, which led to uneven surface texture (relative measure). When the dDG20 layer grew from the interface, it followed the outline, however, this film growth gradually smoothed out the irregularity of the substrate layer. It is worth noting that, the increase in dDG20 layer roughness is proportional to the degree of broadening of the interface. For HMDSO and DG films made at the lower load powers, which possess a greater broadening at the interface, the resultant dDG layer were rougher.

### 5.3.2 Chemical bonds at the interface

It is important to know what causes the difference in the interfacial structure. At first, we turned to the degree of unsaturation between films made at low and high load powers. The XPS high resolution C 1s spectra (Figure 5.4) did not show significant different for the HMDSO and AA films, as the overlay of the spectra presents an identical shape. Once again, all six dDG20 layers show similar bonding environments, which consist of two major components, hydrocarbon bonds (285 eV) and C-O bonds (286.5 eV). So far, it is reasonable to infer that the plasma environment produced in the dDG20 plasma polymerisation was consistent throughout the substrate deposition process.

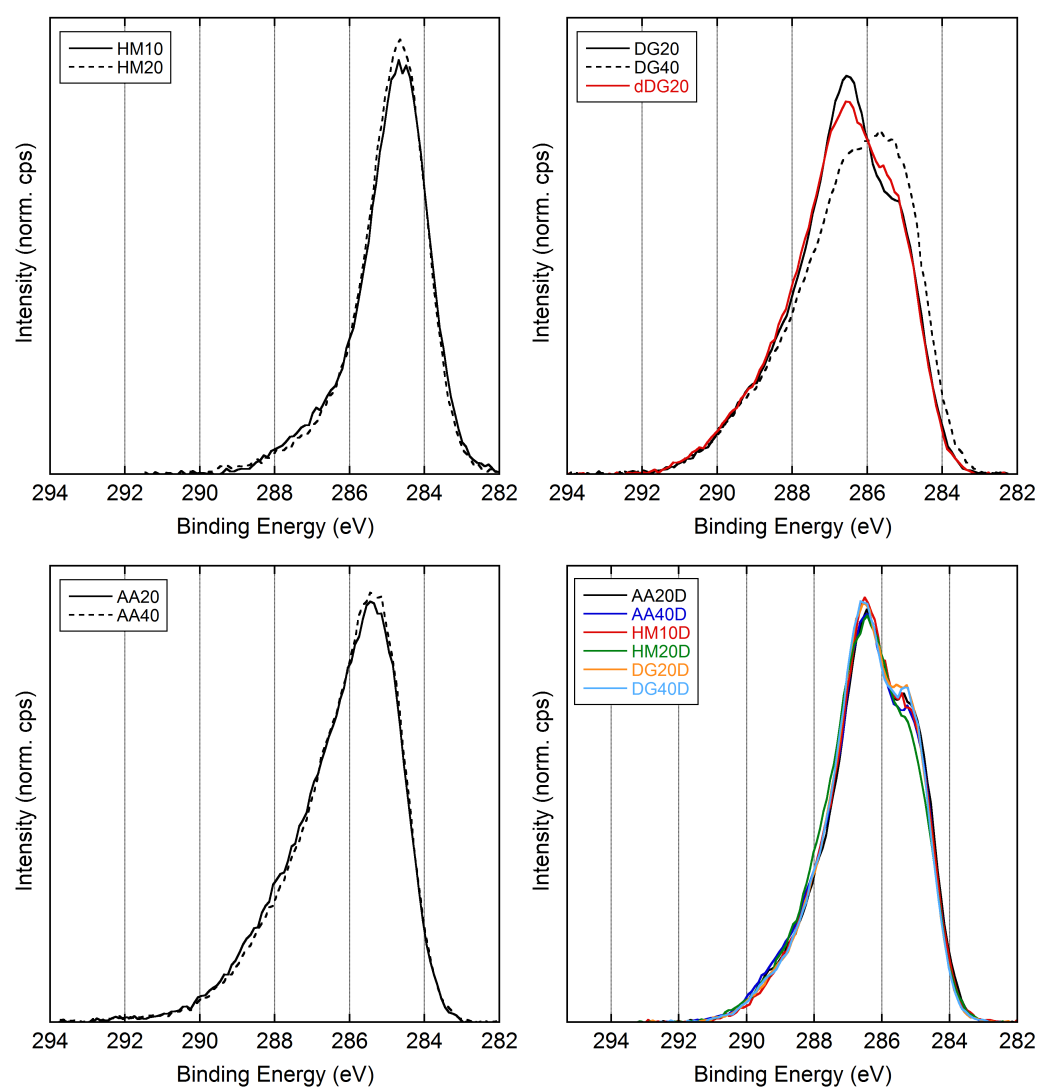


Figure 5.4, Overlay of high-resolution C 1s spectra of HMDSO, DG, AA and dDG plasma polymer films.

By overlaying the average dDG20 profile onto the DG20 spectra (Figure 5.4), a slight decrease in the ether component and increase in hydrocarbon concentration can be observed. This could be ascribed to the presence of deuterium in replacement of hydrogen, which will contribute to subtle changes in the dissociation of chemical bonds and recombination processes during plasma polymerisation.

It is clear however from figure 5.4 that the DG40 film contained more hydrocarbon and less ether units compared with the DG20 plasma polymer film. This strongly indicates that the DG40 plasma polymer film was more unsaturated. Since the bond energy of unsaturated bonds is significantly higher than those of single bonds,<sup>41</sup> with equal amount of ions/radicals bombardment, the single bonds will fragment more often. Therefore, the film containing more single bonds (the DG20 film) was etched away to a larger extent at the interface compared with the DG40 film that would require more energy to ionise, fragment and remove. Hence the interface of DG20D is rougher than DG40D.

To apply this hypothesis that bond dissociation energy requirement led to a different amount of etching at the dDG/pp interface, it is essential to be able to distinguish the variation in bonding environments of HMDSO and AA films. To gain insight into the major difference in chemical binding of those films, full atomic composition of the films can be compared. Herein, by simultaneously fitting the composition and mass density to the average X-ray and neutron SLD values determined from the *Motofit* model along with the XPS results, estimates of the film composition can be made.<sup>27</sup> The assumption in these calculations is that the surface composition (atomic %) determined by XPS is an accurate representation to those in the bulk. The estimated full composition and the film mass density are shown in table 5.4.

For HMDSO film, when we compare the composition of both HM10 and HM20 to the monomer composition, there is significantly less C and H, which confirmed the argument that during HMDSO plasma polymer formation process methyl abstraction is the major fragmentation pathway. Inside each plasma polymer, the bonds would be distinctly different from the original monomer and the highly crosslinked network make it impossible to determine a chemical structure from the stoichiometric composition

alone. Herein, a simpler approach will be used to point out the potential difference in the bonding environment. Since the bond energy of O-Si in HMDSO is estimated to be 8.31 eV, which is two times higher than that of C-Si bond (4.53 eV), there should be a larger extent of O-Si retention in the plasma polymerised films.<sup>42</sup> Herein, we assume the O in HM10 (0.52) and HM20 (0.52) pp films were bound to Si first at 1:2 ratio, and the 'extra' O would form new bonds with C or H or Si. The amount of 'extra' O in HM10 and HM20 were 0.16 and 0.2 respectively, i.e. there is higher concentration of O-C or O-H or O-Si bonds in HM20 film. Given same amount of plasma bombardment from dDG 20 W film, more bonds in HM10 film would be dissociated. This is consistent with the results discussed earlier that HM10D have broader interface compared with HM20D.

Table 5.4, Mass density and composition of all single and bilayer plasma polymer films as determined by NR and XRR in combination with XPS elemental ratios. Layer 1 refers the dDG layer on the top, while layer 2 represents the underlying plasma polymer film that is close to the Si wafer substrate. The theoretical monomer compositions are shown for comparison.

<b>Single layer</b>	<b>Composition</b>		<b>Mass density (g cm<sup>-3</sup>)</b>	
<b>HM monomer</b>	C <sub>1</sub> O <sub>0.17</sub> Si <sub>0.33</sub> H <sub>3</sub>		-	
<b>HM10</b>	C <sub>1</sub> O <sub>0.51</sub> Si <sub>0.70</sub> H <sub>3.02</sub>		1.06	
<b>HM20</b>	C <sub>1</sub> O <sub>0.52</sub> Si <sub>0.64</sub> H <sub>2.89</sub>		1.25	
<b>DG monomer</b>	C <sub>1</sub> O <sub>0.5</sub> H <sub>2.33</sub>		-	
<b>DG20</b>	C <sub>1</sub> O <sub>0.43</sub> H <sub>1.61</sub>		1.29	
<b>DG40</b>	C <sub>1</sub> O <sub>0.36</sub> H <sub>1.56</sub>		1.03	
<b>AA monomer</b>	C <sub>1</sub> N <sub>0.33</sub> H <sub>0.33</sub>		-	
<b>AA20</b>	C <sub>1</sub> O <sub>0.20</sub> N <sub>0.13</sub> H <sub>1.23</sub>		1.34	
<b>AA40</b>	C <sub>1</sub> O <sub>0.21</sub> N <sub>0.12</sub> H <sub>1.06</sub>		1.35	
<b>Bilayer</b>	1	2	1	2
<b>HM10D</b>	C <sub>1</sub> O <sub>0.41</sub> D <sub>1.07</sub>	C <sub>1</sub> O <sub>0.52</sub> Si <sub>0.70</sub> H <sub>2.58</sub>	1.47	1.11
<b>HM20D</b>	C <sub>1</sub> O <sub>0.42</sub> D <sub>1.15</sub>	C <sub>1</sub> O <sub>0.51</sub> Si <sub>0.63</sub> H <sub>2.55</sub>	1.42	1.21
<b>DG20D</b>	C <sub>1</sub> O <sub>0.40</sub> D <sub>1.12</sub>	C <sub>1</sub> O <sub>0.43</sub> H <sub>1.56</sub>	1.35	1.36
<b>DG40D</b>	C <sub>1</sub> O <sub>0.40</sub> D <sub>1.01</sub>	C <sub>1</sub> O <sub>0.37</sub> H <sub>1.17</sub>	1.42	1.09
<b>AA20D</b>	C <sub>1</sub> O <sub>0.41</sub> D <sub>0.94</sub>	C <sub>1</sub> O <sub>0.20</sub> N <sub>0.13</sub> H <sub>1.25</sub>	1.46	1.46
<b>AA40D</b>	C <sub>1</sub> O <sub>0.40</sub> D <sub>1.05</sub>	C <sub>1</sub> O <sub>0.21</sub> N <sub>0.12</sub> H <sub>1.09</sub>	1.41	1.36

For AA films deposited at 20 and 40 W load power, their compositions were similar, with slight difference in H content. Hence, from the bond dissociation energy theory, it is not surprising the interface roughening of AA20D and AA40D are quite similar. Nonetheless, employing bond energy as the sole factor that determines the trend we obtain among HMDSO, DG and AA films is difficult.

## 5.4. Conclusions

In this chapter, nanometer thin plasma polymer films were prepared via radio frequency glow discharge from four monomers. HMDSO, DG and AA were employed to produce single layer coatings on top of Si wafer substrates. It was found that films deposited at 40 W load power were rougher at the pp/air interface compared with the films generated at lower powers. A set of single layer films was subjected to dDG 20 W plasma polymerisation to over coat a second layer. The interface between dDG/pp was studied with neutron and X-ray reflectometry. Through the model fitting of the NR data, it was found that deposition of the dDG layer roughens the film/film interface. The magnitude of interfacial broadening was dependent on the underlying plasma polymer film chemistry. For HMDSO, DG and AA films prepared at lower powers, the trend in interface roughening is HM10D > DG20D > AA20D. For films deposited at 40 W load power, the extent of increase in roughness is similar. When the starting monomer is the same for the underlying layer, the interface region of bilayer film is wider if the film is made at lower load power. It is proposed that the differences in binding environment and bond dissociation energy led to the varying extent of roughening between films of same starting monomer.

## 5.5 References

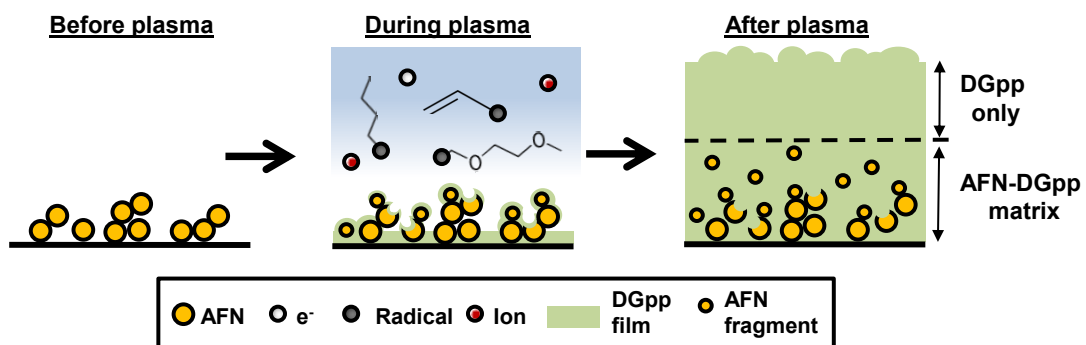
1. P. M. Martin, in *Introduction to Surface Engineering and Functionally Engineered Materials*, John Wiley & Sons, Inc., 2011, DOI: 10.1002/9781118171899.ch8, pp. 457-507.
2. A. Biswas, I. S. Bayer, A. S. Biris, T. Wang, E. Dervishi and F. Faupel, *Advances in Colloid and Interface Science*, 2012, 170, 2-27.

3. H. Yasuda and M. Gazicki, *Biomaterials*, 1982, 3, 68-77.
4. H. Biederman and D. Slavínská, *Surface and Coatings Technology*, 2000, 125, 371-376.
5. T. Desmet, R. Morent, N. D. Geyter, C. Leys, E. Schacht and P. Dubruel, *Biomacromolecules*, 2009, 10, 2351-2378.
6. M. P. Bonnar, J. I. B. Wilson, B. M. Burnside, R. L. Reuben, T. R. Gengenbach, H. J. Griesser and G. Beamson, *Journal of Materials Science*, 1998, 33, 4843-4855.
7. B. W. Muir, A. Tarasova, T. R. Gengenbach, D. J. Menzies, L. Meagher, F. Rovere, A. Fairbrother, K. M. McLean and P. G. Hartley, *Langmuir*, 2008, 24, 3828-3835.
8. Q. Cheng and K. Komvopoulos, *The Journal of Physical Chemistry C*, 2008, 113, 213-219.
9. K. Vasilev, A. Michelmore, P. Martinek, J. Chan, V. Sah, H. J. Griesser and R. D. Short, *Plasma Processes and Polymers*, 2010, 7, 824-835.
10. L. Denis, D. Cossement, T. Godfroid, F. Renaux, C. Bittencourt, R. Snyders and M. Hecq, *Plasma Processes and Polymers*, 2009, 6, 199-208.
11. J. Tyczkowski, in *Plasma Polymer Films*, Imperial college press and distributed by world scientific publishing CO. ,2004, pp. 143-216.
12. N. P. Reynolds, K. E. Styan, C. D. Easton, Y. Li, L. Waddington, C. Lara, J. S. Forsythe, R. Mezzenga, P. G. Hartley and B. W. Muir, *Biomacromolecules*, 2013, 14, 2305-2316.
13. C. Choi, D. Jung, D. W. Moon and T. G. Lee, *Surface and Interface Analysis*, 2011, 43, 331-335.
14. A. J. Beck, S. Candan, R. D. Short, A. Goodyear and N. S. J. Braithwaite, *The Journal of Physical Chemistry B*, 2001, 105, 5730-5736.
15. L. H. Andrew, T. Helmut, Q. Jamie and H. V. Nicolas, *Surface Science*, 2008, 602.
16. D. E. Robinson, L. E. Smith, D. A. Steele, R. D. Short and J. D. Whittle, *Biomaterials Science*, 2014, 2, 875-882.
17. W.-J. Yoon, D. Bhattacharyya, R. B. Timmons and P. R. Berger, *Organic Electronics*, 2010, 11, 1767-1771.
18. R. P. Patel, D. Chiavetta and C. A. Wolden, *Journal of Vacuum Science & Technology A: Vacuum, Surfaces, and Films*, 2011, 29, 061508-061508-061506.
19. T.-N. Chen, D.-S. Wu, C.-C. Wu, C.-C. Chiang, Y.-P. Chen and R.-H. Horng, *Plasma Processes and Polymers*, 2007, 4, 180-185.

20. W. E. S. Unger, S. Swaraj, U. Oran and A. Lippitz, *Surface and Interface Analysis*, 2006, 38, 522-525.
21. S. Swaraj, U. Oran, J. F. Friedrich, A. Lippitz and W. E. S. Unger, *Plasma Processes and Polymers*, 2007, 4, 376-389.
22. I. Retzko, J. F. Friedrich, A. Lippitz and W. E. S. Unger, *Journal of Electron Spectroscopy and Related Phenomena*, 2001, 121, 111-129.
23. A. G. Shard, J. D. Whittle, A. J. Beck, P. N. Brookes, N. A. Bullett, R. A. Talib, A. Mistry, D. Barton and S. L. McArthur, *The Journal of Physical Chemistry B*, 2004, 108, 12472-12480.
24. S. Sharma, R. W. Johnson and T. A. Desai, *Biosensors and Bioelectronics*, 2004, 20, 227-239.
25. Y. Zhang, J. Arfsten, S. Pihan, T. Kaule, R. Förch and R. Berger, *Journal of Colloid and Interface Science*, 2010, 351, 532-536.
26. V. Cech, R. Trivedi and D. Skoda, *Plasma Processes and Polymers*, 2011, 8, 1107-1115.
27. B. W. Muir, A. Nelson, A. Fairbrother, C. Fong, P. G. Hartley, M. James and K. M. McLean, *Plasma Processes and Polymers*, 2007, 4, 433-444.
28. J. A. Dura, D. J. Pierce, C. F. Majkrzak, N. C. Maliszewskyj, D. J. McGillivray, M. Lösche, K. V. O'Donovan, M. Mihailescu, U. Perez-Salas, D. L. Worcester and S. H. White, *Review of Scientific Instruments*, 2006, 77, 074301-074301-074311.
29. A. Nelson, B. W. Muir, J. Oldham, C. Fong, K. M. McLean, P. G. Hartley, S. K. Øiseth and M. James, *Langmuir*, 2005, 22, 453-458.
30. D. J. Menzies, A. Nelson, H.-H. Shen, K. M. McLean, J. S. Forsythe, T. Gengenbach, C. Fong and B. W. Muir, *Journal of The Royal Society Interface*, 2012, 9, 1008-1019.
31. H. S. Jeon, J. Wyatt, D. Harper-Nixon and D. H. Weinkauff, *Journal of Polymer Science Part B: Polymer Physics*, 2004, 42, 2522-2530.
32. S. Peri, B. Akgun, S. Satija, H. Jiang, J. Enlow, T. Bunning and M. Foster, *ACS applied materials & interfaces*, 2011, 3, 3375-3383.
33. S. R. Peri, B. Habersberger, B. Akgun, H. Jiang, J. Enlow, T. J. Bunning, C. F. Majkrzak and M. D. Foster, *Polymer*, 2010, 51, 4390-4397.
34. H. Kim, M. D. Foster, H. Jiang, S. Tullis, T. J. Bunning and C. F. Majkrzak, *Polymer*, 2004, 45, 3175-3184.

35. M. James, A. Nelson, S. A. Holt, T. Saerbeck, W. A. Hamilton and F. Klose, *Nuclear Instruments and Methods in Physics Research Section A: Accelerators, Spectrometers, Detectors and Associated Equipment*, 2011, 632, 112-123.
36. A. Nelson, *Journal of Applied Crystallography*, 2006, 39, 273-276.
37. A. Michelmore, P. M. Bryant, D. A. Steele, K. Vasilev, J. W. Bradley and R. D. Short, *Langmuir*, 2011, 27, 11943-11950.
38. T. R. Gengenbach and H. J. Griesser, *Polymer*, 1999, 40, 5079-5094.
39. S. Lucas, G. Genard, C. Michiels, B. Masereel, O. Feron, B. Gallez, T. Vander Borghet and N. Moreau, *Nuclear Instruments and Methods in Physics Research Section B: Beam Interactions with Materials and Atoms*, 2008, 266, 2494-2497.
40. Y. Li, B. W. Muir, C. D. Easton, L. Thomsen, D. R. Nisbet and J. S. Forsythe, *Applied Surface Science*, 2014, 288, 288-294.
41. R. T. Sanderson, in *Polar Covalence*, ed. R. T. Sanderson, Academic Press, 1991, pp. 91-99.
42. D. Magni, D. Ch, H. Ch, A. Creatore and P. Fayet, *Journal of Physics D: Applied Physics*, 2001, 34, 87.

## Chapter 6 Diglyme film growth on amyloid fibril network



*"The snow highlights the contours of the land."  
- NASA Earth Observatory*

---

## Abstract

Within the area of biomaterials research, the ability to tailor the surface chemistry while presenting biomimetic topography is a useful tool for studying cell-surface and cell-cell interactions. For the study reported here we investigated the deposition of diglyme plasma polymer films (DGpp) onto amyloid fibril networks (AFNs), which have morphologies that mimic the extracellular matrix. We extended previous work (**Appendix 3**) to observe that the nanoscale contours of the AFNs are well preserved even under very thick layers of DGpp, but that the width of the surface features is positively correlated to DGpp thickness. DGpp thickness growth was conformal to the underlying fibril features, with a gradual smoothing out of the resultant surface topography. Further, to understand how the films grow on top of AFNs, X-ray photoelectron spectroscopy depth profiling was employed to determine the elemental composition within the coating perpendicular to the plane of the substrate. It was found that AFNs partially fragment during the initial stage of plasma polymerisation, and these fragments then mixed with the growing DGpp to form an intermixed interface region above the AFN. The findings in this study are likely applicable to situations where plasma polymerisation is used to apply an overcoat to adsorbed organic and/or biological molecules.

## 6.1 Introduction

The host response to a particular biomaterial is largely governed by the surface chemistry and topography of that material.<sup>1</sup> Modification of the outermost layers of a biomaterial is commonly employed as a means to provide desired biological responses and thus retain device functionality.<sup>2-5</sup> Subtle variations in surface morphology can lead to changes in cell attachment and proliferation,<sup>6-8</sup> and in the case of stem cells, differentiation.<sup>9-11</sup> A number of methods are available for creating nano- to microscale features on a substrate surface.<sup>12-16</sup> A drawback of these techniques is that the surface structures produced do not mimic the typical nanoscale fibrous morphology of the extracellular matrix (ECM) where cells normally reside. Therefore, approaches to obtain fibrous biomimetic surface architectures have attracted more attention.

Biomimetic nanostructured fibril networks can be fabricated in two or three dimensions through the self-assembly of peptides or proteins, into nanoscale fibrils.<sup>17-20</sup> Non-toxic amyloid fibrils represent one promising subset of such self-assembled materials due to their ease of formation and the ability to accurately control the fibrous morphology. Amyloid fibril networks (AFNs) deposited on solid supports have been previously shown to promote cell adhesion and spreading in a variety of cell types.<sup>21, 22</sup> To mask the effect of native functional groups present within AFNs and study the topographical effects in isolation, we have previously reported on utilising plasma polymerisation to coat the AFN (**Appendix 3**).<sup>23</sup>

Plasma polymerisation is a solvent-less process that produces uniform, defect free coatings in one step. It is frequently used to produce functional coatings for biological applications.<sup>24-26</sup> This convenient technology permits the use of an exceptionally wide range of precursors, including gases, volatile compounds, and solids that can release vapour upon sublimation. Recently, peptides, amino acids<sup>27-29</sup> and other biological molecules<sup>30</sup> have been exploited as precursors for plasma polymerisation. In other studies, antibiotics<sup>31, 32</sup> were first deposited onto a substrate and subsequently coated

with a plasma polymer film, which served as a barrier for the controlled diffusion of the underlying antibacterial molecules. Future research on the direct interaction of biological molecules with the plasma glow discharge environment is warranted.

In our previous study, plasma polymer films were prepared from diethylene glycol dimethyl ether (diglyme) precursor on top of AFNs that was adsorbed on mica.<sup>23</sup> The diglyme plasma polymer (DGpp) coatings displayed the contours of the AFNs, preserving the fibrous topography with only a slight broadening effect of the fibril widths. Here, we employed a series of diglyme plasma polymer deposition times, thus producing films of different thickness to explore this phenomenon. Remarkably, the fibrous structure was found to be visible via atomic force microscopy (AFM) on the surface of DGpp films of thicknesses up to 1  $\mu\text{m}$ , albeit with a 3 fold increase in the fibril width. We also investigated the growth mechanisms of the AFN-DGpp constructs. During plasma deposition, the substrate, AFN, and the growing coating will each be exposed to energetic ions from the plasma. We hypothesised that the AFNs will be fragmented to a certain extent in this environment, but then eventually buried and protected by the growing DGpp films. The distribution of AFN fragments throughout the constructs was probed by X-ray photoelectron (XPS) depth profiling. A model of the growth process is presented based on the XPS chemical analysis.

## **6.2 Materials and methods**

### **6.2.1 Substrate preparation**

Ultra-flat single crystal silicon wafers were cleaned in the same way as outlined in previous chapters, and were used as substrates for the deposition of diethylene glycol dimethyl ether (BDH, 99 % purity) plasma polymer films. Mica pieces were cleaved from the middle using tweezers and the exposed clean surface was used immediately.

### 6.2.2 Amyloid fibril network

Hen egg white lysozyme (HEWL) (Sigma) was self-assembled into amyloid fibrils in controlled reaction conditions. HEWL was first dialysed following the method used in Jung et al.<sup>33</sup> HEWL solutions (2 wt %) were prepared in glass vials by dissolving the purified protein in Milli-Q water and adjusting the pH to 2 using HCl. Solutions were placed in an oil bath where the temperature were kept at 90 °C constant for 24 h. Solutions were stirred at 300 rpm using a 20 x 5 mm Teflon magnetic stirrer bar during the whole reaction time, following the established method by Lara et al.<sup>17</sup> After the reaction, solutions were quenched by immersion the glass vials in a water-ice bath. To form amyloid fibril networks (AFNs), 100 µL of the fibril solution was pipetted onto mica substrates and incubated for 10 min at room temperature, followed by rinsing in Milli-Q water (1 mL), and drying under a gentle stream of nitrogen.

### 6.2.3 Plasma polymerisation

Deposition of plasma polymer films was carried out in the custom-built reactor as described in **chapter 3**. The parameters chosen for deposition of DGpp films were load power of 50 W with an initial monomer pressure of 20 Pa at 125 KHz. The treatment time ranged from 30 s to 33 min. For treatments of more than 3 min, the deposition was performed in 3 min increments, with 15 min intervals to avoid overheating of the electrodes.

### 6.2.4 Profilometry

A Veeco Dektak 6M Stylus profilometer was used to determine the film thickness. Masked areas were prepared using 10 w/v % solution of poly(D,L-lactide) (Boehringer Ingelheim) in acetone.<sup>34</sup> One drop of the solution was placed on a substrate and dried in air 10 min prior to film deposition. Following plasma polymerisation, the mask was lifted off the substrate using tweezers. Then, the profilometry stylus (width 12.5 µm),

with force set to 10 mg, was drawn a distance of 400  $\mu\text{m}$  across the edge of the masked area and the film over 10 s.

### **6.2.5 Focused Ion Beam Scanning Electron Microscopy**

The thickness of the 50 W DGpp films deposited on AFN coated mica was determined using a focused ion beam scanning electron microscope (FIB-SEM) (FEI Helios NanoLab 600 DualBeam FIB-SEM, Eindhoven, Netherlands). Prior to FIB-SEM analysis, the samples were coated with a layer of Au for better conductivity. Cross sections on the samples were created by focused ion beam (FIB) of Ga<sup>+</sup> ions emitted with an accelerating voltage of 30 kV at normal incidence to the sample. All cross sections were then milled by a selective carbon gas injection system with ion current of 98 pA for creating the trench, followed by polishing step at 28 pA to minimise FIB-induced artefacts. The milled cross sections were then imaged in situ using the SEM component of the FIB-SEM system.

### **6.2.6 Atomic force microscopy**

AFM measurements were performed using the same instrument as described in previous chapters. Typical scan settings include an applied piezo deflection voltage of 0.6 – 0.7 V at a scan rate of 0.8 Hz. All images were processed (1<sup>st</sup> order flattening algorithm) using Igor Pro software. Three 3.5  $\mu\text{m}$  x 3.5  $\mu\text{m}$  scan images per coating condition were imported to Image J software (National Institutes of Health, USA) for determination of fibril widths. After setting appropriate scale to the images, lines were drawn on the fibril structure perpendicular to the longitudinal direction to record the width of the fibril.

### 6.2.7 X-ray photoelectron spectroscopy

X-ray photoelectron spectroscopy (XPS) analysis was performed using the AXIS Ultra DLD spectrometer described in chapter 3. The detection limit of nitrogen was lowered to approximately 0.01%, through addition of a separate scan with reduced sweep range but at longer sweep time over the N region.

Depth profiling was performed using an ion gun employing alternately an Ar and a polyatomic hydrocarbon (PAH; coronene) ion source. The operating conditions for Ar etching were 5 kV and 10 mA emission current, while for PAH etching they were 12 kV filament voltage and 5 mA emission current. For both ion sources, a 2 x 2mm etch crater was employed.

## 6.3 Results and discussion

### 6.3.1 Thickness measurements of DGpp + AFN constructs

The deposition rate of DGpp on Si wafer was examined by measuring thickness with profilometry (Figure 6.1a). A linear trend was observed in the thickness as a function of time, with a deposition rate of approximately 1.34 nm/s. The same methodology for measuring thickness was not applicable to films on mica as its transparency made it difficult to locate the masked area, and so a combination of three alternative techniques was used; (i) FIB-SEM, (ii) AFM measurements of a masked area, and (iii) XPS overlayer thickness calculations for very thin samples (Figure 6.1b). A linear trend in thickness was also observed for the DGpp + AFN construct, providing confidence in the validity of combining these alternative techniques. The rate of deposition of the DGpp on top of the AFN on mica (approximately 0.48 nm/s) was substantially reduced when compared to the deposition rate on a Si wafer, which is consistent with our previous work where a 180 s DGpp film grown on an AFN coated mica substrate was thinner than the corresponding film grown on either clean mica or Si wafer.<sup>23</sup> A summary of the

thickness measurements (Table 6.1) and a representative image from FIB-SEM analysis (Figure 6.2) are presented here.

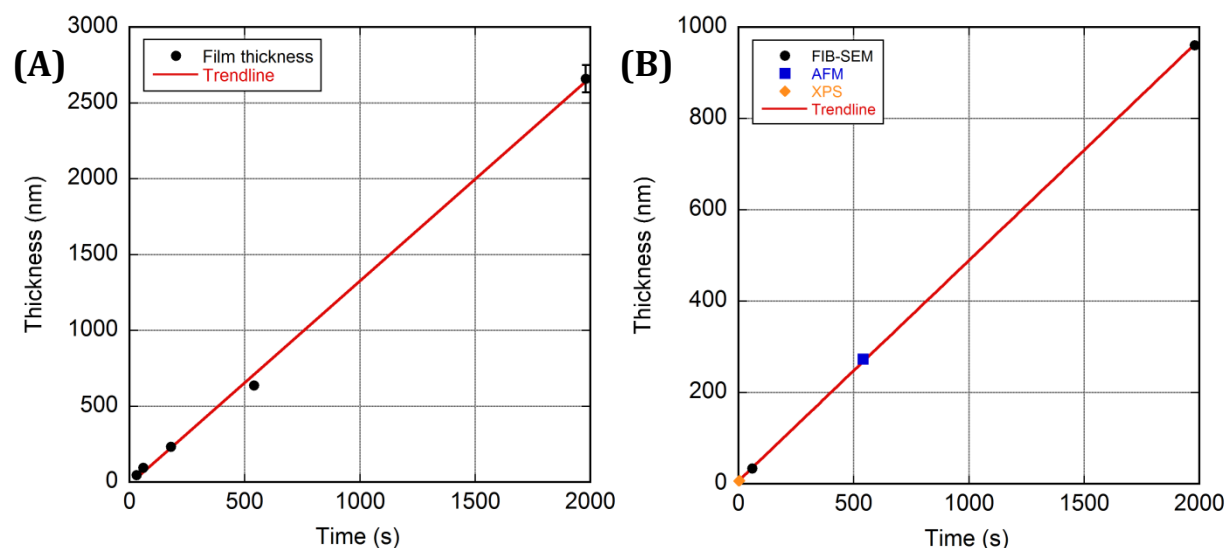


Figure 6.1: Film thickness vs. deposition time for (a) DGpp on Si wafer measured using profilometry and (b) DGpp + AFN on mica measured using a combination of three alternative techniques; (i) FIB-SEM, (ii) AFM measurements of a masked area, and (iii) XPS overlayer thickness calculations for very thin samples.

Table 6.1, Thickness data of DGpp + AFN on mica at various time points, measured using XPS, AFM, and FIB-SEM techniques. These data can fit a linear trendline, as shown in figure 6.1. The values for 30 s and 180 s are derived from the linear model fit.

<i>Time (s)</i>	<i>Thickness (nm)</i>	<i>Measurement method</i>
2	6.47	XPS
4	7.43	XPS
60	$33.71 \pm 2.49$	FIB-SEM
540	$273.58 \pm 6.35$	AFM
1980	$961.05 \pm 14.99$	FIB-SEM
30	21.218	-
180	93.638	-

\* Where data presented in mean  $\pm$  standard error,  $n \geq 4$ . (for FIB-SEM,  $n > 7$ )

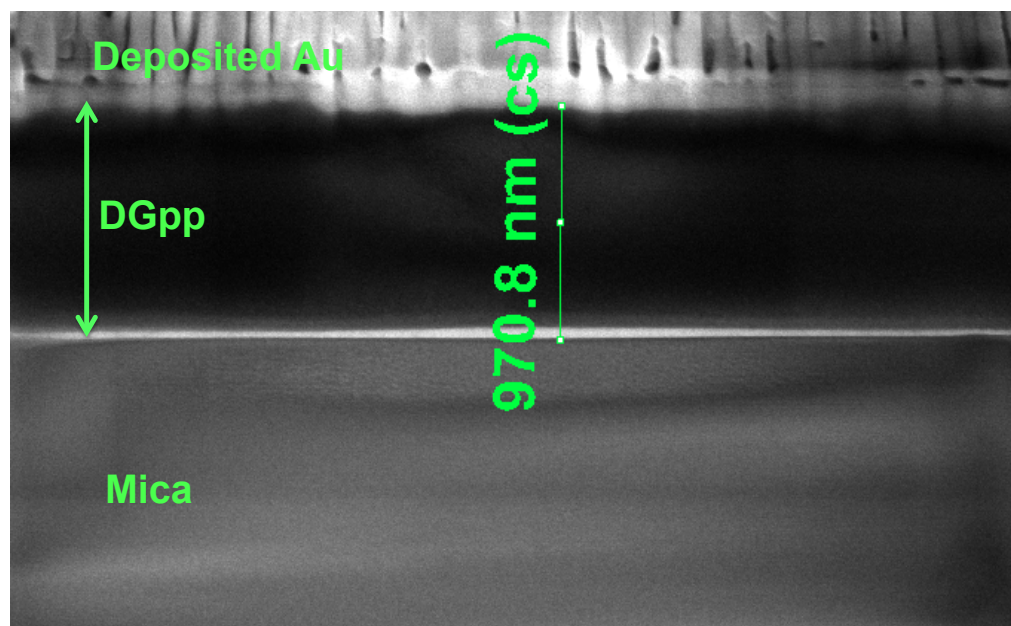


Figure 6.2, SEM image of the cross section of FIB-milled area of 50 W DGpp + AFN on mica (recorded at 70°), the measurement shown here was taken within FIB-SEM operating software; DGpp deposition time of 1980 s, and the thickness of plasma polymer layer is  $961.05 \pm 14.99$  nm.

### 6.3.2 Retention of the AFN topography with increasing DGpp deposition times

AFM was used to further examine the growth of DGpp on bare AFN (Figure 6.3). At all deposition times explored, the structure of the AFN was observed on the top surface of the DGpp layer. At the shortest deposition time, 30 s, the width of the features on the AFN + DGpp construct ( $40.7 \pm 7.8$  nm) were approximately equal to those on the uncoated AFN ( $40.9 \pm 3.1$  nm), albeit with a larger standard deviation (Figure 6.4). An increase in deposition time resulted in an initial sharp increase in feature broadening; the rate of increase in feature broadening reduced for increasing deposition times, resulting in an exponential trend for feature width as a function of deposition time. The results presented herein clearly demonstrate that we are able to easily tune the fibril width observed on the top surface of the DGpp layer by simply controlling the deposition time of the plasma polymer. This methodology thus provides a means of creating a surface that presents a biologically relevant surface topography, where the spatial dimensions and surface chemistry can be easily tuned during the fabrication process.

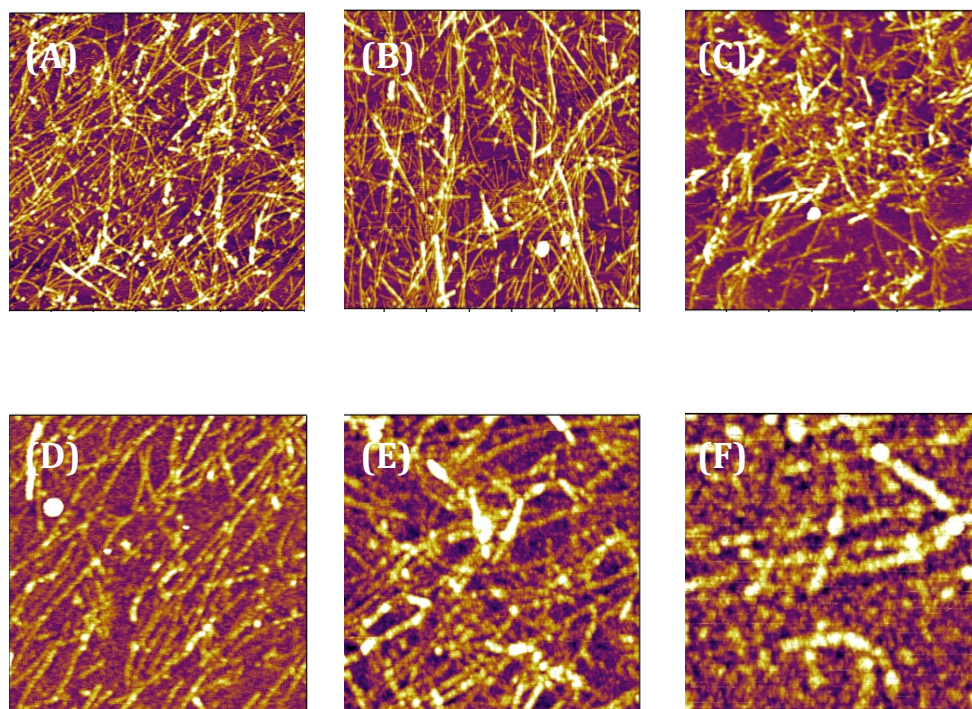


Figure 6.3: AFM images of the topography of bare AFN and 50 W DGpp film coated surfaces,  $3.5 \times 3.5 \mu\text{m}$  scans. (A) AFN, z scale = 10 nm; 50 W DGpp film on AFN with a deposition time of (B) 30s, z scale = 6 nm; (C) 60s, z scale = 6 nm; (D) 180s, z scale = 4 nm; (E) 540s, z scale = 4 nm; (F) 1980s, z scale = 3 nm. The height scale of each image was adjusted to highlight the fibril structure.

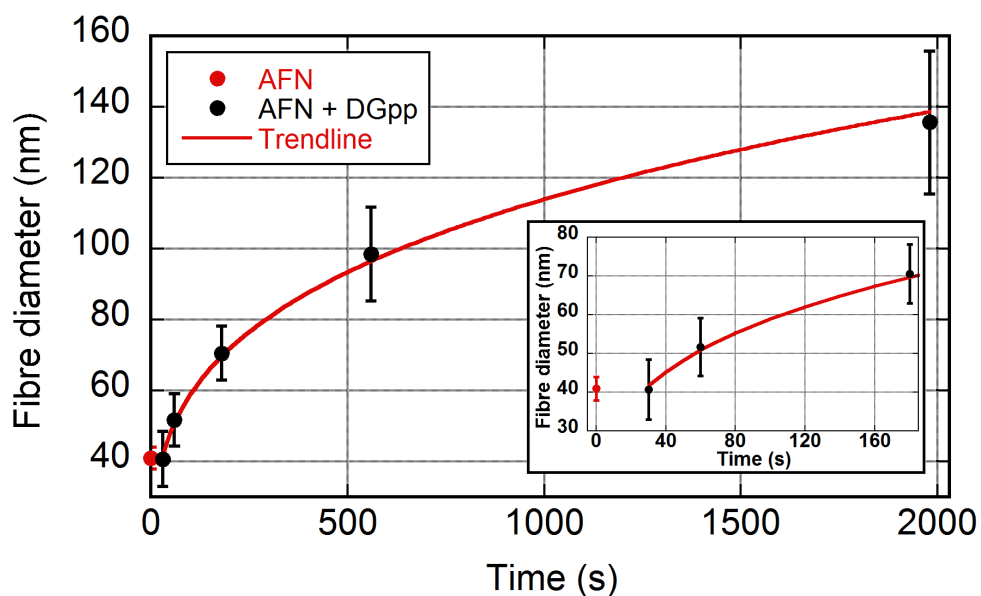


Figure 6.4: Fibril width measured on AFN and DGpp + AFN constructs using AFM as a function of deposition time. Insert highlights first 4 data points corresponding to AFN only or DGpp + AFN fabricated with relatively short deposition times.

### 6.3.3 Elemental distribution through DGpp + AFN constructs

XPS depth profiling provided an insight into the location of the AFN within the DGpp + AFN construct. Both Ar and polyatomic (coronene) ion sources were used. A profile of the elemental composition throughout the bulk of the material can be generated as ions etch through the DGpp + AFN construct by pausing at predetermined times during the etch process to allow collection of XPS data. As a first study, the stability of the AFN on mica to ion etching was examined (Figure 6.5). It is apparent that both sources were able to etch the AFN, however each ion source has differing properties. The Ar ion source etched rapidly, with the bulk of the AFN being removed after only one 10 s etch, as indicated by the significant reduction of N and C, the former unique to the AFN, and the increase in Al, which is unique to mica. Use of the polyatomic source provided a gentler etch of the AFN such that in excess of 300 s was required to obtain similar atomic concentrations. In both cases, the etch rate was lowered as the surface resembled that of pure mica, suggesting that both ion sources are less effective at etching mica when compared with the organic AFN.

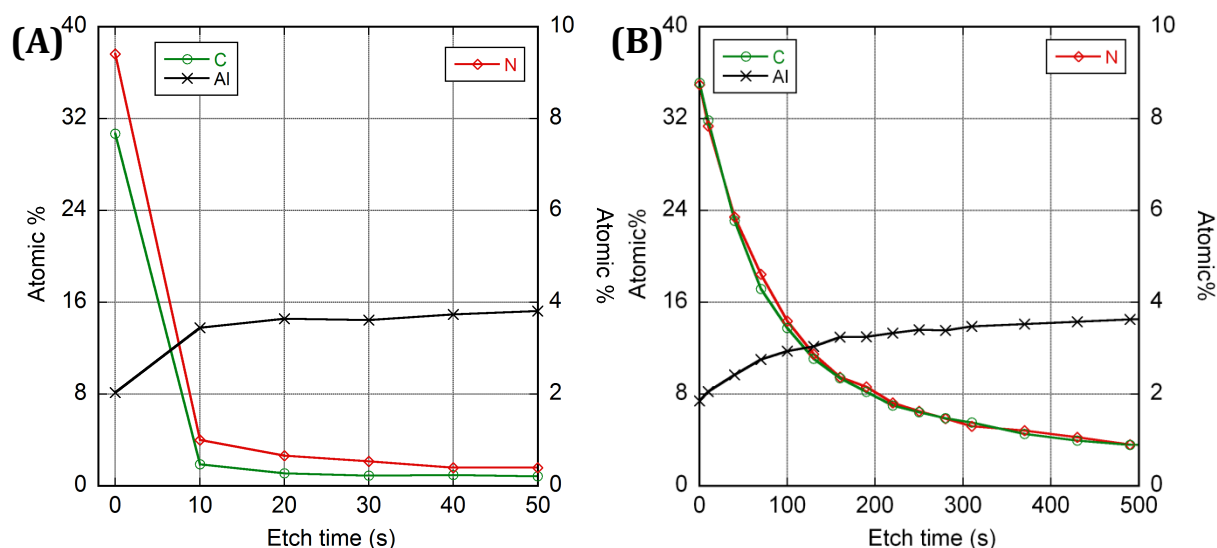


Figure 6.5: Etch profiles of AFN on mica using (A) Ar ion source and (B) PAH ion source.

Then, the AFN + DGpp constructs were analysed. Firstly, the faster Ar ion source was used to explore a relatively thick (180 s, 93.6 nm) sample (Figures 6.6a and b). In Figure 6.6a, a significant decrease in the O content was observed after a single etch cycle, indicating that the Ar ions deoxygenate the DGpp film during the etching process. Deoxygenation of polymers as a result of exposure to ion etching is a known phenomenon and has been examined in detail previously.<sup>35</sup> Thereafter, however, the elemental composition remained approximately constant for 1680s suggesting the presence of a homogenous region, presumably pure DGpp. Then, a small N signal was detected indicating the first appearance of the AFN, and this signal was roughly constant for 180s. At approximately 1900s of etch time the elemental composition began to undergo several significant changes, with C decreasing and O and N increasing, along with first appearance of Al. It is worth noting that the Al 2p peak has the largest inelastic mean free path of the elements examined here, meaning that the sampling depth of Al is the largest (~ 4 nm vs. 3.25 nm for N). Further etching revealed a peak in the N concentration observed at 2100 s, and the C and Al concentrations eventually approach that of freshly cleaved mica.

The interface region where pure DGpp transitions to DGpp + AFN and then to mostly pure mica of the etch profile is replicated in Figure 6.6b focusing on N and Al, which are unique to the AFN and mica, respectively. Since XPS does not sample a discrete atomically thin monolayer, but rather a region representing the sampling depth related to the inelastic mean free path of the individual elements, the position of the mica was estimated to be where the atomic concentration of Al was half of that observed for freshly cleaved mica (i.e. 6.1 %). Based on the etch time required to reach this interfacial concentration (2172 s) and the thickness of the DGpp + AFN construct as determined in Figure 6.1 (93.6 nm), the etch rate was calculated as 0.043 nm/s. Assuming a linear etch profile, N was absent in the first 72.4 nm of material removed suggesting this layer to consist entirely of DGpp. The 21.2 nm below this level, and above the mica surface, would then comprise both AFN and DGpp. The profile of the N concentration vs. time provides further insight into the AFN distribution within this deeper region, as N concentration is initially stable before displaying a rapid increase.

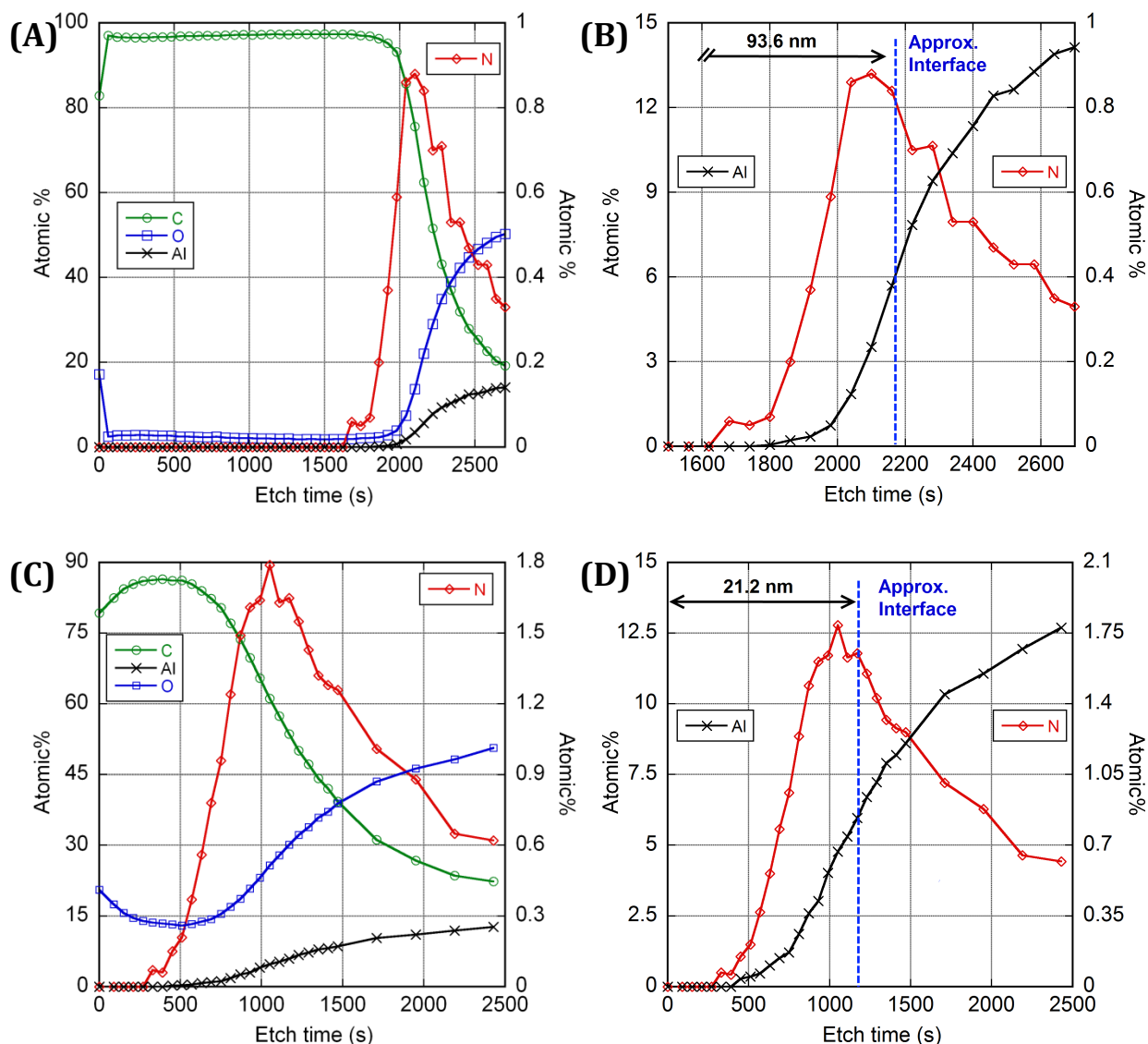


Figure 6.6: Etch profiles of DGpp + AFN constructs. (A) AFN + 180 s DGpp using Ar ion source, (B) focus on interface region of etch profile (A); (C) AFN + 30 s DGpp using PAH ion source, (D) focus on interface region of etch profile (C).

The same analysis was also conducted with a polyatomic source, however a thinner sample (30 s, 21.2 nm) sample was chosen based on the reduced etch rate previously observed for this ion source. The etch profiles are presented in Figures 6.6c and d. Again deoxygenation of the DGpp is observed with the PAH source, however not to the same extent or as rapidly with the Ar source. Earlier than the thicker Ar etched sample, N was detected after only 330 s of etch time, but again it appeared before Al was detected. Also in agreement with previous example, the N content was not detected for 270 s before rapidly increasing, alongside increases to O and decreases to C. A peak in N was again

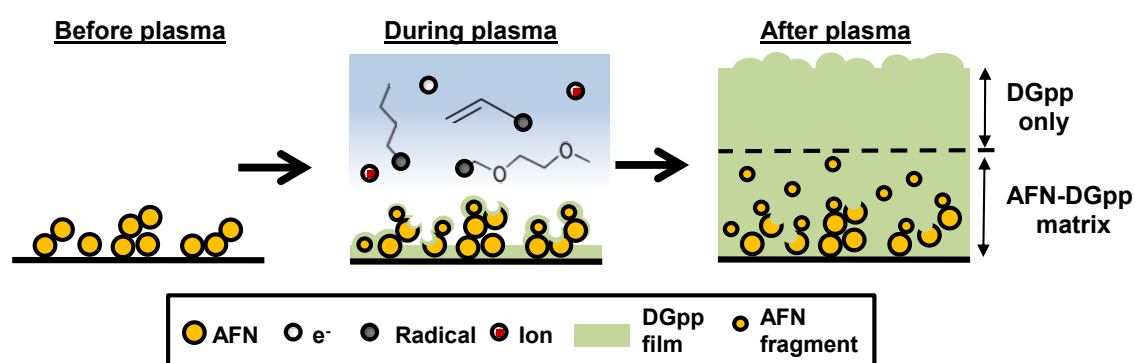
observed, this time at 1050 s, and the Al concentrations eventually approach that of freshly cleaved mica.

The etch profile is replotted in Figure 6.6d focusing on the elements unique to the AFN (N) and mica (Al). The etch time required to reach the mica was calculated as 1182 s, giving an etch rate of 0.018 nm/s through the 21.2 nm thick DGpp + AFN construct. As expected, the etch rate for the PAH source was about half that of the Ar source. If we again assume a linear etch profile, we can calculate that N was absent in the first 5.91 nm of material removed suggesting the uppermost layer to consist entirely of DGpp. At 15.29 nm below this level, and above the mica surface, the film comprised of both AFN and DGpp.

Comparing Figure 6.6b and 6d, it is apparent that the etch profile of the interface region obtained using both ion sources look similar, thus providing confidence in the observed distribution of elements within the DGpp + AFN constructs. Both sets of data indicate that the AFN is not concentrated purely at the mica interface. For the Ar source, N is first detected 21 nm above the mica interface, and 15 nm for the PAH source. Here it should be noted that the morphology of the surface bound fibrils is not cylindrical but that of a flat ribbon structure, as noted by AFM.<sup>17</sup> Thus, whilst the fibrils in the bare AFN have observed widths of approximately 40 nm the vast majority of the fibrils extend less than 10 nm from the surface of the substrate. The differences observed in the absolute value may be due to a number of factors, including sample to sample variation.

In this particular case, however, it is likely that the use of Ar ions has smeared the interface to a certain degree. This assumption is supported by the N concentration profile where the initial N atomic % is stable for 3 cycles (180 s) for Ar, but only 2 cycles (60 s) for PAH. While the AFM images of all the samples studied demonstrate the replication of the AFN structure on the top surface of the DGpp + AFN constructs, the data obtained from both ion sources indicate that there is no evidence of AFN in the vicinity of the top surface of the DGpp. An interesting observation was made after

examining the fibril width data in Figure 6.4; the fibril width of the uncoated AFN was approximately equal to the AFN + DGpp deposited at the shortest time, albeit with a larger standard deviation. This indicates a greater distribution of fibril width values in the measurement for the AFN + DGpp sample. Through the etching and re-deposition process it can be envisaged how a greater spread of fibril width values can be obtained. Thus, providing support to the idea that the AFN is etched during the plasma process. Based on these observations, a mechanism for film formation was devised as detailed in Scheme 6.1.



Scheme 6.1: **Before plasma**, an AFN network is deposited onto mica. **During plasma**, a combination of etching and deposition occurs; fragments of the AFN are created through etching while the DGpp gradually builds. **After plasma**, the AFN + DGpp construct comprises of two regions, an AFN-DGpp matrix with the bulk of the AFN located at the mica substrate with a concentration gradient moving away from the substrate. The second region is comprised of DGpp only while replicating the topographical structure of the AFN network on the very top surface.

Before deposition, an intact AFN is assembled on to mica and is placed within the plasma chamber. Once the plasma is ignited, a combination of etching and deposition occurs. Etching will occur on any exposed mica, on any adventitious carbon present, and the AFN itself. Some fragments of the AFN generated during this etching will be redeposited on the surface at the same time as the DGpp film is deposited. As the DGpp film grows, fragments of the etched AFN are dispersed through the DGpp immediately above the original AFN. Once all of the etched AFN has redeposited and the original AFN surface is covered with DGpp, any source of AFN has been extinguished, thus the remaining deposition is comprised of only the DGpp.

## 6.4 Conclusions

Lysozyme amyloid fibres deposited onto mica display a nanoscale surface topography analogue to that of the extracellular matrix. This nanotopography is well preserved after thick layers of plasma polymer films were grown on top of the AFN. In this study it was found that by defining the DGpp film deposition time, the width of the fibril structure was affected in a controlled manner and therefore the surface structure can be manipulated easily. In addition, based on XPS chemical analysis, a model of the DGpp growth mechanism on the AFN was proposed. This includes two distinct regions within the DGpp + AFN construct: 1) An AFN-DGpp matrix with the bulk of the AFN located at the mica substrate surface and in a concentration gradient moving away from the interface, and 2) A DGpp only region, where the topographical structure of the AFN is replicated on the top surface and the resolution of these features is determined by the deposition time.

## 6.5 References

1. K. S. Masters and K. S. Anseth, in *Advances in Chemical Engineering*, eds. A. Peppas and M. V. Sefton, Academic Press, 2004, vol. Volume 29, pp. 7-46.
2. M. Milan, *Current Opinion in Chemical Biology*, 2002, 6, 794-797.
3. D. G. Castner and B. D. Ratner, *Surface Science*, 2002, 500, 28-60.
4. C. Werner, in *Polymer Surfaces and Interfaces*, ed. M. Stamm, Springer Berlin Heidelberg, 2008, pp. 299-318.
5. K. Kolind, K. W. Leong, F. Besenbacher and M. Foss, *Biomaterials*, 2012, 33, 6626-6633.
6. A. S. G. Curtis and C. D. W. Wilkinson, *Journal of Biomaterials Science, Polymer Edition*, 1998, 9, 1313-1329.
7. P. Clark, P. Connolly, A. S. Curtis, J. A. Dow and C. D. Wilkinson, *Development*, 1987, 99, 439-448.
8. D. D. Deligianni, N. Katsala, S. Ladas, D. Sotiropoulou, J. Amedee and Y. F. Missirlis, *Biomaterials*, 2001, 22, 1241-1251.
9. K. Anselme and M. Bigerelle, *Acta Biomaterialia*, 2005, 1, 211-222.

10. M. J. Dalby, N. Gadegaard, R. Tare, A. Andar, M. O. Riehle, P. Herzyk, C. D. W. Wilkinson and R. O. C. Oreffo, *Nat Mater*, 2007, 6, 997-1003.
11. L. E. McNamara, R. Burchmore, M. O. Riehle, P. Herzyk, M. J. P. Biggs, C. D. W. Wilkinson, A. S. G. Curtis and M. J. Dalby, *Biomaterials*, 2012, 33, 2835-2847.
12. A. Citeau, J. Guicheux, C. Vinatier, P. Layrolle, T. P. Nguyen, P. Pilet and G. Daculsi, *Biomaterials*, 2005, 26, 157-165.
13. J. Huang, S. N. Jayasinghe, S. M. Best, M. J. Edirisinghe, R. A. Brooks and W. Bonfield, *Journal of Materials Science*, 2004, 39, 1029-1032.
14. D. Sasaki, T. Shimizu, S. Masuda, J. Kobayashi, K. Itoga, Y. Tsuda, J. K. Yamashita, M. Yamato and T. Okano, *Biomaterials*, 2009, 30, 4384-4389.
15. A. Perl, D. N. Reinhoudt and J. Huskens, *Advanced Materials*, 2009, 21, 2257-2268.
16. Y. Xia and G. M. Whitesides, *Angewandte Chemie - International Edition*, 1998, 37, 550-575.
17. C. c. Lara, J. Adamcik, S. Jordens and R. Mezzenga, *Biomacromolecules*, 2011, 12, 1868-1875.
18. A. Shekaran and A. J. Garcia, *Biochimica et Biophysica Acta (BBA) - General Subjects*, 2011, 1810, 350-360.
19. M. Zhou, A. M. Smith, A. K. Das, N. W. Hodson, R. F. Collins, R. V. Ulijn and J. E. Gough, *Biomaterials*, 2009, 30, 2523-2530.
20. S. Marchesan, L. Waddington, C. D. Easton, D. A. Winkler, L. Goodall, J. Forsythe and P. G. Hartley, *Nanoscale*, 2012, 4, 6752-6760.
21. M. N. Bongiovanni, D. B. Scanlon and S. L. Gras, *Biomaterials*, 2011, 32, 6099-6110.
22. N. P. Reynolds, M. Charnley, R. Mezzenga and P. G. Hartley, *Biomacromolecules*, 2014, 15, 599-608.
23. N. P. Reynolds, K. E. Styan, C. D. Easton, Y. Li, L. Waddington, C. Lara, J. S. Forsythe, R. Mezzenga, P. G. Hartley and B. W. Muir, *Biomacromolecules*, 2013, 14, 2305-2316.
24. T. Desmet, R. Morent, N. D. Geyter, C. Leys, E. Schacht and P. Dubruel, *Biomacromolecules*, 2009, 10, 2351-2378.
25. M. C. Vasudev, K. D. Anderson, T. J. Bunning, V. V. Tsukruk and R. R. Naik, *ACS Applied Materials & Interfaces*, 2013, 5, 3983-3994.
26. A. Pegalajar-Jurado, C. D. Easton, K. E. Styan and S. L. McArthur, *Journal of Materials Chemistry B*, 2014, 2, 4993-5002.
27. P. Heyse, A. Van Hoeck, M. B. J. Roeffaers, J.-P. Raffin, A. Steinbüchel, T. Stöveken, J. Lammertyn, P. Verboven, P. A. Jacobs, J. Hofkens, S. Paulussen and B. F. Sels, *Plasma Processes and Polymers*, 2011, 8, 965-974.

- 
28. K. D. Anderson, J. M. Slocik, M. E. McConney, J. O. Enlow, R. Jakubiak, T. J. Bunning, R. R. Naik and V. V. Tsukruk, *Small*, 2009, 5, 741-749.
  29. K. D. Anderson, S. L. Young, H. Jiang, R. Jakubiak, T. J. Bunning, R. R. Naik and V. V. Tsukruk, *Langmuir*, 2011, 28, 1833-1845.
  30. I. Braceras, P. Azpiroz, N. Briz, R. M. Fratila, J. Oyarbide, E. Ipiñazar, N. Álvarez, G. Atorrasagasti and J. M. Aizpurua, *Plasma Processes and Polymers*, 2011, 8, 599-606.
  31. C. Susut and R. B. Timmons, *International Journal of Pharmaceutics*, 2005, 288, 253-261.
  32. K. Vasilev, N. Poulter, P. Martinek and H. J. Griesser, *ACS Applied Materials & Interfaces*, 2011, 3, 4831-4836.
  33. J.-M. Jung, G. Savin, M. Pouzot, C. Schmitt and R. Mezzenga, *Biomacromolecules*, 2008, 9, 2477-2486.
  34. B. W. Muir, A. Fairbrother, T. R. Gengenbach, F. Rovere, M. A. Abdo, K. M. McLean and P. G. Hartley, *Advanced Materials*, 2006, 18, 3079-3082.
  35. T. Nobuta and T. Ogawa, *Journal of Materials Science*, 2009, 44, 1800-1812.

## PART B: Suggested Declaration for Thesis Chapter

[This declaration to be completed for each conjointly authored publication and to be placed at the start of the thesis chapter in which the publication appears.]

### Monash University

#### Declaration for Thesis Chapter 7

#### Declaration by candidate

In the case of Chapter 5, the nature and extent of my contribution to the work was the following:

Nature of contribution	Extent of contribution (%)
Experimental design, conduct, data processing and writing	

The following co-authors contributed to the work. If co-authors are students at Monash University, the extent of their contribution in percentage terms must be stated:

Name	Nature of contribution	Extent of contribution (%) for student co-authors only
Yue Qu	Assisted in experiment and manuscript correction	N/A
Christopher D. Easton	Assisted in experiment	N/A
David R. Nisbet	Manuscript correction	N/A
John S. Forsythe	Manuscript correction, assisted in experimental planning	N/A
Trevor Lithgow	Manuscript correction	N/A
Benjamin W. Muir *	Assisted in planning, experimental design and manuscript correction	N/A

The undersigned hereby certify that the above declaration correctly reflects the nature and extent of the candidate's and co-authors' contributions to this work\*.

Candidate's  
Signature

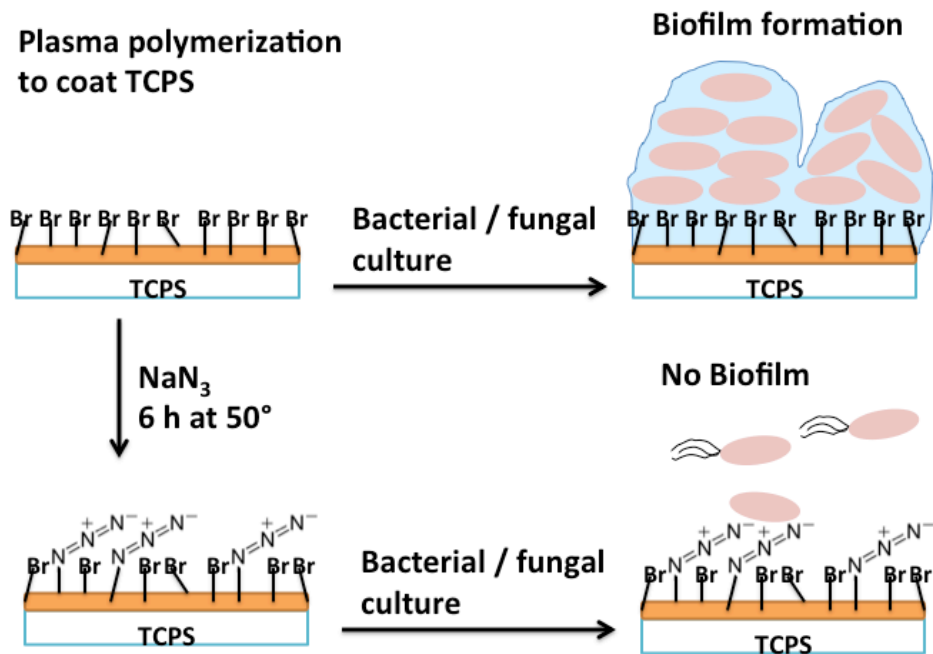
	<b>Date</b>
--	-------------

Main  
Supervisor's  
Signature

	<b>Date</b>
--	-------------

\*Note: Where the responsible author is not the candidate's main supervisor, the main supervisor should consult with the responsible author to agree on the respective contributions of the authors.

## Chapter 7 Antimicrobial coatings



*"What boots it at one gate to make defence, and at another to let in the foe?"*  
 - John Milton

**Abstract**

The attachment of microbes and subsequent biofilm formation causes significant problems in a wide range of applications. While much research has been directed at combatting microbial infections, effective and economical products that resist a variety of microorganisms are yet to be created or manufactured. Herein, we fabricated a surface coating via plasma polymerisation and tested it with clinically relevant bacterial pathogens, *Staphylococcus epidermidis* and *Pseudomonas aeruginosa*, and a fungal pathogen *Candida albicans*. Polystyrene surfaces were coated with brominated plasma polymer films, followed by reaction with sodium azide solutions to incorporate azide functional groups onto the surface at various concentrations. Azide-functionalised surfaces prevented biofilm growth of all three pathogens. The coatings were shown not to be toxic to cultured human fibroblasts nor induce haemolysis of human erythrocytes. These surfaces can be easily deposited onto different substrate materials. Furthermore, the azide group offers flexibility in tethering specific antibiotics through azide-alkyne “click” reactions.

## 7.1. Introduction

Biomedical devices have been used widely to save lives and improve the quality of life for many patients. It is anticipated that the demand for synthetic devices will grow even further as life spans in modern societies increase.<sup>1</sup> Opportunistic pathogens readily colonize the surface of biomedical devices: firstly by cell attachment, to ultimately form biofilms that are refractory to antimicrobial treatment.<sup>2</sup> Once these infections develop, consequences to the patient are serious and can be fatal.<sup>3-5</sup> Thus, there is a pressing need to modify the surface of biomedical devices to possess properties unfavorable for microbial attachment. Necessarily, the modified surfaces must be compatible for insertion into human tissues.

In addition to the architectural modification of a surface, common chemical treatment strategies used to resist microbe attachment are: (i) coating biomaterials with non-fouling or bactericidal functional films,<sup>6-9</sup> (ii) grafting of biocidal polymers,<sup>10, 11</sup> (iii) immobilisation of antibiotics or antiseptic agents<sup>12</sup> or, (iv) controlled release of antibiotics, metal ions or germicidal compounds from the surface.<sup>13-18</sup> These approaches have only limited success due to the complexity of host environments and the large variety of medical devices used, as this typically requires surfaces to be optimized to specific product needs. For example, the use of metallic silver, silver nanoparticles and ions has been a constant theme in antibacterial surface design due to its activity against a broad spectrum of pathogenic bacteria.<sup>19-21</sup> However, the potential toxicity of such surfaces to human tissues remains as subject of major concern.<sup>22, 23</sup> Options such as short-term contact wound dressings or urinary catheters where silver concentrations are unlikely to build up in the body due to fast removal are often exploited.<sup>24</sup> Other metallic ions face the same issues in terms of the dosages and application.<sup>25</sup>

For device related infections, short-term release of antimicrobial substances is not a complete solution as the implant is likely to accompany the patient for many months or years. A stable microorganism-resistant surface would be ideal in this scenario. The

covalent immobilisation of quaternary ammonium compounds, other cationic compounds, and antibiotics to materials surfaces are a subject of intensive studies.<sup>26-29</sup> However, the potential downsides include restricted effectiveness to a specific genus of microorganism, or adverse effects to the surrounding biological environment.<sup>30, 31</sup> In order to find optimal surfaces that show both anti-microbial effects and low side effects to human tissues, naturally derived agents are being put into use.<sup>32</sup>

Amongst the various ways of conjugating biomolecules to a surface, “click” chemistry - in particular the ‘alkyne-azide’ reaction - has received widespread use. Several groups have also investigated the azide chemistry ( $N^+=N=N^-$ ) itself for antibacterial usage. Lakshmi et al. bound the azide group onto a plasticised poly(vinyl chloride) (PVC) surface and reported significantly reduced amount of bacteria adhesion (*Staphylococcus aureus* and *Escherichia coli*) compared with the PVC control.<sup>33</sup> However, in another study, the azide groups immobilised onto PVC substrates displayed only a minor decrease in adhesion of *E. coli* compared with unmodified PVC.<sup>34</sup> In a recent study by Ho and co-worker, azide chemistry was introduced to glass coverslips as intermediate step in click chemistry, where it was also tested against *Pseudomonas aeruginosa* and *Staphylococcus aureus*.<sup>35</sup> They found that the azide bound surface reduced adhesion of both Gram-positive and Gram-negative bacteria by more than 50 %. The variance in these studies may have arisen from the difference in reaction conditions for azide immobilisation, in turn the varying the amount of azide covalently bonded on the substrate surface. In this work, the amount of azide immobilized was systematically varied to examine the effect of azide towards pathogenic microbes.

In this paper, azide functionality was attached to a substrate surface through nucleophilic substitution. The leaving group in this reaction is bromine, which is present in the coating produced via plasma polymerisation of 1-bromopropane.<sup>36, 37</sup> Plasma polymerisation is a versatile surface modification technique that can deposit uniform thin films onto various substrates with good adhesion.<sup>38, 39</sup> Plasma polymerised films can be employed for antimicrobial applications in a few strategies, such as direct antifouling<sup>40</sup> or killing of microbes,<sup>41</sup> act as a barrier coating for controlled release of

antibiotics,<sup>42, 43</sup> or deposit as interlayer for subsequent immobilisation of antimicrobial agents.<sup>44, 45</sup> Herein, the resultant azide coated films were incubated with three clinically relevant biofilm-forming pathogens: a Gram-positive bacterium *Staphylococcus epidermidis* (*S. epidermidis*) RP62a (ATCC35984), a Gram-negative bacterium *Pseudomonas aeruginosa* (*P. aeruginosa*) ATCC 27853, and a fungal pathogen *Candida albicans* (*C. albicans*) DAY185. Antimicrobial properties were observed and quantified in all three cases.

## 7.2. Materials and methods

### 7.2.1 Substrate materials

Tissue culture polystyrene (TCPS) 96-well flat-bottom microplates (FALCON®) were used directly from the sterile package. Thermanox™ coverlips ( $\varnothing = 25$  mm, NUNC™) were cut into 5 mm x 5 mm pieces in a sterile hood, and then used as a substrate for film deposition.

### 7.2.2 Plasma polymerisation

Deposition of Br plasma polymer (Brpp) film was carried out in a custom-built reactor. Briefly, the plasma reactor consists of two capacitively coupled copper electrodes (spaced 15 cm apart) in a cylindrical glass bell jar with a height of 36 cm and a diameter of 18 cm. The top electrode has a diameter of 11 cm and is connected to the plasma generator. The bottom electrode is rectangular (length = 12 cm, width = 8 cm) and is grounded. The monomer 1-bromopropane (99 %, Aldrich) was placed in a round-bottom flask, which was connected to the reactor chamber via a stainless steel line. The flow of monomer vapour was adjusted manually using a control valve. Prior to plasma deposition, the monomer was degassed three times. The parameters chosen for Brpp film deposition were a load power of 20 W, a frequency of 175 kHz, an initial monomer pressure of 25 Pa with a treatment time of 45 seconds. Then the reactor chamber was

pumped down to base pressure. The substrate was further treated by a 15 second deposition with the same parameters. After these two depositions, the reactor was pumped down to base pressure then was vented to collect the samples. For biofilm formation experiments, the coated plate was used as prepared. Alternatively, the bottom of the well was cut out using a drill for surface chemistry and topography analysis.

Deposition of diethylene glycol dimethyl ether plasma polymer (DGpp) was carried out in the reactor described in **chapter 3**. The plasma deposition of DGpp film was performed using a frequency of 125 kHz, load power of 5 W and an initial monomer pressure of 20 Pa for a treatment of 120 seconds (final pressure of 26 Pa).

### 7.2.3 Azide nucleophilic exchange

Azide solution (1 M) was made by dissolving  $\text{NaN}_3$  ( $\geq 99\%$ , Merck, Germany) in Milli-Q water. A small amount (5 % w/v) of NaI (99 % purity, Aldrich) was added to facilitate the exchange reaction. The solution was buffered to pH 5 with acetic acid. Then, 0.1 M and 0.5 M azide solutions were made by diluting the 1 M stock. For the 96-well microplate samples, 100  $\mu\text{L}$  of azide solution was added to each well and the plate was sealed with parafilm before being placed in a 50 °C water bath for 6 h. After the reaction, azide solution was removed and the plate was then rinsed with running Milli-Q water for a few min before being submerged in a 2 L beaker containing milli-Q water overnight. The plate was then dried in a fume hood and used for biofilm cultivation experiments. For coverslip samples, the cut-outs were placed in Eppendorf tubes filled with azide solutions. The tubes were incubated for 6 h at 50 °C in a water bath. After the reaction, coverslips were rinsed with Milli-Q water and then soaked in Milli-Q water overnight. These samples were dried with nitrogen and used for haemolysis tests. Samples prepared in this way were incubated in rich culture media to be certain against the possibility of microorganism contamination; no microbial growth was found. The azide solutions referred in these methods are hazardous and can cause serious injury unless performed, handled, and used with care.

### 7.2.4 X-ray photoelectron spectroscopy

X-ray photoelectron spectroscopy (XPS) analysis and XPS depth profiling was performed using an AXIS Ultra DLD described in the previous chapters.

### 7.2.5 Atomic force microscopy

A Bruker FastScan atomic force microscope (AFM) employing an Icon scanner head with NanoScope 9.0 software was used to measure surface topography in tapping mode with ultrasharp silicon tips (OTESPA, Bruker Corporation). The tips used in this study have a typical force constant of 42 N/m and a resonant frequency of 300 kHz. Scans were performed at 1 Hz and 512 data points per scan line. All images were processed (1<sup>st</sup> order flattening algorithm) using NanoScope Analysis 1.5 software.

### 7.2.6 Biofilm cultivation and quantitative determination

Three biofilm-forming reference strains: *S. epidermidis* RP62a (ATCC35984), *P. aeruginosa* ATCC 27853 and *C. albicans* DAY185 were used in this study. Bacterial stocks (stored at -80 °C in nutrient broth with 15 % glycerol) were streaked onto nutrient agar (NA, Oxoid) plates for use as the working stock. *C. albicans* (stored at -80°C in 15 % glycerol) was streaked onto yeast extract peptone dextrose (YPD, 2 % glucose, 2 % peptone, 1 % yeast extract, 2 % agar) plates for use as the working stock. These working stocks were stored at 4 °C (*S. epidermidis* and *P. aeruginosa*) or room temperature (*C. albicans*) and replaced every two weeks.

Bacterial biofilm culture was set up using a modification of a previously established method.<sup>46</sup> Briefly, an overnight bacterial culture grown in nutrient broth (NB) was diluted 1:100 into biofilm-specific growth media, including tryptic soya broth for *S. epidermidis* (TSB, Oxoid), or Luria-Bertani (LB) broth for *P. aeruginosa*. One hundred

microlitres of the diluted bacterial suspensions were pipetted into a well in 96-well flat-bottom polystyrene microplates which had received different coating treatments and were incubated for 20 h at 37 °C with gentle agitation (75 rpm). To grow fungal biofilms, 100 µL of cultures of *C. albicans* ( $10^7$  CFU/mL in Spider medium, 1 % nutrient broth, 1 % D-mannitol, 2 g K<sub>2</sub>HPO<sub>4</sub>) were added to wells and incubated at 37 °C with gentle shaking (75 rpm) for 90 min (adhesion phase).<sup>47</sup> Non-adherent cells were discarded and the microplates were washed once with sterile PBS before 100 µL of fresh Spider medium were added into the microwell. Biofilms were allowed to further develop for 48 h. The medium was replenished after 24 h by aspiration and addition of fresh Spider medium. After overnight or 48 h incubation, the cell suspensions were aspirated and the microwells were rinsed twice with 110 µL of PBS per well to remove non-adherent cells. To quantify biofilms formed on surfaces of different treatments, the microplate containing biofilms was heat-fixed in a 60 °C oven for 1 hour and then stained with 110 µL of 1 % (W/V) crystal violet (CV) for 10 min. The CV solution in the wells was then discarded and the microplates were washed four times to remove excess stain by submerging them in tubs of clean water. The microplates were gently tapped on paper towels to remove excess water in microwells. 200 µL of 95 % ethanol and 5 % acetic acid were added into each well and incubated at room temperature for 15 min. 100 µL of solution from each well was transferred to a new microplate. The amount of biofilm formed in each well was determined by reading its optical density with a Tecan Infinite M200 Plate Reader at 595 nm.

### 7.2.7 Confocal laser scanning microscopy

Polystyrene pieces were cut from the bottom of a 96-well microplate, with extreme caution to avoid any scratch to the treated or control surfaces. The polystyrene pieces were stained and analysed using the same method outlined in **chapter 3**.

### 7.2.8 Haemolysis assay

The haemolysis assay was performed as described by Ciornei et al.<sup>48</sup> with modifications. Thermox™ coverslips were used as the base substrate. A batch of Brpp coated coverslips (both sides) was made in identical conditions. Selected samples were further treated with sodium azide 0.1 M, 0.5 M, and 1 M solutions. In addition, double-side DGpp coated coverslips were prepared in triplicate for comparison.

The erythrocytes were rinsed three times and then resuspended in phosphate-buffered saline (PBS, pH 7.4). Next, 500 µL of erythrocyte suspension was added into Eppendorf tubes containing the coverslip cutouts (5 mm x 5 mm), followed by 2 h incubation at 37 °C with gentle end-over-end rotation. Thermox™ coverslip cutouts were coated with a thin layer of Triton X-100 at 10 % (Sigma-Aldrich) and served as a positive control. This was done by dipping the untreated coverslips into Triton X-100 and then gently touching them with Kimwipes to remove any excess solution. Thermox™ coverslip cutouts washed with PBS served as a negative control. After incubation, the samples were centrifuged at 800 × g for 10 min. Erythrocyte stability in the presence of plasma polymer coatings was monitored by measuring the absorbance of the supernatant at 570 nm and is expressed as a percentage of that induced by Triton X-100-coated surfaces.

### 7.2.9 HeLa cell culture

The *in vitro* biocompatibility of prepared Brpp films and azide treated surfaces were assessed by visualising the attachment of HeLa cells after overnight incubation at 37 °C with 5 % CO<sub>2</sub>/air atmosphere. TCPS 96-well plates were used as controls. 100 µL of 2 x Anti-Anti (Antimycotic-Antibiotic, GIBCO) solution was added to each well 1 h before cell seeding, incubated at room temperature. HeLa cells were cultured in media (DMEM + GlutaMAX-I, GIBCO), supplemented with 10 % FBS (foetal bovine serum, SAFC Biosciences), 1 % (v/v) NEAA (nonessential amino acids, GIBCO), and 1 % Anti-Anti.

HeLa cells were seeded to each multiwell plate at a concentration of 25,000 cell/cm<sup>2</sup> of well area. After overnight incubation, the plates were rinsed with fresh cell culture media (warmed to 37 °C) to remove any non-adherent cells. Cell viability was examined using LIVE/DEAD assay (2 μM calcein AM, 4 μM ethidium homodimer-1, Invitrogen). Stained adhered cells were then imaged with an inverted microscope (Nikon Eclipse TE2000-U). Calcein was excited at 465 - 495 nm resulting emissions ranging at 515 to 555 nm. Ethidium homodimer-1 was excited at 510 – 560 nm with an emission above 590 nm.

## 7.3. Results and discussion

### 7.3.1 Surface topography

A thin layer of Brpp film coating was deposited onto the TCPS 96-well microplate via radio frequency glow discharge plasma polymerisation. After a 60 s treatment, the plate was brown in colour due to the formation of the Brpp film. The surface of the freshly deposited Brpp is significantly rougher than that of the original TCPS plate (Figure 7.1 a, b). The large spherical features are likely due to polymerisation above the substrate in the plasma glow discharge. We have previously reported on this unique morphology of Brpp fabricated from 1-bromopropene.<sup>49</sup> After nucleophilic exchange reactions were conducted with sodium azide, the resultant azide containing surfaces remained significantly rougher than the original TCPS.

Compared with the Brpp surface, the azide reacted surface contains a greater amount of small clustered features distributed uniformly across the surface (Figure 7.1 c, d, e); however, the values obtained from the standard roughness parameters, R<sub>rms</sub> and R<sub>a</sub>, did not confirm the observed difference (Figure 7.2).

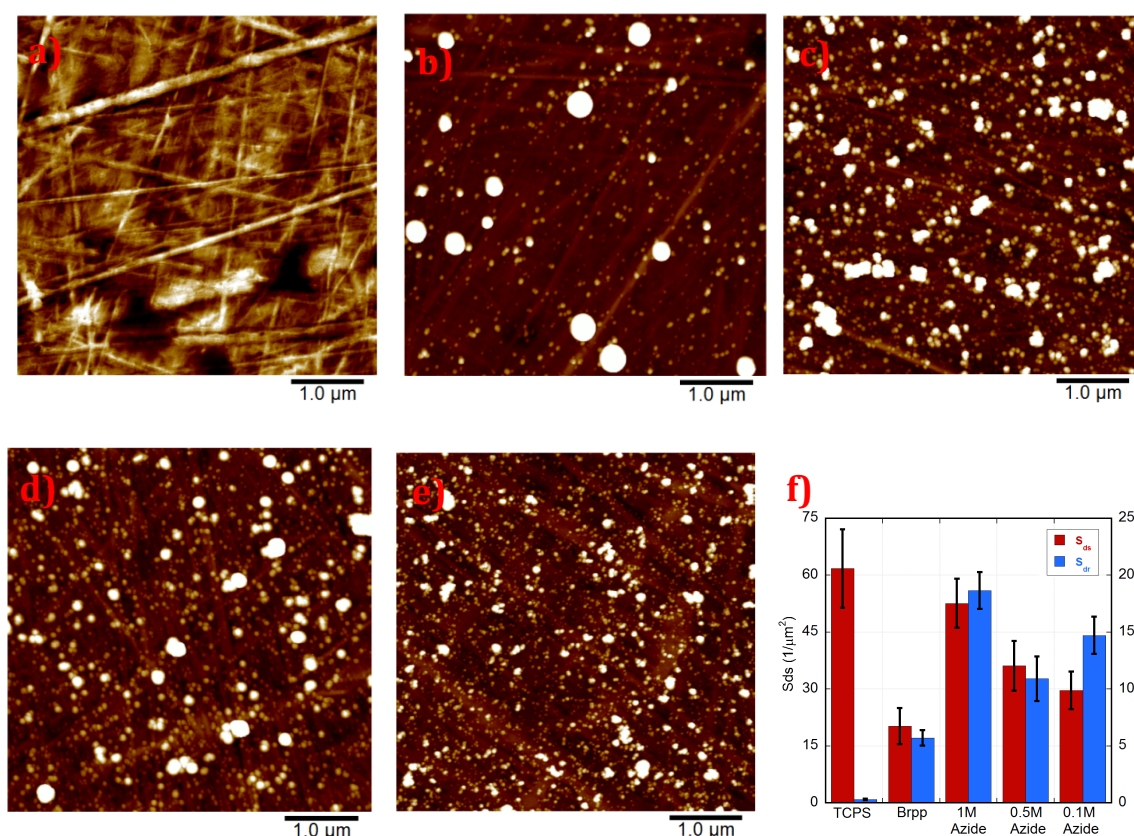


Figure 7.1. Nanoscale topography of bare TCPS, Brpp and azide treated surfaces. AFM topographical images, 5.0 μm x 5.0 μm scan, of (a) tissue culture polystyrene (TCPS) 96-well microplates (FALCON®), height scale 14 nm; (b) Br plasma polymer film (Brpp) coated TCPS, height scale is 65 nm (the z scales of other three are the same); (c) 0.1 M NaN<sub>3</sub> solution treated Brpp on top of TCPS; (d) 0.5 M NaN<sub>3</sub> solution treated Brpp on top of TCPS; (e) 1 M NaN<sub>3</sub> solution treated Brpp on top of TCPS; (f) S<sub>ds</sub> and S<sub>dr</sub> values derived from AFM images, showing a significant difference in the number of features between Brpp and high concentration sodium azide treated surfaces; in addition, all azide treated surfaces have dramatically increased surface area compared with Brpp and TCPS. Presented in mean ± standard error.

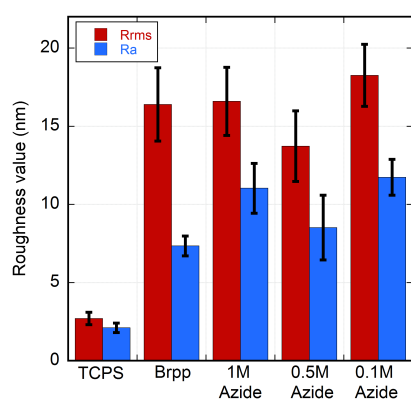


Figure 7.2, R<sub>rms</sub> and R<sub>a</sub> roughness values calculated from AFM images of TCPS, Brpp and azide treated surfaces, showing dramatically increased roughness after Brpp deposition on TCPS, but similar values after azide treatments. Presented in mean ± standard error.

Thus, S-parameters based on ISO 25178 were measured for each surface (Figure 7.1 f). Briefly,  $S_{ds}$  (Density of States) is a measure of the number of features per unit area, while  $S_{dr}$  (Developed Interfacial Area ratio) represents the percentage of additional surface area that is introduced by features relative to a flat surface. The values for  $S_{ds}$  confirmed that there is a significant difference in the number of features between Brpp and the surface treated with 1 M or 0.5 M azide, while the values for  $S_{dr}$  demonstrate that all azide treated surfaces have a significantly greater increase in additional surface area (i.e.  $S_{dr}$ ) compared to both Brpp and TCPS.

### 7.3.2 Surface chemistry

The elemental composition of the Brpp film was characterised with XPS, which showed the presence of bromine, carbon and oxygen (Table 7.1). The film is thicker than the XPS analysis depth (< 10 nm) based on the absence of the aromatic shake-up in the high-resolution C 1s spectra (Figure 7.3 a) that is characteristic for TCPS substrates. Following exchange reactions, the XPS analysis of the film revealed the emergence of nitrogen with a drop in Br concentration (approximately by 3 at. %). No sodium was detected but a small amount of iodine (0.03 at. %) was present in the azide functionalised surfaces, which can be attributed to the NaI surface reaction catalyst.

The high resolution C 1s spectra of azide reacted film is slightly different from Brpp films possibly due to post reaction oxidation and removal of C-Br groups from within the sampling depth of the measurement. Nonetheless, the high resolution N 1s spectrum (Figure 7.3 b) demonstrated the incorporation of azide with two distinct peaks at 400.6 and 404.5 eV at a ratio of approximately 2:1. The peak at 400.6 eV is attributed to the electron enriched N species while the other peak arise from the electron deficient N species of the azide group.<sup>36, 50</sup> This confirms the nucleophilic exchange of bromine groups with azide groups. The concentration of N increased by 33 % when the  $\text{NaN}_3$  solution molar concentration increased from 0.1 M to 0.5 M. However, there was no

significant difference (0.16 at. % increase) in nitrogen incorporation when double the amount of  $\text{NaN}_3$  (1 M) was used.

Table 7.1, Elemental composition (atomic %) of the tissue culture polystyrene (TCPS) 96-well microplate control, 1-bromopropane plasma polymer (Brpp) coated TCPS, Sodium azide 0.1 M, 0.5 M and 1 M exchange reaction with Brpp coated TCPS derived from XPS survey spectra. Presented in mean  $\pm$  standard error.

Atomic %	<b>Br 3d</b>	<b>C 1s</b>	<b>N 1s</b>	<b>O 1s</b>	<b>I 3d</b>
TCPS	-	83.64 $\pm$ 0.29	-	16.36 $\pm$ 0.29	-
Brpp	14.23 $\pm$ 0.46	81.44 $\pm$ 0.61	-	4.33 $\pm$ 0.19	-
Azide 0.1 M	11.85 $\pm$ 0.09	77.25 $\pm$ 0.38	4.57 $\pm$ 0.11	6.31 $\pm$ 0.18	0.03 $\pm$ 0.00
Azide 0.5 M	11.14 $\pm$ 0.34	76.53 $\pm$ 0.39	6.08 $\pm$ 0.22	6.22 $\pm$ 0.22	0.03 $\pm$ 0.00
Azide 1 M	11.62 $\pm$ 0.14	76.53 $\pm$ 0.46	6.24 $\pm$ 0.22	5.58 $\pm$ 0.15	0.04 $\pm$ 0.01

In order to determine whether there are sodium azide absorbed in the bulk of plasma polymer film, XPS depth profiling was performed to etch through the azide treated films after standard washing protocols. The results, as shown in figure 7.4, show that there is no sodium throughout the film. This indicates that during cell and microbial culture no azide is released from the coating, and the antimicrobial effect is from the covalently immobilised azide.

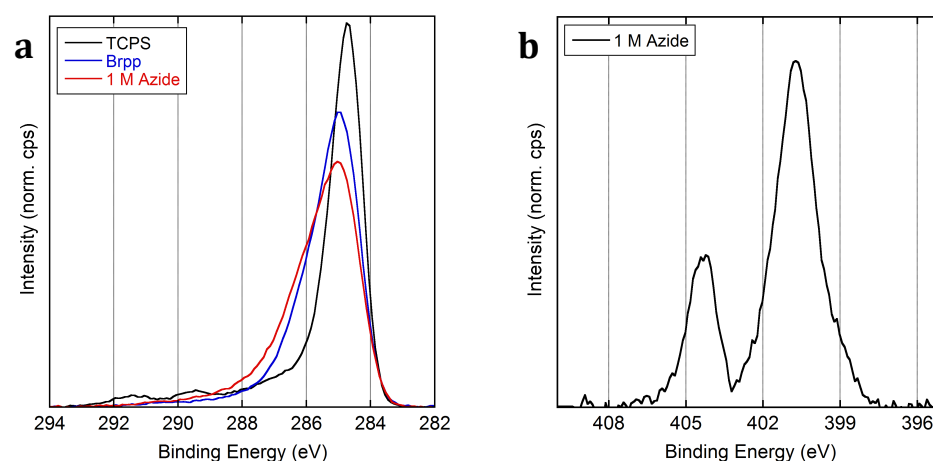


Figure 7.3. XPS high resolution C 1s and N 1s spectra from bare TCPS, Brpp and azide treated surfaces. (a) Overlay of the high resolution C 1s spectra of TCPS, Brpp and sodium azide reacted surface; (b) Representative high resolution N 1s spectrum of the azide treated surfaces showing two peaks at 400.6 eV and 404.5 eV, characteristic of azides.

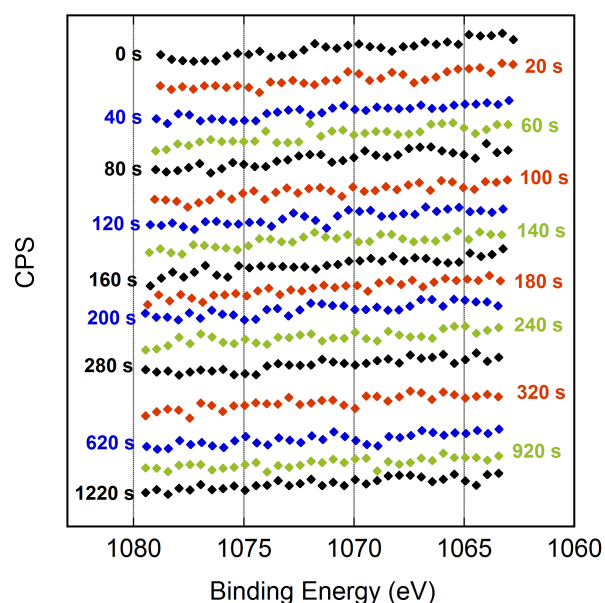


Figure 7.4, XPS survey scans of 1 M azide treated Brpp film deposited on TCPS zoomed in binding energy between 1060 to 1080 eV. The XPS spectra were taken after each etch. 0 s represents the data taken at the top surface of just made azide treated film. 1220 s is where the film has been etched through and hit the TCPS substrate itself. The presence of Na 1s is typically detected at 1072 eV. There is no evidence of sodium (from unbound sodium azide) incorporated in the bulk of the coating.

### 7.3.3 Anti-microbial performance

Based on the quantitative measurements of the bacteria and fungi adhered to the azide functionalised surfaces (Figure 7.5), use of azide at either 0.5 M or 1.0 M in the functionalisation reaction generated a surface to which neither of the bacterial species could form biofilms, and where biofilm formation by the fungal pathogen *C. albicans* was inhibited by 76 – 88 %.

Biofilm formation by microbes is a complex process that requires initial surface adhesion mediated through diverse cell surface structures, and the features of these surface interactions vary between species.<sup>51</sup> This complexity and diversity may go some way to explain the differences seen in the effects of the Brpp surface compared to the same surface with azide functionalisation. For example, the freshly deposited Brpp film has no effect on *P. aeruginosa* biofilm formation (Figure 7.5), yet the Brpp coating inhibited biofilm formation by *S. epidermidis* to an appreciable extent.

The use of 0.1 M azide in the immobilisation step had no significant effect on either *S. epidermidis* or *P. aeruginosa*, suggesting that low concentration of azide chemistry does not affect the bacterial cell function. The surfaces produced from 0.5 M and 1 M  $\text{NaN}_3$  solutions each gave the same degree of reduction of microbial attachment (Figure 7.5). Both films inhibited the growth of Gram-positive and Gram-negative bacteria almost completely (> 97 %). The surfaces very clearly function as antimicrobial agents.

We further sought to understand what this meant in terms of cell attachment to the surfaces, and used confocal laser scanning microscopy to quantify cell number or determine cell viability to this end. The CLSM images for all three microbial species demonstrated that very few, small microcolonies were formed on the azide-functionalised surface, and that these cells failed to grow into anything like the biofilms formed on the control surface (Figure 7.6).

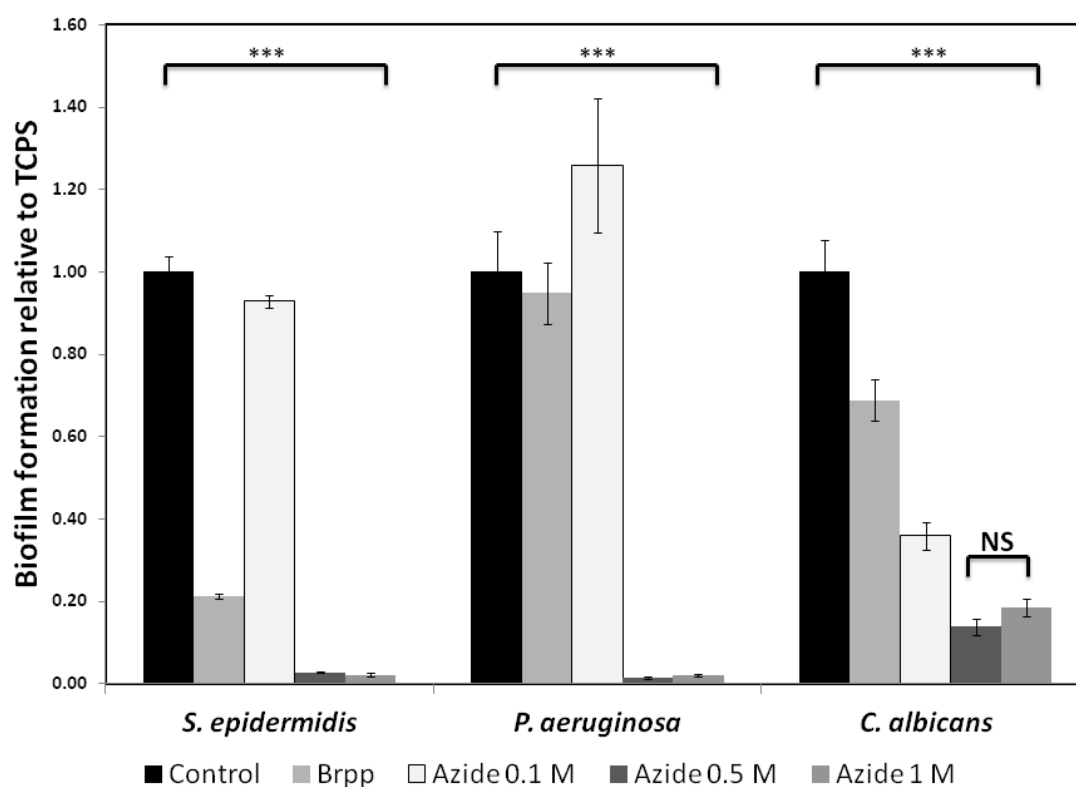


Figure 7.5. Biofilm formation of three representative microorganisms on surfaces receiving different treatments relative to the TCPS control. Biofilms of *S. epidermidis* were grown in TSB medium at 37 °C for 18 h with agitation (75 rpm). Biofilms of *P. aeruginosa* were grown in LB medium 37 °C for 18 h with agitation (75 rpm) and *C. albicans* biofilms were grown in Spider medium 37 °C for 48 h with agitation (75 rpm). Biofilm production on different surfaces was assessed by a crystal violet staining assay and represented as percentage relative to that grown on the TCPS control. There are considerable differences in the amount of microbes attached to the high concentration sodium azide solution treated surfaces from the TCPS control. In 0.5 M and 1 M sodium azide treated surfaces, there is no significant difference. NS = No Significance:  $p > 0.05$ ; \*\*\*,  $p < 0.001$

In the case of *P. aeruginosa*, dead bacteria were found on the TCPS substrate but were not present on the Brpp surface, although the average number of live cells was the same (Figure 7.6). Co-existence of live cells and dead cells (ratio=1.8:1) in a microplate-supported *P. aeruginosa* biofilm under both aerobic and anaerobic conditions has been reported.<sup>52</sup> This is of biological relevance given observations that an early phase of biofilm formation by *P. aeruginosa* requires altruistic cell death and extrusion of cell

contents to provide the extracellular DNA that the neighbouring, viable bacteria use as a matrix in which to grow and divide to form the mature biofilm.<sup>53</sup>

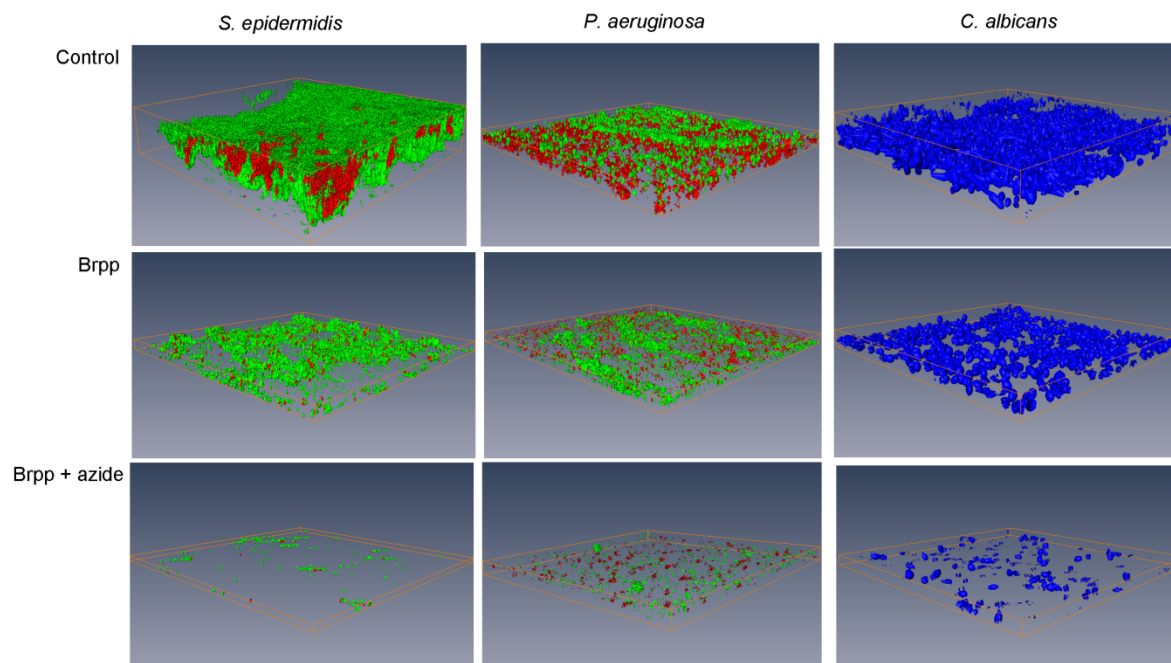


Figure 7.6. Confocal Laser Scanning Microscopy (CLSM) of biofilms produced by *S. epidermidis*, *P. aeruginosa* and *C. albicans* on surfaces of TCPS, Brpp coated TCPS, and 1 M azide reacted films. Biofilms of *S. epidermidis* and *P. aeruginosa* were grown for 18 h in TSB and LB respectively, and then stained with SYTO-9 (bright green for live cells) and PI (red or orange, or loss of bright green for dead cells). Biofilms of *C. albicans* were grown for 48 h in Spider medium, and then stained with calcofluor white (1 mg/ml for 1 minute). 3D structure of biofilms was reconstructed with software Amira 5.4. 1.

The mechanisms by which the azide treated surfaces inhibit microbial attachment and biofilm formation remain to be analysed, and it is highly likely to be different from the action of sodium azide in solution; immobilised azide cannot access the membrane-located cytochrome oxidase. Our current hypothesis is that the azide modified surfaces has properties that are less attractive to cell-surface structures such as fimbriae and cell wall polysaccharides, so that these surfaces suppress attachment and organisation of the microbes into biofilms.

### 7.3.4 Initial studies on toxicity towards cells

Biocompatibility of azide functionalised surfaces was assessed using human fibroblasts (HeLa cells) and human erythrocytes. HeLa cells were seeded onto TCPS, Brpp coated, and azide functionalised 96-well microplates. After an overnight incubation, cell numbers and morphology were assessed by fluorescence microscopy (Figure 7.7).

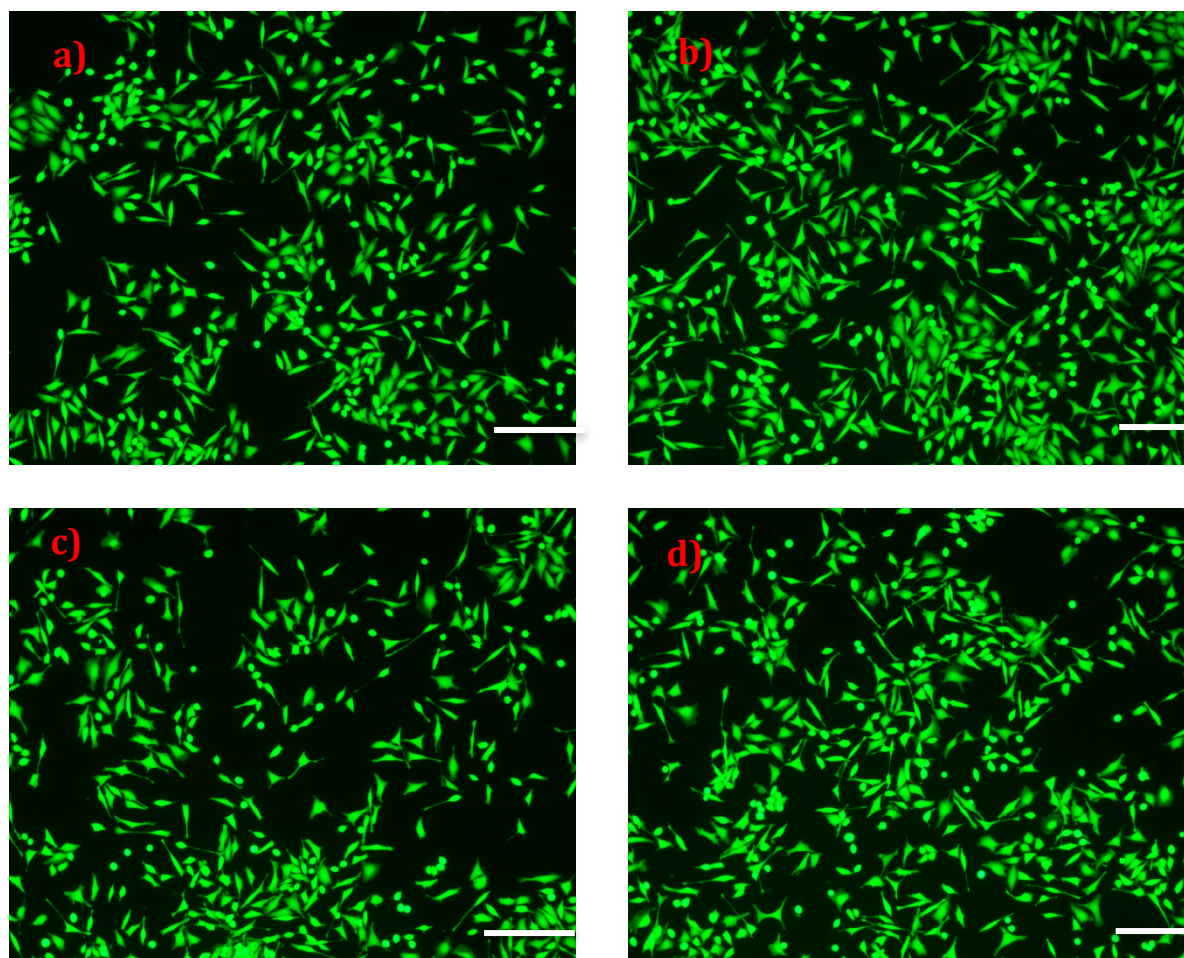


Figure 7.7. Calcein labelled HeLa Cells cultured overnight on a) TCPS, (b) 0.1 M azide, (c) 0.5 M azide and (d) 1 M treated surfaces. Cells were labelled with Live/Dead assay. (10 X objective) Scale bar is 200  $\mu\text{m}$ .

HeLa cells did not attach to the Brpp-coated surfaces (not shown) after incubation, unless the surface had been azide-functionalised (Figure 7.7). All azide-reacted surfaces showed similar amounts of HeLa cell attachment, and the morphology of the cells do not

differ greatly compared with the TCPS control. This indicates that all azide surfaces display a low level of toxicity towards HeLa cells.

The plasma polymer coated surfaces with  $\text{NaN}_3$  demonstrated only a minor haemolytic effect on human erythrocytes (Figure 7.8). The level of haemolysis induced by the azide coated surfaces is similar to that by Brpp and DGpp coatings, corresponding to 10 % relative to that by a thin layer of Triton X-100 coating, which readily lyses erythrocytes and was used as the positive control in this study (Figure 7.8). No difference was found among the plasma coated surfaces and the negative control non-coated Thermanox™ coverslip, suggesting the haemolysis related to the plasma-coated surfaces might be a collateral result from mechanical disruption of the erythrocytes by the shear force of the coverslip during the experimental procedure. Thus, the surfaces developed in this study allow for the inhibition of biofilm formation, without producing undesired haemolytic side-effects.

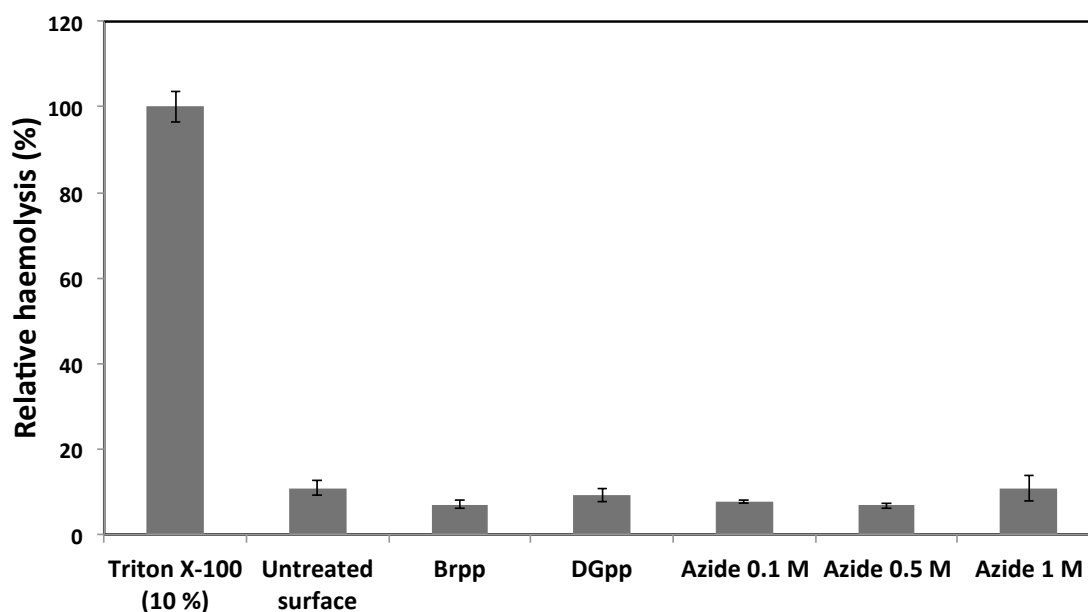


Figure 7.8. Haemolysis assay for surfaces developed in this study.

## 7.4. Conclusions

We have found that azide groups tethered to a TCPS surface through nucleophilic exchange on a brominated plasma polymer display detrimental effects on microbial cell attachment and biofilm maturation across a variety of bacterial and fungal species. The azide treated surfaces appear to be compatible with viability of human cells *in vitro*. This immobilisation process of azide groups involves two steps, firstly deposition of brominated plasma polymer onto a polymer surface and then react with sodium azide solutions. Depending on the concentration of sodium azide, the amount of incorporation within the coatings differs. This fast and versatile technique can be adapted to coat different substrates and offer great promise to combat device related infections.

## 7.5 References

1. N. Huebsch and D. J. Mooney, *Nature*, 2009, 462, 426-432.
2. D. Lebeaux, A. Chauhan, O. Rendueles and C. Beloin, *Pathogens*, 2013, 2, 288-356.
3. J. W. Costerton, P. S. Stewart and E. P. Greenberg, *Science*, 1999, 284, 1318-1322.
4. L. Hall-Stoodley, J. W. Costerton and P. Stoodley, *Nat Rev Micro*, 2004, 2, 95-108.
5. J. D. Bryers, *Biotechnology and Bioengineering*, 2008, 100, 1-18.
6. E. Ostuni, R. G. Chapman, M. N. Liang, G. Meluleni, G. Pier, D. E. Ingber and G. M. Whitesides, *Langmuir*, 2001, 17, 6336-6343.
7. A. R. Denes, E. B. Somers, A. C. L. Wong and F. Denes, *Journal of Applied Polymer Science*, 2001, 81, 3425-3438.
8. W. C. E. Schofield and J. P. S. Badyal, *ACS Applied Materials & Interfaces*, 2009, 1, 2763-2767.
9. S. Theapsak, A. Watthanaphanit and R. Rujiravanit, *ACS Applied Materials & Interfaces*, 2012, 4, 2474-2482.
10. E.-R. Kenawy, F. I. Abdel-Hay, A. E.-R. R. El-Shanshoury and M. H. El-Newehy, *Journal of Controlled Release*, 1998, 50, 145-152.

11. E.-R. Kenawy, A. E.-R. R. El-Shanshoury, N. Omar Shaker, B. M. El-Sadek, A. H. B. Khattab and B. Ismail Badr, *Journal of Applied Polymer Science*, 2011, 120, 2734-2742.
12. I. Braceras, J. Oyarbide, P. Azpiroz, N. Briz, E. Ipiñazar, N. Álvarez, G. Atorrasagasti, R. M. Fratila and J. M. Aizpurua, *Plasma Processes and Polymers*, 2013, 10, 328-335.
13. C. S. Kwok, T. A. Horbett and B. D. Ratner, *Journal of Controlled Release*, 1999, 62, 301-311.
14. D. J. Balazs, K. Triandafillu, E. Sardella, G. Iacoviello, P. Favia, R. d'Agostino, H. Harms and H. J. Mathieu, in *Plasma Processes and Polymers*, Wiley-VCH Verlag GmbH & Co. KGaA, 2005, DOI: 10.1002/3527605584.ch26, pp. 351-372.
15. K. Vasilev, V. Sah, K. Anselme, C. Ndi, M. Mateescu, B. r. Dollmann, P. Martinek, H. Ys, L. Ploux and H. J. Griesser, *Nano Letters*, 2009, 10, 202-207.
16. S. Lischer, E. Körner, D. J. Balazs, D. Shen, P. Wick, K. Grieder, D. Haas, M. Heuberger and D. Hegemann, *Journal of The Royal Society Interface*, 2011, 8, 1019-1030.
17. K. Vasilev, S. S. Griesser and H. J. Griesser, *Plasma Processes and Polymers*, 2011, 8, 1010-1023.
18. D. Campoccia, L. Montanaro and C. R. Arciola, *Biomaterials*, 2013, 34, 8533-8554.
19. R. Kumar and H. Münstedt, *Biomaterials*, 2005, 26, 2081-2088.
20. M. Ip, S. L. Lui, V. K. M. Poon, I. Lung and A. Burd, *Journal of Medical Microbiology*, 2006, 55, 59-63.
21. J. S. Kim, E. Kuk, K. N. Yu, J.-H. Kim, S. J. Park, H. J. Lee, S. H. Kim, Y. K. Park, Y. H. Park, C.-Y. Hwang, Y.-K. Kim, Y.-S. Lee, D. H. Jeong and M.-H. Cho, *Nanomedicine: Nanotechnology, Biology and Medicine*, 2007, 3, 95-101.
22. M. D. Arjun Srinivasan, M. M. Tobi Karchmer, B. S. Ann Richards, M. D. Xiaoyan Song and M. D. M. Trish M. Perl, *Infection Control and Hospital Epidemiology*, 2006, 27, 38-43.
23. D. W. Brett, *Ostomy/wound management*, 2006, 52, 34-41.
24. J. J. Castellano, S. M. Shafii, F. Ko, G. Donate, T. E. Wright, R. J. Mannari, W. G. Payne, D. J. Smith and M. C. Robson, *International Wound Journal*, 2007, 4, 114-122.
25. J. A. Lemire, J. J. Harrison and R. J. Turner, *Nat Rev Micro*, 2013, 11, 371-384.

26. R. S. Greco, R. A. Harvey and S. Z. Trooskin, Google Patents, 1989.
27. A. Siddiqui and A. K. Schultz, Google Patents, 2001.
28. B. Gottenbos, H. C. van der Mei, F. Klatter, P. Nieuwenhuis and H. J. Busscher, *Biomaterials*, 2002, 23, 1417-1423.
29. Z. Li, D. Lee, X. Sheng, R. E. Cohen and M. F. Rubner, *Langmuir*, 2006, 22, 9820-9823.
30. J. A. Loontjens, in *Biomaterials Associated Infection*, eds. T. F. Moriarty, S. A. J. Zaat and H. J. Busscher, Springer New York, 2013, DOI: 10.1007/978-1-4614-1031-7\_15, ch. 15, pp. 379-404.
31. B. R. Coad, S. E. Kidd, D. H. Ellis and H. J. Griesser, *Biotechnology Advances*, 2014, 32, 296-307.
32. M. Salwiczek, Y. Qu, J. Gardiner, R. A. Strugnell, T. Lithgow, K. M. McLean and H. Thissen, *Trends in Biotechnology*, 2014, 32, 82-90.
33. S. Zhang and J. T. Koberstein, *Langmuir : the ACS journal of surfaces and colloids*, 2012, 28, 486-493.
34. J. Lafarge, N. Kébir, D. Schapman, V. Gadenne and F. Burel, *Cellulose*, 2013, 20, 2779-2790.
35. K. K. K. Ho, R. Chen, M. D. P. Willcox, S. A. Rice, N. Cole, G. Iskander and N. Kumar, *Biomaterials*, 2014, 35, 2336-2345.
36. R. T. Chen, B. W. Muir, G. K. Such, A. Postma, R. A. Evans, S. M. Pereira, K. M. McLean and F. Caruso, *Langmuir*, 2009, 26, 3388-3393.
37. R. T. Chen, S. Marchesan, R. A. Evans, K. E. Styan, G. K. Such, A. Postma, K. M. McLean, B. W. Muir and F. Caruso, *Biomacromolecules*, 2012, 13, (3), 889-895.
38. H. Biederman and D. Slavínská, *Surface and Coatings Technology*, 2000, 125, 371-376.
39. T. Desmet, R. Morent, N. D. Geyter, C. Leys, E. Schacht and P. Dubruel, *Biomacromolecules*, 2009, 10, 2351-2378.
40. E. Johnston, B. Ratner and J. Bryers, *NATO ASI Series E Applied Sciences-Advanced Study Institute*, 1997, 346, 465-476.
41. S. Sarghini, S. Paulussen and H. Terry, *Plasma Processes and Polymers*, 2011, 8, 59-69.

42. M. J. Garcia-Fernandez, L. Martinez-Calvo, J.-C. Ruiz, M. R. Wertheimer, A. Concheiro and C. Alvarez-Lorenzo, *Plasma Processes and Polymers*, 2012, 9, 540-549.
43. S. Simovic, D. Losic and K. Vasilev, *Chemical Communications*, 2010, 46, 1317-1319.
44. I. Braceras, J. Oyarbide, P. Azpiroz, N. Briz, E. Ipiñazar, N. Álvarez, G. Atorrasagasti, R. M. Fratila and J. M. Aizpurua, *Plasma Processes and Polymers*, 2013, 10, (4), 328-335.
45. E. B. H. Hume, J. Baveja, B. Muir, T. L. Schubert, N. Kumar, S. Kjelleberg, H. J. Griesser, H. Thissen, R. Read, L. A. Poole-Warren, K. Schindhelm and M. D. P. Willcox, *Biomaterials*, 2004, 25, 5023-5030.
46. M. A. Deighton, J. Capstick, E. Domalewski and T. van Nguyen, *Methods in enzymology*, 2001, 336, 177-195.
47. Y. Jin, H. K. Yip, Y. H. Samaranayake, J. Y. Yau and L. P. Samaranayake, *Journal of clinical microbiology*, 2003, 41, 2961-2967.
48. C. D. Ciornei, T. Sigurdardóttir, A. Schmidtchen and M. Bodelsson, *Antimicrobial Agents and Chemotherapy*, 2005, 49, 2845-2850.
49. S. Marchesan, C. D. Easton, K. E. Styan, P. Leech, T. R. Gengenbach, J. S. Forsythe and P. G. Hartley, *Colloids and Surfaces B: Biointerfaces*, 2013, 108, 313-321.
50. A. C. Gouget-Laemmel, J. Yang, M. A. Lodhi, A. Siriwardena, D. Aureau, R. Boukherroub, J. N. Chazalviel, F. Ozanam and S. Szunerits, *The Journal of Physical Chemistry C*, 2013, 117.
51. G. A. O'Toole and R. Kolter, *Molecular microbiology*, 1998, 30, 295-304.
52. S. S. Yoon, R. F. Hennigan, G. M. Hilliard, U. A. Ochsner, K. Parvatiyar, M. C. Kamani, H. L. Allen, T. R. DeKievit, P. R. Gardner, U. Schwab, J. J. Rowe, B. H. Iglewski, T. R. McDermott, R. P. Mason, D. J. Wozniak, R. E. Hancock, M. R. Parsek, T. L. Noah, R. C. Boucher and D. J. Hassett, *Developmental cell*, 2002, 3, 593-603.
53. T. Das and M. Manefield, *PloS one*, 2012, 7, e46718.

## Chapter 8 Conclusions and outlook

*"The end of a melody is not its goal; but nonetheless, had the melody not reached its end it would not have reached its goal either. A parable."  
- Friedrich Nietzsche*

## 8.1 Conclusions

In this thesis, the generation, characterisation and development of thin plasma polymer films, their growth mechanisms and application for manipulation of surface interactions with cell and microbe have been reported. Radio frequency glow discharge (RFGD) plasma polymerisation of several monomers was employed for coating fabrication. By changing RFGD process parameters, in concert with varying substrate materials, plasma polymer films with distinct chemical and physical properties were produced. The results component of this thesis can be categorised into three main sections: 1) application of diglyme plasma polymer (DGpp) films to direct cell fate; 2) growth mechanisms of diglyme plasma polymer films on various substrates; 3) characterisation of brominated plasma polymer (Brpp) films and their usage in resisting biofilm formation. As such, I will discuss the findings and contributions of this work for each of these topics separately.

### 8.1.1 DGpp film chemistry and its applications

**Chapter 3** and **Appendix 3** present both uniform and patterned DGpp films that were extensively characterised in terms of chemical properties, and the resulting capability in resisting protein, cell and microbe attachment to material surfaces. **Chapter 3** investigated the dependence of DGpp film chemistry on the RFGD process parameters. A series of DGpp films were deposited at systematically increasing load powers while keeping other process conditions the same, including 10, 20, 30, 40 and 50 W. The chemical analysis of the films was performed on XPS and NEXAFS. Results concluded that increasing the load power led to more fragmentation of the precursor, hence greater loss of the original functional groups, which is ether (-C-O-C-) for DGpp films. The retention of ether affected subsequent biological tests. With high ether content, i.e. similar to PEG coatings, there is less protein adsorption, fewer cell adhesion and reduced amount of microbe attachment. This chapter also reports on the generation of patterned DGpp films at 5 W load power, where ether contents in defined areas can be manipulated so that both antifouling and fouling regions exist at the same time. These

patterned films were tested with fibroblast cell adhesion and showed good local confinement of cells.

DGpp coatings were often applied to material surfaces for their antifouling properties as mentioned in chapter 2. However, in this work, the cell adhesive DGpp film was favorable as well. **Appendix 3** exemplifies the use of both cell-repellent and cell-adhesive DGpp coatings for study of cell responses. 5 W and 50 W DGpp coatings were deposited onto mica (flat) and amyloid fibril networks (AFNs) coated mica (nanoscale structures) to generate chemically homogeneous surfaces. In general, high ether containing 5 W surfaces showed low level of L929 cell attachment. Meanwhile, no difference was observed between cell number on flat mica and that of AFN coated mica. In contrast, low ether containing 50 W DGpp coated surfaces were populated with L929 cells. In addition, a significant increase in cell attachment was found on 50 W DGpp coated AFN surfaces compared with flat mica. This work demonstrates a platform where surface chemistry and topography can be turned individually to control cell fate. The novelty, however, was the fact that plasma polymer films were deposited onto self-assembled protein network with minimal disruption to the surface structure, even after > 100 nm DGpp was built up. In this thesis, more work has been conducted to decipher the mechanism of DGpp growth on AFN.

### 8.1.2 DGpp growth on different substrates

The enquiry on the influence of the substrate to plasma polymer film growth is largely overlooked in this field compared to chemical analysis. Therefore, the role of substrates and how it affects the resultant plasma polymer films has more to be discovered. In this work, beside AFN, other substrates, including Si wafer, ITO glass and plasma polymer films were all used to decode the physical properties of DGpp films. The results of these studies were reported in **Chapter 4, 5** and **6**.

**Chapter 4** offers insight on growth of DGpp films on Si wafer and ITO glass. Using the same deposition conditions, it was found that DGpp film grew at a greater rate on Si wafers than on ITO glass. It was argued in the chapter that Si wafer and ITO glass

obtained surface potential bias in the plasma environment, which led to different amount of ion and radical bombardment. The growth of the plasma polymer film was governed by those plasma species, thus a difference in growth rate were observed. This finding challenges the common notion that plasma polymerisation is a substrate independent process.

**Chapter 4** also compared the film chemistry at the ITO glass/DGpp interface (underside) and the top surface of DGpp film (topside) to elucidate the initial growth of DGpp films. The method used to expose the underside was simple delamination using a double sided tape. Interestingly, the 20 W deposited films adhered to the ITO glass more firmly than the 50 W ones. It was concluded from the XPS and NEXAFS data that at high deposition powers, the underside contained a considerably greater concentration of oxygen ( $O/C = 0.376$ ) when compared to the topside ( $O/C = 0.230$ ). On the other hand, at lower deposition power, the film compositions of top- and underside were similar. This knowledge laid the foundation for the development of the DGpp film structure model obtained through neutron reflectometry in **chapter 5**.

**Chapter 5** presented the interfacial structures of bilayer plasma polymer films. Hexamethyldisiloxane (HMDSO), di(ethylene glycol) dimethyl ether (DG) and allylamine (AA) were employed to generate single layer plasma polymer films on top of Si wafer substrates. Two conditions were used for each starting monomer; therefore, six types of plasma polymer coatings were produced. On top of these plasma polymerised films, a deuterated di(ethylene glycol) dimethyl ether (dDG) films were deposited at 20 W load power. All films were characterised with XPS, neutron and X-ray reflectometry (NR, XRR). According to the model fitting of the NR data, it was found that the deposition of the dDG layer roughens the dDG/pp interface. The interface broadening was most dramatic on HMDSO film generated at 10 W load power, followed by 20 W DGpp and then 20 W AApp. For the films made at 40 W load power, the magnitudes of roughness increase at the interface were similar among HMDSO, DG and AA films. Comparing the two conditions applied to each monomer, the interface region was wider if the film was made at lower load power. Since the dDG deposition conditions were the same, the plasma environment is consistent for all six overlying coatings. The discrepancy in the extent of etching and roughening at the dDG/pp interface is probably a product of

varying the degree of bond dissociation in the underlying plasma polymer film. This hypothesis can be applied to other types of plasma polymer films. The interface property is important as more and more multilayer films are incorporated into biomaterials fabrication.

**Chapter 6** examined the interface of DGpp films and AFNs. DGpp films, up to 961 nm thick, were deposited onto AFN coated mica substrates. The nanoscale contours of the AFNs were well preserved (shown in AFM images). To understand how DGpp films build up on the fibril networks, chemical maps were generated through the film and AFN construct via XPS depth profiling. A profile of elemental composition throughout the bulk of the DGpp + AFN construct was obtained as ions etched through the material which was paused at predetermined intervals to allow collection of XPS data. Based on the XPS chemical analysis, two regions were identified in the DGpp + AFN construct: 1) an AFN plus DGpp mixture at the DGpp/AFN interface; 2) DGpp only region with no trace of fibril elements after the mixed layer. This model suggests that at the initial stage of DGpp deposition, etching and deposition occurs simultaneously. The fragments of the AFN were created due to etching and mixed together with growing DGpp film. The plasma polymer grew conformably on the top, hence maintained the nanostructure of the surface, with slight smoothing effect. This study leads the way for research on interaction of plasma polymeration with substrate containing biological molecules.

### 8.1.3 Antimicrobial coatings

**Chapter 7** investigated the interactions of microorganisms with material surfaces, where brominated plasma polymer coatings were studied for the generation of antimicrobial surfaces. The motivation for using Brpp was that it could react with  $\text{NaN}_3$  in mild conditions. The azide groups were immobilised onto material surfaces through nucleophilic exchange. In this work, 0.1 M, 0.5 M and 1 M of  $\text{NaN}_3$  solution were prepared. Higher azide concentration resulted in larger percentage of azide incorporation at the surface. Both 0.5 M and 1 M  $\text{NaN}_3$  treated surfaces prevented biofilm growth of *Staphylococcus epidermidis* and *Pseudomonas aeruginosa*, *Candida albicans* relative to tissue culture polystyrene control. The azide functionalised coatings

proved to be not toxic to HeLa cells nor did they induce haemolysis of human erythrocytes. This work embodies an easy and versatile method for generation of antimicrobial coatings.

## 8.2 Future outlook

It is hoped that this thesis will lead to more research at the fundamental of plasma polymerisation and the interaction of plasma polymer films with mammalian cells and microorganisms.

In the aspect of plasma polymer growth, the substrate induced difference should be considered in making decisions about materials selection. The techniques described for study of DGpp growth at the interface, that is delamination, neutron reflectometry and depth profiling, can be applied for other plasma polymer films. Provided that the investigator take into account the accessibility of instruments, such as FIB-SEM, NR and XRR. It is envisaged that information on plasma polymer growth can be beneficial to other research fields where plasma polymer coatings were frequently used, such as optics and electronics.

In terms of cell-materials interactions, more sensitive cells, such as stem cells, can be used. The behaviours of stem cells on top of DGpp coated flat or nanotopographic surface can be interesting. One way to differentiate from this thesis is to use patterned or gradient DGpp films rather than uniform coatings to coat the substrates. The other possibility lies in the nanoscale structure, either machine manufactured or self-assembled networks provide new opportunities.

When it comes to microbes, a lot more can be done for both DGpp and Brpp systems. For DGpp films, the low ether content can only resist pathogens for a short period of time. It is advisable to embed antimicrobial compounds inside or underneath the DGpp coating to build a two level system that possess both release-killing and adhesion-resistant capabilities. For azide functionalised surfaces, a key point for the advancement of these coatings is to test the stability of the films. The next step will be study on long

term storage of these films. The ability of azide to resist a broad spectrum of pathogens offers great promise for preventing biofilm formation. Depends on the application, the biocompatibility and toxicity of azide containing films should be tested against more cell lines.



## Appendix 1

### Supporting Information for Chapter 4

Table S4.1, Elemental composition (atomic%) of clean ITO glass and 50 W delaminated area on DGpp coated ITO sample.

<i>Atomic%</i>	<i>C</i>	<i>In</i>	<i>Sn</i>	<i>O</i>
Clean ITO glass	34.06 ± 0.23	22.99 ± 0.47	2.61 ± 0.01	40.34 ± 0.23
50 W delaminated area on ITO	34.17 ± 0.50	22.44 ± 0.10	2.65 ± 0.05	40.75 ± 0.35

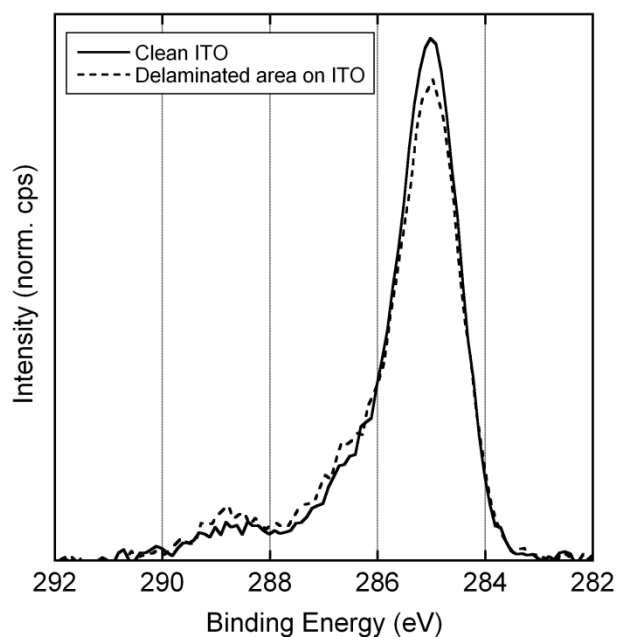


Figure S4.1, Representative high resolution C 1s spectra of clean ITO glass sample (black solid line) and 50 W delaminated area on DGpp coated ITO glass sample.

## Appendix 2

### Supporting Information for Chapter 5

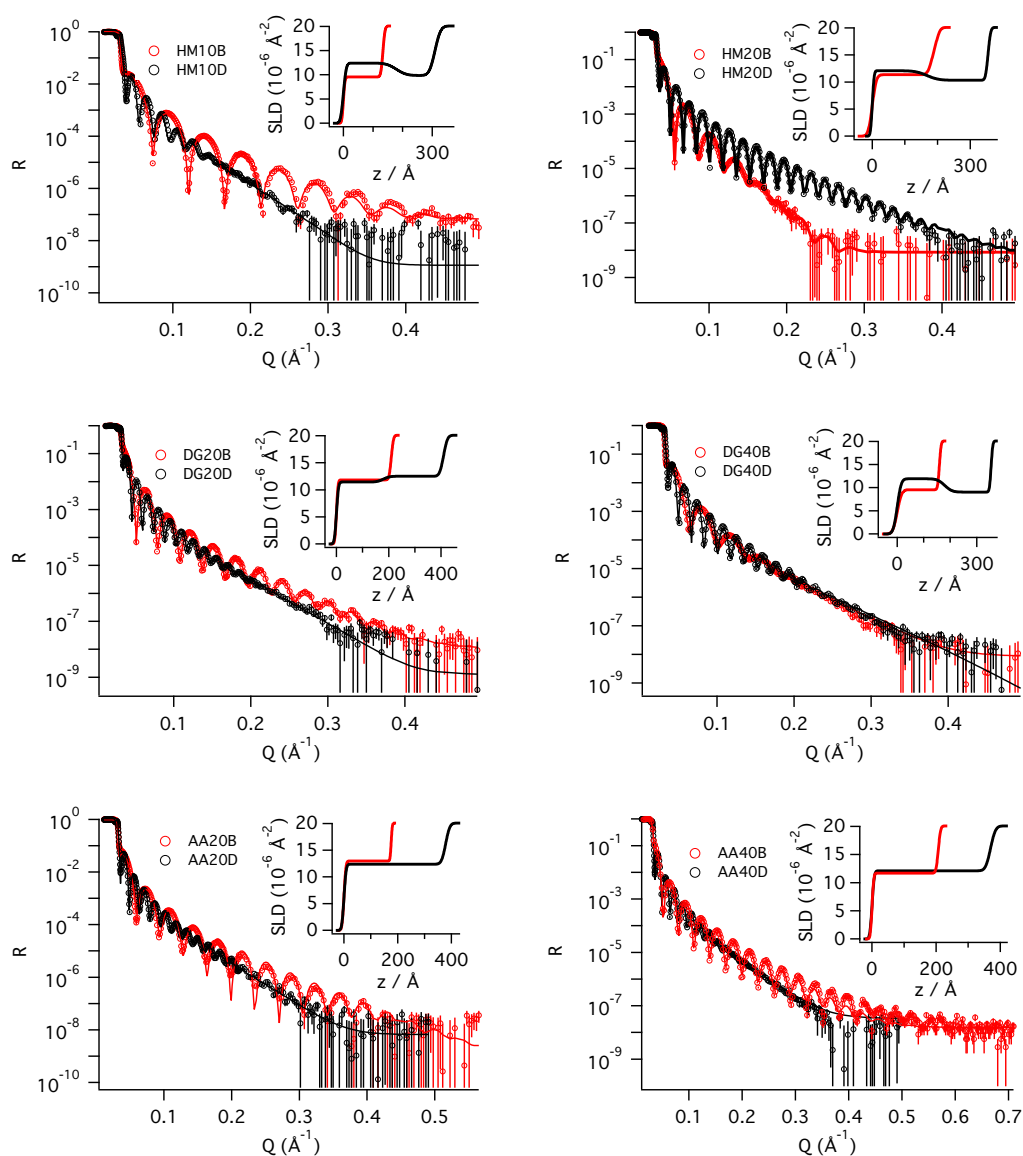


Figure S5.1. XRR spectra from the air-plasma polymer film-Si system. Each figure contains the single and double layer spectra for a given base polymer layer, e.g. HM10B and HM10D. The symbols represent the observed reflectivity data while the solid lines are fits to the data determined from the structural models using *Motofit* software. The inset is the scattering length density profiles of the films.

Table S5.1. Film thickness, scattering length density and roughness of single and bilayer plasma polymer films as used for XRR model fitting. For single layer film, layer 1 refers to the bulk of the pp, and layer 2 is the transition region between pp and Si wafer. For the bilayer system layer 1 means the deuterated DG layer on the top, while layer 2 refers to the underlying plasma polymer film that is close to the Si wafer substrate. For the single layer system it was possible to distinguish two regions of slightly different SLD, with a thin layer of different SLD adjacent to the silicon wafer.

<b>XRR</b>	<b>Thickness (Å)</b>		<b>SLD (x 10<sup>6</sup> Å<sup>-2</sup>)</b>		<b>Roughness (Å)</b>	
	<b>1</b>	<b>2</b>	<b>1</b>	<b>2</b>	<b>Air/1</b>	<b>1/2</b>
<b>Single</b>						
<b>HM10</b>	131.2		9.84±0.06		2.5±0.5	
<b>HM20</b>	182.2±2.4	17.4±0.1	11.41±0.13	16.85±1.49	9.8±0.1	10.2±1.4
<b>DG20</b>	209.6±1.6		11.7±0.5		4.8±0.4	
<b>DG40</b>	158.5±0.7		9.56±0.26		13.0±0.5	
<b>AA20</b>	175.5±0.9		12.09±0.67		5.1±0.5	
<b>AA40</b>	206.2±0.1		12.25±0.2		3.7±0.1	
<b>Bilayer</b>	<b>1</b>	<b>2</b>	<b>1</b>	<b>2</b>	<b>Air/1</b>	<b>1/2</b>
<b>HM10D</b>	169.0±13	130.4±12.9	12.35±0.84	9.24±0.87	16.9±1.3	26.8±6.0
<b>HM20D</b>	176.5±2	176.4±1.9	12.17±0.58	10.11±0.77	4.7±0.4	15.2±6.3
<b>DG20D</b>	181.1±7.6	228.2±7.9	11.43±0.16	12.56±0.17	6.2±0.1	18.7±5.6
<b>DG40D</b>	179.8±5.1	175.7±6.0	11.93±1.53	9.06±1.00	12.4±1.1	23.0±7.1
<b>AA20D</b>	214.2±12.2	171.1±12.2	13.39±0.50	14.97±0.74	7.4±0.2	23.3±9.8
<b>AA40D</b>	185.8±9.0	185.8±9.1	11.85±0.18	12.43±0.23	5.6±0.07	7.7±5.0

## Appendix 3

### Supporting Information for Chapter 6

Reproduced with permission from “Nicholas, P. Reynolds; Katie, E. Styan; Christopher, D. Easton; Yali, Li; Lynne, Waddington; Cecile, Lara; John, S. Forsythe; Raffaele Mezzenga; Patrick, G. Hartley; Benjamin W. Muir, Nanotopographic Surfaces with Defined Surface Chemistries from Amyloid Fibril Networks Can Control Cell Attachment. *Biomacromolecules* 2013, 14 (7), 2305-2316.” Copyright © 2013, American Chemical Society.

<http://pubs.acs.org/doi/full/10.1021/bm400430t>



## Nanotopographic Surfaces with Defined Surface Chemistries from Amyloid Fibril Networks Can Control Cell Attachment

Nicholas P. Reynolds,<sup>\*,†</sup> Katie E. Styan,<sup>†</sup> Christopher D. Easton,<sup>†</sup> Yali Li,<sup>†</sup> Lynne Waddington,<sup>‡</sup> Cecile Lara,<sup>§</sup> John S. Forsythe,<sup>||</sup> Raffaele Mezzenga,<sup>§</sup> Patrick G. Hartley,<sup>†</sup> and Benjamin W. Muir<sup>†</sup>

<sup>†</sup>Materials Science and Engineering, CSIRO, Private Bag 10, Bayview Avenue, Clayton, Vic 3169, Australia

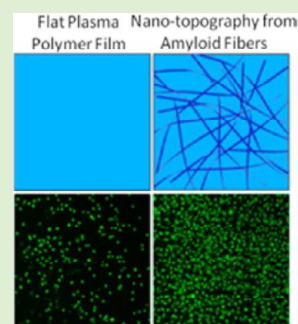
<sup>‡</sup>Materials Science and Engineering, CSIRO 343 Royal Parade, Parkville, Vic 3052, Australia

<sup>§</sup>Department of Health Science and Technology, Food & Soft Materials, ETH, Schmelzbergstrasse 9, 8092 Zurich, Switzerland

<sup>||</sup>Department of Materials Engineering, Monash University, Clayton, 3800, Vic 3800, Australia

### Supporting Information

**ABSTRACT:** We show for the first time the possibility of using networks of amyloid fibrils, adsorbed to solid supports and with plasma polymer coatings, for the fabrication of chemically homogeneous surfaces with well-defined nanoscale surface features reminiscent of the topography of the extracellular matrix. The robust nature of the fibrils allows them to withstand the plasma polymer deposition conditions used with no obvious deleterious effect, thus enabling the underlying fibril topography to be replicated at the polymer surface. This effect was seen despite the polymer coating thickness being an order of magnitude greater than the fibril network. The *in vitro* culture of fibroblast cells on these surfaces resulted in increased attachment and spreading compared to flat plasma polymer films with the same chemical composition. The demonstrated technique allows for the rapid and reproducible fabrication of substrates with nanoscale fibrous topography that we believe will have applications in the development of new biomaterials allowing, for example, the investigation of the effect of extracellular matrix mimicking nanoscale morphology on cellular phenotype.



### INTRODUCTION

Interactions of cells with their surrounding microenvironment are both chemically- and physically mediated. The significance of chemically mediated interactions, through specific intercellular epitopes,<sup>1,2</sup> is well accepted in the scientific community. Physically mediated interactions, such as responses to elasticity or stiffness, are a more recent finding, and there are already a number of studies in the literature showing such effects.<sup>3–5</sup> Surface nanotopography has also been demonstrated to affect cell attachment,<sup>6,7</sup> proliferation,<sup>8</sup> and, in the case of stem cells, differentiation.<sup>9,10</sup>

A thorough understanding of the effect of topography on cell response is yet to be gained.<sup>11</sup> This is highlighted by conflicting observations in the literature. For example, Dalby et al.<sup>12</sup> generated nanoscale topography by employing polymer demixing to create nanoscale islands with specific heights. Nanoscale arrays of islands 50 nm in height caused an increase in the attachment of fibroblast cells.<sup>12,13</sup> Conversely, Penissi et al. recently showed that disordered nanoroughened platinum surfaces with root-mean-square average (Rrms) roughness values between 7.5 and 15.2 nm all resulted in reduced fibroblast growth.<sup>14</sup> However, some studies on other cell types have resulted in no variation in attachment.<sup>15</sup> To elucidate the role of surface topography in mediating cell-surface interactions, it is necessary to accurately reproduce and isolate it from all other parameters (e.g., surface chemistry). The importance of developing such reductionist systems is often

overlooked, and may account for some of the variability in findings.

Traditional methods of generating nanoscale topography include relatively 'low-tech' techniques such as 'blasting' the substrate with micrometer-sized particles.<sup>7</sup> Blasting techniques are inexpensive and fast, however they can introduce surface contamination and struggle to reproduce the nanoscale length scales that have been shown to provide improved cellular responses.<sup>16–18</sup> More elaborate surface features have been prepared whereby libraries of substrates with random topographies are generated and investigated for cellular response.<sup>10,19</sup> Other more readily applied surface modifications have been achieved, using methods such as electron beam lithography (EBL),<sup>9</sup> however the expense of these approaches limits the range of their applicability. 'Bottom up' methods such as colloidal lithography<sup>20,21</sup> or anodizing metal oxide surfaces,<sup>22</sup> have been shown to generate nanoscale features in a more cost-effective manner. However, the surfaces generated by all the above methods generally fail to consider how the shape and morphology of the nanoscale features relate to the typical cellular microenvironment. Therefore, there is merit in the exploration of new methods for routinely producing surfaces

Received: March 27, 2013

Revised: May 9, 2013

Published: May 23, 2013

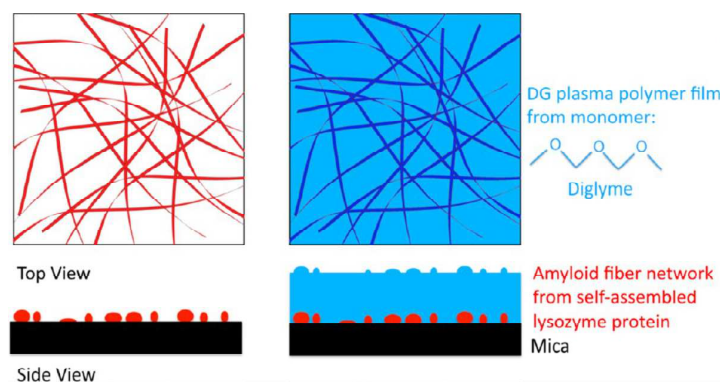


**Figure 1.** AFNs formed from the hydrolyzed peptide fragments of lysozyme (red) are deposited on fresh mica (black; left) onto which DGpp (blue) films are deposited at a load power of either 50 or 5 W (right).

with well-defined nanoscale fibrous topography that mimics the extracellular matrix (ECM).

In the present study, we utilize a method capable of creating a fibrous surface nanotopography while at the same time ensuring that surface chemistry is conserved relative to a flat control surface. The nanotopography is provided by amyloid fibrils formed *in vitro* by subjecting globular proteins to specific reaction conditions,<sup>23</sup> and subsequently deposited on solid supports as amyloid fibril networks (AFNs). To ensure chemical homogeneity, plasma polymers of selected chemical composition were deposited on the AFNs. Plasma polymers have previously been shown to make good platforms for the study of cell attachment to topographically<sup>24</sup> and chemically defined films.<sup>24,25</sup> Such templating of polymers from proteins has been reported for a number of different systems,<sup>26</sup> but to the best of our knowledge, this work is the first report of plasma polymers being used to coat amyloid fibrils. Using AFNs to generate nanotopography in plasma polymer films has a number of advantages over other methods. First, the deposition of the plasma polymer films creates a chemically homogeneous surface thus allowing chemical and topographical influences to be distinguished. Second, the AFNs induce a highly disordered fibrous topography on the plasma polymer surface that we believe more closely resembles the topography of the ECM and may produce more biologically relevant cellular responses. Techniques such as colloidal lithography typically create very highly ordered nanotopographical patterns, and the morphology and degree of order of the topography generated has previously been shown to have a large effect on cellular response.<sup>9</sup> Third, by altering the fibril forming reaction conditions, it is possible to control the morphology of the amyloid fibrils used. The ability to control fibril morphologies combined with the wide range of monomers available for plasma polymerization provides a large number of different combinations of topography and chemistry that can be investigated relatively easily and quickly.

The use of plasma polymers as molecular recognition templates was first reported by Shi et al.<sup>27</sup> Proteins encased in disaccharides were adsorbed on mica and used as templates for the deposition of plasma polymers. In another example, Heyse et al.<sup>28,29</sup> deposited enzymes during an atmospheric glow discharge polymerization to produce hybrid protein films. Recently, Amorosi et al.<sup>30</sup> have shown that atmospheric plasma polymers of ethylene glycol dimethacrylate can be deposited onto enzymes, apparently without loss of their function.

Like all amyloids, the protein fibrils that compose the AFNs are aggregated peptides with a secondary structure rich in  $\beta$ -sheets.<sup>23,31–34</sup> Amyloid fibrils are generally micrometers in length and have diameter of less than 100 nm,<sup>35</sup> making them distinct from the biomolecules used in previous studies. Although traditionally associated with neurodegenerative disease, more recent studies suggest that mature amyloids may merely be inert byproducts of disease,<sup>36–38</sup> and there have been some cases where physiological amyloids have been found to possess beneficial functions.<sup>39,40</sup> Furthermore, the unique morphology, mechanical properties and self-assembling nature of AFNs has made them attractive prospects for use in the field of biomaterials<sup>41,42</sup> and biomimetic hybrids.<sup>43</sup> Amyloid fibrils generated from lysozyme were chosen over other fibrous systems since the well characterized self-assembly process offers a high degree of control of the resulting fibril morphology.<sup>23</sup> In addition, the nanoscale morphology of networks of AFNs mimics the fibrous structure of the ECM<sup>44,45</sup> and corresponds with the length-scales upon which cells interact with their microenvironment.<sup>17,18</sup>

In this study, we investigate to what extent the nanoscale topography of the underlying AFN is preserved and transferred to the surface of diethyleneglycol dimethyl ether (diglyme) plasma polymer (DGpp) films (Figure 1). Two plasma polymers providing both low-fouling<sup>46,47</sup> and protein adhesive surface chemistries were explored. The films were characterized by complementary techniques and the surface chemistry compared to equivalent flat control surfaces. Subsequently, the attachment and spreading of fibroblast cells on the nanotopographical surfaces was compared to equivalent flat control surfaces.

## ■ MATERIALS AND METHODS

**Amyloid Self-Assembly.** To obtain protein of sufficient purity to allow a well controlled self-assembly reaction, hen egg white lysozyme (HEWL) (Sigma) was dialyzed according to the protocol used in Jung et al.<sup>48</sup> Solutions of 2 wt % HEWL were prepared in Milli-Q water and adjusted to pH 2, before being filtered through a 0.45  $\mu$ m membrane in order to remove any pre-existing aggregates before use. Solutions were transferred to sealed glass vials and placed in an oil bath at 90 °C for 24 h while undergoing constant stirring (300 rpm, using a 20  $\times$  5 mm Teflon magnetic stirrer bar) as described in Lara et al.<sup>23</sup> To stop the fibril self-assembly reaction, solutions were quenched in a water-ice mixture. The quenched solutions of fibrils were then dialyzed into Milli-Q water at pH 7.4 (MWCO 1000 Da, 24 h, 4 °C) and stored at 4 °C. Freshly cleaved mica substrates were prepared for plasma polymer

deposition by incubating 100  $\mu\text{L}$  of the fibril solution (pH 7.4) for 10 min, followed by rinsing in Milli-Q water (1 mL), and drying under a gentle nitrogen stream.

**Plasma Polymer Deposition.** Plasma polymer thin films were deposited onto freshly cleaved mica with or without AFN present via the radio frequency glow discharge (RFGD) of the monomer diethylene glycol dimethyl ether (DG; BDH, 99% purity) in a custom-built reactor. The plasma reactor consisted of a cylindrical glass chamber (height of 35 cm and diameter of 17 cm) and was fitted with two capacitively coupled electrodes, spaced 10 cm apart. The top electrode ( $d = 9.5$  cm) was connected to a RF power supply (125 kHz), while the bottom electrode ( $d = 14$  cm) was grounded. A round-bottom flask containing the monomer diglyme was connected to the reactor chamber via a stainless steel line, and the flow of the monomer vapors was controlled via a manual valve. Substrates were placed on the lower electrode, and a rotary pump was used to evacuate the chamber. The DG monomer was degassed three times prior to deposition. The plasma was ignited at a starting monomer pressure of 20 Pa. For depositions at load powers of 5 W treatment times of 540 s were used. For the higher load power an initial protective 5 W coating was deposited for 30 s (<5 nm), followed by a 180 s deposition at 50 W.

**Atomic Force Microscopy.** An Asylum Research MFP-3D atomic force microscope (Santa Barbara, CA) was used to measure surface topography. Tapping mode was used for imaging in air with ultrasharp silicon nitride tips (NSC15 noncontact silicon cantilevers, Mikro-Masch, Spain). The tips had a typical force constant of 40 N/m and a resonant frequency of 320 kHz. For imaging in fluid the samples were mounted in a closed fluid cell and left to equilibrate for at least 3 h in phosphate buffered saline (PBS) solution. Images were recorded in contact mode and the deflection voltage was minimized so as to exert minimal force on the substrate. The tips had a typical force constant of approximately 0.12 N/m. Typical scan settings involved the use of an applied piezo deflection voltage of 0.7 V at a scan rate of 0.8 Hz. All images were processed (1st order flattening algorithm and roughness parameters) using Igor Pro software, and at least 3 independent substrates were analyzed when calculating Rms and arithmetic mean (Ra) roughness parameters. Fibril thickness measurements were taken from  $2 \times 2 \mu\text{m}$  scans and the full width at half-maximum height (fwhm) was recorded for at least 10 fibrils per scan, mean values were calculated from at least 3 scans per sample and an overall average thickness was determined from at least 3 samples. As the same batch of AFM tips was used for all experiments (other than the fwhm recordings) no further corrections for broadening of the features by the AFM tip were considered.

**Transmission Electron Microscopy.** Transmission electron microscopy (TEM) analysis was performed using a Tecnai 12 Transmission Electron Microscope (FEI, Eindhoven, The Netherlands) at an operating voltage of 120 kV. Images were recorded using a Megaview III CCD camera and AnalySIS camera control software (Olympus). Carbon-coated 300-mesh copper grids were glow-discharged in nitrogen to render the carbon film hydrophilic. A 4  $\mu\text{L}$  aliquot of the sample was pipetted onto each grid. After 30 s adsorption time, the excess was drawn off using Whatman 541 filter paper, followed by staining with 2% aqueous potassium phosphotungstate at pH 7.2, for 10 s. Grids were air-dried until needed. Each grid was systematically examined and imaged to reflect a representative view of the sample. This was important as samples of this type can be very nonhomogeneous on the grid; they tend not to disperse evenly and the fibrils occur in distinct patches. For the labeling of the fibrils with gold nanoparticles, as before, fibrils were allowed to adhere to a glow-discharged carbon-coated grid for 30 s, the excess was drawn off and a drop of undiluted 5 nm colloidal gold solution (British BioCell Int., Cardiff, U.K.) was applied and drawn off after a few seconds. It was clear on examination by TEM that the colloidal gold did not nonspecifically adhere to the grid, but was arranged along the fibrils with minimal background labeling.

**Focused Ion Beam Scanning Electron Microscopy.** The thickness of DGpp deposited either directly on mica or onto the AFN was determined using a focused ion beam scanning electron

microscope (FIB-SEM) (FEI Helios NanoLab 600 DualBeam FIB-SEM, Eindhoven, Netherlands). Before imaging by FIB-SEM the samples were coated with an Au coating (7 nm) in order to promote electrical conduction through the sample. Cross sections were milled using a focused ion beam (FIB) of Ga<sup>+</sup> ions emitted with an accelerating voltage of 30 kV at normal incidence to the sample surface. Each sample was first coated with a protective layer of platinum deposited by the FIB at 93 pA (0.5  $\mu\text{m}$ ). All cross sections were then milled at an ion beam current of 93 pA, followed by a cleaning step at 28 pA to minimize FIB-induced artifacts in the cross-sectional images. The milled cross sections were then imaged *in situ* using the SEM capability of the FIB-SEM.

**X-ray Photoelectron Spectroscopy.** X-ray photoelectron spectroscopy (XPS) analysis was performed using an AXIS Ultra DLD spectrometer (Kratos Analytical Inc., Manchester, U.K.) with a monochromated Al K <sub>$\alpha$</sub>  source at a power of 144 W (12 kV  $\times$  12 mA), a hemispherical analyzer operating in the fixed analyzer transmission mode and the standard aperture (analysis area: 0.3  $\mu\text{m}$   $\times$  0.7  $\mu\text{m}$ ). The total pressure in the main vacuum chamber during analysis was less than  $10^{-8}$  mbar. Survey spectra were acquired at a pass energy of 160 eV. To obtain more detailed information about chemical structure, oxidation states, etc., high resolution spectra were recorded from individual peaks at 40 eV pass energy (yielding a typical peak width for polymers of 1.0–1.1 eV).

Each specimen was analyzed at an emission angle of 0° as measured from the surface normal. Assuming typical values for the electron attenuation length of relevant photoelectrons, the XPS analysis depth (from which 95% of the detected signal originates) ranges between 5 and 10 nm.

Data processing was performed using CasaXPS processing software version 2.3.16 (Casa Software Ltd., Teignmouth, U.K.). All elements present were identified from survey spectra. The atomic concentrations of the detected elements were calculated using integral peak intensities and the sensitivity factors supplied by the manufacturer. Binding energies were referenced to the aliphatic hydrocarbon peak at 285.0 eV. The accuracy associated with quantitative XPS is ca. 10–15%. Precision (i.e., reproducibility) depends on the signal/noise ratio but is usually much better than 5%. The latter is relevant when comparing similar samples.

**Cell Culture.** Samples were placed in the wells of a 24-well plate (Nunc) and then sterilized by immersion in 2 $\times$  Anti-Anti (Antimycotic-Antibiotic, GIBCO) solution for at least 60 min. An L929 mouse fibroblast monolayer was cultured in media (MEM + GlutaMAX-I, GIBCO), supplemented with 1% (v/v) NEAA (nonessential amino acids, GIBCO), 1% (v/v) Anti-Anti, and 10% (v/v) FBS (fetal bovine serum, SAFC Biosciences) at 37 °C with 5% CO<sub>2</sub>/air atmosphere to 80% confluence. Cells were harvested by trypsinization (2 mL Tryple Express, Invitrogen) and then washed by a twice repeated cycle of dilution in 30 mL media followed by centrifugation (300g for 5 min). Processed cells were counted, resuspended in media (75 000 cells/mL), and then added to samples (0.6 mL, 25 000 cells/cm<sup>2</sup> of well area) and incubated overnight at 37 °C with 5% CO<sub>2</sub>/air atmosphere. After 24 h incubation, nonadherent cells were removed by rinsing the samples in fresh media. Cell viability was investigated via esterase activity and membrane integrity using the LIVE/DEAD assay (2  $\mu\text{M}$  Calcein AM, 4  $\mu\text{M}$  ethidium homodimer-1, Invitrogen) solution in DPBS (Dulbecco's phosphate buffered saline, GIBCO) supplemented with 2% (v/v) FBS for at least 20 min. Stained adhered cells were imaged on an inverted microscope (Nikon Eclipse TE2000-U), with Calcein excited at 465–495 nm and the resulting emission observed between 515 and 555 nm, and ethidium homodimer-1 excited at 510–560 nm, and resulting emission observed above 590 nm.

Cell counts were performed using the particle analysis function in the software Image J. Before the particle analysis, the images were converted to 8 bit black and white images and the threshold set to ensure the software only counted features that were actual cells. The results obtained by the software were compared to images counted by hand and were within 5% accuracy. To perform a statistical analysis of each of the substrates, the average number of cells was determined

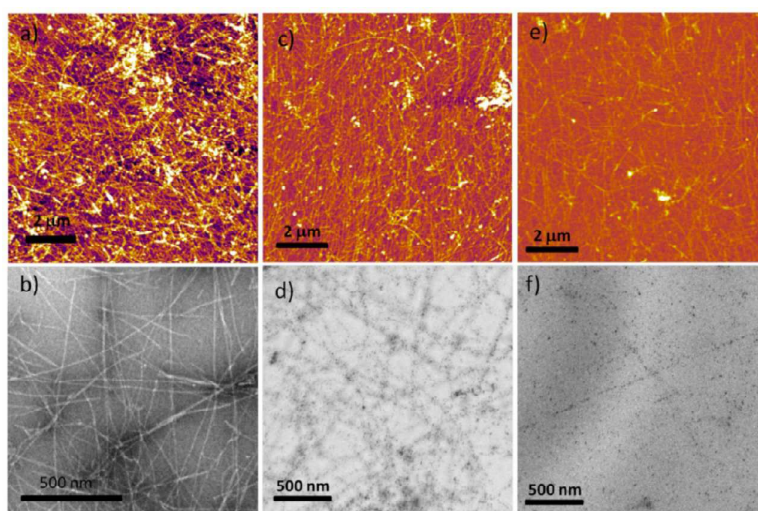


**Figure 2.** Surfaces with nanoscale surface topography. (a) AFM image of amyloid fibril network (AFN) deposited on freshly cleaved mica ( $z$ -scale = 10 nm); (b) TEM image of AFN, potassium phosphotungstate was used to stain the fibrils to improve contrast (negative staining); (c) AFM image of 50 W DGpp deposited on an AFN on mica ( $z$ -scale 10 nm); (d) TEM image of 50 W DGpp film deposited onto an AFN decorated with gold nanoparticles; (e) AFM image of AFN + 5 W DGpp on mica ( $z$ -scale 10 nm); (f) TEM image of 5 W DGpp film deposited onto a AFN decorated with gold nanoparticles. All AFNs were deposited at 2 wt % for 10 min, before rinsing in MQ water. All TEM samples were prepared on carbon-coated copper mesh grids.

from 3 individual nonoverlapping regions on the surface of each sample. To account for variations of cell attachment within each experiment, 3 individual samples were prepared. Finally, to account for batch to batch variations, the experiment was repeated 3 times on different days. As variation in the seeding density and inherent cell behavior across the 3 experiments is uncontrollable, the test results are reported as attached counts normalized to a mica control surface included in each experiment repeat. Cell area was quantified from the same images used for cell number using the wand (tracing) tool and measure function in Image J. A line bisecting the image was randomly drawn and the first 10 cells along that line were measured in each image. Statistical analysis of both cell numbers and cell spreading area across the 3 experiments was performed using ANOVA with Tukey tests for multiple comparisons.

**Fourier Transform Infra-Red Spectroscopy.** Results were obtained on a liquid nitrogen cooled Nicolet 6700 Fourier transform infrared spectrometer (FT-IR) (Thermo Scientific), on either flat or nanotopographical DGpp films that had been incubated in 10% FBS in DPBS for 24 h. In addition, spectra were recorded of bare AFN films as a negative control. The films were washed in MQ water and gently dried under a stream of nitrogen before their spectra was recorded. The spectra were displayed as an average of 50 runs, and corrected for background against freshly cleaved mica. Spectra shown are representative of at least 3 repeat experiments from each surface.

## RESULTS

AFNs were deposited on freshly cleaved mica substrates in order to generate the desired nanotopography. The morphology of the AFNs was characterized by AFM and TEM and representative images chosen from at least 3 repeated experiments can be seen in Figure 2a and 2b, respectively. The coverage of the AFN on mica in Figure 2a is in excess of 90%; however, some areas of underlying substrate can be seen through the AFN.

DGpp films were deposited onto the AFN so that well characterized, chemically homogeneous surfaces could be fabricated. DGpp films were deposited at an RF power of 50 W (low ether content) or 5 W (high ether content), to create

surfaces that were either protein adhesive or low protein fouling, respectively. The morphology of the AFN + DGpp films was investigated by AFM and TEM; representative images are shown in Figure 2c,d (50 W) and Figure 2e,f (5 W), respectively. These were compared to images of the DGpp films directly deposited on mica (Supporting Information, Figure S1). Considering first the AFM results, images of the AFN + 50 W DGpp films (Figure 2c) show that the underlying fibrous topography of the AFN is largely replicated in the DGpp surface. However, the AFM image shows less defined contrast compared to the AFN without the polymer layer (Figure 2a), which can be interpreted as a smoothing out of the 3D fibrous structure due to the presence of the plasma polymer film. AFM imaging of the AFN + 5 W DGpp films (Figure 2e) showed a further reduction in contrast compared to the images of the AFN + 50 W DGpp (Figure 2c), suggesting that there is a reduction in fidelity of the topography transfer at lower RF power.

To aid the visualization of the AFN + DGpp films in the TEM images (Figure 2d,f), fibrils were labeled with gold nanoparticles (GNP) (diameter 5 nm) before plasma deposition; these can be seen in Figure 2d where the dark spheres are co-localized along the fibrils. The morphology of the GNP labeled fibrils prior to plasma coating (Supporting Information, Figure S2) appeared qualitatively identical by TEM to the fibrils without labeling (Figure 2b), suggesting that the GNPs had no observable effect on the fibril morphology and is thus a viable visualization tool. TEM of the AFN + 50 W DGpp with GNP (Figure 2d) was used to verify the integrity of the underlying AFN structure after plasma polymerization. The fibrillar structures were not as clear in the TEM images of the AFN + 5 W DGpp with GNP (Figure 2f), as compared to the 50 W AFN + DGpp film. It appears that the composition of the 5 W DGpp layer prevented the TEM from clearly imaging the underlying AFN structure. However, the outline of the fibrils can still be observed due to the co-localized GNPs. The fibrous

structures visible in the TEM images indicate that the structure of the AFN is conserved after the deposition of the plasma polymer films.

To determine the variation in height of the surface features, cross sections of lines scans from the AFM images were plotted for the bare AFN, and both the AFN + 50 W and AFN + 5 W DGpp film (Supporting Information, Figure S3). From the cross sections it was determined that the maximum height difference for the bare AFN is approximately 10 nm, and for the AFN + DGpp films, the maximum height differences are approximately 5 and 3 nm for the 50 and the 5 W films, respectively. Although the plasma coating causes an unavoidable smoothing out of the 3D fibrous structure, the AFM line scans in Figure S3 show that some nanoscale fibrous topography is retained in the surface of the plasma polymer.

To quantify the extent of nanoscale topography conserved after deposition of the DGpp on the AFNs, the surface roughness was quantified by AFM analysis of  $10 \times 10 \mu\text{m}$  scans. Rrms and Ra values were calculated from an average of at least 3 individual images for each polymer film (Rrms values in Figure 3, and Ra values in Supporting Information, Figure S4).

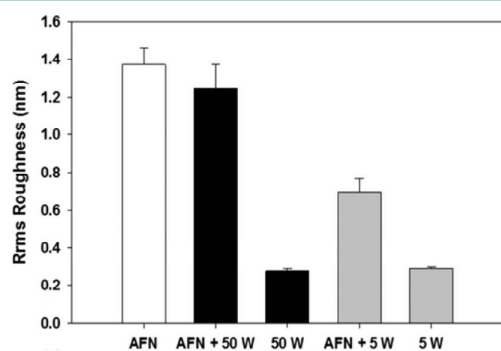


**Figure 3.** Rrms roughness values calculated from AFM images (values calculated from at least three  $10 \times 10 \mu\text{m}$  scans), showing that the nanoscale topography of the AFN is reproduced in both the 5 and 50 W substrates. However, replication of the fibrous nanoscale topography is better conserved in the 50 W substrates. Data is mean  $\pm$  standard error of mean.

The average roughness values for the precoated AFNs were calculated to be 1.371 and 1.061 nm for Rrms and Ra, respectively. Little difference in roughness was observed between the AFN and the AFN + 50 W DGpp films where values of 1.247 and 0.854 nm for Rrms and Ra were calculated, respectively. The roughness of the AFN + 5 W DGpp films

dropped to 0.701 and 0.504 nm for Rrms and Ra, respectively. The Rrms of the DGpp deposited directly onto mica was relatively low, with 0.277 and 0.291 nm for the 50 and 5 W films, respectively. These results confirm that while both coatings reproduce, to some extent, the nanoscale topography of the AFN, the fidelity of the fibrous morphology is best conserved when depositing DG plasma polymers at the higher power (50 W).

In addition to roughness measurements (Figure 3) and variation in height (Figure S3), the thickness of the fibrous features in the observed AFM images was analyzed before and after plasma deposition. It was found that the average width of the fibril-like features on the surface was increased from  $42.5 \pm 1.9$  nm on the bare AFN to  $82.7 \pm 2.8$  and  $162.6 \pm 3.9$  nm on the AFN + 50 W and AFN + 5 W, respectively. To confirm that the nanotopographical features remained throughout the cell culture experiments, AFM was also performed in a fully hydrated environment achieved by immersion in PBS in a fluid cell for at least 3 h before imaging. Figure S5 compares the nanotopography of a dry AFN + 50 W DGpp surface (Figure S5a) and a fully hydrated surface (Figure S5b). Little difference in topography is observable between the images; thus, it was concluded that the nanotopography is retained even when the plasma polymer films are hydrated.

X-ray photoelectron spectroscopy (XPS) was employed to confirm the presence and integrity of the DGpp deposited on the AFNs, and to ensure chemical homogeneity among comparative samples. First, elemental quantification of the surface chemistry confirmed the presence of the AFN on mica by the introduction of a nitrogen peak associated with the amide backbone of the peptides in the lysozyme fibrils (Table 1). Second, as no peaks were observed for elements specific to mica (e.g., Al) or the AFN (e.g., N) in the substrates with DGpp present, it was determined that the deposition of DGpp on top of the AFN on mica resulted in a continuous film with thickness greater than the XPS sampling depth ( $> \sim 10$  nm). The ratio of oxygen to carbon peaks (O/C) of DGpp was unaffected by the presence of the AFN, suggesting complete coverage and chemical homogeneity. The 5 W DGpp coatings demonstrated an O/C much closer to the DG monomer than the 50 W samples, as previously seen.<sup>46</sup> High resolution C 1s spectra of the 50 and 5 W DGpp films were used to gain a greater understanding regarding the chemical functionality of the coatings and thus aid in interpretation of cellular response. For the 50 W DGpp coatings (Figure 4a), the hydrocarbon peak ( $\sim 285$  eV) was the dominant contribution, though the shoulder at  $\sim 286.5$  eV indicates the presence of some ether functional groups. The spectra for the 5 W DGpp coatings was

**Table 1.** Selected Elemental Quantification Data Measured by X-ray Photoelectron Spectroscopy XPS (Atomic Concentrations Relative to the Total Concentration of C, i.e., Atomic Ratios X/C)<sup>a</sup>

sample	atomic ratio (X/C)		
	O	N	Al
DG Monomer (theoretical)	0.5	-	-
Mica	$5.030 \pm 0.082$	-	$1.142 \pm 0.021$
AFN on mica	$0.648 \pm 0.005$	$0.283 \pm 0.000$	$0.129 \pm 0.002$
5 W DGpp on mica	$0.406 \pm 0.001$	-	-
AFN + 5 W DGpp on mica	$0.404 \pm 0.000$	-	-
50 W DGpp on mica	$0.219 \pm 0.001$	-	-
AFN + 50 W DGpp on mica	$0.216 \pm 0.001$	-	-

<sup>a</sup>Listed are the mean values based on 2 analysis points.

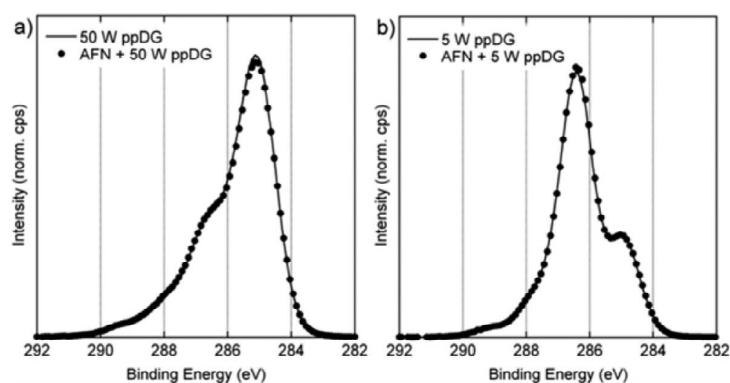


**Figure 4.** Representative XPS C 1s spectra from (a) DGpp film deposited at 50 W on either freshly cleaved mica (solid line) or a network of amyloid fibrils adsorbed to a mica substrate (AFN + 50 W DGpp, dots); (b) DGpp film deposited at 5 W on either freshly cleaved mica (solid line), or AFN adsorbed to a mica substrate (AFN + 5 W DGpp, dots).

dominated by the ether peak centered at  $\sim 286.5$  eV, which was expected as it is known that the extent of cross-linking and degree of residual ether groups is dependent on the plasma deposition conditions. It has previously been shown that the concentration of ether groups in plasma polymers produced from diethylene glycol dimethylether is greater at lower plasma deposition load powers (Figure 4b).<sup>46</sup> Both the 50 and 5 W coatings had spectral contributions at higher binding energies, most likely associated with carbonyl groups ( $\sim 288$  eV: ketone, aldehyde groups;  $\sim 289$  eV: acid, ester groups). Considering now AFN + DGpp films, for both 50 and 5 W the C 1s profile corresponded well with that of the spectra obtained for DGpp on bare mica, further indicating that the underlying AFN had no effect on the resulting chemical functionality of the DGpp films. In addition to the elemental analysis shown in Table 1, a complete analysis of all the main elements present in the sample is shown in the Supporting Information (Table S1).

To gain greater insight into the thickness of the DGpp films, focused ion beam-scanning electron microscopy (FIB-SEM) experiments were performed, representative results of which are shown in Figure 5. Figure 5a shows a representative SEM image of a polymer surface after a microscopic segment has been carefully ablated by the FIB, to demonstrate the technique. Figure 5b–d shows SEM images taken at  $\sim 70^\circ$  to that in Figure 5a to image the cross section of the polymer. Figure 5b shows such a cross section through an AFN coating without the deposited DGpp film; the bright features at the interface with the top surface are from the Au coating deposited under vacuum on the fibril network to prevent charging during imaging. The solid line underneath the gold grains shows the top surface of the mica substrate. Unfortunately, the AFN itself was unresolvable in cross section using this technique. However, to confirm the AFNs continued presence after SEM sample preparation, an SEM image was recorded at  $90^\circ$  to the substrate on a nonablated region (Supporting Information, Figure S6a), clearly showing the AFN on the mica substrate. Figure 5c, interpreted similarly to Figure 5b, shows a FIB-SEM image of the AFN + 50 W DGpp, but once again the fibrils lack sufficient contrast to be resolved in cross section in the FIB-SEM image. *In situ* analysis of the thickness of at least 3 AFN + 50 W DGpp films reveals a continuous plasma polymer film with a thickness of  $143 \pm 2.2$  nm. Figure 5d, again interpreted similarly to Figure 5b, shows a corresponding FIB-SEM image of the AFN + 5 W DGpp film. While the AFN cannot be

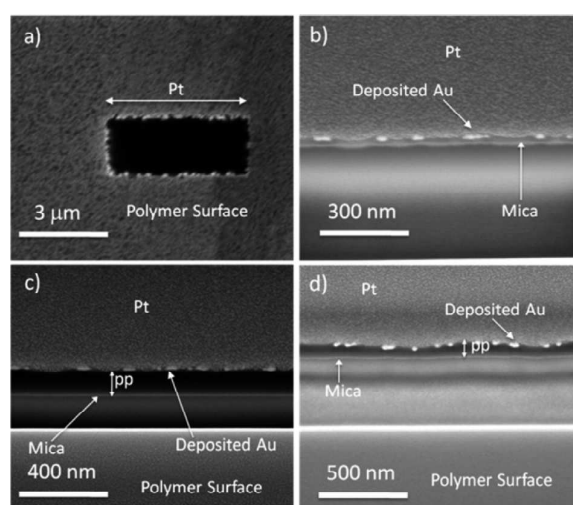


**Figure 5.** Focused Ion Beam-Scanning Electron Microscopy (FIB-SEM) of AFN + DGpp films, (a) SEM image of micrometer scale region of representative sample ablated by FIB, (b) SEM image of cross section of FIB ablated area of an AFN adsorbed to freshly cleaved mica substrates, (c) SEM image of cross section (recorded at  $70^\circ$ ) of FIB ablated area of AFN + 50 W DGpp on mica (thickness of plasma polymer layer =  $143 \pm 2.2$  nm), (d) SEM image of cross section of FIB ablated area of AFN + 5 W DGpp on mica (thickness of plasma polymer layer =  $111 \pm 10.0$  nm).

resolved, the average AFN + 5 W DGpp film is confirmed to be continuous with a thickness of  $111 \pm 10$  nm. To compare the deposition rates of the plasma polymer on substrates with and without the AFN, FIB-SEM images were recorded for films deposited identically but without AFN. Representative images, shown in the Supporting Information (50 W Figure S6b and 5 W Figure S6c), demonstrate that the 50 W DGpp films deposited on directly on mica were thicker ( $243 \pm 5.2$  nm) than the corresponding AFN + DGpp films (143 nm, see above), while for the 5 W DGpp film, the thickness ( $111 \pm 8.2$  nm) was approximately the same as for the corresponding AFN + DGpp film (the contribution to the thickness from the AFN being less than 10 nm). Thus, the presence of the fibril network significantly reduced the deposition rate of the 50 W DGpp film.

The effects of the fibrous nanoscale topography of the DGpp surfaces on cell attachment were studied and the results presented in Figures 6 and 7. All experiments were repeated

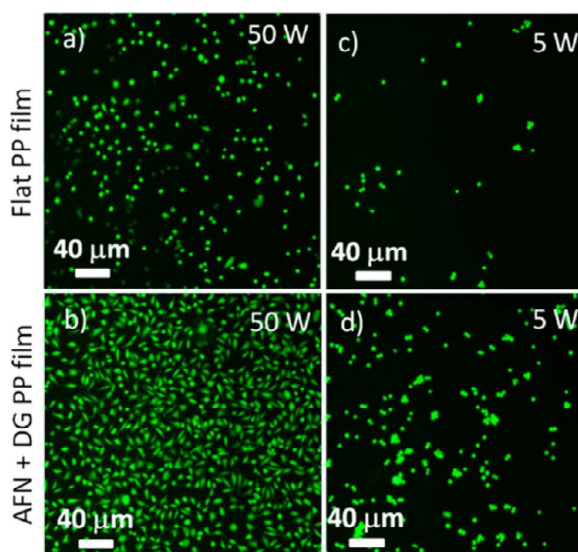


**Figure 6.** Calcein labeled L929 mouse fibroblast cells cultured for 24 h on )a) 50 W DGpp coated mica substrates, (b) AFN + 50 W DGpp on mica, (c) 5 W DGpp coated mica, (d) AFN + 5 W DGpp on mica.

multiple times ( $3 \times 3$  images recorded for 3 separate experiments performed on different days) to ensure repeatability of the fabricated substrates. Mouse L929 fibroblast cells were cultured on the polymer surfaces both with and without the underlying AFN (Figure 6a–d) and also directly on top of the AFN (Supporting Information, Figure S7). It is evident that cells remaining after the wash step were viable in all cases, with intact membranes resisting penetration/staining by ethidium homodimer (Supporting Information, Figure S8) indicating that the surfaces were noncytotoxic. To be more precise, quantification revealed that <1% nonviable cells remained attached after the wash step to the AFN + 50 W DGpp and 50 W films; however, this increased to 2% and 11% for the AFN + 5 W DGpp and 5 W films, respectively. The majority of the cells were also found to be metabolically functional, at least to the extent of generating the fluorescent calcein (Figure 6). Cell quantification (Figure 7a) and cell morphology (Figure 7b) were also investigated. Considering first the DGpp deposited on bare mica, based on previous reports<sup>49</sup> it was expected that the plasma polymer films deposited at 5 W would be less conducive to cell attachment than the 50 W films (Figure 6a,c). Indeed, the 50 W substrates showed a 2.4-fold increase in cell attachment over the 5 W substrates (Figure 7a). The higher ether content of the 5 W DGpp, as confirmed by XPS, is generally accepted to be responsible for the generation of low fouling surfaces.<sup>46,47</sup> The same trend was seen for the plasma polymer films displaying AFN topography (Figures 6b and 7a), with the AFN + 50 W DGpp films showing a 4.6-fold increase in the number of attached cells as compared to the equivalent AFN + 5 W DGpp substrates (Figure 7a). Additionally, a higher proportion of the cells adopted a more spread morphology on the 50 AFN + W DGpp surfaces (Figure 7a) than the AFN + 5 W DGpp (Figure 7b).

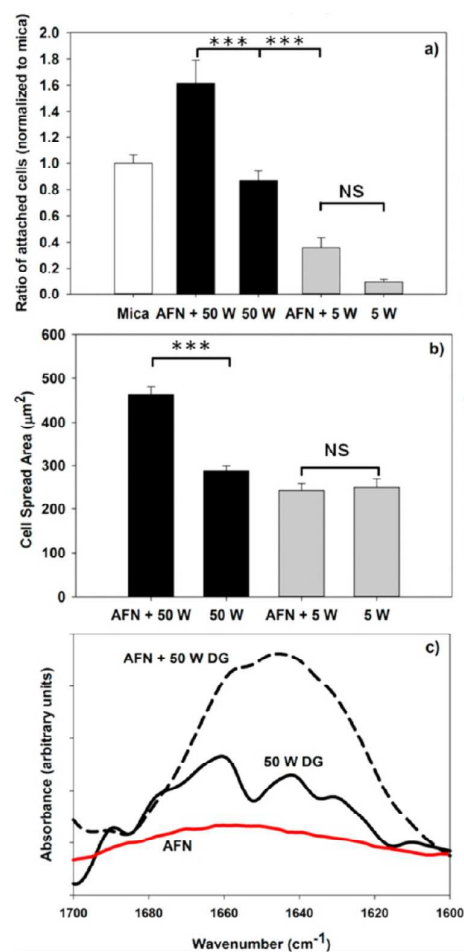


**Figure 7.** (a) Analysis of L929 fibroblast cell number on flat plasma polymer films and films displaying AFN topography, after 24 h culture. All cell numbers are normalized to the number of cells adsorbed to bare mica in order to eliminate errors in seeding density. (b) Analysis of 2D cell spread area on flat plasma polymer films and films displaying AFN topography, after 24 h culture, NS = No Significance;  $***p < 0.001$ , all error bars show the standard error of mean. (c) FT-IR showing the amide I band of 50 W DGpp films (solid line) and AFN + 50 W DGpp films (dashed line) after 24 h incubation in 10% FBS, and the amide I band of the bare AFN (red line) showing increased protein adsorption and stabilization on the nanotopographical films.

The effect of the AFN topography on cell response was compared between the flat DGpp films and the AFN + DGpp films displaying nanoscale topography. The AFN + 50 W DGpp films show a 1.8-fold increase in attached cells relative to the flat surfaces as a result of the increased nanoscale topography present in the AFN + DGpp substrates. Given that the 50 W DGpp surface is inherently cell adhesive, this is significant. For the AFN + 5 W DGpp films, a 3.8-fold increase was observed relative to the flat 5 W DGpp films, indicating the mere presence of the AFN morphology turned a relatively non-adherent coating into one of greater cell adhesiveness. In terms of cell morphology, cells on the AFN + 50 W DGpp films adopted a considerably more spread morphology compared to the equivalent DGpp films on bare mica (Figures 6b and 7b, respectively) indicating a more favorable attachment to the

AFN + 50 W DGpp films. However, no such increase in cell spreading was observed for the films deposited at 5 W (Figure 7d,c). This observation was confirmed upon analysis of the cell spreading area. Cells cultured on the AFN + 50 W DGpp surfaces had a mean spread area of  $464 \mu\text{m}^2$  after 24 h, whereas cells cultured on all the remaining surfaces had mean spread areas below  $300 \mu\text{m}^2$  (288, 249, and  $241 \mu\text{m}^2$  for 50 W DGpp, AFN + 5 W DGpp and 5 W DGpp surfaces, respectively).

Differences in cell attachment and spreading on the different DGpp films may be due to variations in the structure of adsorbed serum proteins from the cell growth media.<sup>50</sup> This was investigated using FT-IR spectroscopy. Spectra from serum proteins adsorbed to the DGpp films (10% FBS, 24 h) on both the flat 50W DGpp and the AFN + 50 W DGpp films are shown in Figure 7c. Similar spectra were measured for the 5 W films (data not shown) however spectra with sufficient signal-to-noise ratios were not obtained, presumably due to the inert nature of these films and the reduced presence of adsorbed serum protein. The amide I band of the adsorbed serum proteins ( $1600\text{--}1700 \text{ cm}^{-1}$ ) arises due to the presence of secondary structure in protein molecules ( $\alpha$ -helix,  $\beta$ -sheet, random coil). The increase in absorbance in this region from the serum proteins adsorbed to the AFN + 50 W DGpp films (dashed line), compared to the flat 50 W DGpp film (solid line) suggest an increased absorption of serum proteins on the substrates with the fibrous nanotopography. Moreover, analysis of the FT-IR spectra of adsorbed serum proteins to the nanotopographical films shows a maximum absorbance at around  $1650 \text{ cm}^{-1}$  suggesting a strong contribution from proteins in an  $\alpha$ -helical conformation. This maxima is not present in the FT-IR spectra of the serum proteins adsorbed to the flat DGpp films, where the peak is instead shifted to a higher wavenumber ( $1665 \text{ cm}^{-1}$ ) suggesting a significant drop in the helical nature of the serum adsorbed serum proteins. FT-IR spectra were also recorded on the bare AFN (without the plasma polymer layer) substrates to confirm that the shape of the amide I band was not being influenced by the presence of the underlying AFN. Indeed only very weak absorbance spectra were recorded, so the IR contribution from the AFN was assumed to be negligible.

## DISCUSSION

The effects of nanoscale surface topography on cell attachment and growth are important for various biomedical applications.<sup>51</sup> Progress in this field has been hampered due to a number of scientific challenges including difficulties in reproducibly fabricating surfaces with well-defined topographies.<sup>9</sup> Traditional methods of generating surface topography, can struggle to reproduce nanoscale dimensions. Such dimensions are vitally important as they have been shown to promote cell adhesive interactions (such as focal adhesions).<sup>16</sup> Even if there have been some examples of using both 'top-down'<sup>9,52</sup> and 'bottom up'<sup>20</sup> lithographic techniques to generate accurate nanoscale topographies with good reproducibility, the former is complex and slow and both fail to accurately mimic the fibrous morphology of typical cellular microenvironments.

It has previously been shown that proteins in their native state can be used as templates for the deposition of plasma polymer films in order to aid the development of new biomaterials.<sup>27–29</sup> However, in order to preserve the structure and function of the proteins, either very mild atmospheric plasma deposition conditions were used,<sup>28,29</sup> or the proteins were protected by an adsorbed polysaccharide coating.<sup>27</sup>

By using robust and structurally stable AFNs, we have shown for the first time it is possible to deposit plasma polymers from a vacuum directly onto amyloid fibrils (Figures 1 and 2). Furthermore, the biomimetic nanoscale fibrous topography of the fibrils is reproduced in the surface of the plasma polymer films with remarkable fidelity (Figure 2c). This reproduction of fibrous topography combined with the TEM images shown in Figure 2 indicates the structural integrity of the fibrils remains throughout the plasma deposition. This discovery enables one to quickly and cheaply fabricate chemically homogeneous surfaces with well-defined biomimetic nanoscale surface topographies in a "bottom up" manner. AFM roughness analysis revealed that the  $R_{\text{rms}}$  roughness increases by approximately 1.2 nm from the flat 50 W DGpp to the AFN + 50 W DGpp films (Figure 3). Previous research has shown changes in roughness in the order of 3–5 nm to affect cell responses,<sup>53,54</sup> but to the best of our knowledge, this is the first report of such small changes in roughness affecting cell attachment and spreading.

Figure 5 and Figure S6 show the comparative thicknesses of the DGpp films deposited on the AFN and directly onto the solid substrate, respectively. The results indicate that the polymer deposition rate is reduced when deposited on the AFN. For the polymer deposited at 50 W, the average film thickness dropped from 243 nm (Figure S6) to 143 nm (Figure 5c); however, no difference in film thickness was observed for the polymer deposited at 5 W. The reason for this drop in deposition rate of the DGpp film at a 50 W load power remains undetermined. The deposition rate also varies with the deposition power, and considerably thicker films were produced at 50 W compared to 5 W. This is commonly observed in the RFGD of plasma polymer thin films and relates to the greater extent of monomer fragmentation and larger pressure rise in the plasma reactor system during the glow discharge. Thickness has some relevance in a biological setting. In a recent study performed by Amorosi et al.,<sup>30</sup> it was observed that the activity of an enzyme coated with a thin layer of plasma polymer (30 nm) remained to some degree. In our experiments the thickness of the DGpp film was in excess of 100 nm in all cases, thus we expect the underlying AFN (<10 nm) to have no chemical influence on the cellular response. The results from the XPS (Figure 4) confirm that the AFN does not affect the surface chemistry in the dry state.

A notable finding from our study is that the nanotopography of the AFN is preserved on the top surface of a relatively thick plasma polymer coating. The DGpp coating (>100 nm, Figure 5) is an order of magnitude thicker than the AFN itself (<10 nm, Supporting Information Figure S3); however, the fine structure of the AFN is still present at the surface of the films. While the ability of the 50 W coatings to reproduce the AFN topography was superior (Figure 2, panels c and e, respectively), as seen from the AFM line scans (Supporting Information, Figure S3) and confirmed by the roughness analysis (Figure 3), the phenomenon also occurred for the 5 W coatings. At a constant monomer flow rate during plasma polymerization, plasma polymer films are thought to increase in thickness at a constant rate in all dimensions and one may expect that any nanostructure present on the substrate would be filled in and lost, as the DGpp grows circumferentially from the fibrils and from the bare mica between fibrils, leading to a uniform and 'flat' surface. Surprisingly, the results presented here indicate that this is not the case, hence providing the

opportunity to produce the nanotopographical coatings with specifically defined surface chemistries.

Conversely, the underlying AFN template is not perfectly mirrored on the surface, and some fibril broadening is seen. Analysis of the broadening of the features in the AFM images shows an average width increase in AFN features of 40.2 and 120 nm for the 50 and 5 W DGpp films, respectively, compared to the uncoated fibrils. This increased feature broadening on the 5 W DGpp films goes some way to explain the greater reduction in *R*<sub>rms</sub> roughness compared to uncoated AFN seen for the AFN + 5 W DGpp films (49%) (cf. only a 9% drop in *R*<sub>rms</sub> was seen for the AFN + 50 W DGpp films). However, the observed feature broadening does not indicate a conformal plasma deposition process where it would be expected that the features of the AFN would be broadened to roughly twice the thickness of the polymer layer (i.e., ~ 100 nm in both *x* and *y* dimensions). The measured feature broadening is considerably less than this; thus, the presence of the AFN must result in nonuniform plasma polymer deposition across the surface. The reduced feature broadening, combined with the considerably reduced DGpp deposition rate, for the AFN + 50 W DGpp indicates that this nonuniformity in plasma deposition is load dependent. It would appear that the plasma deposition does occur in all dimensions, but not uniformly, and that the degree of nonuniformity varies with the plasma deposition power.

An explanation for the origin of the nonuniform plasma deposition is not currently available, although it is becoming clear in the literature that the underlying substrate can strongly affect plasma polymer deposition rates.<sup>55,56</sup> One could hypothesize that the deposition rate would be affected by the distribution of (positively) charged amino acid residues on the surface of the fibrils causing differing deposition rates across the surface. An alternative explanation could be that, initially the polymer does grow conformally around each fibril until the polymer film growing from two adjacent fibrils meets (thus filling in the horizontal space). Once all the horizontal space is filled the polymer can only continue to grow vertically, therefore no more feature broadening would be seen. We believe it is the nonuniform plasma deposition process that results in the at least partial reproduction of the AFN nanotopography and further work is currently underway to determine the source of this nonuniformity.

The nanotopographical substrates were developed as a platform to investigate the effects of nanoscale fibrous topography on cell physiology. Thus, we performed a number of experiments whereby cells cultured on both flat and nanotopographical DGpp surfaces were assessed, by fluorescent microscopy, for attachment and viability. As previously noted, increasing the deposition power results in better cell attachment<sup>49</sup> due to a reduction of protein-resistant ether groups in the plasma polymers. This trend is observed in Figure 6 where for both the flat DGpp films on mica and the AFN + DGpp films, there is a greater amount of viable cells attached to the films deposited at 50 W (Figure 6). Analysis of the cell number revealed a statistically significant 4.6-fold increase in cell attachment on the AFN + 50 W DGpp substrates compared to the equivalent 5 W surfaces.

Quantitative investigations into the number of attached cells revealed that significantly more cells attached to the surfaces possessing the biomimetic nanoscale topography than the flat polymer films (Figure 7a). The films deposited at 50 W showed a 1.8-fold increase after 24 h, which upon statistical analysis was determined to be highly significant ( $p < 0.001$ ). The films

deposited at 5 W showed a 3.8-fold increase in cell attachment after 24 h culture. However, in this instance, statistical analysis showed this was not statistically significant; this is likely due to the low number of attached cells on the inert 5 W polymer surfaces, resulting in a larger percentage variation in the number of viable cells between experiments. Furthermore, cells cultured on the 50 W AFN + DGpp surfaces have a more spread morphology than the corresponding flat polymer films indicating better attachment to the substrate. Such an increase in cell spreading was not observed in the films deposited at load powers of 5 W (Figure 6d). Analysis of the cell spread area in 2D (Figure 7b) revealed that the cell areas were between 240 and 290  $\mu\text{m}^2$  for the 5 W films both with and without the AFN present. The same finding was observed for the flat 50 W DGpp films. The only statistically significant variation in cell spreading was seen on the AFN + 50 W DGpp nanotopographical films where the average spread area increased to 463  $\mu\text{m}^2$  ( $p < 0.001$ ). The XPS analysis shown in Figure 4 and Table 1 revealed that the surface chemistry of the plasma polymer substrates is identical both with and without the AFN present, thus the increase in cell number and spreading must be due to the introduction of nanoscale surface topography. Evidence to support this can be seen in the work of Yan et al.,<sup>44</sup> who reported the development of actin stress fibers (closely linked to the presence of focal adhesions) in cells cultured on lysozyme hydrogels. The fibrils that made up the hydrogels in that study were not functionalized with any motifs that encouraged cell-matrix interactions (e.g., RGD or IKVAV). Therefore, it is reasonable to hypothesize that the high levels of cell attachment (inferred from the presence of stress fibrils) is due to the nanoscale fibrous morphology of the interior of their lysozyme gels.

Clearly, the nanotopography is influencing both the degree of cellular adhesion and the interaction of the cells with the substrate. It is well-known that the first stage of cellular adhesion to organic substrates in a serum-containing culture is the adsorption of serum proteins, such as fibronectin, albumin, laminin, and collagen, that contain cell adhesive moieties such as integrin-binding motifs.<sup>57</sup> The conformation of the proteins adsorbed to the surface is a critical determinant in how cells respond.<sup>58</sup> As known in the literature, the 5 W DGpp elicits reduced protein adsorption, and hence reduced cellular adhesion, compared to the 50 W DGpp due to its high ether content.<sup>46</sup> Interestingly, on the 5 W DGpp films the presence of the AFN topography only resulted in an increase in cell number, but on the 50 W DGpp films the topography affected both cell number and shape. The surface morphology presented by the AFN + 50 W DGpp results in greater serum protein detection by FTIR (Figure 7c), but it remains to be determined whether the increased detection is due to an increase in adsorbed protein per area or simply an increase in surface area being measured. That is, while the 2-dimensional window sampled by the IR measurement does not change, the actual surface area within that window will change among samples due to the changing nanotopography. Analysis of the area under the AFN + 50 W DGpp and the flat 50 W DGpp IR adsorption spectra in Figure 7c reveal an approximate 2.6-fold increase in detected serum proteins on the AFN + 50 W DGpp film compared to the flat 50 W film (Figure 7c). The *R*<sub>rms</sub> roughness however increases 4-fold between the AFN + 50 W DGpp (1.2 nm) films and the flat DGpp (0.3 nm). If a proportional relationship is assumed between *R*<sub>rms</sub> roughness and actual surface area then the 2.6 fold increase in attached

serum proteins may be a result of the 4-fold increase in surface area. However, Donoso et al.<sup>59</sup> show that the relationship between Rrms roughness and surface area is complex and not usually proportional. Thus, it is not possible to unequivocally state that there is greater protein adsorption per area on the AFN + 50W DGpp.

However, in the case that we assume no increase in protein adsorption per area, an explanation for the favorable spread morphology on the AFN + 50 W DGpp films is still required. That is, some difference is still being perceived by the cells. It has previously been shown that cells adsorb more strongly to fibronectin (one of the components of the cell serum mixture) coated substrates when its native conformation is retained.<sup>50</sup> Furthermore, Grant et al.<sup>60</sup> showed that integrin mediated cell adhesion to fibronectin depends not only on the presence of specific interaction sites (i.e., the RGD motif) but also the relative orientation and conformation of these sites. Previous studies have shown that the surfaces displaying nanoscale topography can cause an increase in protein stabilization, and we hypothesize the same in this study. Elter et al.<sup>61</sup> showed that the convex features on a surface consisting of arrays of nanoscale grooves, caused an increase in protein–protein interactions resulting in less denaturation due to non-physiological protein–surface interactions. The shape of the amide I band, and in particular the peak maxima at 1650 cm<sup>-1</sup>, in Figure 7c indicates that the adsorbed serum proteins on the 50W AFN + DGpp films have substantive  $\alpha$ -helical conformation. This peak is not evident to the same degree for adsorbed serum proteins on flat DGpp films, thus suggesting the  $\alpha$ -helical conformation is reduced on these surfaces. Since a loss of  $\alpha$ -helical nature has been associated with denaturation,<sup>62</sup> this IR data supports the proposition that adsorbed serum proteins on the 50W AFN + DGpp films show reduced protein denaturation. We believe that the FT-IR spectra, combined with the increased cell attachment and spreading, suggests that the protein adhesive 50W substrates (relative to the 5 W substrates) and biomimetic morphology of the fibrous structure of the 50 W AFN + DGpp substrates result in a reduction in denaturation. We propose that the stabilization of adsorbed serum proteins, provided by the nanotopographic surface allows interaction motifs on the serum proteins to be presented in a more biomimetic manner. Thus, the generation of more physiological cell to substrate interactions may be the cause of the increased spread morphology observed on the AFN + 50 W DGpp films. More work is required in order to fully characterize the protein adsorption and conformation on the nanotopographic films; this is currently underway in our laboratories.

The method of generating nanoscale topography, presented here, overcomes some of the problems in reproducibility and non-native morphology mentioned throughout this discussion, as the amyloid fibrils possess a nanoscale topography that encourages cell adhesions<sup>44</sup> and is reminiscent of the native topography of the ECM.<sup>45</sup> Thus, we propose that such substrates better mimic the cellular microenvironment than many other methods of investigating nanoscale topography. It is this biomimetic environment that, when combined with favorable surface chemistries (i.e. protein adhesive) results in a stabilization of adsorbed serum proteins on the nanotopographical surfaces, which, in turn resulted in improved cell attachment and spreading. The protein stabilization offered by the fibrous topography may aid the culture of less robust cell lines. For instance, stabilized adsorbed matrix proteins may aid

the expansion of stem cells. Furthermore, we believe the results presented here represent a novel and convenient method of fabricating biomimetic surface topographies with controllable surface chemistries. These surfaces will allow the effects of nanoscale surface topography to be studied for various cellular applications, with a focus on the biomedical materials and devices research field.

## CONCLUSIONS

We have developed an inexpensive, rapid and reproducible method of generating biomimetic nanoscale topography on the surface of plasma polymer films deposited under vacuum. We have demonstrated this new technique using networks of lysozyme amyloid fibrils onto which a diglyme plasma polymer film is grown, and we have shown that it is possible to reproduce the topography of the fibril network with high fidelity. Moreover, as the polymer film is continuous and has a thickness in excess of 100 nm, the surface of the polymer is chemically homogeneous. In addition, we have shown that the substrates are noncytotoxic and through a combination of surface chemistry and nanotopography we can control attachment and spreading of fibroblast cells. Thus, this platform is suitable for a wide range of cell culture applications investigating the effects of nanoscale surface topography. Such investigations could have important consequences for the design of novel biomaterials. Furthermore, the inherent stability of the amyloid fibrils has allowed us, to the best of our knowledge, to present the first example of the deposition of a plasma polymer film directly onto fibrillar protein structures in vacuum without any initial protective coating.

## ASSOCIATED CONTENT

### Supporting Information

TEM Image of GNP decorated AFN, AFM images of flat DGpp films, AFM line sections of nanostructured DGpp films, Ra roughness analysis of all films (from AFM data), AFM of fully hydrated films, FIB-SEM of flat DGpp films and AFN on mica, fluorescent images of AFN + DGpp films after 24 h cell culture and ethidium homodimer staining, full elemental quantification data (from XPS), fluorescent images of Live/Dead stained cells cultured directly onto AFN. This material is available free of charge via the Internet at <http://pubs.acs.org>.

## AUTHOR INFORMATION

### Corresponding Author

[REDACTED]

### Notes

The authors declare no competing financial interest.

## ACKNOWLEDGMENTS

The authors would like to thank the Swiss National Science Foundation (personal fellowship for Nicholas Reynolds) and CSIRO for funding this work. For assistance with the FIB-SEM analysis the authors would like to thank D. Mair, Dr. M. Sridhar and Dr. A. Van Der Meene. This work was performed in part at the Melbourne Centre for Nanofabrication, an initiative partly funded by the Commonwealth of Australia and the Victorian Government.

## REFERENCES

- (1) Charnley, M.; Fairfull-Smith, K.; Haldar, S.; Elliott, R.; McArthur, S. L.; Williams, N. H.; Haycock, J. W. *Adv. Mater.* **2009**, *21*, 2909–2915.
- (2) Gelain, F.; Bottai, D.; Vescovi, A.; Zhang, S. G. *PLoS One* **2006**, *1*, No. e119.
- (3) Engler, A. J.; Sen, S.; Sweeney, H. L.; Discher, D. E. *Cell* **2006**, *126*, 677–689.
- (4) Engler, A.; Bacakova, L.; Newman, C.; Hategan, A.; Griffin, M.; Discher, D. *Biophys. J.* **2004**, *86*, 617–628.
- (5) Schuh, E.; Hofmann, S.; Stok, K. S.; Notbohm, H.; Muller, R.; Rotter, N. *J. Tissue Eng. Regen. Med.* **2012**, *6*, e31–e42.
- (6) Anselme, K.; Bigerelle, M. *Acta Biomater.* **2005**, *1*, 211–222.
- (7) Citeau, A.; Guicheux, J.; Vinatier, C.; Layrolle, P.; Nguyen, T. P.; Pilet, P.; Daculsi, G. *Biomaterials* **2005**, *26*, 157–165.
- (8) Dalby, M. J.; Di Silvio, L.; Gurav, N.; Annaz, B.; Kayser, M. V.; Bonfield, W. *Tissue Eng.* **2002**, *8*, 453–467.
- (9) Dalby, M. J.; Gadegaard, N.; Tare, R.; Andar, A.; Riehle, M. O.; Herzyk, P.; Wilkinson, C. D. W.; Oreffo, R. O. C. *Nat. Mater.* **2007**, *6*, 997–1003.
- (10) Unadkat, H. V.; Hulsman, M.; Cornelissen, K.; Papenburg, B. J.; Truckenmuller, R. K.; Post, G. F.; Uetz, M.; Reinders, M. J. T.; Stamatialis, D.; van Blitterswijk, C. A.; de Boer, J. *Proc. Natl. Acad. Sci. U.S.A.* **2011**, *108*, 16565–16570.
- (11) Lord, M. S.; Foss, M.; Besenbacher, F. *Nano Today* **2010**, *5*, 66–78.
- (12) Dalby, M. J.; Riehle, M. O.; Johnstone, H. J. H.; Affrossman, S.; Curtis, A. S. G. *J. Biomed. Mater. Res., Part A* **2003**, *67A*, 1025–1032.
- (13) Dalby, M. J.; Riehle, M. O.; Johnstone, H. J. H.; Affrossman, S.; Curtis, A. S. G. *Tissue Eng.* **2002**, *8*, 1099–1108.
- (14) Pennisi, C. P.; Dolatshahi-Pirouz, A.; Foss, M.; Chevallier, J.; Fink, T.; Zachar, V.; Besenbacher, F.; Yoshida, K. *Colloid Surf., B* **2011**, *85*, 189–197.
- (15) Castellani, R.; De Ruijter, A.; Renggli, H.; Jansen, J. *Clin. Oral Implants Res.* **1999**, *10*, 369–378.
- (16) Cavalcanti-Adam, E. A.; Volberg, T.; Micoulet, A.; Kessler, H.; Geiger, B.; Spatz, J. P. *Biophys. J.* **2007**, *92*, 2964–2974.
- (17) Stevens, M. M.; George, J. H. *Science* **2005**, *310*, 1135–1138.
- (18) Palin, E.; Liu, H. N.; Webster, T. J. *Nanotechnology* **2005**, *16*, 1828–1835.
- (19) Moe, A. A. K.; Suryana, M.; Marcy, G.; Lim, S. K.; Ankam, S.; Goh, J. Z. W.; Jin, J.; Teo, B. K. K.; Law, J. B. K.; Low, H. Y.; Goh, E. L. K.; Sheetz, M. P.; Yim, E. K. F. *Small* **2012**, *8*, 3050–3061.
- (20) Sardella, E.; Detomaso, L.; Gristina, R.; Senesi, G. S.; Agheli, H.; Sutherland, D. S.; d'Agostino, R.; Favia, P. *Plasma Processes Polym.* **2008**, *5*, 540–551.
- (21) Lipski, A. M.; Pino, C. J.; Haselton, F. R.; Chen, I. W.; Shastri, V. P. *Biomaterials* **2008**, *29*, 3836–3846.
- (22) Park, J.; Bauer, S.; Schlegel, K. A.; Neukam, F. W.; von der Mark, K.; Schmuki, P. *Small* **2009**, *5*, 666–671.
- (23) Lara, C.; Adamcik, J.; Jordens, S.; Mezzenga, R. *Biomacromolecules* **2011**, *12*, 1868–1875.
- (24) Yang, J.; Rose, F. R. A. J.; Gadegaard, N.; Alexander, M. R. *Adv. Mater.* **2009**, *21*, 300–304.
- (25) Sandstrom, A. M.; Jasieniak, M.; Griesser, H. J.; Grondahl, L.; Cooper-White, J. J. *Plasma Processes Polym.* **2013**, *10*, 19–28.
- (26) Kryscio, D. R.; Peppas, N. A. *Acta Biomater.* **2012**, *8*, 461–473.
- (27) Shi, H. Q.; Tsai, W. B.; Garrison, M. D.; Ferrari, S.; Ratner, B. D. *Nature* **1999**, *398*, 593–597.
- (28) Heyse, P.; Van Hoeck, A.; Roeyers, M. B. J.; Raffin, J.-P.; Steinbuechel, A.; Stoeveken, T.; Lammertyn, J.; Verboven, P.; Jacobs, P. A.; Hofkens, J.; Paulussen, S.; Sels, B. F. *Plasma Processes Polym.* **2011**, *8*, 965–974.
- (29) Ortore, M. G.; Sinibaldi, R.; Heyse, P.; Paulussen, S.; Bernstorff, S.; Sels, B.; Mariani, P.; Rustichelli, F.; Spinozzi, F. *Appl. Surf. Sci.* **2008**, *254*, 5557–5563.
- (30) Amorosi, C.; Michel, M.; Averous, L.; Toniazzi, V.; Ruch, D.; Ball, V. *Colloid Surf., B* **2012**, *97*, 124–131.
- (31) Pepys, M. B. Amyloidosis. In *Annual Review of Medicine*; Annual Reviews: Palo Alto, CA, 2006; Vol. 57, pp 223–241.
- (32) Reynolds, N. P.; Soragni, A.; Rabe, M.; Verdes, D.; Liverani, E.; Handschin, S.; Riek, R.; Seeger, S. *J. Am. Chem. Soc.* **2011**, *133*, 19366–19375.
- (33) Domanov, Y. A.; Kinnunen, P. K. J. *J. Mol. Biol.* **2008**, *376*, 42–54.
- (34) Rabe, M.; Soragni, A.; Reynolds, N. P.; Verdes, D.; Liverani, E.; Riek, R.; Seeger, S. *ACS Chem. Neurosci.* **2012**, *4*, 408–417.
- (35) Sawaya, M. R.; Sambashivan, S.; Nelson, R.; Ivanova, M. I.; Sievers, S. A.; Apostol, M. I.; Thompson, M. J.; Balbirnie, M.; Wiltzius, J. J. W.; McFarlane, H. T.; Madsen, A. O.; Riek, C.; Eisenberg, D. *Nature* **2007**, *447*, 453–457.
- (36) Kaye, R.; Head, E.; Thompson, J. L.; McIntire, T. M.; Milton, S. C.; Cotman, C. W.; Glabe, C. G. *Science* **2003**, *300*, 486–489.
- (37) Goldberg, M. S.; Lansbury, P. T. *Nat. Cell Biol.* **2000**, *2*, E115–E119.
- (38) Conway, K. A.; Lee, S. J.; Rochet, J. C.; Ding, T. T.; Williamson, R. E.; Lansbury, P. T. *Proc. Natl. Acad. Sci. U.S.A.* **2000**, *97*, 571–576.
- (39) Fowler, D. M.; Koulou, A. V.; Alory-Jost, C.; Marks, M. S.; Balch, W. E.; Kelly, J. W. *PLoS Biol.* **2006**, *4*, 100–107.
- (40) Maji, S. K.; Perrin, M. H.; Sawaya, M. R.; Jessberger, S.; Vadodaria, K.; Rissman, R. A.; Singru, P. S.; Nilsson, K. P. R.; Simon, R.; Schubert, D.; Eisenberg, D.; Rivier, J.; Sawchenko, P.; Vale, W.; Riek, R. *Science* **2009**, *325*, 328–332.
- (41) Gras, S. L.; Tickler, A. K.; Squires, A. M.; Devlin, G. L.; Horton, M. A.; Dobson, C. M.; MacPhee, C. E. *Biomaterials* **2008**, *29*, 1553–1562.
- (42) Bongiovanni, M. N.; Scanlon, D. B.; Gras, S. L. *Biomaterials* **2011**, *32*, 6099–6110.
- (43) Li, C.; Adamcik, J.; Mezzenga, R. *Nat. Nanotechnol.* **2012**, *7*, 421–427.
- (44) Yan, H.; Nykanen, A.; Ruokolainen, J.; Farrar, D.; Gough, J. E.; Saiani, A.; Miller, A. F. *Faraday Discuss.* **2008**, *139*, 71–84.
- (45) Graham, H. K.; Hodson, N. W.; Hoyland, J. A.; Millward-Sadler, S. J.; Garrod, D.; Scothern, A.; Griffiths, C. E. M.; Watson, R. E. B.; Cox, T. R.; Erler, J. T.; Trafford, A. W.; Sherratt, M. *Matrix Biol.* **2010**, *29*, 254–260.
- (46) Muir, B. W.; Tarasova, A.; Gengenbach, T. R.; Menzies, D. J.; Meagher, L.; Rovere, F.; Fairbrother, A.; McLean, K. M.; Hartley, P. G. *Langmuir* **2008**, *24*, 3828–3835.
- (47) Muir, B. W.; Fairbrother, A.; Gengenbach, T. R.; Rovere, F.; Abdo, M. A.; McLean, K. M.; Hartley, P. G. *Adv. Mater.* **2006**, *18*, 3079–+.
- (48) Jung, J. M.; Savin, G.; Pouzot, M.; Schmitt, C.; Mezzenga, R. *Biomacromolecules* **2008**, *9*, 2477–2486.
- (49) Menzies, D. J.; Gengenbach, T.; Forsythe, J. S.; Biribilis, N.; Johnson, G.; Charles, C.; McFarland, G.; Williams, R. J.; Fong, C.; Leech, P.; McLean, K.; Muir, B. W. *Chem. Commun.* **2012**, *48*, 1907–1909.
- (50) Keselowsky, B. G.; Collard, D. M.; Garcia, A. J. *J. Biomed. Mater. Res., Part A* **2003**, *66A*, 247–259.
- (51) Price, R. L.; Ellison, K.; Haberstroh, K. M.; Webster, T. J. *J. Biomed. Mater. Res., Part A* **2004**, *70A*, 129–138.
- (52) Raffa, V.; Vittorio, O.; Pensabene, V.; Menciassi, A.; Dario, P. *IEEE Trans. Nanobiosci.* **2008**, *7*, 1–10.
- (53) Dolatshahi-Pirouz, A.; Pennisi, C. P.; Skeldal, S.; Foss, M.; Chevallier, J.; Zachar, V.; Andreasen, P.; Yoshida, K.; Besenbacher, F. *Nanotechnology* **2009**, *20*.
- (54) Kim, M. H.; Kino-Oka, M.; Kawase, M.; Yagi, K.; Taya, M. J. *Biosci. Bioeng.* **2007**, *103*, 192–199.
- (55) Vasilev, K.; Michelmore, A.; Martinek, P.; Chan, J.; Sah, V.; Griesser, H. J.; Short, R. D. *Plasma Processes Polym.* **2010**, *7*, 824–835.
- (56) Vasilev, K.; Michelmore, A.; Griesser, H. J.; Short, R. D. *Chem. Commun.* **2009**, 3600–3602.
- (57) Canavan, H. E.; Cheng, X. H.; Graham, D. J.; Ratner, B. D.; Castner, D. G. *J. Biomed. Mater. Res., Part A* **2005**, *75A*, 1–13.
- (58) Iuliano, D. J.; Saavedra, S. S.; Truskey, G. A. *J. Biomed. Mater. Res* **1993**, *27*, 1103–1113.

**Biomacromolecules**

Article

(59) Donoso, M. G.; Mendez-Vilas, A.; Bruque, J. M.; Gonzalez-Martin, M. L. *Int. Biodeterior. Biodegrad.* **2007**, *59*, 245–251.

(60) Grant, R. P.; Spitzfaden, C.; Altroff, H.; Campbell, I. D.; Mardon, H. J. *J. Biol. Chem.* **1997**, *272*, 6159–6166.

(61) Elter, P.; Lange, R.; Beck, U. *Colloid Surf, B* **2012**, *89*, 139–146.

(62) Moriyama, Y.; Watanabe, E.; Kobayashi, K.; Harano, H.; Inui, E.; Takeda, K. *J. Phys. Chem. B* **2008**, *112*, 16585–16589.